Durham E-Theses

Feshbach spectroscopy of an ultracold Rb-Cs mixture

JENKIN, DANIEL,LESTER

How to cite:

JENKIN, DANIEL,LESTER (2012) *Feshbach spectroscopy of an ultracold Rb-Cs mixture*, Durham theses, Durham University. Available at Durham E-Theses Online: http://etheses.dur.ac.uk/5799/

Use policy

The full-text may be used and/or reproduced, and given to third parties in any format or medium, without prior permission or charge, for personal research or study, educational, or not-for-profit purposes provided that:

- a full bibliographic reference is made to the original source
- a link is made to the metadata record in Durham E-Theses
- the full-text is not changed in any way

The full-text must not be sold in any format or medium without the formal permission of the copyright holders.

Please consult the full Durham E-Theses policy for further details.

Academic Support Office, The Palatine Centre, Durham University, Stockton Road, Durham, DH1 3LE
e-mail: e-theses.admin@durham.ac.uk Tel: +44 0191 334 6107
http://etheses.dur.ac.uk

Feshbach spectroscopy of an ultracold Rb-Cs mixture

Daniel L. Jenkin

A thesis submitted in partial fulfilment
of the requirements for the degree of
Doctor of Philosophy

Department of Physics
Durham University

November 14, 2012

Feshbach spectroscopy of an ultracold Rb-Cs mixture

Daniel L. Jenkin

Abstract

This thesis reports the observation of interspecies Feshbach resonances in an ultracold mixture of Rb and Cs atoms. A versatile combined magnetic and optical potential has been designed and constructed which is capable of bringing both ^{87}Rb and ^{133}Cs to degeneracy, and reaching high phase-space density in ^{85}Rb. High phase-space density mixtures are the first step required in the production of ultracold polar molecules, the topic of much current research.

The apparatus capitalises on the efficient capture of atoms by a magnetic trap from a magneto-optical trap, and the efficient sympathetic cooling of Cs by Rb therein. Upon transfer to the crossed optical dipole trap condensates in excess of 1×10^6 ^{87}Rb atoms and approximately 1×10^5 ^{133}Cs atoms are produced after direct evaporation and gravito-magnetic tilting of the potential. The observation of six interspecies ^{87}Rb^{133}Cs Feshbach resonances are reported, three of which had only been predicted theoretically, allowing testing and development of the theoretical model. Furthermore, the extrapolation of this model has predicted numerous Feshbach resonances between ^{85}Rb and ^{133}Cs, none of which have been experimentally observed prior to this work. The versatile nature of this apparatus is discussed, including the application of the current system to cooling of ^{85}Rb. Initial experiments observed seven interspecies resonances, including a broad $s-$wave resonance at a magnetic field of (644 ± 2) G which is in excellent agreement with the theoretical prediction. Further work has revealed that fourteen Feshbach resonances exist in the 0-700 G magnetic field range between ^{85}Rb and ^{133}Cs atoms in the $|2, +2\rangle$ and $|3, +3\rangle$ states, respectively. Several of these resonances would be ideal for magneto-association of RbCs molecules, prior to transfer to the rovibrational ground-state.

Declaration

I confirm that no part of the material offered has previously been submitted by myself for a degree in this or any other university. Where material has been generated through joint work, the work of others has been indicated.

Daniel L. Jenkin
Durham, November 14, 2012

The copyright of this thesis rests with the author. No quotation from it should be published without their prior written consent and information derived from it should be acknowledged.

Dedicated to mum,
for everything

Acknowledgements

My first thanks must go to everyone that I have worked with directly on the mixture project over the last four years, in particular my supervisor Simon Cornish and also Steve Hopkins for organisational support and explanation of concepts, fellow PhD students Michael Köppinger and Danny McCarron for help in the lab, and Hung-Wen Cho for guiding me through every measurement. I must also thank everyone in the labs next door and over the hall, Tim for everything Matlab, Kirsteen for helping me take data, Anna for her humour and Sylvi for introducing me to the merits of keeping rats.

The wider AtMol group as a whole have been supportive throughout my time here and have provided a friendly atmosphere to work in. In particular my fellow 'Durham class of 2008' students have always been a source of amusement in the office and on my infrequent trips to the tea room. The department's academic support staff and those in the mechanical and electronic workshops also deserve my gratitude as without them progress would have been a lot more difficult.

Outside of physics I have made a lot of good friends in my eight years here in Durham, and would like to thank all of those from my undergrad days that kept me going whilst doing my degree, especially my housemates for making my initial stint in Durham what it was. Of course the Galaxy football team remain the greatest club I have ever been a part of and the Mildert MCR of 2008-2010 were great fun to be around while I lived in college. Also, I could not have stayed sane throughout the PhD days without the local running and triathlon communities being what they are, or without my running shoes, thank you all for being with me in the 7000+ miles I've had to cover since starting.

I would like to thank everyone in my family and Liz's family for all of the support over the years, in particular mum and Michelle, who I thank for all of the emotional and financial support. Finally, the largest thanks of all must go to Liz, my long suffering girlfriend, she needs a medal for putting up with all the broken laser related moods, and making them all go away.

Contents

List of Figures

Figure Page

List of Tables

Chapter 1

Introduction

Since the first observation of Bose-Einstein condensation (BEC) in 1995 [1–3] the field of matterwave optics has progressed enormously. In addition to the original condensates of ^{87}Rb, ^{23}Na and ^{7}Li, degenerate gases are now routinely produced in other isotopes of these species and different alkali-metals such as ^{40}K [4], ^{41}K [5], ^{85}Rb [6–8], ^{6}Li [9] and ^{133}Cs [10–12]. Additional developments of the field have allowed degeneracy to be reached in the alkaline earth elements ^{40}Ca [13] and Sr [14–19] and in other systems such as ^{52}Cr [20], Yb [21–26], atomic H [27] and metastable He [28, 29]. More recently BEC has been achieved in exciton polaritons [30], magnons [31] and photons [32]. Prior to the Nobel prize being awarded for the realisation of BEC other atomic physics work in laser cooling was also awarded the Nobel prize [33–35]. Laser cooling is often the first step in trapping an ultracold cloud of atoms. BECs have many practical applications within atomic, molecular and condensed matter physics such as the atom laser [36–38] and matter-wave interferometry [39]. They also allow study of vortices [40–42] and vortex lattices [43], condensate collapse [44], soliton formation [45–48] and Anderson localisation [49, 50], all contributing towards knowledge of the behaviour of matter at ultracold temperatures.

Precise control over interactions within a BEC can be achieved in certain atomic species such as ^{85}Rb and ^{133}Cs through variation of the magnetically tunable scattering length. The creation of condensates in these species relied on control of the scattering length around Feshbach resonances [51] to produce a favourable ratio of elastic to inelastic collisions [6, 10]. Molecules may also be formed by ramping over a Feshbach resonance [52], providing an alternative to photoassociation [53]. Feshbach resonances also open up avenues to explore the aforementioned condensate collapse and soliton formation as well as modelling of cold atom collisions [54, 55].

The creation of ultracold molecules, via Feshbach resonances or otherwise, has been the subject of intense research in recent years after the demonstration of optically trapped fermionic [56, 57] and bosonic molecules [57, 58]. The transfer of these molecules to the absolute ground-state via stimulated Raman adiabatic passage (STIRAP) [59] proves to be the first step in studying interacting molecular gases. Being able to control the internal degrees-of-freedom of a homonuclear molecule is an important stepping stone on the way to studying dipolar quantum effects however the dipole moment of these single-species molecules is small [60]. Long-range magnetic dipole moments in Cr BECs have been observed to cause collapse in the condensate [61] and these long range interactions are predicted to be a feature of heteronuclear alkali-alkali molecules [62, 63]. Thus mixtures of quantum gases have been extensively studied in recent years due to their myriad of applications, from different spin-state mixtures [64, 65], to isotopic mixtures [9, 18, 66, 67] to heteronuclear mixtures [12, 68–84].

1.1 Ultracold mixtures and molecules

Quantum degenerate mixtures of atoms have received much attention due to the large range of experiments not possible in single-species experiments. Studies of interactions between the mixtures including phase separation between the constituent species is a rich area in both theoretical and experimental physics [64, 65, 85–88], with studies of the superfluid to Mott insulator transition [89] and novel quantum phases also possible within an optical lattice [90–92]. The choice of species with which to implement a mixture experiment is driven by the fascinating results that it is possible to produce by studying such a mixture, however the choice is often a technical one.

Atoms that cool efficiently such as ^{87}Rb are often employed as a refrigerant that will sympathetically cool another species - due to their favourable ratio of elastic to inelastic collisions they are employed as a collisional bath for the minority species. This technique was instrumental in reaching Fermi degeneracy [73], where s-wave collisions, vital for rethermalisation during evaporation, are forbidden due to the Pauli exclusion principle. The addition of a second species lifts this restriction and allows efficient sympathetic cooling to ensue. The technique has also been utilised in cooling of 'difficult' bosonic species such as ^{41}K [5], ^{133}Cs [12] or ^{85}Rb [7, 66].

There are two routes to the production of cold molecules, direct and indirect. The direct methods address a range of diatomic molecules which are typically cooled directly, with no need for initial association of atoms. Due to the rotational and vibrational structure in molecules being very complex adequate laser cooling has not been fully developed yet, however large strides are being taken in this field [93, 94]. Other techniques that are receiving attention are Stark deceleration [95, 96], buffer gas cooling [97, 98], sympathetic cooling [99], optical Stark deceleration [100], cooling molecules from a rotating source [101], photostop [102] and magnetic deceleration [103]. Whilst progress is being made in the direct cooling methods, typical temperatures after cooling are currently capped around the millikelvin range and the samples are far from degeneracy [104]. At present the phase-space densities (PSDs) achievable by indirect methods are much larger.

The indirect method of producing ultracold molecules harnesses the powerful laser cooling techniques available to individual atoms such as the alkali-metals and molecules are associated from these pre-cooled atomic clouds. The method of association can involve formation of molecules in an excited state after two colliding atoms absorb a photon, known as photoassociation [53], or magneto-association by ramping over a Feshbach resonance [52]. Photoassociation has recently been successful in transferring Cs_2 [105], LiCs [80] and RbCs [106] molecules into the ground-state, however due to its non-coherent nature transfer is inefficient resulting in low molecule number. Since transfer typically occurs from a magneto-optical trap (MOT) the molecular temperature is also limited to the MOT temperature.

Molecules associated via a Feshbach resonance are formed in an excited level, and transfer into the ground-state requires implementation of the STIRAP technique [59]. The magnetic resonance couples a bound molecular state with that of the atoms, hence by sweeping over the magnetic resonance we can produce weakly-bound Feshbach molecules. Feshbach molecules have been created in both homonuclear and heteronuclear mixtures, which is the first step towards creating a dipolar quantum gas. Importantly the transfer to the rovibrational ground-state has been performed with high efficiency for Rb_2 [107], Cs_2 [108] and for KRb, a molecule which consists of a fermion and a boson and has a large dipole moment [75]. Experiments are currently on the verge of producing a degenerate molecular gas of bosons [109].

The vast number of applications that ultracold polar molecules are applicable to justifies the amount of current research surrounding them. Potentially the most exciting of these is the possibility that polar molecules may be utilised as qubits in a quantum computer whereby the molecules, transferred to a lattice with a single-occupancy per lattice site, could be addressed individually via an electric field [110]. Polar molecules are also proposed to be instrumental in the precision measurement of fundamental constants such as the time dependency of the proton to electron mass ratio or the fine structure constant [111–114]. Indeed experimental measurements of the electron electric dipole moment [115] and the proton to electron mass ratio variation by observing absorption lines from molecular clouds [116] have already been obtained. The field of ultracold dipolar molecules is thus set to continue expanding.

1.2 Ultracold mixtures of RbCs

Cold mixtures of ^{87}Rb and ^{133}Cs atoms have been studied over the past decade for multiple reasons. From a technical standpoint, laser cooling of the two atoms is not challenging as diode lasers are available at the laser cooling frequencies for both atoms and single species condensates have been produced in the two atoms individually [1, 10]. The properties of the two atoms are complementary from the point of view that evaporation of ^{87}Rb in both magnetic and dipole traps is efficient, however high inelastic losses have plagued attempts to reach degeneracy in ^{133}Cs in magnetic traps [117]. Evaporation efficiency can drastically be increased with the implementation of sympathetic cooling of the ^{133}Cs after rethermalising collisions with ^{87}Rb.

At low magnetic fields the magnetic moment to mass ratios of the two species are a maximum of 2% different, hence good overlap is achieved within a magnetic trap leading to a high interspecies collision rate.

Scientific motivation for studying a mixture of ^{87}Rb^{133}Cs arose from the fact that the interspecies scattering properties were relatively unknown, despite the intraspecies interactions being well defined [118, 119]. Initial experiments focussed on trap loss within the two-species MOTs, where the time-evolution of trapped Rb atoms with and without Cs atoms present was studied.

More recent studies have confirmed that sympathetic cooling of ^{133}Cs by ^{87}Rb is indeed efficient, and temperatures of 6 μK have been reached prior to dipole trap transfer [12, 70]. Good sympathetic cooling is consistent with an appreciable interspecies scattering length and studies of rethermalisation between the two atomic species confirmed this, a scattering length of $(a_{\mathrm{RbCs}} = \left(700^{+700}_{-300}\right)\ a_0)$ being extracted from the data [120]. Knowledge of the system was advanced further upon observation of 25 interspecies Feshbach resonances between ^{133}Cs in the $|F = 3,\ m_F = +3\rangle$ state and ^{87}Rb in the $|F = 1,\ m_F = +1\rangle$ and $|F = 2,\ m_F = -1\rangle$ states. The ensuing analysis of the additional Feshbach and bound-state spectrum studies have resulted in a complete model of the system, with resonances up to magnetic fields of 667 G observed [121].

In theory any Feshbach resonance can be used to form Feshbach molecules, however a broad, entrance-channel dominated resonance is the ideal candidate, many of which exist and can be seen in figure 1.1. Transfer of these molecules to the rovibrational ground-state is perfomed via the STIRAP technique where a state superposition is formed from the initial Feshbach molecular state and the deeply bound molecular state, via an intermediate state [59]. The superposition state is formed by overlapping two light pulses in a ‘counterintuitive’ manner. The coupling laser between the ground-state and the intermediate level is first switched on, followed by the light that couples the Feshbach molecular state and the intermediate state. A good overlap of the Franck-Condon factors of the three states determines the efficiency of this method, hence molecular state selection is critical. The theory behind the STIRAP process is discussed in more detail in chapter 8.2. Current work is focussed on determining the best route to ground-state transfer [109].

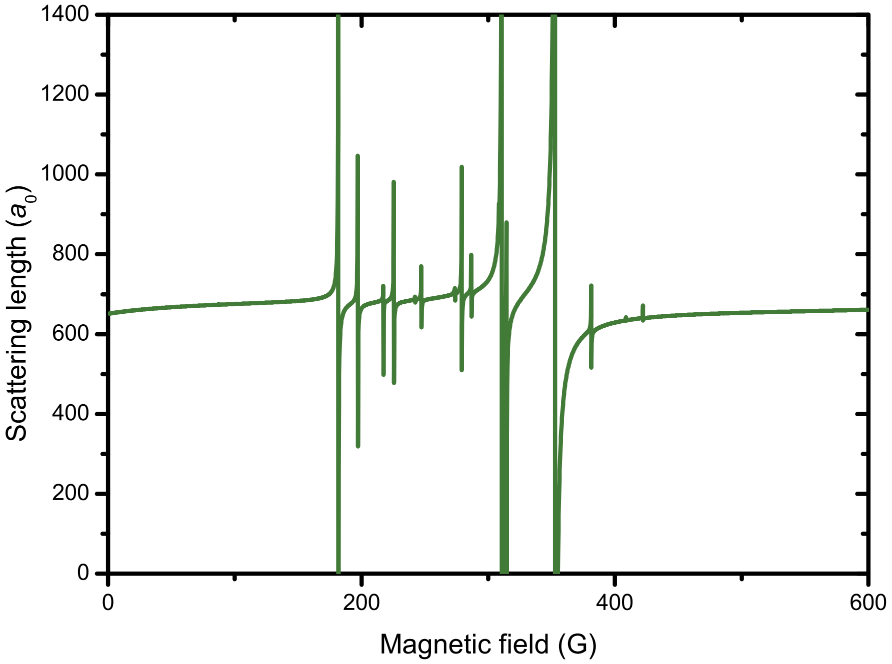

Figure 1.1: Interspecies ^{87}Rb^{133}Cs scattering length as a function of magnetic field for ^{87}Rb and ^{133}Cs atoms in the $|1,+1\rangle$ and $|3,+3\rangle$ states, respectively. All Feshbach resonances depicted in this plot have previously been observed [72, 121].

In addition to being polar the RbCs molecules are long lived. Unlike KRb molecules, RbCs is stable against the atom exchange interaction RbCs + RbCs → Rb_2 + Cs_2 [122]. They are therefore long-lived and are predicted to exhibit a dipole moment of 1.25 Debye [63], which is approximately a factor of 2 larger than for KRb [75], and several orders of magnitude larger than the atomic dipole moments. If an external DC electric field is applied to a polar molecule an electronic dipole moment is induced, and this makes them an ideal candidate for a quantum computer as the energy of dipolar interactions exceeds the thermal energy of the molecules at low temperature. Additionally the rotational constant of RbCs molecules is lower than that of KRb, hence smaller electric fields are required to achieve sizeable dipole moments [123, 124].

1.3 Overview of thesis

This thesis presents work on a system constructed to optically trap Rb and Cs atoms simultaneously and perform measurements of interspecies Feshbach resonances between Cs and the two naturally abundant isotopes of Rb. The document is largely focussed on the measurements taken using a system whose setup is discussed elsewhere [125–127], however in addition any technical improvements made are discussed in detail.

In brief the experimental procedure begins with the collection of atoms in a two-species MOT using a pyramid-MOT as a cold atom source. The two atomic species are separated from each other in the MOT by utilising a beam of light resonant with the Rb atoms to ‘push’ the Rb cloud, reducing the overlap of the two species [71]. Following compressed-MOT and molasses phases the atoms are optically pumped into the magnetically trappable stretched states to increase the spin-state purity of atoms when captured in the magnetic trap.

We load a quadrupole magnetic trap generated by a pair of coils in the anti-Helmholtz configuration. The magnetic field gradient is increased to values much larger than the minimum required to trap the Rb and Cs atoms in order to increase the collision rate. The Rb atoms are cooled using RF evaporation in the magnetic trap, a process which results in sympathetic cooling of Cs atoms after collisions with Rb atoms. As atoms cool they are captured in an optical potential generated by a high power fibre laser crossing at a point $\approx 70\ \mu$m below the magnetic trap centre. Once magnetic trap evaporation becomes less efficient the field gradient is reduced, resulting in more atoms being loaded into the optical trap. Within the optical trap fast, efficient evaporative cooling is performed by reducing the power of the trapping beams or by ‘tilting’ the potential with a magnetic field gradient [11]. At this stage a high phase-space density atomic mixture is realised, which is the ideal starting point for measurements of Feshbach resonances and molecule formation. The experimental procedure is summarised in figure 1.2.

The remaining chapters are arranged as follows:

- Chapter 2 discusses the basic theory involved in the different aspects

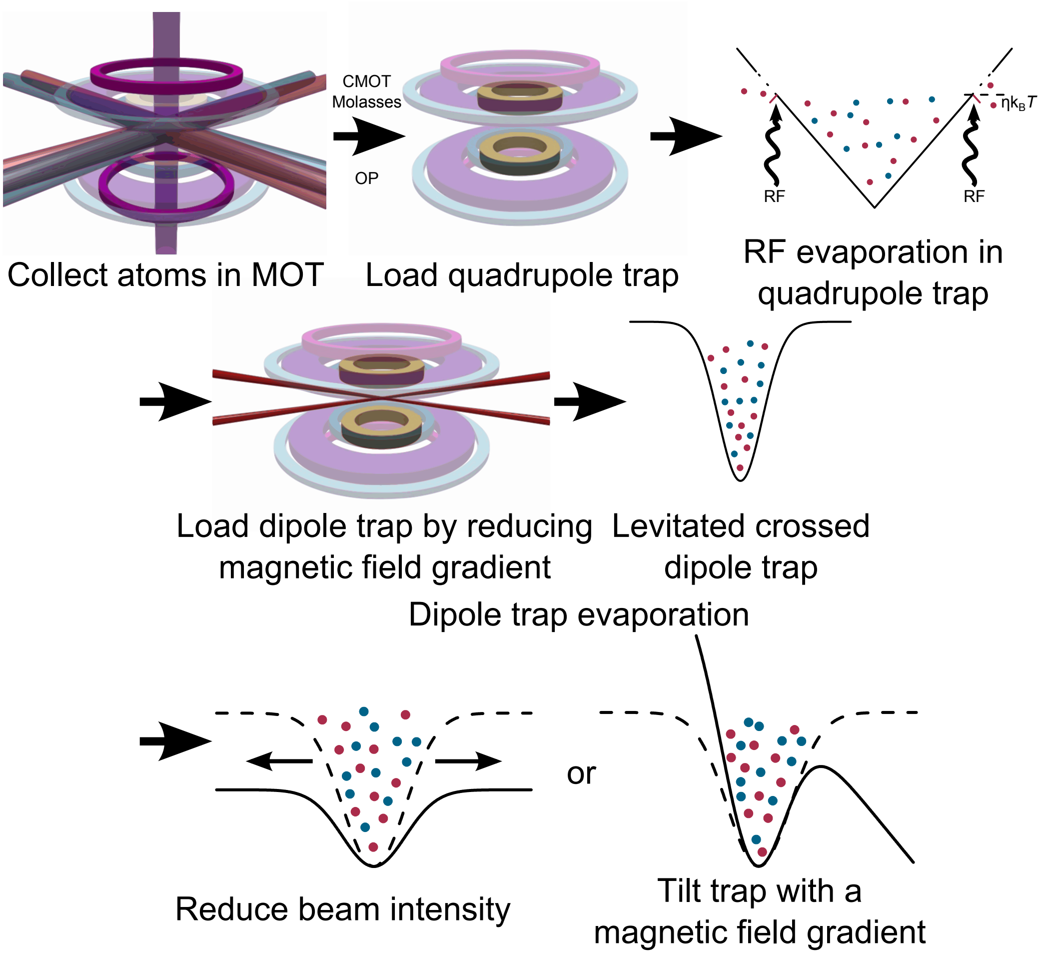

Figure 1.2: Illustration summarising the different stages of the experimental procedure. Atoms are collected in a two-species MOT before transfer to a quadrupole trap where the cloud temperatures are reduced efficiently via forced RF evaporation and sympathetic cooling of Cs. Once the evaporation in the quadrupole trap becomes less efficient the magnetic field gradient is reduced such that the atoms are trapped in a levitated crossed dipole trap. Evaporation continues in the dipole trap either by decreasing the beam powers to reduce the trap depth, or by applying a magnetic field gradient to ‘tilt’ the trap.

covered in this thesis. Only a brief treatment of each topic is reported and for a more detailed study the reader is referred to more comprehensive references.

- Chapter 3 gives an account of the experimental techniques utilised in this work to produce an ultracold atomic mixture. Many technical details can be found elsewhere in references [125–127], this section is only intended to introduce the reader to the methods used here.

- Chapter 4 describes modelling, design and implementation of the optical dipole trap used in this work. The chapter then covers the optimisation of evaporation taking place within the dipole trap and the condensation of ^{87}Rb.

- Chapter 5 contains data highlighting the gains made in the magnetic trap sympathetic cooling of ^{133}Cs by ^{87}Rb due to the other improvements made during the course of this work. The corresponding improvement in ^{133}Cs evaporation within the optical trap is then discussed, which consequently leads to larger ^{133}Cs BECs being produced.

- Chapter 6 reports the single-species results obtained at high-fields and the observation of interspecies ^{87}Rb^{133}Cs Feshbach resonances are then reported.

- Chapter 7 presents the results of theoretical models that predict a series of Feshbach resonances in a system of ^{85}Rb^{133}Cs, the alterations made to the setup in order to trap ^{85}Rb and the observation of many of these resonances.

- Chapter 8 draws conclusions made using the data presented in the previous chapters and presents an outlook towards the future goals of the experiment and the field of ultracold dipolar molecules.

Chapter 2

Background theory

Ultracold atomic mixtures and molecules are a rich and interesting area of physics that have been studied extensively. This chapter contains an introduction to various theoretical concepts that are required to understand the different sections of this thesis. A brief account of each concept is given, however the references within this chapter and the many review articles provide a more complete treatment [33–35, 41, 51, 52, 128, 129].

2.1 Scattering theory

Collisions between cold atoms are the fundamental building block behind evaporative cooling and the ability to reach degeneracy within a system of ultracold atoms. On a basic level they can be divided into two main categories: elastic and inelastic. Elastic collisions allow rethermalisation to occur resulting in a decrease in ensemble temperature, whereas inelastic collisions generally result in heating and losses. A favourable ratio of elastic to inelastic collisions is desirable and can dictate whether or not degeneracy within a system is possible. Interactions between the atoms in the ensemble are characterised by the s-wave scattering length.

2.1.1 Elastic collision cross section

The Hamiltonian describing the relative motion of two colliding atoms is the sum of the relative kinetic energy of the atoms and the interaction potential

$$H = \frac{\vec{p}^2}{2M} + V(\vec{r}), \tag{2.1}$$

where $\vec{p} = \vec{p}_1 - \vec{p}_2$, $\vec{r} = \vec{r}_1 - \vec{r}_2$ and $M = m_1 m_2/(m_1 + m_2)$ is the reduced mass. The spherical symmetry of the interaction potential allows it to be written in the form

$$H = \frac{\hbar^2}{2M}\left(\frac{1}{r^2}\frac{d}{dr}\left(r^2\frac{d}{dr}\right) - \frac{l(l+1)}{r^2}\right) + V(r), \tag{2.2}$$

where l is the angular momentum quantum number. The solutions to this Hamiltonian take the form

$$\psi_k(r) = e^{ikr} + f(\vec{k})\frac{e^{ikr}}{r}, \tag{2.3}$$

where $f(\vec{k})$ is the scattering amplitude, $\vec{k}$ is the wavevector of the scattered wave and $k = M\langle v_\mathrm{R}\rangle/\hbar$. Here $\langle v_\mathrm{R}\rangle = (16k_\mathrm{B}T/\pi M)^{1/2}$ is the mean relative velocity. The potential is assumed to vanish as $r \to \infty$.

The differential scattering cross section is the cross section per unit solid angle, given by

$$\frac{d\sigma(\vec{k})}{d\Omega} = \left|f(\vec{k})\right|^2. \tag{2.4}$$

The scattering amplitude can then be written in terms of Legendre polynomials ($P_l(\cos(\theta))$) if we assume the interaction to be symmetric and to only depend on θ [130]

$$f(\theta) = \frac{1}{2ik}\sum_{l=0}^{\infty}(2l+1)(e^{i2\delta_l} - 1)P_l(\cos(\theta)), \tag{2.5}$$

where δ_l are the phase shifts associated with each partial wave and the $l = 1, 2, 3, ...$ denote the contribution to the total scattering amplitude from each $s, p, d, ...$ partial wave. Integrating equation 2.5 over the full solid angle we obtain

$$\sigma = \frac{4\pi}{k^2} \sum_{l=0}^{\infty} (2l+1) \sin^2 \delta_l. \tag{2.6}$$

Due to the indistinguishable nature of the two particles the wavefunction must be symmetric for bosons and anti-symmetric for fermionic particles. If we exchange the particles' coordinates we in effect change the sign of the relative coordinates, hence $\vec{r} \to -\vec{r}$, $r \to r$, $\theta \to \pi - \theta$ and $\varphi \to \pi + \varphi$, where φ is the azimuthal angle. Hence the wavefunction becomes symmetric

$$\psi = e^{ikz} \pm e^{-ikz} + (f(\theta) \pm f(\pi - \theta)) \frac{e^{ikr}}{r}. \tag{2.7}$$

To calculate the scattering cross section for indistinguishable particles we must take into account the fact that the wavefunction must be (anti-)symmetric for bosonic (fermionic) particles, hence

$$\psi(\vec{r}_1, \vec{r}_2) = \epsilon \psi(\vec{r}_2, \vec{r}_1), \tag{2.8}$$

where $\epsilon = 1(-1)$ for bosons (fermions). We can construct an (anti-)symmetric scattering state such that the differential cross section reads [131]

$$\frac{d\sigma}{d\Omega} = \left| f(k,\theta) + \epsilon f(k, \pi - \theta) \right|^2. \tag{2.9}$$

Here $0 \leq \theta \leq \pi/2$.

Due to the $(-1)^l$ parity of the Legendre polynomials only even (odd) partial waves contribute to the bosonic (fermionic) scattering cross section. Thus the contribution of the even partial waves is doubled for bosons, whereas the contribution from odd partial waves is cancelled

$$\sigma = \frac{8\pi}{k^2} \sum_{l \text{ even}}^{\infty} (2l+1) \sin^2 \delta_l. \tag{2.10}$$

The converse is true for fermions, contributions from odd partial waves are doubled, whereas they are cancelled for even partial waves. The summation in equation 2.10 is then modified to count odd values of l only. Thus reaching quantum degeneracy in a single-species fermionic system is impossible to achieve due to the existence of the potential barrier on all partial waves other than for $l = 0$ (see section 2.1.3). The inclusion of a second species allows degeneracy to be achieved via sympathetic cooling [4]. Similarly the inclusion of an additional species in the bosonic case allows odd partial wave collisions to occur, important in a RbCs system. This also reduces the 8π prefactor of equation 2.10 to 4π.

2.1.2 Low energy scattering

The contribution of different partial waves in a collision process is dependent on the energy of the colliding particles. Partial waves with $l \neq 0$ experience a centrifugal barrier as well as the interaction potential (the $V(r)$ term in equation 2.2). If the relative kinetic energy is not large enough to overcome the barrier height scattering will not take place as the interparticle separation never becomes small enough such that $V(r)$ is non-negligible. In this situation all collisions are purely $s-$wave in origin and equation 2.10 becomes

$$\sigma = \frac{8\pi}{k^2} \sin^2 \delta. \tag{2.11}$$

Ignoring the effective range of the interaction the cross section becomes [132]

$$\sigma = \frac{8\pi a^2}{1 + k^2 a^2}, \tag{2.12}$$

where a is the s-wave scattering length.

It is possible to define two limits for equation 2.12. In the ultracold limit, where $ka \ll 1$, the de Broglie wavelength

$$\lambda_{\mathrm{dB}} = \sqrt{\frac{2\pi\hbar^2}{m k_{\mathrm{B}} T}}, \tag{2.13}$$

becomes much larger than the scattering length, hence σ is dependent only on a and saturates to a value of

$$\sigma_{\mathrm{ultracold}} = 8\pi a^2. \tag{2.14}$$

This is known as the ultracold limit, where σ is independent of E and T. Conversely, for $ka \gg 1$, the elastic cross section becomes unitarity limited and $\lambda_{\mathrm{dB}} \ll a$. This occurs at higher T, and σ is limited by the de Broglie wavevector

$$\sigma_{\mathrm{unitarity}} = \frac{8\pi}{k^2}. \tag{2.15}$$

These two limits are highlighted in figure 2.1.

Figure 2.1(a) shows that for small scattering lengths similar cross sections are predicted by equations 2.12 and 2.14 [133]. As the scattering length increases the ultracold limit becomes inaccurate, similarly for higher temperatures the ultracold limit becomes less applicable as we transfer into the unitarity limit. Figure 2.1(b) highlights the transfer between the two regimes at different temperatures. In the ultracold limit (dashed lines) the cross section is a constant value of $8\pi a^2$. Equation 2.12 saturates in the ultracold limit to approximately 3.6×10^{-9} cm^2 for ^{133}Cs and 7.3×10^{-12} cm^2 for ^{87}Rb. At higher temperatures the cross section is better approximated by the unitarity limit and becomes independent of scattering length.

2.1.3 Higher partial waves

At higher temperatures the kinetic energy of the atoms may be large enough such that contributions to the cross section from other partial waves become significant as their energy is larger than the centrifugal barrier. This potential is of the form

$$V_{\mathrm{cen}} = \frac{\hbar^2 l(l+1)}{2mr^2}. \tag{2.16}$$

For higher partial waves to contribute to the cross section the minimum energy required is

$$E_{\mathrm{min}} = \frac{\hbar^2 l(l+1)}{2MR_{\mathrm{min}}^2} - \frac{C_6}{R_{\mathrm{min}}^6}, \tag{2.17}$$

where C_6 is the van der Waals coefficient and R_{min} is the separation for which the effective potential is a maximum

$$R_{\mathrm{min}} = \sqrt{\frac{6MC_6}{\hbar^2 l(l+1)}}. \tag{2.18}$$

Using the values for the C_6 coefficients given in table 2.1 and equations 2.17 and 2.18 it is possible to calculate the relevant threshold tem-

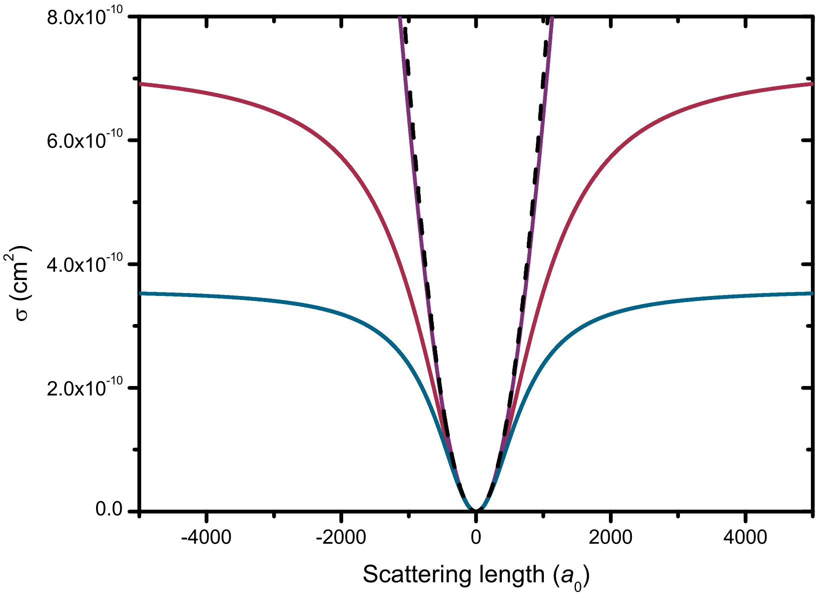

(a)

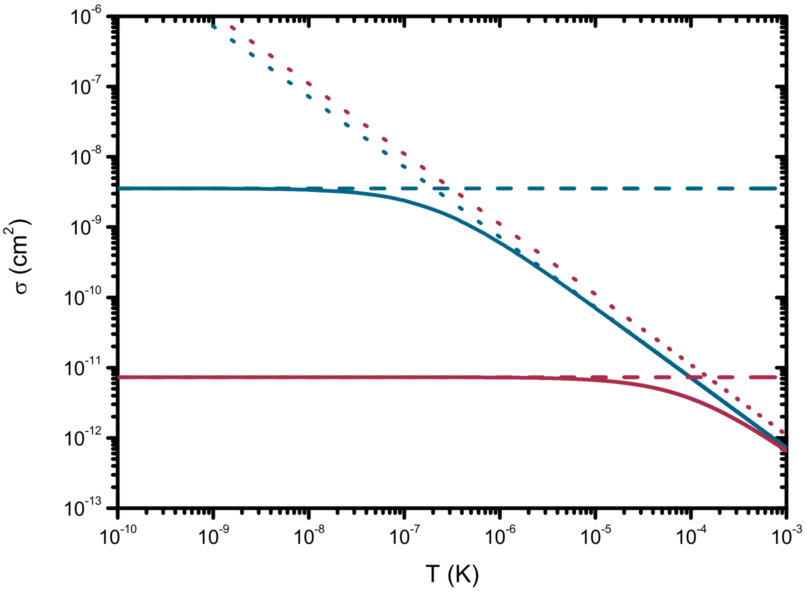

(b)

Figure 2.1: Elastic cross section as a function of scattering length (a) and of temperature (b). In (a) the cross section has been calculated for ^{133}Cs at temperatures of 2 μK (blue), 1 μK (red) and 0.1 μK (purple) using equation 2.12. The cross section in the ultracold limit (equation 2.14) is also displayed (black dashed). In (b) the cross section is displayed for ^{87}Rb (red) for the background scattering length of 102 a_0 and for ^{133}Cs (blue) with a background scattering length of 2250 a_0, where $a_0 = 0.0529$ nm is the Bohr radius. Also displayed are the cross sections in the ultracold limit (dashed lines) and in the unitarity limit (dotted lines).

Species	C_6 (a.u.)
^{87}Rb-^{87}Rb	4691
^{133}Cs-^{133}Cs	6851
^{87}Rb-^{133}Cs	5284

Table 2.1: C_6 coefficients for ^{87}Rb-^{87}Rb scattering, ^{133}Cs-^{133}Cs scattering and ^{87}Rb-^{133}Cs scattering in atomic units [134, 135]. To convert the values of C_6 into S. I. units the coefficient is multiplied by a_0^6 and $E_\mathrm{h} = \hbar^2/(m_\mathrm{e}a_0^2)$, the Hartree energy.

peratures for d-wave scattering in homonuclear systems of ^{87}Rb and ^{133}Cs. For ^{133}Cs at a temperature of 180 μK $d-$wave collisions begin to contribute, and in ^{87}Rb the temperature is 410 μK. Due to the distinguishable nature of ^{87}Rb-^{133}Cs collisions $p-$wave collisions also contribute to the elastic cross section. Here $d-$wave collisions begin to contribute at 290 μK and $p-$wave collisions at temperatures of 56 μK. It is worth noting that the $d-$wave threshold temperatures are larger than typical MOT temperatures hence we will not consider $d-$wave collisions here, however the $p-$wave threshold is lower for ^{87}Rb-^{133}Cs, hence will contribute during the MOT and magnetic trap phases of the experiment.

2.1.4 Inelastic collisions

The elastic collision rate provides an upper bound to the efficiency of evaporation, however it is limited by the presence of inelastic collisions which change the total kinetic energy of the system. This gain in kinetic energy is generally larger than the trap depth of the potential, resulting in atom loss. Generally speaking inelastic collisions can be categorised into three broad types of loss; background gas collisions of cold atoms with residual gas in the system, two-body collisions which change the electronic structure of the system and three-body collisions in which molecule formation may occur.

Background gas collisions

Collisions with the background gas in the vacuum system result in the loss of one cold atom per collision event. The rate of loss of this nature depends only on the background gas pressure and the total atom number, not the density of the ensemble. Hence these collisions will result in a reduction of atom number but do not lead to significant increases in temperature. The loss rate due to background gas collisions is given by $1/\tau_B$. Typical background lifetimes are of the order of hundreds of seconds.

Two-body collisions

Two-body collisions result in a change of the atoms' internal states. The only two-body inelastic mechanisms which are not energetically forbidden are dipolar angular momentum changing collisions. The two possible processes by which this may occur are direct spin-spin coupling between colliding atoms and the 2^{nd}-order spin-orbit interaction. In the alkali metals these interactions are opposite in sign, so one has the effect of working to cancel the other. In ^{87}Rb their magnitudes are so similar that two-body losses are effectively suppressed, hence the anomolously low two-body loss rate (K_2) in ^{87}Rb. Conversely for ^{133}Cs in the $|3,-3\rangle$ state K_2 is much larger [60], resulting in an increase in inelastic loss processes, an effect which has hampered condensation of ^{133}Cs in many experiments [117, 136]. Transferring the atoms into the absolute ground state suppresses two-body losses for energetic reasons [137], a step which was required for the production of a ^{133}Cs condensate [10]. K_2 is dependent on the density of the atoms, hence a higher loss rate is observed in higher PSD ensembles.

Three-body collisions

Three-body processes occur when two particles form a compound while interacting with a third atom (required to conserve energy and momentum), resulting in the formation of a diatomic molecule. The molecular binding energy is then released as kinetic energy. The energy of both the molecule and the atom is generally greater than the trap depth, hence three atoms are lost per collision event. Occasionally the third atom remains trapped and collides with an additional atom, distributing the kinetic energy as recombination energy [138]. The three-body loss rate, K_3, is dependent on the square of the atomic density therefore, as in two-body processes, it occurs most at the centre of the trap where the density is largest. The average energy of the atoms at this location is smaller than the average energy of the ensemble, so after rethermalisation the average ensemble energy, and hence temperature increase, in a process known as 'anti-evaporation'.

Experimentally inelastic loss rates are identified by measuring loss from conservative traps, however distinguishing between two- and three-body processes can be difficult. This complication is removed however by either using ^{87}Rb or transferring atoms to the absolute ground state [139, 140]. Previous work reports an increase in loss processes near a Feshbach resonance [141, 142].

Single species inelastic collision rates

The time-evolution of the ensemble atom-number is described by the sum of the loss rates due to the three distinct processes described above [143]

$$\frac{dN}{dt} = -\frac{N}{\tau_{\mathrm{B}}} - K_2 < n > N - K_3 < n^2 > N, \tag{2.19}$$

where $1/\tau_{\mathrm{B}}$ is the background gas collision rate and n is the atomic density. We can calculate

$$< n >= \frac{1}{N} \int n(\vec{r})^2 d^3r, \tag{2.20}$$

and

$$< n^2 >= \frac{1}{N} \int n(\vec{r})^3 d^3r = \frac{8}{\sqrt{27}} < n >^2, \tag{2.21}$$

for a Gaussian distribution.

Two-species inelastic collision rates

The presence of a second species within a trap results in extra terms being introduced to equation 2.19. For example in a RbCs system the additional loss terms involve two-body losses due to Rb colliding with Cs and three-body losses due to Rb-Rb-Cs and Rb-Cs-Cs collisions

$$
\begin{aligned}
\frac{dN_{\mathrm{Rb}}}{dt} = & -\frac{N_{\mathrm{Rb}}}{\tau_{\mathrm{B,Rb}}} - K_{2,\mathrm{RbRb}} \int n_{\mathrm{Rb}}(\vec{r})^2 d^3r - K_{2,\mathrm{RbCs}} \int n_{\mathrm{Rb}}(\vec{r}) n_{\mathrm{Cs}}(\vec{r}) d^3r \\
& - K_{3,\mathrm{RbRbRb}} \int n_{\mathrm{Rb}}(\vec{r})^3 d^3r - K_{3,\mathrm{RbRbCs}} \int n_{\mathrm{Rb}}(\vec{r})^2 n_{\mathrm{Cs}}(\vec{r}) d^3r \\
& - K_{3,\mathrm{RbCsCs}} \int n_{\mathrm{Rb}}(\vec{r}) n_{\mathrm{Cs}}^2(\vec{r}) d^3r,
\end{aligned}
\tag{2.22}
$$

where $n_{\mathrm{Rb(Cs)}}$ is the density of trapped Rb (Cs) atoms, $K_{2,\mathrm{RbCs}}$ is the two-body loss coefficient due to Rb-Cs collisions and $K_{3,\mathrm{RbRbCs(RbCsCs)}}$ is the three-body loss rate due to Rb-Rb-Cs (Rb-Cs-Cs) collisions [68]. It may be noted that switching the subscripts Rb and Cs in equation 2.22 will describe the time-evolution of the Cs atom number in the trap.

Results of previous studies have revealed that the two- and three-body loss coefficients are similar for both isotopes of Rb in a MOT. Further, it was discovered that there is an order of magnitude difference between the loss rate of ^{87}Rb as compared to that of ^{133}Cs, which, although to be expected due to the mass difference between the atoms, is larger than can be attributed to the mass ratio alone. It has been suggested that it is due to different interaction potentials and changes in trap depth between the two cases [68].

2.2 Feshbach resonances

2.2.1 Basic theory

Feshbach resonances have become the topic of intense research since their first observation [144] and have now been observed in most of the alkali atoms, and in many heteronuclear mixtures [51]. They can be understood by considering two molecular potentials, $V_{\mathrm{o}}(r)$ and $V_{\mathrm{c}}(r)$, where for large separations V_{o} connects two free atoms [51]. For low energy (E_{c}) scattering this potential represents an energetically open channel, alternatively called the entrance channel. Feshbach resonances occur when the entrance channel is coupled to a molecular bound state supported by $V_{\mathrm{c}}(r)$ (the closed channel). The coupling strength can be tuned via a magnetic field if the open and closed channel have different magnetic moments, resulting in high tunability of scattering length around a Feshbach resonance, as described in figure 2.2. Feshbach resonances now have many applications including molecule formation [52] and condensate collapse and soliton formation [44–48].

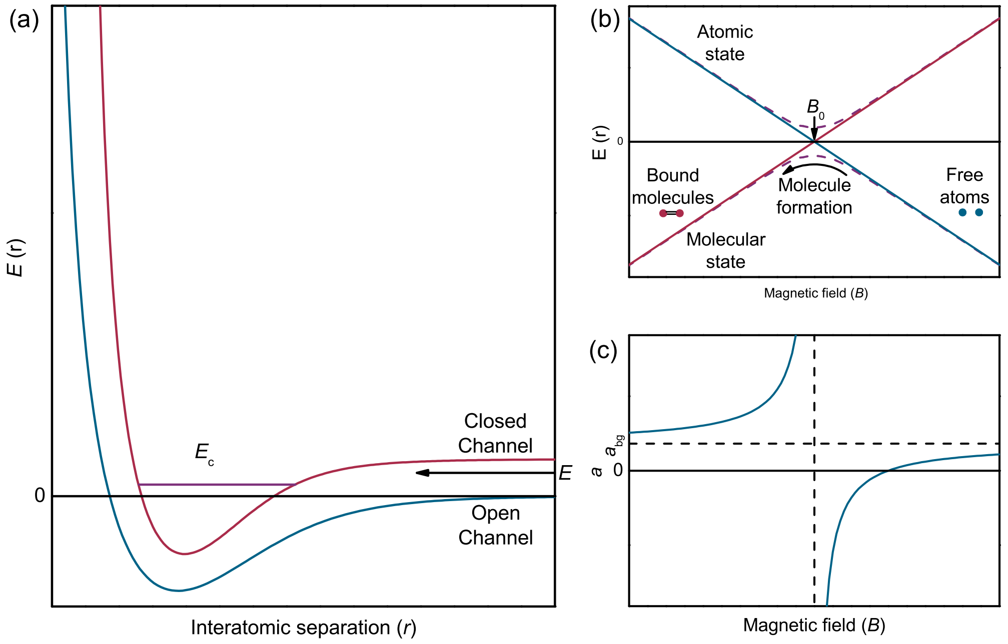

Figure 2.2: Schematic of a Feshbach resonance. (a) When two atoms collide if their energy E (blue) is similar to that of a bound molecular state (red) of energy E_c they can couple resonantly. The energy difference may then be tuned by the magnetic field if the atomic and molecular magnetic moments differ. (b) The magnetic field dependence of the energy of the atomic continuum (blue) and molecular bound state (red). The two energies coincide at the location of the resonance (B_0) and the corresponding strong coupling between the open and closed channels leads to an avoided crossing (purple dashed lines). Molecule formation is performed by adiabatically sweeping the magnetic field in the appropriate direction to convert free atoms into loosely bound molecules (see section 2.2.2). (c) The scattering length becomes highly tunable in the vicinity of a Feshbach resonance, following the form of equation 2.23. The resonance is centred on B_0, where $a \rightarrow \pm\infty$ and the width is defined as $B - B_0$ when $a = 0$. Far away from the resonance centre $a \rightarrow a_\mathrm{bg}$.

In the vicinity of a Feshbach resonance the scattering length varies as [145]

$$a(B) = a_\mathrm{bg}\left(1 - \frac{\Delta B}{B - B_0}\right), \tag{2.23}$$

where a_{bg} is the background scattering length far from the resonance, ΔB is the resonance width, the change in field required for a to be equal to 0 and B_0 is the resonance centre where the scattering length becomes infinity. The entrance channel's last bound vibrational level determines a_{bg}. Due to the divergence of the scattering length and the a^4 dependence of three-body loss rate, enhanced inelastic losses are an experimental feature used to detect the location of a Feshbach resonance [138].

2.2.2 Molecule formation

As shown in figure 2.2(b) loosely bound molecules can be formed by adiabatically ramping the magnetic field through the resonance, such that the atoms follow the avoided crossing. The direction of the sweep is dictated by the fact that the association technique only works for real bound molecular states where $E_{\mathrm{c}} < 0$ [146], in the figure this represents a sweep from high to low fields. Molecules formed via this method have large separations, are loosely bound and are known as Feshbach molecules. Ramping back over the resonance above the scattering continuum causes the molecules to rapidly dissociate into atoms.

The nature of the molecules being short lived with very small trap lifetimes necessitates a transfer into an optical lattice with only one molecule per lattice site [147]. This method has resulted in increased lifetimes in the trap of up to 700 ms. To obtain longer trap lifetimes transfer to the ground-state is required, one of the many ongoing challenges, as discussed in chapter 1 [107, 148, 149].

2.2.3 Feshbach structure of ^{133}Cs

The collisional properties of ^{133}Cs have been well known since the year 2000 when the results of two studies were published [54, 55]. Experimental work focussed on the identification of Feshbach resonances in the 0-230 G field range [54]. In excess of 25 resonances were observed across the different spin states, and K_2 was determined. The resulting theoretical study [55] involved a coupled-channel analysis and was able to predict all the observed Feshbach resonances. A zero crossing of the scattering length was predicted at 17.1 G which allows precise control of interactions [150] and the possibility for soliton production [44]. Moreover, the existence of a small field range between 21-25 G where the scattering length is favourable for rethermalisation opened up the possibility of Bose-Einstein condensing ^{133}Cs [10]. Extrapolating the calculation allows a calculation of the scattering length to be made for field values in excess of 1000 G. This reveals the existence of various other Feshbach resonances, including broad resonances at approximately 549 G and 787 G [151]. The ^{133}Cs scattering length for magnetic fields of 0-1000 G can be observed in figure 2.3.

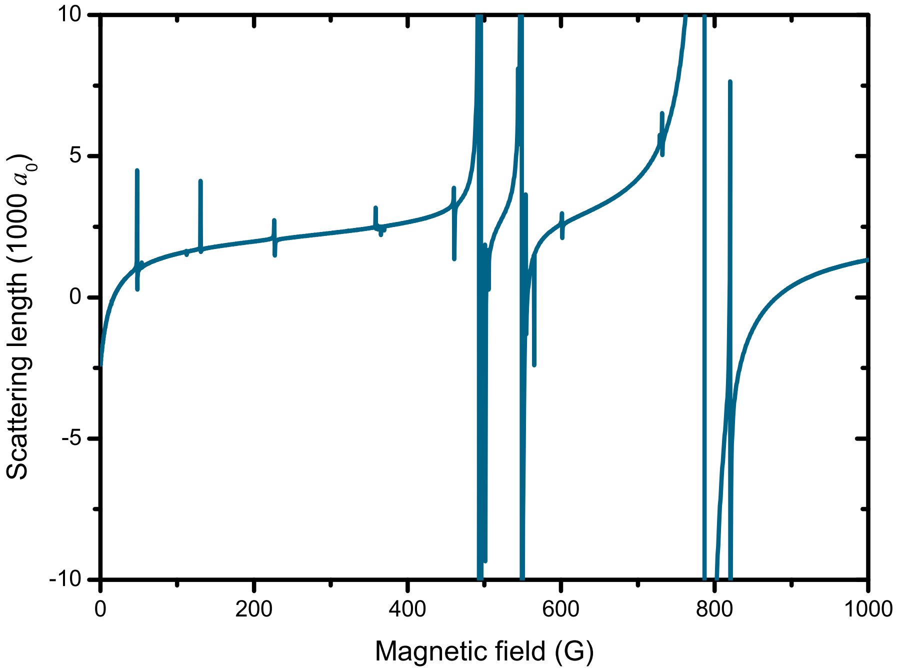

Figure 2.3: ^{133}Cs scattering length between magnetic fields of 0-1000 G for the $|3, +3\rangle$ state [151].

Many of the features displayed in figure 2.3 have been observed [152, 153]. One interesting feature of the data is the large s-wave Feshbach resonance at 787 G which is broad so would allow precise control of the scattering length in the region. This region is also potentially more promising for the formation of solitons than the low-field region as there are no Feshbach resonances between the field where $a \sim 200\ a_0$ and the zero crossing in the scattering length at ≈ 881 G. Additionally, evidence for the existence of Efimov features in ^{133}Cs have also been observed at various magnetic fields [152, 154].

2.2.4 Feshbach structure of ^{87}Rb^{133}Cs

As described in chapter 1 the properties of a ^{87}Rb and ^{133}Cs mixture have been well studied and the culmination of this work resulted in the observation of twenty-three resonances in the $|1, +1\rangle$ and $|3, +3\rangle$ states, and two resonances in the $|2, -1\rangle$ and $|3, +3\rangle$ states, in ^{87}Rb and ^{133}Cs respectively [72]. The locations and widths of these resonances have been precisely obtained [153] and the existence of many additional resonances up to magnetic fields of 667 G have led to a coupled-channel model of the ^{87}Rb^{133}Cs scattering length being developed for fields in excess of 1000 G. This complete model has predicted several resonances at magnetic fields higher than the 0-667 G field range that have not been observed to date. The ^{87}Rb^{133}Cs scattering length as a function of magnetic field is presented in figure 2.4.

2.3 Bose-Einstein condensation

Since the prediction of the BEC phase in 1925 and the first experimental observation 70 years later much experimental and theoretical work has been performed in the field [1–3, 155, 156]. Here we consider basic theory surrounding condensates, for a full treatment see the literature on the subject [38, 41].

2.3.1 Basic theory

For an ideal system of bosons (integer spin particles) the energy distribution as a function of temperature is described by the Bose-Einstein distribution

$$f(\epsilon) = \frac{1}{e^{(\epsilon-\mu)/k_B T} - 1}, \tag{2.24}$$

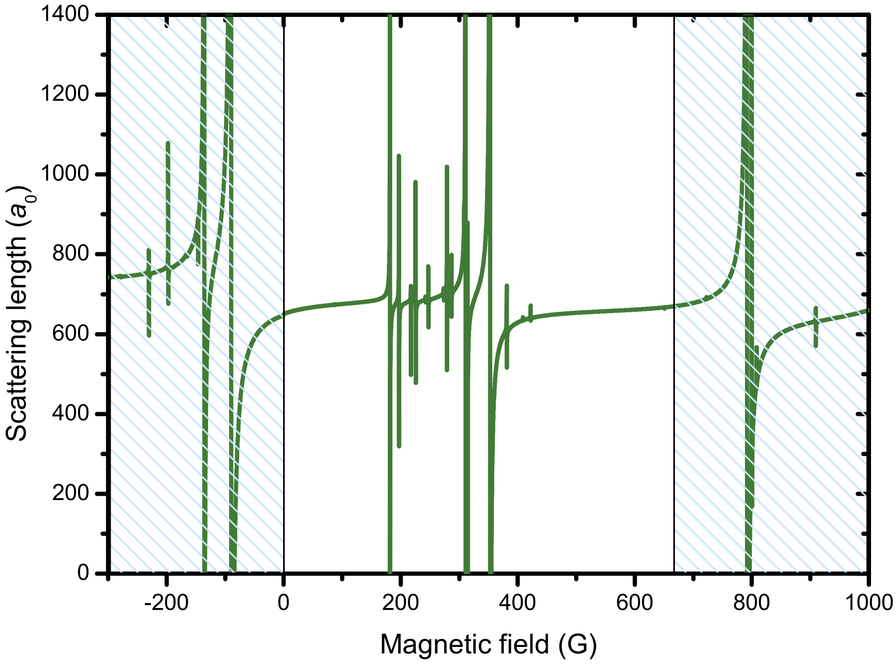

Figure 2.4: Interspecies ^{87}Rb^{133}Cs scattering length as a function of magnetic field for ^{87}Rb and ^{133}Cs atoms in the $|1,+1\rangle$ and $|3,+3\rangle$ states (positive fields) and for the $|1,-1\rangle$ and $|3,-3\rangle$ states (negative fields), respectively. Feshbach resonances have been observed in the 0-667 G region previously [72, 121], however those in the shaded regions are predicted but not yet observed.

where ϵ is the particle energy and μ is the chemical potential. Apart from a sign change in the denominator this expression is identical when applied to fermions (spin-1/2 particles). Occupation of the ground-state increases as $T \to 0$, and the population of the ground-state becomes macroscopically large. The atoms remaining in the excited states continue to behave as thermal atoms, however the condensed fraction are described by a single wavefunction.

At colder temperatures the atoms can be visualised as wavepackets and they can be assigned a de Broglie wavelength (see equation 2.13). λ_{dB} increases as temperature decreases, and when the de Broglie wavelength approaches the separation distance between the atoms their wavefunctions overlap. Thus the atoms condense, which can be parameterised in terms of the PSD exceeding

2.612

$$n\lambda_{\mathrm{dB}}^{3} \geq 2.612, \tag{2.25}$$

where n is the number density of the atoms [130].

2.3.2 Bose-Einstein condensation in a harmonic trap

In experiments atomic gases are non-uniform and are typically trapped in potentials providing harmonic confinement, which is the case in this work

$$U(\vec{r}) = \frac{1}{2}m\left(\omega_x^2 x^2 + \omega_y^2 y^2 + \omega_z^2 z^2\right), \tag{2.26}$$

where $\omega_{x,y,z}$ are the trap frequencies in the $x-$, $y-$ and $z-$directions respectively. In the scenario where all particles in the system are just located in the excited states, where any further reduction in temperature would result in ground-state occupation, the total number of particles can be calculated

$$N_{\mathrm{tot}}\left(T_{\mathrm{c}}, \mu = 0\right) = \int_0^{\infty} g(\epsilon)\frac{1}{e^{\epsilon/k_{\mathrm{B}}T_{\mathrm{c}}} - 1}d\epsilon \tag{2.27}$$

where $g(\epsilon)$ is the density of states, which is dependent on the potential used. Here the chemical potential must be zero, as we stipulated that if any particle were to be added, it would have to go into the ground state, thus there would be no change to the energy, assuming N is large and the zero-point energy may be neglected. For the harmonic potential described by equation 2.26, the solution to equation 2.27 is [130]

$$T_{\mathrm{c}} = \hbar\omega_{\mathrm{ho}}\left(\frac{N}{\zeta(3)}\right)^{1/3} = \hbar\omega_{\mathrm{ho}}\left(\frac{N}{1.202}\right)^{1/3} = 0.94\hbar\omega_{\mathrm{ho}}N^{1/3}, \tag{2.28}$$

where $\zeta(3)$ is the Riemann zeta function and ω_{ho} is the geometric mean trap frequency.

Above T_{c} the chemical potential becomes N-dependent and the population of the ground-state is zero. As the temperature decreases below T_{c} the number of thermal atoms drops far below N_{tot}, and thus to conserve total atom number the other atoms are in the condensed state. The number of particles within the condensate is given by [130]

$$N_0(T) = N_{\text{tot}} - N_{\text{ex}}(T). \tag{2.29}$$

Inserting equation 2.28 into equation 2.29 the condensate fraction as a function of temperature can be found [41, 157]

$$\frac{N_0}{N} = 1 - \left(\frac{T}{T_{\text{c}}}\right)^3. \tag{2.30}$$

2.3.3 Interactions within a Bose-Einstein condensate

We have previously considered only a gas without interactions, to take account of interactions within a condensate the mean-field or Hartree approach is applied [130]. In the condensate all particles are in the same condensed state $\phi(\vec{r})$, therefore the $N-$particle wavefunction can be written

$$\Psi\left(\vec{r}_1, \vec{r}_2, ..., \vec{r}_N\right) = \prod_{i=1}^{N} \phi\left(\vec{r}_i\right), \tag{2.31}$$

where $\phi\left(\vec{r}_i\right)$ are the single-particle wavefunctions and are normalised to unity. Using mean-field theory the interactions taking place over distances smaller than the interparticle spacing are not taken into account, and the effective Hamiltonian is

$$H = \sum_{i=1}^{N}\left(\frac{\vec{p}_i^2}{2m} + U_{\text{ext}}\left(\vec{r}_i\right)\right) + g\sum_{i<j}\delta\left(\vec{r}_i - \vec{r}_j\right), \tag{2.32}$$

where U_{ext} is the external potential and g is the interaction term

$$g = \frac{4\pi\hbar^2 a}{m}. \tag{2.33}$$

The Hamiltonian in equation 2.32 yields the time-dependent Gross-Pitaevski equation (GPE)

$$i\hbar\frac{\partial}{\partial t}\Psi\left(\vec{r}, t\right) = \left(\frac{-\hbar^2}{2m}\nabla^2 + U_{\text{ext}}\left(\vec{r}\right) + g\left|\Psi\left(\vec{r}, t\right)\right|^2\right)\Psi\left(\vec{r}, t\right). \tag{2.34}$$

Here $|\Psi(\vec{r},t)|^2$ is the number density ($n(\vec{r})$). This describes the condensate's time-evolution. If $\Psi(\vec{r},t)$ is expressed in terms of a product of $\phi(\vec{r})$ and the time-dependent exponential $e^{-i\mu t/\hbar}$, minimising the energy with respect to variations of the condensed state wavefunction yields the time-independent GPE

$$\left(-\frac{\hbar^2\nabla^2}{2m} + U_{\mathrm{ext}}(\vec{r}) + g\,|\psi(\vec{r})|^2\right)\psi(\vec{r}) = \mu\psi(\vec{r}), \tag{2.35}$$

where μ is the chemical potential and

$$\psi(\vec{r}) = N^{1/2}\phi(\vec{r}), \tag{2.36}$$

is the condensed state wavefunction. The GPE has the form of a non-linear Schrödinger equation due to the interaction term being quadratic in $|\psi(\vec{r})|^2$. If the interaction is 'switched off', equation 2.35 is reduced to a linear Schrödinger equation.

Dynamics within a two-species Bose-Einstein condensate

Interactions within a two-species BEC provide access to physics inaccessible within a single-species condensate, in addition to allowing condensation of species that are 'difficult' to evaporatively cool [5, 10] and the onset of Fermi degeneracy to be reached [4]. Quantum degenerate mixtures are analytically described by a pair of coupled GPEs which incorporate an additional interaction term to account for interspecies interactions [87, 158]

$$\left(-\frac{\hbar^2}{2m_1}\nabla^2 + U_1(\vec{r}) + g_{11}\,|\psi_1(\vec{r})|^2 + g_{12}\,|\psi_2(\vec{r})|^2\right)\psi_1(\vec{r}) = \mu_1\psi_1(\vec{r}), \tag{2.37}$$

$$\left(-\frac{\hbar^2}{2m_2}\nabla^2 + U_2(\vec{r}) + g_{21}\,|\psi_1(\vec{r})|^2 + g_{22}\,|\psi_2(\vec{r})|^2\right)\psi_2(\vec{r}) = \mu_2\psi_2(\vec{r}), \tag{2.38}$$

where the subscripts denote which species the individual terms apply to. The interspecies interaction strengths are the g_{11} and g_{22} terms and the interspecies interactions are described by the g_{12} and g_{21} terms [87]

$$
\begin{aligned}
g_{11} &= \frac{4\pi\hbar^2 a_{11}}{m_1}, && (2.39)\\
g_{22} &= \frac{4\pi\hbar^2 a_{22}}{m_2}, && (2.40)\\
g_{12} = g_{21} &= 2\pi\hbar^2 a_{12}\left(\frac{m_1+m_2}{m_1 m_2}\right), && (2.41)
\end{aligned}
$$

where a_{11} and a_{22} are the intraspecies scattering lengths and a_{12} is the interspecies scattering length.

The mixture dynamics are dictated by the relative strength between the intra- and interspecies interaction strengths [87]

$$\Delta = \frac{g_{12}}{\sqrt{g_{11}g_{22}}} = \frac{a_{12}}{\sqrt{a_{11}a_{22}}}\sqrt{\frac{(m_1+m_2)^2}{4m_1 m_2}} \approx \frac{a_{12}}{\sqrt{a_{11}a_{22}}}. \tag{2.42}$$

There are three regions of interest that concern equation 2.42, each of these is highlighted in figure 2.5. They are stable and miscible condensates ($|\Delta| < 1$), forming interpenetrating superfluids [64], stable and immiscible condensates ($\Delta > 1$), where the condensate phases separate and don't overlap, and unstable condensates that are miscible ($\Delta < -1$), which are attractive.

Due to the a terms in equation 2.42 the interspecies interactions can be tuned by the scattering length and hence the magnetic field. This can be via the dependence of the intra- or interspecies scattering lengths on magnetic field, or both, which has already been demonstrated in a system of ^{87}Rb-^{85}Rb[84], and more recently in a ^{87}Rb^{133}Cs system [12].

2.3.4 The Thomas-Fermi approximation

In sufficiently large harmonically trapped condensates the ratio between the kinetic and interaction energies becomes small. In this limit the GPE can be solved by neglecting the kinetic term in equation 2.35, which is known as

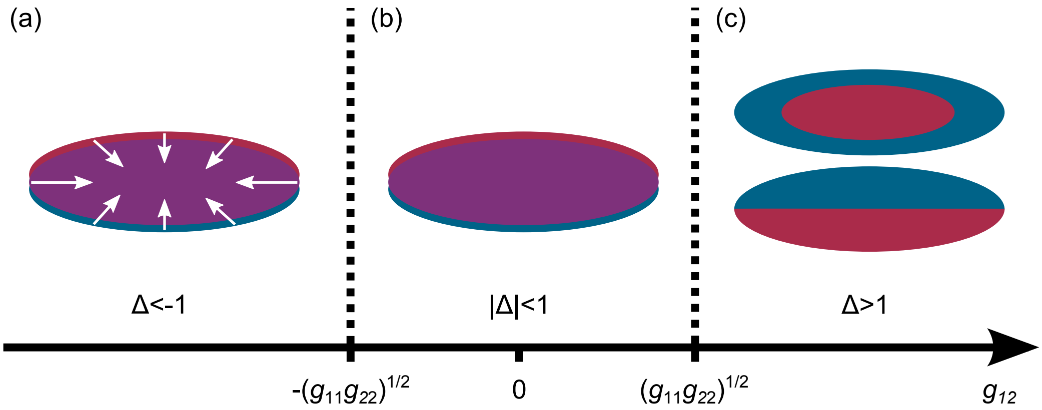

Figure 2.5: Interactions between two-species BECs as a function of the relative interaction strength, Δ (equation 2.42). Miscibility is determined by the value of Δ. For $\Delta < -1$ (a) the system is miscible (purple regions highlight the overlap of the mixture), however the attractive interspecies interactions dominate and the system becomes unstable against collapse. For $|\Delta| < 1$ the system is stable and miscible as the intraspecies interactions are larger and two interpenetrating superfluids coexist. For $\Delta > 1$ the interspecies interactions are repulsive and overwhelm the intraspecies interactions, hence the condensates are stable, however they are immiscible and phase separation occurs. Positive single species scattering lengths are assumed here.

the Thomas-Fermi approximation. The solution to this equation is [130]

$$n(\vec{r}) = \left|\psi(\vec{r})^2\right| = \begin{cases} \left(\mu - U_{\mathrm{ext}}(\vec{r})\right)/g & \text{for } \mu - \mathrm{U}_{\mathrm{ext}}(\tilde{\mathrm{r}}) > 0, \\ 0 & \text{otherwise.} \end{cases} \tag{2.43}$$

Since the potential is zero when the right hand side of this equation is negative, the cloud density is zero where $U_{\mathrm{ext}}(\vec{r}) = \mu$. These points are defined as the Thomas-Fermi radii, and mark the extension of the cloud in each dimension [41]

$$R_{\mathrm{TF,i}} = \sqrt{\frac{2\mu}{m\omega_i^2}} = a_{\mathrm{ho}} \left(\frac{15Na}{a_{\mathrm{ho}}}\right)^{1/5}, \tag{2.44}$$

for $i = x, y, z$. Here

$$a_{\mathrm{ho}} = \sqrt{\frac{\hbar}{m\omega_{\mathrm{ho}}}} \tag{2.45}$$

sets a characteristic length scale for the system.

The normalisation condition for ψ gives the relation

$$N = \frac{8\pi}{15}\left(\frac{2\mu}{m\omega_{\mathrm{ho}}^2}\right)^{3/2}\frac{\mu}{g}, \tag{2.46}$$

hence, solving for μ

$$\mu = \frac{\hbar\omega_{\mathrm{ho}}}{2}\left(\frac{15Na}{a_{\mathrm{ho}}}\right)^{2/5}. \tag{2.47}$$

By definition $\mu = \partial E/\partial N$ and $\mu \propto N^{2/5}$ hence we can calculate the average energy per particle

$$E_{\mathrm{ave}} = \frac{5}{7}\mu. \tag{2.48}$$

From the solution to equation 2.43 and neglecting the kinetic energy it is possible to calculate the ratio between the interaction energy per particle and the potential energy. From the resulting calculation

$$\frac{E_{\mathrm{int}}}{N} = \frac{2}{7}\mu. \tag{2.49}$$

Both the average energy and the release energy (equations 2.48 and 2.49) are dependent on μ, which is in turn dependent on a, hence the scattering length can be tuned to vary the condensate interactions [6]. If the scattering length is varied slowly the condensate remains in equilibrium as the wavefuntion can follow the change adiabatically [159]. However, in the case where the condensate is released from the trap and the scattering length is rapidly switched the wavefunction cannot react to the change in interaction energy and a vastly different condensate expansion is observed to the equilibrium case. The expansion of the non-equilibrium condensate is much faster than one in equilibrium, and due to the linear relationship between the mean-field interaction energy and the scattering length there is also a linear relationship between the release energy and a [160].

Physically this means that there are three scattering length regimes of experimental interest. For $a > 0$ the condensate is stable as the interactions are repulsive. Conversely, for $a < 0$ the attractive nature of the interactions result in the condensate being inherently unstable with an increase in trap density at the centre of the trap in order to reduce the interaction energy. In a harmonic potential, however, if the condensate number is lower than the critical value it is possible for the zero-point kinetic energy to stabilise the condensate. The critical value is defined as [48]

$$N_{\mathrm{crit}} = k\frac{a_{\mathrm{ho}}}{|a|}, \tag{2.50}$$

where k is known as the stability coefficent, a dimensionless constant dependent on the ratio of the trap frequencies. If the atom number is larger than N_{crit} the condensate is unstable against collapse. When condensates are released and a is quickly jumped to a negative value the condensate collapses, there is a large spread of momentum and a large loss of atoms [44], the well known 'Bosenova'. The final case is for $a = 0$, where interactions are minimised, hence there is little internal energy. Upon release from the trap minimal expansion of the condensate is observed and the BEC is said to be 'frozen'.

2.3.5 Condensate expansion

The shape of the condensate within the confining potential is dependent on the trapping frequencies. Anisotropic trapping frequencies lead to cigar shaped condensates as $\omega_{\mathrm{rad}} > \omega_{\mathrm{ax}}$, where $\omega_{\mathrm{rad(ax)}}$ is the radial (axial) trapping frequency. Acceleration is greatest in the direction of the greatest trapping frequency, as the force is provided by the internal mean-field energy, which is proportional to the density gradient. Hence, in the trap the axial size is larger than the radial size, however upon release due to the anisotropic forces the aspect ratio inverts, one of the signatures of a BEC [161].

The time-evolution of the condensate's radii after being released from an axially symmetric trap is described by

$$R_{\mathrm{TF,rad}}\left(t\right) = \lambda_{\mathrm{rad}}\left(t\right) R_{\mathrm{TF,rad}}\left(0\right), \tag{2.51}$$

$$R_{\mathrm{TF,ax}}\left(t\right) = \lambda_{\mathrm{ax}}\left(t\right) R_{\mathrm{TF,ax}}\left(0\right), \tag{2.52}$$

where $R_{\mathrm{TF,rad(ax)}}\left(0\right)$ is the Thomas-Fermi radius in the radial (axial) direction, which can be calculated by equation 2.44, and the λ are scaling parameters. In the simple case of the trap being switched off at $t = 0$ their time-evolution is described by [161]

$$\begin{aligned} \frac{d^2}{d\tau^2}\lambda_{\text{rad}} &= \frac{1}{\lambda_{\text{rad}}^3\lambda_{\text{ax}}}, \\ \frac{d^2}{d\tau^2}\lambda_{\text{ax}} &= \frac{\epsilon^2}{\lambda_{\text{rad}}^2\lambda_{\text{ax}}^2}. \end{aligned} \tag{2.53}$$

Here τ is a dimensionless time variable equal to $\omega_{\text{rad}}(0)\,t$ and $\epsilon = \omega_{\text{ax}}/\omega_{\text{rad}} \ll 1$. This inequality for ϵ defines when equations 2.53 are valid.

This anisotropic expansion is in stark contrast to the symmetric expansion in the widths of thermal clouds of atoms

$$\sigma_{\text{rad,ax}}^2 = \frac{k_{\text{B}}T}{m}\left(\frac{1}{\omega_{\text{rad,ax}}^2} + t^2\right). \tag{2.54}$$

Explicit in this equation is the dependence of the width on the trap frequency, however after a long time-of-flight the widths become dependent on temperature as the expansion rate is determined by the in-trap temperature. Hence $\sigma_{\text{rad}}/\sigma_{\text{ax}} \to 1$.

2.4 Magnetic trapping

The total magnetic field at a particular point in space is the vector summation of all the contributing elements at that point, the calculations of which will be discussed in chapter 4. The magnetic potential is then given by

$$U_B = -\vec{\mu}(B).\vec{B} = m_F g_F \mu(B)\,B, \tag{2.55}$$

where μ is the magnetic moment which is calculated by differentiating the Breit-Rabi equation (equation A.1) with respect to B. At low magnetic fields this reduces to

$$U_B = m_F g_F \mu_B B. \tag{2.56}$$

The magnetic potential may be used to form traps for some m_F states, depending on the value of equation 2.55. To form such a trap this value must be positive, hence only weak field seeking states are trapped. The following sections discuss various concepts surrounding the magnetic trap used in this work.

2.4.1 Quadrupole traps

The magnetic quadrupole field is generated using a pair of identical copper coils connected in the 'anti-Helmholtz' configuration - a pair of coils separated by a distance d with current flowing in the opposite sense. If a coil of N turns and radius R is arranged in the $x-y$ plane with current I flowing through the coil, the Biot-Savart law may be used to calculate the magnetic field produced in the z-direction, a distance z from the coil's centre

$$B_z = \frac{\mu_0 N I R^2}{2\left(R^2+z^2\right)^{3/2}}. \tag{2.57}$$

Extending this to the aforementioned pair of coils connected in the anti-Helmholtz configuration, the magnetic field gradient at the centre of the coils is

$$\partial B_{z,\mathrm{AH}}/\partial z = -\frac{3\mu_0 N I R^2\,(d/2)}{\left(R^2+(d/2)^2\right)^{5/2}}. \tag{2.58}$$

The potential created by this field gradient forms a magnetic trap. The most uniform magnetic field gradient is produced when the third derivative of B_z is zero.

2.4.2 Bias field generation

In contrast to the anti-Helmholtz case, when coils are connected in the 'Helmholtz' configuration the current flows through the coils in the same sense. Here the field at the centre of the trap geometry is non-zero, hence a uniform finite magnetic field may be produced

$$B_{z,\mathrm{H}} = -\frac{\mu_0 N I R^2}{2}\left(\frac{1}{\left(R^2+(z+d/2)^2\right)}+\frac{1}{\left(R^2+(z-d/2)^2\right)}\right). \tag{2.59}$$

2.4.3 Levitating atoms with a magnetic field gradient

An additional technique regularly used for various purposes throughout this work is that of separating the different atomic states via a Stern Gerlach method. Due to the different magnetic moments of the various m_F states and thus the magnetic moment to mass ratio the rate of vertical acceleration can be tuned using a magnetic field gradient. If the optical trap and any bias field are switched off the atoms can be levitated against gravity by applying a magnetic field gradient such that

$$\mu \frac{\partial B}{\partial z} - mg = 0, \tag{2.60}$$

where $\mu = m_F g_F \mu_{\mathrm{B}}$ is the magnetic moment of the atom. Alternatively, a bias field can be used to shift the field-zero upward and allow the high field seeking states to be levitated. It is possible to see that the rate of downward acceleration can also be tuned by varying $\partial B/\partial z$. The field gradients required to levitate ^{87}Rb, ^{85}Rb and ^{133}Cs against gravity are displayed in table 2.2. By allowing the atom cloud to evolve for a short period before a free time-of-flight expansion the different m_F states can be spatially separated. Experimentally this is useful when calibrating bias fields using RF or microwave frequencies to drive transitions between different energy levels (see section 3.9) or when diagnosing rapid adiabatic passage. Typical images of the three m_F sublevels in ^{87}Rb can be seen in reference [162] that demonstrate sympathetic cooling of the $m_F = -1$ and $m_F = 0$ atoms by $m_F = +1$ atoms.

2.4.4 Majorana transitions

The precession of the magnetic moment of an atom in a $B-$field about the magnetic quantisation axis has a frequency equal to the Larmor freqeuncy

$$\omega_{\mathrm{L}} = \frac{\mu B}{\hbar}. \tag{2.61}$$

If μ can no longer adiabatically follow the quantisation axis of the magnetic field the atom can no longer remain trapped. This occurs when the rate of change of the magnetic field direction is $\sim \omega_{\mathrm{L}}$. The atom may undergo a ‘spin

(a) ^{87}Rb

F	m_F	$\partial B/\partial z$ (G cm^{-1})
1	0	-
1	±1	30.53
2	0	-
2	±1	30.53
2	±2	15.27

(b) ^{85}Rb

F	m_F	$\partial B/\partial z$ (G cm^{-1})
2	0	-
2	±1	44.74
2	±2	22.37
3	0	-
3	±1	44.74
3	±2	22.37
3	±3	14.91

(c) ^{133}Cs

F	m_F	$\partial B/\partial z$ (G cm^{-1})
3	0	-
3	±1	93.38
3	±2	46.69
3	±3	31.13
4	0	-
4	±1	93.38
4	±2	46.69
4	±3	31.13
4	±4	23.34

Table 2.2: The required magnetic field gradients for levitation of ^{87}Rb (a), ^{85}Rb (b) and ^{133}Cs (c) in their ground states in the absence of any bias field.

flip' to a magnetically untrappable state [163] or one that is not trapped by the current potential. This process causes anti-evaporation as it occurs close to the trap centre where the coldest atoms are located. An estimate that the Majorana loss rate (Γ_{m}) scales with $\hbar/m\sigma^2$ [164] can be made, where σ is the radial half width half maximum cloud size, and then [165]

$$\Gamma_{\mathrm{m}} = 1.85\frac{\hbar}{m}\left(\frac{m_F g_F \mu_B \frac{\partial B}{\partial z}}{k_{\mathrm{B}}T}\right)^2. \tag{2.62}$$

This loss results in a limit to the maximum achievable PSD in a quadrupole trap.

2.4.5 Evaporative cooling

Evaporative cooling is the method by which most atomic physics experiments access the lowest possible temperatures. The process works by removing the hottest atoms from an ensemble, thus after evaporation the average temperature of the atoms decreases as the high energy Boltzmann tail is removed from the velocity distribution of the atoms. In the magnetic trap used in this work forced evaporative cooling is performed using an RF 'knife' to remove the hotter atoms (in some experiments microwaves are also used). Initially the RF knife is set to a frequency that drives transitions at a magnetic field corresponding to an energy much higher than the sample average, so only the hotter atoms are removed by the trap. These atoms have larger Zeeman shifts.

The RF frequency is maintained so that atoms with energy above

$$E_{\mathrm{cut}} = \eta k_{\mathrm{B}} T \tag{2.63}$$

are removed from the trap, where η is the ratio of the desired cut energy to the mean energy of the sample. To drive an atom into an untrapped state, the photon energy required is

$$h\upsilon = g_F \mu_{\mathrm{B}} \left| \frac{\partial B}{\partial z} \right| z, \tag{2.64}$$

where υ is the RF frequency. The RF knife's position is then

$$E_{\mathrm{cut}} = m_F g_F \mu_{\mathrm{B}} \left| \frac{\partial B}{\partial z} \right| z. \tag{2.65}$$

Thus, rearranging equation 2.64 to obtain z_{Rb} and z_{Cs} we can substitute these values into equation 2.65. This yields the relation $E_{\mathrm{cut,Rb}} = 3E_{\mathrm{cut,Cs}}$. Thus, in the magnetic trap, ^{87}Rb is preferentially evaporated at higher RF frequencies, whilst ^{133}Cs can be cooled sympathetically, a powerful technique for the production of a ^{133}Cs BEC [12]. This is highlighted in figure 2.6.

2.5 Optical trapping

The traditional starting point for the trapping of neutral atoms is the MOT where the confinement is due to the radiation pressure force. The first observations of BECs were realised after transfer from the MOT to a magnetic trap and forcing evaporation therein [1–3]. More recently, optical dipole traps have been used to reach the onset of BEC [166]. Among many other advantages (see below), a degenerate system of ^{133}Cs in the $|F = 3, m_F = +3\rangle$ state has been achieved [10, 11, 167]. The use of an optical dipole trap allowed confinement of this magnetically untrappable state which eliminates

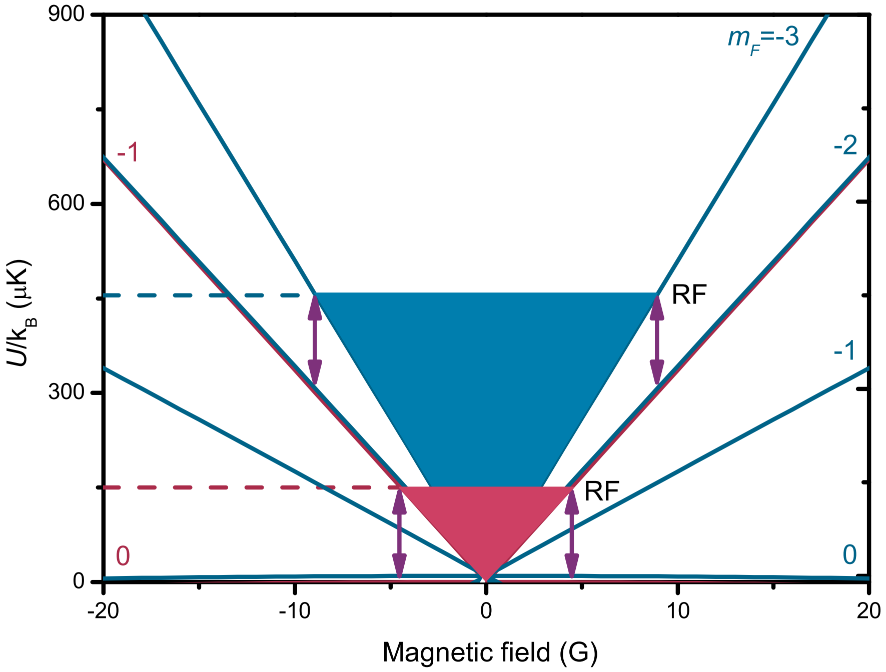

Figure 2.6: Application of the experiment to sympathetic cooling of ^{133}Cs. The magnetic quadrupole potentials for ^{87}Rb (red) and ^{133}Cs (blue). The depth of the quadrupole trap determined by the RF frequency is 3× larger for ^{133}Cs than for ^{87}Rb thereby permitting sympathetic cooling. The purple arrows indicate RF transitions and the dashed lines are for construction purposes.

inelastic two-body collisions, and tuning of the bias field and thus scattering length allowed regions of high three-body loss and unfavourable evaporation conditions to be avoided. Evaporation to BEC was found to be possible in the 21−25 G range.

Both magnetic and optical traps have their own distinct advantages. Magnetic quadrupole traps, the simplest configuration of a magnetic trap, are easy to implement, boast good, efficient capture due to good mode-matching with a MOT, and allow efficient forced evaporation due to the potential remaining linear as the trap depth is decreased [168]. Magnetic traps are, however, only able to capture low-field seeking states and a zero potential in some magnetic traps such as the quadrupole exists at the trap centre (see section 2.4.4). Due to the lack of a quantisation field here, Majorana spin flip losses occur at an increasing rate as the atomic cloud is cooled, limiting the PSD achievable in this type of trap. Techniques exist to remove this weakness from this type of trap, such as the time-averaged, orbiting potential (TOP) trap [164], or alternatively an optical trap may be utilised [166, 169].

Optical dipole traps have the advantage that all m_F states observe the same dipole potential, and hence all states can be trapped. Implementation is simplified by the fact that fewer, less complicated coils are required and hence good optical access is possible without obstruction from the coils. Due to the lack of magnetic field this becomes a free parameter allowing the transfer of the atomic state to any desired one (generally the absolute ground state) [170] and tuning of the bias field for experiments involving Feshbach resonances [51]. To obtain a sizeable trap depth the beam waist is necessarily small, limiting the capture volume of dipole traps. Due to the comparatively small trap depth atomic clouds generally require pre-cooling prior to loading.

Hybrid traps that combine the advantages of both magnetic and optical traps have been explored in order to combat the negative effects of each distinct type of trap [2, 11, 165, 171]. Often the optical trap is used as a ‘dimple’, relying on collisions within the magnetic trap ‘reservoir’ to load the optical potential [159, 165, 172, 173]. This allows the coldest fraction of the magnetically trapped atoms to be loaded into the optical trap, resulting in large gains in PSD. An additional magnetic field gradient can be included such that the total potential is tilted (see section 4.5). This allows evaporation of atoms with little reduction in the trap frequency [11].

2.5.1 Optical trapping theory

The optical potential

Optical dipole traps rely on the dipole interaction between neutral atoms and far off resonance light. The trapping force is generally much weaker than that in the case of traps utilising the radiation pressure force (MOTs) or magnetic forces. The interaction between the atomic dipole moment ($\vec{p}$) and a gradient in a light field results in the optical dipole force, which can be derived from an optical potential due to its conservative nature [174]. $\vec{p}$ is given by the product of the complex polarisability (α) and the electric field amplitude, E. The optical dipole potential is then [174]

$$U_{\mathrm{dip}} = -\frac{\Re\left(\alpha\right) I}{2\epsilon_0 c}, \tag{2.66}$$

where I is the intensity of the light and α is the complex polarisability. The factor of 1/2 derives from the fact that the dipole moment is induced and not permanent.

Perturbation theory may be used to calculate the polarisability [175], however the calculation is simplified if we only consider the real part of the polarisability, assume the detuning is large and only take the valence electron into account. It can then be shown [176]

$$\Re\left(\alpha\right) = 3\pi\epsilon_0 c^3 \sum_{i\neq j} \frac{\Gamma_{ij}}{\omega_{ij}^3}\left(\frac{1}{\omega_{ij}-\omega}+\frac{1}{\omega_{ij}+\omega}\right), \tag{2.67}$$

where ω is the driving frequency and ω_{ij} and Γ_{ij} are the frequency and rate of transition from state i to state j. In the limit of large detuning and negligible saturation the fine and hyperfine structure can be neglected and only a summation of all the light shift potentials of the relevant transitions is required. We are able to arrive at the following expressions for the dipole potential and the scattering rate following the arguments in [174]

$$U_{\mathrm{dip}}\left(\vec{r}\right) = -\frac{3\pi c^2}{2\omega_0^3}\left(\frac{\Gamma}{\omega_0-\omega}+\frac{\Gamma}{\omega_0+\omega}\right) I\left(\vec{r}\right), \tag{2.68}$$

$$\Gamma_{\mathrm{SCAT}}\left(\vec{r}\right) = \frac{3\pi c^2}{2\hbar\omega_0^3}\left(\frac{\omega}{\omega_0}\right)^3\left(\frac{\Gamma}{\omega_0-\omega}+\frac{\Gamma}{\omega_0+\omega}\right)^2 I\left(\vec{r}\right), \tag{2.69}$$

where Δ is the detuning of the beam. In the alkali atoms the contributions are dominated by the D lines and if we apply the rotating wave approximation these equations simplify to

$$U_{\mathrm{dip}}\left(\vec{r}\right) = \frac{3\pi c^2}{2\omega_0^3}\frac{\Gamma}{\Delta} I\left(\vec{r}\right), \tag{2.70}$$

$$\Gamma_{\mathrm{SCAT}}\left(\vec{r}\right) = \frac{3\pi c^2}{2\hbar\omega_0^3}\left(\frac{\Gamma}{\Delta}\right)^2 I\left(\vec{r}\right). \tag{2.71}$$

Hence

$$\hbar\Gamma_{\mathrm{SCAT}} = \frac{\Gamma}{\Delta}U_{\mathrm{dip}}. \tag{2.72}$$

Inspection of equations 2.70-2.72 clearly shows that the depth of the potential will increase as I/Δ and the scattering rate increases as I/Δ^2. Ideally an optical dipole trap is therefore produced using a large intensity to increase the trap depth, at a large detuning to reduce the scattering rate and hence heating mechanisms within the trap.

The optical potential at a given point may be found using equation 2.70 and the intensity of a Gaussian beam at a given point

$$I\left(\vec{r}\right) = \frac{2P}{\pi w\left(z\right)^2}\exp\left(-2\left(\frac{r}{w\left(z\right)}\right)^2\right), \tag{2.73}$$

where P is the power of the beam, $w\left(z\right)$ is the $1/e^2$ radius and $r^2 = x^2 + y^2$. $w\left(z\right)$ in equation 2.73 is calculated via

$$w\left(z\right) = w_0\sqrt{1 + \frac{\left(z - z_{\mathrm{w}}\right)^2}{Z_{\mathrm{R}}^2}}, \tag{2.74}$$

where w_0 is the beam waist, z_{w} is the position of the beam waist and

$$Z_{\mathrm{R}} = \pi w_0^2/\lambda, \tag{2.75}$$

is the Rayleigh range - the distance over which a beam's area increases by a factor of 2.

Equations 2.66 and 2.70, which are equivalent in the appropriate limit, can then be calculated. When modelling the potential they are calculated over a finite grid in space. The experimental parameters are clearly specific to the experiment, and the polarisabilities used in this work are those reported in reference [175]. Table 2.3 presents the polarisability (in atomic units) at a wavelength of 1550 nm for Rb and Cs.

Species	$\alpha\,(a_0^3)$
Rb	(424.7 ± 0.7)
Cs	(572.2 ± 1.2)

Table 2.3: Polarisability of Rb and Cs at a wavelength of 1550 nm, in atomic units of a_0^3 [175].

The Gaussian beam

Given the Gaussian nature of a laser beam it is possible to determine its properties at all points along its beam path, given knowledge of the 'q-value' (the complex beam parameter) of the output. The q-value at point z is [177]

$$q = z - z_{\mathrm{w}} - iZ_{\mathrm{R}}. \tag{2.76}$$

To define q at any point, only knowledge of the Rayleigh range (or conversely the beam waist) and the position of the beam's waist are required.

To take account of any deviation of the laser's output from a true Gaussian beam, we can define a factor, M^2, that corrects for this [178]

$$M^2 = \pi w_0^2/\lambda Z_{\mathrm{R}}'. \tag{2.77}$$

For an ideal Gaussian beam $M^2 = 1$ whereas for a real beam $M^2 > 1$.

Using the q-value of the laser beam and an adaptation to standard ray transfer matrices one can determine the beam's properties after any transformation of the beam. The resultant q after an operation is given by equation 2.78

$$\begin{pmatrix} q/n \\ 1 \end{pmatrix}_{z=z_2} = (\alpha) \begin{pmatrix} A & B \\ C & D \end{pmatrix} \begin{pmatrix} q/n \\ 1 \end{pmatrix}_{z=z_1}, \tag{2.78}$$

where z_1 is the initial position of interest where q is known, z_2 is the location where q is to be determined, n is the refractive index of the medium (taken to be $= 1$ here as the medium is air), α is a factor which is cancelled and $\left(\begin{smallmatrix} A & B \\ C & D \end{smallmatrix}\right)$ is the matrix describing the transformation between z_1 and z_2.

The resultant q after a series of transformations is calculated by multiplying the individual $ABCD$ matrices together, in the reverse order that they occur within the optical setup. The resultant matrix may then be substituted into equation 2.78. Two matrices are of concern in this work (neglecting reflection which only affects the direction of propagation). The matrix that describes a translation between z_1 and z_2 is

$$\begin{pmatrix} 1 & (z_2 - z_1)/n \\ 0 & 1 \end{pmatrix}, \tag{2.79}$$

and the matrix describing a thin lens is

$$\begin{pmatrix} 1 & 0 \\ -1/f & 1 \end{pmatrix}, \tag{2.80}$$

where f is the focal length of the lens. Using equation 2.78 the matrices can be multiplied out to obtain two separate equations. Dividing through will remove the factor of α. The q-value that results can be used to calculate w_0, $w(z)$, $(z - z_\mathrm{w})$ and Z_R from equation 2.76. This was used in the design of the optical setup of the dipole trap (chapter 4).

Chapter 3

Experimental overview

The experimental setup of the apparatus is discussed in this chapter. Due to the nature of working on an ongoing experiment many specific details are already reported elsewhere [71, 125–127]. A brief overview of the experiment is given here and any improvements or modifications distinct from the previous work are discussed.

3.1 Summary of experiment

This experiment can be thought of as being divided into smaller subsections which are all necessary to produce a two-species ultracold atomic cloud. The main experiment consists of two separate optical benches, one on which laser light is derived and the other which contains the vacuum system, magnetic field generating coils and optical trapping apparatus. In addition to the experimental hardware, equipment used for computer control of the experiment is also required, which is discussed in section 3.10.

The first optical bench will be referred to as the 'laser table' in this work. On the laser table light of the different required frequencies is derived from a series of lasers using acousto-optic modulators (AOMs) to modulate the optical frequencies. The different frequencies are used for various purposes such as laser cooling, repumping, molasses cooling, optical pumping and imaging. Laser light for trapping of both ^{87}Rb and ^{85}Rb is derived on this bench using the same lasers, as is the corresponding ^{133}Cs light. This light is then transferred via polarisation maintaining optical fibres to the other optical bench, the ‘experimental bench’, which houses the vacuum system. A two-species pyramid MOT [179–181] is used as a cold atom source for the ultra high vacuum (UHV) region of the 2nd MOT which is housed within a glass cell. The atoms are then optically pumped into the magnetically trappable ($|1,-1\rangle$, $|2,-2\rangle$ and $|3,-3\rangle$ for ^{87}Rb, ^{85}Rb and ^{133}Cs respectively) stretched states and transferred to a magnetic quadrupole trap. RF evaporative cooling is used to pre-cool the atoms and increase their PSD prior to transfer to an optical dipole trap. To load the optical dipole trap the magnetic field gradient is decreased to a value close to that which cancels gravity. The atoms are then transferred into the absolute ground state via rapid adiabatic passage [170, 182]. The experiments described in the following chapters are then performed after evaporation within the dipole trap.

3.2 Derivation of laser light

The closed transitions required for laser cooling [33–35] occur at wavelengths of ~ 780.2 nm for Rb atoms and at ~ 852.3 nm for Cs. The atomic transitions and hyperfine structure of ^{87}Rb, ^{85}Rb and ^{133}Cs are displayed in figure 3.1. In this work to produce light that excites these transitions (the D_2 transitions) a series of six lasers are used, which are split into three lasers for each atomic species. For each species a ‘master’ laser (Toptica DL 100) is the source of light used for laser cooling in the 2nd MOT, imaging of the atoms and seeding a home-built slave laser, the output of which is used as cooling light for the pyramid MOT. After the optical isolator the output beam power is 95.5 mW (118.3 mW) for the Rb (Cs) laser. The direct output of the master laser is detuned from the atomic transition $F = 2$ to $F' = 3$ ($F = 4$ to $F' = 5$) by (251.2 ± 0.1) MHz ((251.2 ± 0.1) MHz) and is brought back to the desired frequencies by double passed AOMs. The detuning of the light used for MOT cooling is changed successively throughout the experiment to the required values for the compressed magneto-optical trap (CMOT) stage, molasses cooling and depumping prior to magnetic trapping. The light used for imaging the Rb atoms is also used to displace this MOT slightly with a small ‘push’ from resonant light in order to reduce light assisted interspecies collisions that result in decreased lifetimes in the MOT [68, 71, 183]. A 'slave' laser is seeded using light from the master laser, and the output light, of 55.8 mW (72.4 mW) power, is used for pyramid MOT cooling. Finally, for each atomic species a home-built laser generates repumping light for both the pyramid and 2nd MOTs as well as the optical pumping light on the $F = 1$ to $F' = 1$ ($F = 3$ to $F' = 3$) transition. This laser outputs 49.5 mW (46.9 mW) total power. Figure 3.2 graphically displays how the laser light is divided in the experiment for Rb, with a similar scheme being employed for Cs. Table 3.1 lists the atomic transitions used in this work and the detuning of the laser light from these transitions.

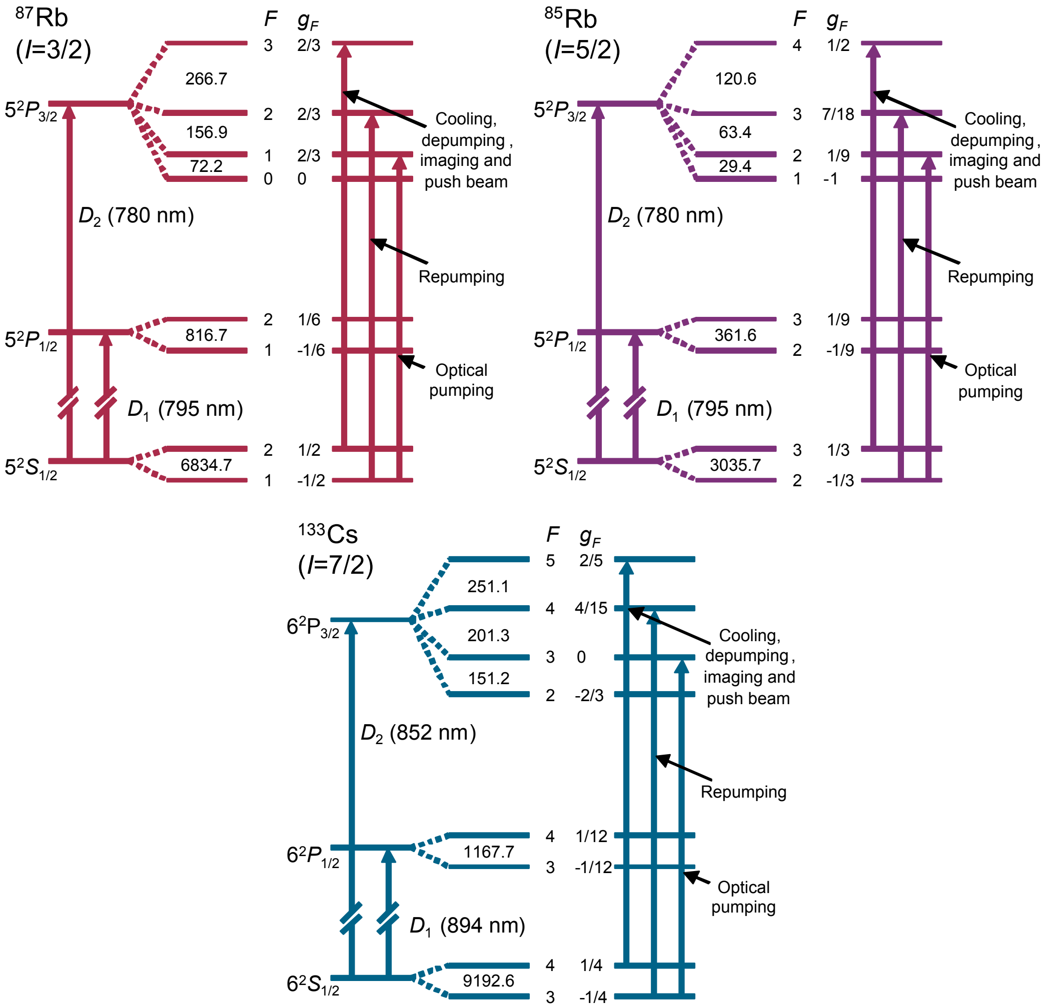

Figure 3.1: Atomic energy level diagrams displaying the hyperfine structure in ^{87}Rb, ^{85}Rb and ^{133}Cs. Arrows on the right indicate the transitions relevant to this work. Splittings are not to scale and all frequencies are in MHz. The hyperfine structure of ^{85}Rb is discussed further in chapter 7.

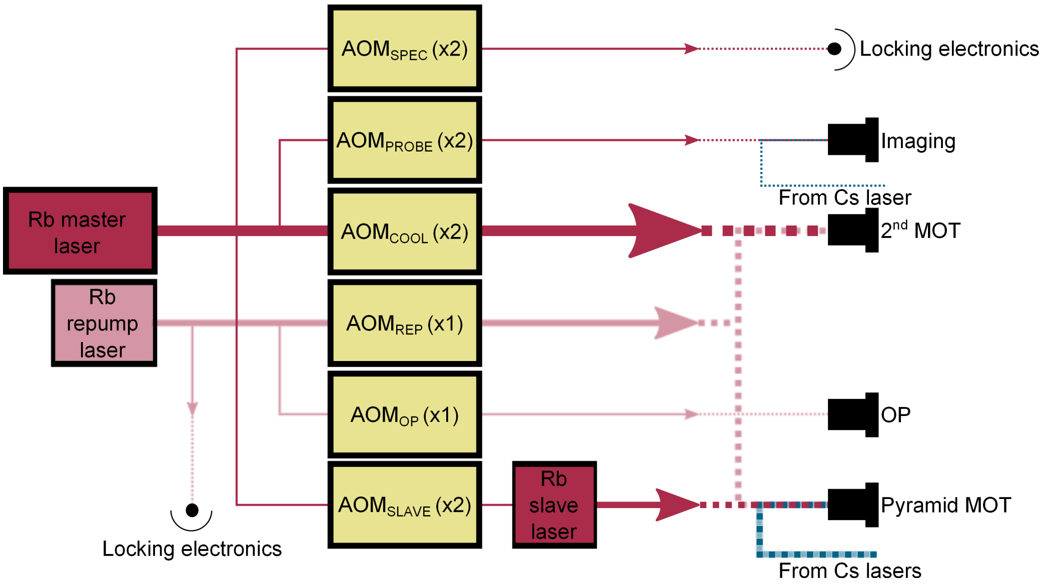

Figure 3.2: Basic schematic describing the optical setup of the laser table for Rb, with a similar scheme being used for the Cs lasers. Light close to the Rb cooling transition is denoted by solid red lines and light close to the Rb repump transition is denoted by transparent red lines, and likewise for Cs light which is denoted by blue lines. Light is picked off using PBS cubes and AOMs are used to increase the frequency (or decrease the frequency in the case of the OP AOM) to that required, and light is coupled to the experimental bench using optical fibres. The ×1/×2 indicate whether the AOM is single passed or double passed. The thickness of the lines indicate relative powers, but are not exactly to scale. The complete optical setup is given in figure B.1.

	^{87}Rb		^{85}Rb		^{133}Cs	
	Transition	Detuning (MHz)	Transition	Detuning (MHz)	Transition	Detuning (MHz)
Master laser	$F = 2$ to $F' = 3$	(-251.2 ± 0.1)	$F = 3$ to $F' = 4$	(-251.2 ± 0.1)	$F = 4$ to $F' = 5$	(-251.2 ± 0.1)
Master spectroscopy	$F = 2$ to $F' = 3$	(0.0 ± 0.1)	$F = 3$ to $F' = 4$	(0.0 ± 0.1)	$F = 4$ to $F' = 5$	(0.0 ± 0.1)
Pyramid cooling	$F = 2$ to $F' = 3$	(-16.0 ± 0.1)	$F = 3$ to $F' = 4$	(-16.0 ± 0.1)	$F = 4$ to $F' = 5$	(-13.1 ± 0.1)
2$^{\text{nd}}$ MOT cooling	$F = 2$ to $F' = 3$	(-10.8 ± 0.1)	$F = 3$ to $F' = 4$	(-10.8 ± 0.1)	$F = 4$ to $F' = 5$	(-10.7 ± 0.1)
CMOT	$F = 2$ to $F' = 3$	(-17.9 ± 0.1)	$F = 3$ to $F' = 4$	(-17.9 ± 0.1)	$F = 4$ to $F' = 5$	(-28.2 ± 0.1)
Molasses	$F = 2$ to $F' = 3$	(-62.9 ± 0.1)	$F = 3$ to $F' = 4$	(-62.9 ± 0.1)	$F = 4$ to $F' = 5$	(-53.5 ± 0.1)
Depumping	$F = 2$ to $F' = 3$	(-95.9 ± 0.1)	$F = 3$ to $F' = 4$	(-95.9 ± 0.1)	$F = 4$ to $F' = 5$	(-72.1 ± 0.1)
Imaging (m_F positive)	$F = 2$ to $F' = 3$	(-4.6 ± 0.1)	$F = 3$ to $F' = 4$	(-4.6 ± 0.1)	$F = 4$ to $F' = 5$	(-2.4 ± 0.1)
Imaging (m_F negative)	$F = 2$ to $F' = 3$	$(+4.0 \pm 0.1)$	$F = 3$ to $F' = 4$	$(+4.0 \pm 0.1)$	$F = 4$ to $F' = 5$	$(+3.6 \pm 0.1)$
Repump laser	$F = 2$ to $X_{1,2}$	(0.0 ± 0.1)	$F = 2$ to $F' = 1$	$(+12.8 \pm 0.1)$	$F = 4$ to $X_{3,4}$	(0.0 ± 0.1)
Repumping	$F = 1$ to $F' = 2$	(-1.5 ± 0.1)	$F = 2$ to $F' = 3$	(0.0 ± 0.1)	$F = 3$ to $F' = 4$	$(+0.3 \pm 0.1)$
Optical pumping	$F = 1$ to $F' = 1$	$(+5.8 \pm 0.1)$	$F = 2$ to $F' = 2$	$(+6.2 \pm 0.1)$	$F = 3$ to $F' = 3$	$(+12.0 \pm 0.1)$

Table 3.1: Optimum detuning of light (in MHz) from the various atomic transitions used in this experiment. More detail is given on the ^{85}Rb transitions in section 7.2.

3.3 Laser stabilisation

Active stabilisation of the laser frequencies was achieved by ‘locking’ the master and repump lasers using an error signal generated using an atomic reference. Electronic feedback to the laser piezo driver is used to stabilise the laser frequency. In this work the master lasers are locked using modulation transfer (MT) spectroscopy [184–186] and the repump lasers are stabilised using frequency modulation (FM) spectroscopy [187, 188] for ^{133}Cs and experiments with ^{87}Rb. For reasons that will be explained in chapter 7 when experiments with ^{85}Rb are being performed the repump laser is instead locked using dichroic atomic vapour laser locking (DAVLL) [189, 190]. The setup of the locking optics and electronics used for MT and FM spectroscopy is described elsewhere, however a brief description is given below [127].

The direct output of the master laser is detuned with respect to the atomic cooling transition, however AOM_{Spec} brings the light back onto resonance. This light is then used to generate the error signal used for locking. The beam is split and a telescope in each branch is used to expand the beam to reduce saturation effects. The pump beam is modulated using a home-built electro-optic modulator (EOM) which consists of a LiTaO_3 crystal mounted on a perspex block. This is connected in a simple LCR circuit with a resonant frequency of $1/\sqrt{LC}$. Sidebands on the pump beam derive from the electro-optic effect, and the error signal originates in the beat of the sidebands generated on the probe beam in the atomic vapour and the probe beam carrier frequency. For MT spectroscopy there is a zero crossing as there is no modulation transfer unless a closed transition exists. Hence we achieve a large error signal gradient for good laser locking at the frequency of the closed atomic transition.

The direct output of the repump laser is on resonance with the crossover transition between $F = 1$ to $F' = 2$ ($F = 3$ to $F' = 4$) for ^{87}Rb (^{133}Cs). This direct output is used in the FM spectroscopy locking of the repump laser. Here the probe beam is modulated by an EOM, and the error signal originates from the beat between the carrier frequency and the sidebands. Locking electronics demodulate this signal and the resulting error signal is utilised for locking. In FM spectrocopy a non-zero background to the signal must be removed to produce a zero-crossing of the error signal for use to lock to. All atomic transitions produce an FM spectroscopy signal, hence it is possble to lock to an open atomic transition.

3.4 Magneto-optical trapping

3.4.1 The pyramid MOT

The cooling and repump light for both MOTs is fibre coupled to the optical bench via polarisation maintaining optical fibres. For the pyramid MOT both Rb and Cs cooling and repump light is overlapped on a dichroic mirror and coupled into the same optical fibre. The fibre output is collimated by a Thorlabs F810APC-780 collimator and the light is circularly polarised using an achromatic Casix WPA1212-700-1000nm $\lambda/4$-plate. The beams are expanded by a telescope comprised of two lenses, one of -30 mm focal length and the second lens of 140 mm focal length. The beam, of approximately 17 mm $1/e^2$-radius, is steered by a mirror and is incident on the viewport of the vacuum chamber. We operate with a fibre output of (46.5 ± 0.1) mW ((38.9 ± 0.1) mW) of cooling light for Rb (Cs) and (7.7 ± 0.1) mW ((4.7 ± 0.1) mW) of repump light.

The pyramid MOT mirrors form a pyramid of $60{\times}60$ mm^2 square base. To allow a flux of cold atoms to the 2$^{\text{nd}}$ MOT the apex of the pyramid has been removed, forming a $2.4{\times}3.0$ mm^2 gap. The lack of a retro-reflected MOT cooling beam at the apex forms an imbalance in the radiation pressure force on the atoms at this location. Thus the atoms are pushed into the UHV region and are then trapped by the 2$^{\text{nd}}$ MOT. The magnetic field gradient for the pyramid MOT is produced by a pair of copper coils in the anti-Helmholtz configuration (see section 2.4.1). The optimum magnetic field gradient for maximising the number of atoms captured by the 2$^{\text{nd}}$ MOT is 7.54 G cm^{-1}. The location of the magnetic field zero, and thus the location over which the MOT forms, is shifted using a pair of shim coils which generate a bias field in the $x-$ and $y-$directions. When the MOT location is above the apex a flux of atoms into the 2$^{\text{nd}}$ MOT is generated. The detuning of the MOT light is reported in table 3.1.

3.4.2 The 2^{nd} MOT

The 2^{nd} MOT is realised using a standard six-beam MOT configuration. Light for cooling and repumping of Rb and Cs is transmitted through different optical fibres to the experimental bench. The fibre outputs are collimated to a $1/e^2$-radius of (3.5 ± 0.1) mm by Thorlabs F810APC-780(850) collimators for the Rb (Cs) fibre. Two telescopes consisting of 80 mm and 125 mm focal length lenses expand the beams to $1/e^2$-radii of approximately 5.5 mm, however this size is limited by the functional area of the optics used later in the beam path. Light is split using PBS cubes and the MOT beam paths in the $x-$ and $y-$directions are independent for the two species, whereas the light is overlapped in the $z-$direction using a non-polarising beam splitting cube. The light in the $x-$ and $y-$directions is circularly polarised using wavelength specific zero-order $\lambda/4$-plates, Casix WPZ1225-780(850) for Rb (Cs), and in the $z-$direction the up (down) beam is polarised using a WPZ1225-780(850) $\lambda/4$-plate as well. The vertical beams propagate at an angle of $4°$ to the vertical and are overlapped in opposite directions. An additional $\lambda/4$-plate for the Rb wavelength has been included for the down beam for reasons that will be discussed in section 3.6. In the horizontal direction light is split such that there are two orthogonal sets of beams that counter propagate, generating the required balance in beam power for laser cooling.

To magneto-optically trap the atoms the beam detunings detailed in table 3.1 are used. The magnetic field gradient is generated by a pair of 2×2 turn coils in the anti-Helmholtz configuration. For the 2^{nd} MOT a magnetic field gradient of 10.3 G cm^{-1} is used, and (35.0 ± 0.1) mW ((40.2 ± 0.1) mW) of Rb (Cs) cooling light and (8.0 ± 0.1) mW ((2.8 ± 0.2) mW) of Rb (Cs) repump light are output by the fibre. The intensity of the cooling beam is (2.9 ± 0.4) mW cm^{-2} ((4.8 ± 0.7) mW cm^{-2}) and for the repump it is (0.7 ± 0.1) mW cm^{-2} ((0.34 ± 0.05) mW cm^{-2}). The offset magnetic field in the 2^{nd} MOT region can also be controlled using a set of shim coils which allow changes to be made to the magnetic field in all three dimensions. During MOT loading the shims are set such that the MOT is formed in a similar location to the magnetic trap centre (see section 3.6.1). In 30 s of typical loading we are able to trap in excess of 1×10^9 ^{87}Rb atoms and up to 3×10^8

^{133}Cs atoms, however the ^{133}Cs MOT load is controlled via an electronic servo circuit. This circuit stabilises the output voltage of a photodiode monitoring the ^{133}Cs MOT fluorescence to a preset value by varying the RF power applied to the Cs repump AOM. The ^{133}Cs MOT number is typically stabilised to a number greater than a factor of ten lower than the maximum possible number, however the exact value is determined by the aim of the experiment, and the desired final ratio of Rb to Cs atoms. These larger MOT loads represent a significant improvement on previous work, which will be discussed in section 3.6.

3.4.3 The ‘push beam’

During the loading of the 2$^{\text{nd}}$ MOT we employ a technique developed in the first generation of this experiment to separate the Rb and Cs MOTs, known as the ‘push beam’. To reduce atom losses due to interspecies light assisted collisions we apply a weak beam which is resonant with the Rb atoms. Since no counter propagating beam is applied the radiation pressure force on the atoms in this direction is unbalanced, and the resultant force on the atoms causes the centre of the Rb MOT to be displaced in the direction of propagation of the beam. The overlap between the two MOTs is thus reduced and larger MOT loads are possible. Previously we had set the centre of the two MOTs to be displaced by ~ 2 mm [127] however in making the improvements highlighted in section 3.6 it was found that magnetic trap loading is improved without the two MOTs being displaced. During the CMOT the push beam is switched off and hence the atoms are brought back into contact.

3.4.4 The compressed magneto-optical trap

In a 40 ms CMOT stage [191] the detunings are changed to those reported in table 3.1 and $\partial B/\partial z$ is decreased to (7.7 ± 0.1) G cm^{-1}. Despite being labelled a CMOT, the magnetic field gradient is decreased in this work. This is to achieve better mode matching into the magnetic trap. Due to the change in $\partial B/\partial z$ and the beam detunings the centre of the CMOT is slightly different to that of the MOT. To achieve optimal loading of the magnetic trap the field produced by the shim coils is set such that the atoms are positioned over the magnetic trap centre, hence increasing the PSD of atoms loaded into the magnetic trap. This occurs as the atoms that are loaded away from the trap centre will begin to oscillate harmonically at the trap frequency. The potential energy increase associated with this will be distributed among the other magnetically trapped atoms, resulting in heating and thus a lower PSD. Experimentally we find the optimal position of the CMOT to be (0.9 ± 0.1) mm displaced from the magnetic trap centre, and (0.4 ± 0.1) mm from the MOT centres. The larger detuning of the beams results in a lower scattering rate and re-absorption of photons, hence this scattering cannot limit the density of the MOT.

3.4.5 Molasses cooling

After the CMOT stage the magnetic field gradient is then switched off and the shim coils switched to cancel any stray bias fields within the science cell (this field was determined via the experiments explained in section 3.6). The beam detunings were then increased further to (-62.9 ± 0.1) MHz for Rb and to (-53.5 ± 0.1) MHz for Cs. The duration of this stage is 15 ms. This optical molasses stage pre-cools the atoms to sub-Doppler temperatures such that optimal loading into the magnetic trap is achieved [192]. The molasses was optimised by measuring the number, temperature and PSD after the magnetic trap was loaded.

3.5 Magnetic trapping

3.5.1 Optical pumping

All atomic m_F states are trapped by the MOT, including the high-field seeking magnetically untrappable states, and all weak-field seeking states, not just the $|1, -1\rangle$, $|2, -2\rangle$ and $|3, -3\rangle$ stretched states in ^{87}Rb, ^{85}Rb and ^{133}Cs respectively. The presence of atoms in these other states would increase inelastic collisions within the magnetic trap, thus limiting the efficiency of cooling. Optically pumping the atoms into the stretched states increases the percentage of atoms trapped by the magnetic trap and additionally reduces inelastic losses during magnetic trap evaporation.

To optically pump the atoms into the stretched states the light output from the optical pumping AOMs is coupled into separate fibres. The light is then combined on a dichroic mirror, and polarised by a broadband PBS. The light is circularly polarised by a Casix WPA1212-700-1000 nm $\lambda/4$-plate, before being aligned through the glass cell such that the beam is incident on the atoms. The beam is retroreflected on itself to remove the centre-of-mass motion that would cause heating due to the scattering of photons in the optical pumping process. The magnetic bias field in the horizontal plane remains cancelled by the shim coils, however a (2.7 ± 0.1) G quantisation field in the $z-$direction is produced by a separate 16 turn coil created for the optical pumping process. The current flows in a direction such that σ^- transitions are driven. In addition to the optical pumping beams the MOT cooling beams are detuned from the cooling transition by the values given in table 3.1. This is done so that the $F = 2$ to $F' = 2$ transition is driven in ^{87}Rb (for ^{85}Rb and ^{133}Cs we drive the $F = 3$ to $F' = 3$ and $F = 4$ to $F' = 4$ transitions respectively). This depumping light ensures that atoms don't remain in the upper hyperfine states. The frequency that the AOMs must be driven at to generate light of this detuning is far from the optimum frequency for the AOMs in use hence the maximum power for depumping light is limited. The intensity of the depumping light is (0.7 ± 0.1) mW cm^{-2} for Rb and (3.6 ± 0.5) mW cm^{-2} for Cs whereas for optical pumping light it is (22 ± 1) μW cm^{-2} and (49 ± 3) μW cm^{-2} respectively.

3.5.2 Magnetic trap loading

The loading of the magnetic trap was optimised by maximising the atom number and PSD once the field gradient had been increased to its maximum value. The field gradient from the quadrupole coils was switched on at (39 ± 1) G cm^{-1} and the atoms are held in this potential for 1 s, thus spin polarising the atoms as the atoms in the incorrect spin states leave the trap. The field gradient was then ramped up in two stages as it was found more atoms remained after the increase in gradient. We first adiabatically increase the field to (59 ± 1) G cm^{-1} in 100 ms, followed by a further 100 ms hold. The field gradient was then linearly ramped to its final value of (187 ± 1) G cm^{-1} in 1 s. A high gradient such as this is used in order to increase the collision rate of the atoms, leading to faster more efficient evaporation. Due to the improvements in atom number and density outlined in section 3.7 we are now able to perform all forced RF magnetic trap evaporation in a single 15.1 s linear ramp of the RF field, which represents a decrease in evaporation time of more than a factor of two [127]. After the onset of Majorana spin flips beginning to limit the evaporation efficiency in the magnetic trap we load the optical dipole trap via the method outlined in chapter 4.

3.6 Improvements made to the MOT setup

Following the installation of the new magnetic field coils [127] the 2$^{\text{nd}}$ MOT optics were completely realigned to take advantage of the increased optical access. The MOT was optimised such that a maximum load of atoms into the MOT was achieved, and from there the following stages of the experiment such as the CMOT, molasses and magnetic trap loading were optimised in sequence. This procedure does not guarantee the maximum possible PSD will be achieved in the magnetic trap, however. The MOT beams have since been fully realigned with a view to increasing the number of atoms transferred into the magnetic trap at as low a temperature as possible.

The role of the CMOT is to move the atomic cloud to the centre of the magnetic trap. If the centre of the MOT is largely displaced from the centre of the CMOT the atoms' position is rapidly changed causing heating of atoms due to 'slosh' and loss [126]. By making a MOT using the MOT beams but with the magnetic trap coils to provide the quadrupole field the centre of the magnetic trap was recorded. This process was repeated using the MOT coils, with the MOT field gradient and detunings, and with the CMOT field gradient and detunings. It was found that in the previous configuration the MOT was displaced by (3.2 ± 0.1) mm from the magnetic trap centre, and the CMOT was displaced by (2.1 ± 0.1) mm from the magnetic trap centre. In an attempt to increase the atom numbers available in the magnetic trap the following procedure was followed to optimise the MOT alignment.

3.6.1 Nullifying the background magnetic field

The field applied by the shim coils to nullify any ambient shim field was first optimised in each direction separately. This was achieved by measuring the efficiency of optical pumping. The efficiency is measured using the recapture technique whereby the MOT fluorescence before and after magnetic trapping is recorded. To nullify the field in the two planes orthogonal to the quantisation field the recapture efficiency as a function of magnetic field applied was measured. If any field is applied in the two directions orthogonal to the quantisation field the efficiency of the optical pumping is reduced, hence the null field is that for which the optical pumping is most efficient. Figure 3.3(a) presents typical data acquired when performing this optimisation.

To nullify the ambient field along the quantisation axis a slightly different technique is applied. The recapture rate is first measured without the optical pumping routine in the sequence. This sets the level of recapture possible without optical pumping, hence it is possible to determine whether the inclusion of the optical pumping sequence makes the magnetic trapping more efficient (pumping) or less efficient (anti-pumping). When optical pumping is efficient there is a non-zero quantisation field in the correct direction, however when the pumping becomes less efficient than the base rate, the quantisation axis has the wrong sense hence atoms are being pumped to the non-magnetically trappable states. The field at which the recapture efficiency is the same with and without pumping is the field at which there is zero ambient field. This test was performed for both ^{87}Rb and ^{133}Cs, the results of which are presented in figure 3.3(b).

The ambient magnetic field was minimised by applying (0.0 ± 0.2) G and (4.8 ± 0.1) G in the $x-$ and $y-$directions respectively, as shown in figure 3.3. In the $z-$direction data was taken using both ^{87}Rb and ^{133}Cs, and the nullifying shim field was measured to be (-0.1 ± 0.2) G and (-0.2 ± 0.2) G respectively. Both values are in agreement with each other. Ultimately it can be seen that the ambient lab field has been cancelled using the shim coils. This field setting is used for the molasses and from all points onwards in the

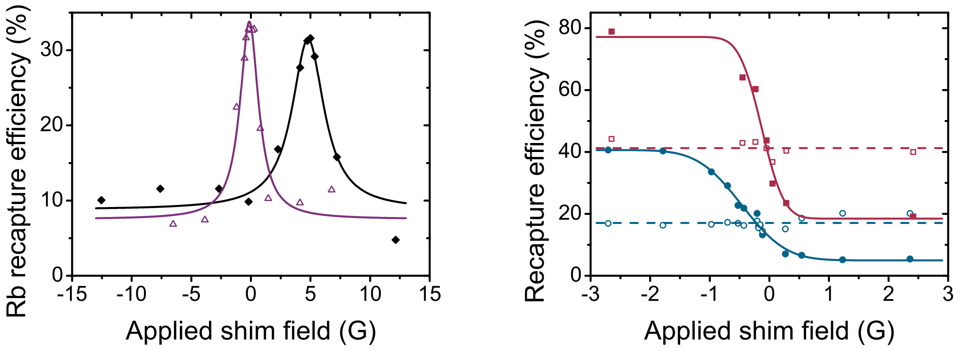

(a) (b)

Figure 3.3: Recapture efficiency in the $x-$, $y-$ (a) and the $z-$directions (b) as a function of the bias field applied with the shim coils in that direction. In the $x-$direction (purple triangles) the field required to nullify the ambient field is (0.0 ± 0.2) G and in the $y-$direction (black diamonds) (4.8 ± 0.1) G is required. In the $z-$direction recapture data are presented for both ^{87}Rb (red squares) and ^{133}Cs (blue circles) with (solid) and without (hollow) optical pumping. At the bias field where optical pumping begins to improve the recapture (as opposed to decreasing the efficiency as the quantisation field is in the wrong direction and 'anti-pumps' the atoms) the ambient field is nulled. For the ^{87}Rb data this field is (-0.1 ± 0.2) G and for the ^{133}Cs data we calculate (-0.2 ± 0.2) G. The absolute recapture possible is lower for the data in the $x-$ and $y-$ directions as this test was performed prior to further improvements in magnetic trapping being made. Lines are added simply to guide the eye.

experiment until the quantisation field is applied during absorption imaging.

3.6.2 Repositioning the MOT

With the ambient field nullified as above a MOT was then made using the smallest magnetic field gradient possible. To be able to magneto-optically trap atoms with a small trapping gradient the beam powers must be well balanced, and the circular polarisation of the beams well aligned. Additionally the direction of propagation of the beams must be optimum. Small apertures were placed in the MOT trapping beams before they were split into the three different beams. The beam power in each beam prior to impinging on the glass cell was then balanced with the counter-propagating beam. Following the balancing of the powers the aperture was removed and a MOT was formed with the MOT gradient of 10.3 G cm^{-1}. Applying an iterative procedure of slightly varying the beam powers to produce a large MOT over the centre of the MOT coils, and then varying the polarisation until the largest MOT was formed the optimum configuration was found. The final beam powers for the balanced ^{87}Rb beams are displayed in figure 3.4. Note that the values are simply fractions of the maximum power in any one beam as the inclusion of the iris drastically reduces the total beam power. It can be seen that in both the horizontal and vertical planes all beam powers are balanced well. In addition to balancing the beam powers it was also verified that all beams were well overlapped and counter-propagating.

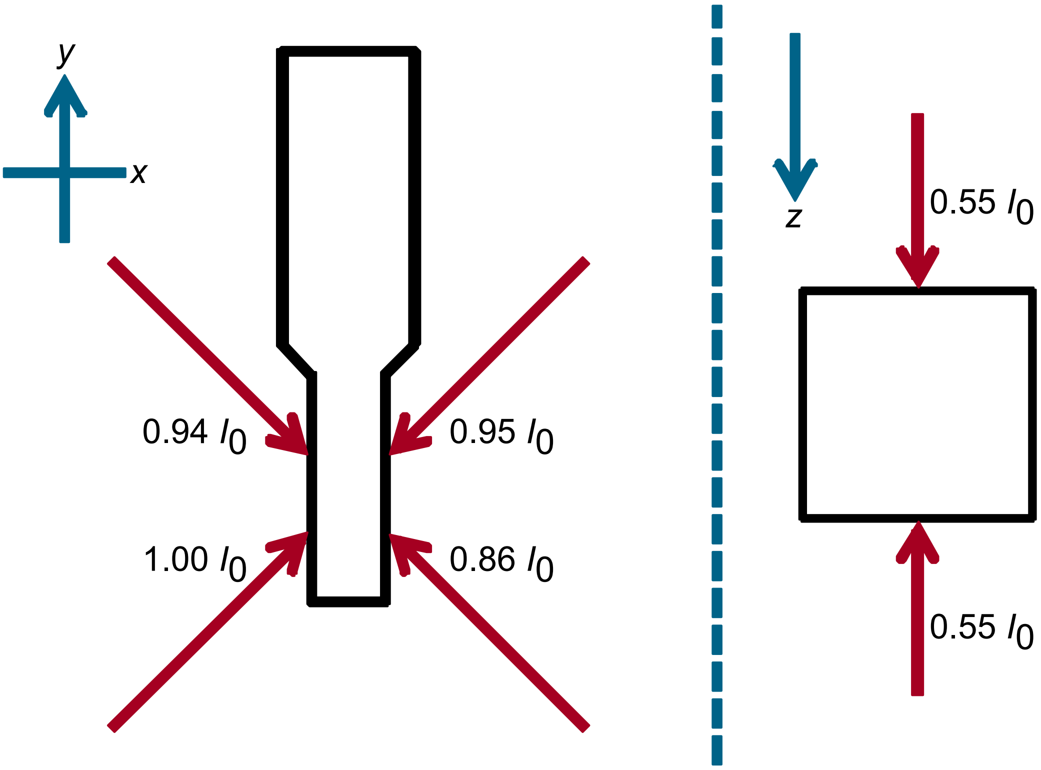

Figure 3.4: Ratio of ^{87}Rb MOT beam powers incident on the glass cell in each direction after the powers were balanced. The axes indicate the $x-$, $y-$ and $z-$directions.

Once the largest MOT had been produced the MOT shim coil settings were varied until the MOT formed over the magnetic trap centre. An additional ^{87}Rb $\lambda/4$-plate was inserted in the beam that propagates in the direction of gravity. This was to ensure that optimum circular polarisation was achieved for ^{87}Rb to improve the ^{87}Rb MOT. The previous setup simply had one $\lambda/4$-plate for each species, hence the optimum wasn't achieved for either. Since the absolute ^{133}Cs number required for measurement of Feshbach resonances is reasonably low, the ^{133}Cs load has been compromised in order to improve the ^{87}Rb load, and thus the sympathetic cooling in the magnetic trap (see section 5.1). The MOT is now aligned in the optimum position for transfer into the magnetic trap, however the absolute maximum number that is trappable in the MOT may be slightly higher than what can be achieved in this configuration.

The magnetic trap loading was then optimised creating a MOT with the CMOT beam detunings and magnetic field gradient. The shim coil settings were changed until the CMOT was formed over the magnetic trap centre, such that in the experimental procedure the atoms would not move much between the MOT, CMOT and magnetic trapping phases. The procedure above was repeated for ^{133}Cs, however the shim settings were not changed as this would affect the ^{87}Rb magnetic trap loading. In addition, it was found to be necessary to use the push beam as discussed in section 3.4.

Using this method we are now able to load $(6.2 \pm 0.2) \times 10^{8}$ ^{87}Rb atoms at a temperature of (140 ± 10) μK and a phase space density of $(2.2 \pm 0.7) \times 10^{-6}$ into the magnetic trap after $\partial B/\partial z$ is increased to 187 G cm^{-1}. Previously $(1.6 \pm 0.1) \times 10^{8}$ ^{87}Rb atoms were loaded into this potential at a temperature of (114 ± 5) μK and a PSD of $(1.5 \pm 0.3) \times 10^{-6}$. At this stage there is only a small improvement in PSD, however throughout the RF evaporation the evaporation was more efficient in the new system due to the increased number of collisions, as will be discussed in section 3.7.

3.7 Improved magnetic trap evaporation

In this section the improvements made to the magnetic trap RF evaporation of ^{87}Rb are discussed. Since the number of atoms loaded into the magnetic trapping potential has increased the optimum RF evaporation ramps were re-optimised for this new experimental situation. All RF evaporation was performed at a magnetic field gradient of 187 G cm^{-1} and the optimisation procedure used is discussed in section 3.7.1. The RF field is broadcast by a rectangular copper coil of two turns of dimension 36×45 mm^2 positioned approximately 20 mm from the glass cell. The orientation of the coil is orthogonal to the x-direction.

If a high frequency field is applied no atoms are cut from the potential, experimentally we find that atoms begin to be lost from the trap once the frequency is approximately 28.8 MHz. Hence this is chosen as the starting frequency for the RF ramps. Figure 3.5 presents data taken to determine the initial RF frequency to use. The initial cloud temperature prior to RF evaporation is (140 ± 10) μK, hence the cut energy is obtained using

$$\Delta E = m_F g_F \mu_B B = k_{\mathrm{B}} T, \tag{3.1}$$

and since the ground state frequency splitting of ^{87}Rb is 0.70 MHz G^{-1} [193] this corresponds to a cut energy of $k_{\mathrm{B}} \times (1.376 \pm 0.001) \times 10^3$ μK. Correspondingly η is calculated using equation 2.63, in this case a value of (9.8 ± 0.7) is obtained.

3.7.1 Optimisation of evaporation

Evaporation within the magnetic trap is forced using an RF field and in the optical trap it was performed via either plain evaporation or by tilting the trap with a B-field gradient. The method of optimisation for each stage of evaporation was the same independent of the technique used, however. For each stage of evaporation, the initial number and PSD were recorded. The next evaporation ramp would approximately quarter the trap depth, and the time taken to perform this evaporation would be varied. The most efficient timing was always chosen, where efficiency is defined as [168]

$$\gamma = \log\left(PSD_2/PSD_1\right)/\log\left(N_1/N_2\right). \tag{3.2}$$

Here PSD$_{1,2}$ is the PSD before or after the evaporation stage and $N_{1,2}$ is the initial number or number after the evaporation stage. This figure of merit was used to optimise every evaporation ramp. The number and temperature after the evaporation ramp were fitted using an exponential decay curve, and from

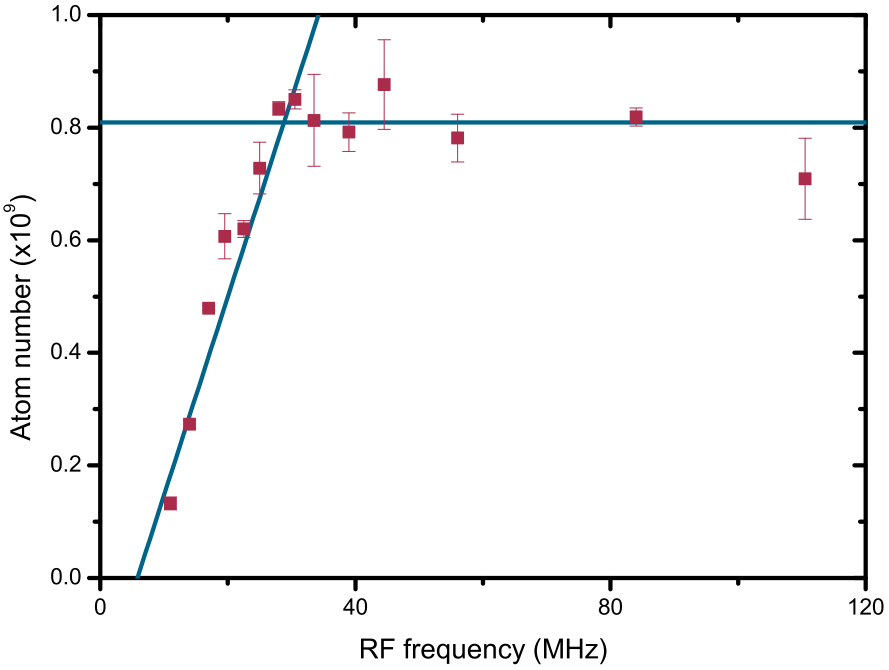

Figure 3.5: The number of ^{87}Rb atoms remaining in the quadrupole trap after different RF cutting frequencies are applied to the trap with a magnetic field gradient of 187 G cm^{-1}. This aids to determine the starting frequency for RF evaporation. The lines are linear fits to the data, and the crossing point was used as the initial RF frequency.

the fit to the data a PSD was calculated. Finally γ was calculated for each ramp time, and the most efficient ramp time was selected. Figure 3.6 presents a typical set of data taken when optimising part of the linear evaporation ramp for ^{87}Rb in the quadrupole trap, between frequencies of 14.6 MHz and 8.8 MHz. The values for γ are calculated using an initial number of $(3.1 \pm 0.2) \times 10^8$ and PSD of $(1.9 \pm 0.1) \times 10^{-5}$.

3.7.2 ^{87}Rb RF evaporation

The optimised ramp was found to be a single linear ramp of 15.1 s duration from the initial frequency of 28.8 MHz to a final frequency of 6.6 MHz. This was originally optimised in three separate stages, which when combined were found to be linear, so were combined for simplicity. The speed of the

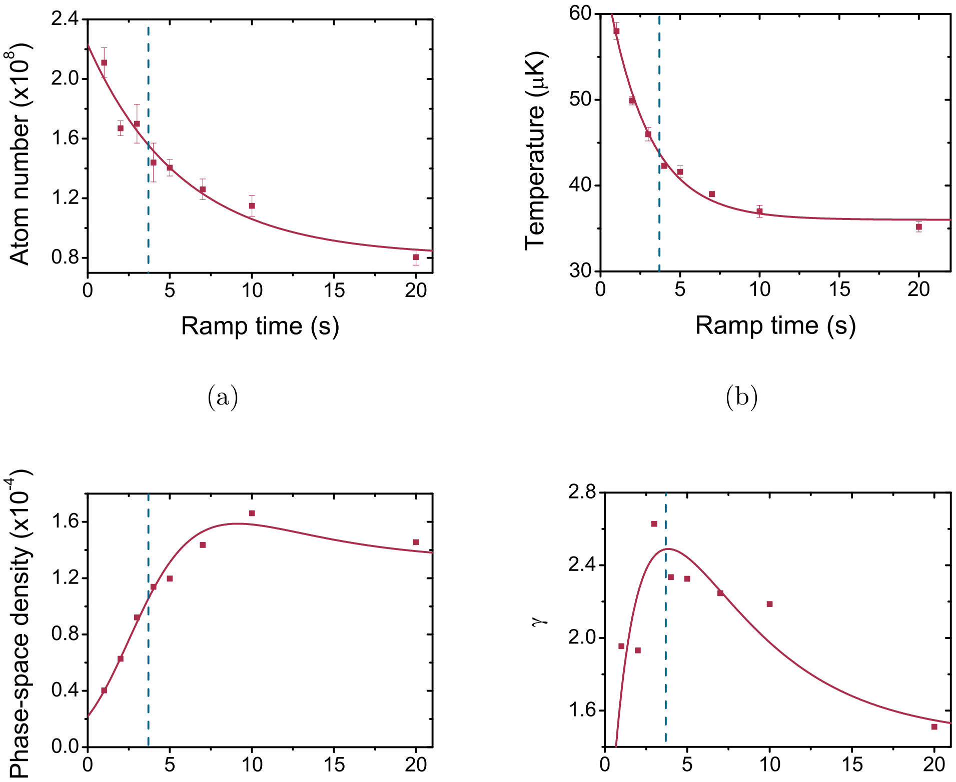

(a) (b)

(c) (d)

Figure 3.6: Typical data obtained when optimising a magnetic trap evaporation ramp against ramp time. The graphs display how the number (a), temperature (b), PSD (c) and efficiency (d) vary with ramp time. The lines in (a) and (b) are fits to the data points. The lines in (c) and (d) are then calculated using these fits. The dashed blue lines indicate the optimum ramp time of 3.7 s.

evaporation is significantly faster than the 34.5 s required previously, hence the duration of each experimental cycle has been reduced accordingly [127]. After this stage the evaporation began to stagnate due to Majorana spin flips at the trap centre [163]. After the RF evaporation in the magnetic trap $(7.3 \pm 0.3) \times 10^7$ atoms remain at a temperature of (33.6 ± 0.3) μK and a PSD of $(1.6 \pm 0.2) \times 10^{-4}$. The progression of the PSD as the evaporation proceeds is presented in figure 3.7. Tables 3.2 and 3.3 reiterate the optimum evaporation ramp for RF evaporation of ^{87}Rb.

Figure 3.7 indicates that currently after the RF evaporation the ^{87}Rb atom

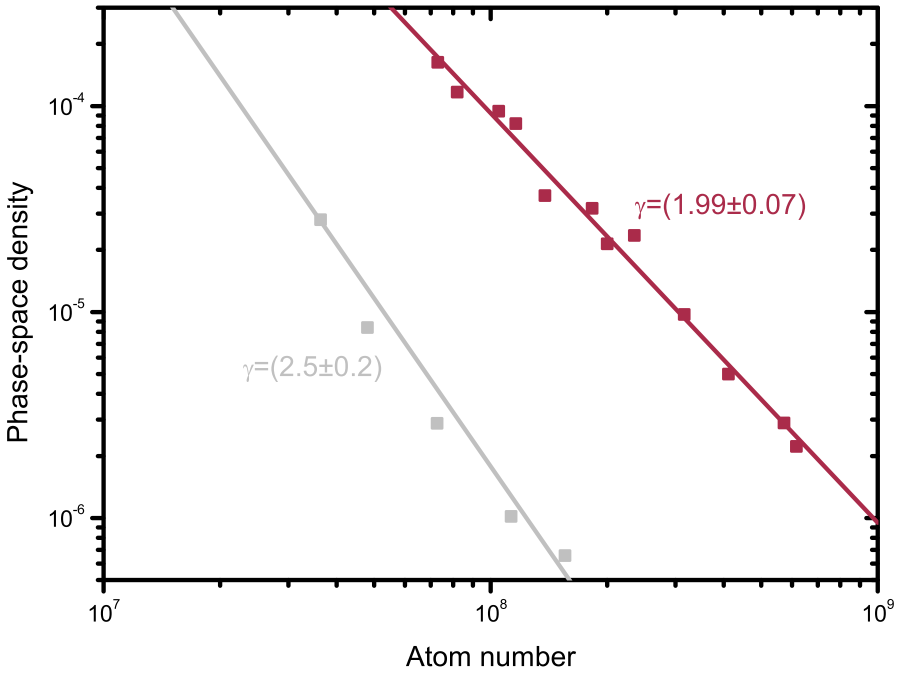

Figure 3.7: PSD as a function of atom number in the quadrupole trap for ^{87}Rb alone. The lines have been added to guide the eye. The grey data points and line represent data taken before improvements to the magnetic trap loading were made [12].

number is much larger ($(7.3 \pm 0.3) \times 10^7$ compared to $(3.6 \pm 0.1) \times 10^7$) than previously and the PSD is accordingly higher, by a factor of approximately six. The temperature reached is also lower (as displayed in figure 5.2). The lines in figure 3.7 that have been included to guide the eye can be used to calculate the efficiency of the evaporation from equation 3.2. We see for the evaporation of ^{87}Rb alone the efficiency for the new data is (1.99 ± 0.07) whereas it was previously (2.5 ± 0.2). The efficiency has therefore dropped

Ramp	t (s)	f_1 (MHz)	f_2 (MHz)
1	15.1	28.8	6.6

Table 3.2: Magnetic trap RF evaporation ramp used for evaporation of ^{87}Rb.

Ramp	N ($\times 10^8$)	T (μK)	PSD
Load	(6.2 ± 0.2)	(140 ± 10)	$(2.2 \pm 0.7) \times 10^{-6}$
1	(0.73 ± 0.03)	(33.6 ± 0.3)	$(1.6 \pm 0.2) \times 10^{-4}$

Table 3.3: Number, temperature and PSD before and after RF evaporation ramp for ^{87}Rb. The ramp labels correspond to those in table 3.2.

due to increased inelastic collisions, however the improved starting conditions mean that more atoms are still present after the evaporation.

3.8 Imaging

In this work we use two diagnostic techniques to determine the parameters of the atom clouds. Fluorescence imaging is a technique which was used heavily during the MOT and magnetic trap loading phases of the experiment due to its non-destructive nature and its versatility in providing information on relative MOT numbers. Absorption imaging was used to obtain information on the spatial profile of the atoms in addition to their absolute number, however this technique is destructive. Additionally, separating the atoms into their different m_F states via the Stern-Gerlach method means information about the different hyperfine states can be accessed. In the following sections the different methods will be discussed in more detail.

3.8.1 Fluorescence imaging

Fluorescence imaging was used extensively during the initial MOT optimisation, where the different parameters were optimised to increase MOT fluorescence, which is a good indicator of the relative number of atoms within the MOT. Further, it is possible to analyse the performance of magnetic trap loading by re-capturing the magnetically trapped atoms in the MOT. Experimentally the fluorescence emitted by the MOT is incident on an 80 mm focal length lens a distance L from the atom cloud. To ensure the relationship between MOT fluorescence and trapped atoms remains linear, an iris of aperture d is placed immediately in front of the lens. For aperture diam-

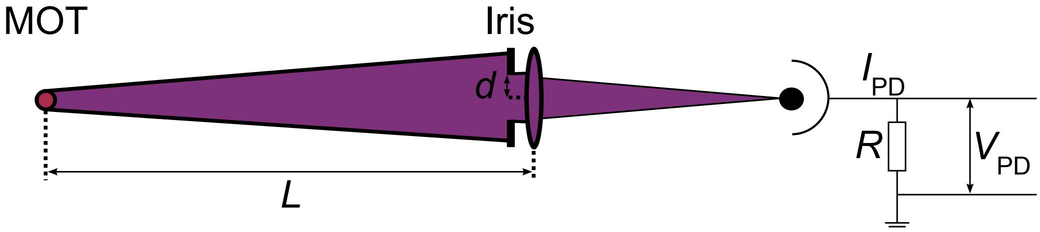

Figure 3.8: Schematic of the experimental setup required to detect MOT fluorescence and a definition of all terms used in the atom number calculations outlined in appendix D. The electronics required to measure the photocurrent of just one photodiode are shown, however they are identical for each photodiode. Diagram not to scale.

eters that are too large, not all of the light is collected by the lens as it is incident on the edge of the lens, hence a deviation from a linear relationship is observed. The lens, which is broadband AR coated focusses the light onto two photodiodes (Thorlabs DET110 for Rb and DET36A for Cs). A dichroic mirror which reflects light of wavelength 850 nm splits the fluorescence due to trapped Rb and Cs atoms. Due to the fact that this mirror still reflects $(1.2 \pm 0.2)\%$ of the 780 nm wavelength light emitted by the Rb MOT, this background must be taken into account when calculating absolute atom numbers. The photocurrent is measured by detecting the voltage across a 1 MΩ resistor. The absolute number of atoms can then be calculated using the calculations presented in appendix D.

3.8.2 Absorption imaging

More detailed information about the atom cloud, its spatial profile and the mixture of hyperfine states present within can be obtained via an absorption image. This is performed by allowing the cloud to evolve in free space for a time known as the time-of-flight. A quantisation field of (2.7 ± 0.1) G is applied in the $y-$direction before atoms are then pumped out of the absolute internal ground state by switching the repump light on 100 μs before switching on a 10 μs pulse of cooling light of intensity $0.1 I/I_{\mathrm{SAT}}$. The cooling light drives either σ^+ or σ^- transitions into the stretched states. To image the magnetically trappable states σ^- transitions are driven, whereas σ^+ transitions are driven to image the high-field seeking states. Once the atoms are

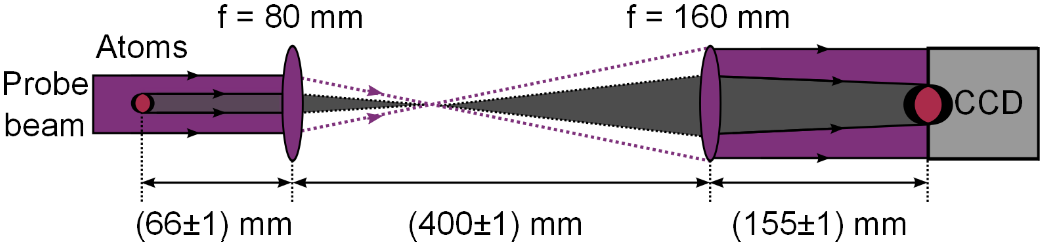

Figure 3.9: Schematic of the apparatus required to take an absorption image of the atoms. The probe beam illuminates the atom cloud, which absorbs some of the probe photons. Two achromatic doublet lenses magnify the absorption profile with a magnification of (1.858 ± 0.002) (see figure 3.10). The probe beam is detected on a CCD camera. Diagram not to scale.

in the stretched states they absorb the photons which reduces the intensity of the beam in this location. The probe beam is incident on a CCD camera (Andor iXon 885) and the sequence of required images is recorded here. A full explanation of the absorption imaging routine including the program used to image both species in the same experimental run and fitting the cloud with a Gaussian function is presented in reference [125]. A schematic of the apparatus required to take an absorption image is provided in figure 3.9.

Three individual ‘shots’ are required to make one absorption image, each one taken shortly after the previous one. The first shot contains the atoms, the probe beam (which ‘destroys’ the atom cloud) and the background which is present without the probe beam. The second shot consists of just the probe beam and the background, and for the third shot the probe beam is switched off, hence only the background light is present in the image. The intensity of each pixel on the camera is read out, and the optical depth of the atom cloud at each point in the image is calculated via

$$OD = \ln\left(\frac{I_2 - I_3}{I_1 - I_3}\right), \tag{3.3}$$

where $I_{1,2,3}$ are the intensities of light on each pixel in the first, second and third shot. For a weak, on resonance probe beam

$$I = I_0 \exp(-OD), \tag{3.4}$$

where I is the intensity of light recorded on the CCD camera and I_0 is the intensity of the probe beam without the atoms’ presence. Hence if there are more atoms in the cloud the optical depth will be larger. The purpose of taking the three images is to remove the background counts from both I_1 and I_2, and then determine the rate of absorption of light.

After fitting the resultant image with a Gaussian lineshape and following the arguments in appendix D we can calculate the number of atoms in the cloud using

$$N = \frac{4\pi^2}{3\lambda^2}\sigma_x\sigma_z OD_{\mathrm{PK}}, \tag{3.5}$$

where $\sigma^2_{x,z} = k_{\mathrm{B}}T/m\omega^2_{x,z}$ are the widths of the Gaussian fit to the cloud, λ is the wavelength of light and OD_{PK} is the peak optical depth.

Assuming a harmonic trapping potential, as is the case in the optical trap, and that the trap frequencies are known, we can also calculate the temperature of the cloud

$$T_{x,z} = \frac{m\omega^2_{x,z}}{k_{\mathrm{B}}}\frac{\sigma^2_{x,z}(TOF)}{1+\omega^2_{x,z}TOF^2}, \tag{3.6}$$

where TOF is the time-of-flight, $\sigma_{x,z}(TOF)$ is the cloud size after the time-of-flight expansion and $\omega_{x,z}$ are the radial and longitudinal trap frequencies. If the cloud size after a time-of-flight expansion is known the size of the cloud in the trap can be calculated using

$$\sigma_{x,z}(0) = \frac{\sigma_{x,z}(TOF)}{\sqrt{1+\omega^2_{x,z}TOF^2}}. \tag{3.7}$$

The derivation of these properties is reported in more detail in appendix D.

The two achromatic lenses are set up such that the second lens, of 160 mm focal length, is positioned with its focus at the location of the CCD chip. The first lens was then positioned such that it brings the atoms into focus. To obtain sharp, well focussed images this lens is mounted on a translation stage with 5 μm accuracy, and a series of images were taken for various positions to locate the optimum position. This optimisation process is discussed in more detail in section 3.8.3. The telescope system of the two lenses obviously magnifies the image. The magnification factor of the telescope setup was determined by measuring the vertical position of the atom cloud as a function of a flight time after the cloud had undergone RF evaporation in the magnetic trap (see figure 3.10).

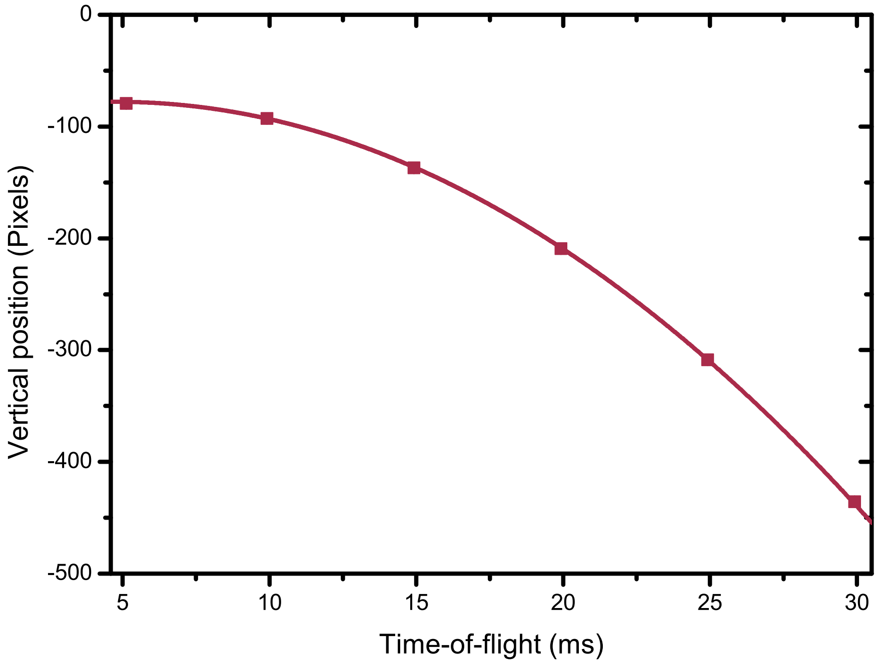

Figure 3.10: The vertical position of the atom cloud after undergoing freefall for various time-of-flights. The vertical position is recorded as the distance in pixels of the cloud's centre from the top of the camera, using a Gaussian fit to the distribution. The pixels are numbered such that zero pixels is at the top of the camera. A parabola is then fit to the data, weighted to the error bars, and it is found that the magnification is $M = (1.858 \pm 0.002)$.

To interpret figure 3.10 one must use

$$s = s_0 + ut + \frac{1}{2}gt^2, \tag{3.8}$$

where s is the vertical position of the atom cloud's centre, s_0 is the initial position of the cloud centre, and u is the initial speed of the atom cloud, assumed to be zero. Hence comparing the equation of the parabola, $y = A + Bx + Cx^2$, with equation 3.8 we see

$$y = \frac{1}{2}gt^2\frac{M}{d_{\mathrm{PIX}}} = Ct^2 \tag{3.9}$$

where d_{PIX} is the length of the side of each pixel (16 μm in this case, as the camera's pixels are 8×8 $\mu\mathrm{m}^2$ in size, but we bin the total charge on four pixels together at once to reduce the processing time) and C is the coefficient of the t^2 term in the parabolic fit to the data. Hence

$$M = \frac{32C}{g}. \tag{3.10}$$

For the data in figure 3.10 we find that the magnification is (1.858 ± 0.002). This value is used in calculating atom numbers and cloud temperatures in this work.

For the atoms to absorb the maximum amount of probe light the frequency of the probe beam must be on resonance, however the application of the (2.7 ± 0.1) G quantisation field creates a Zeeman shift in the energy levels. Therefore the probe beam frequency required detuning in relation to the zero field resonant frequency. The frequency driving the AOM which modulates the probe beam was varied and the optical depth of an image of the atoms was measured. By fitting a Lorentzian function to the data and extracting the centre of the function where the maximum optical depth occurs one can determine the detuning required to bring the light back on to resonance with the atoms. Figure 3.11 presents the optical depth (normalised to a value extracted from a fit to the non-normalised data) as a function of probe beam detuning. Similar experiments were performed to determine the resonant imaging frequency for both isotopes of Rb.

The frequency at which the optical depth is maximised is found to be (-2.41 ± 0.07) G for the σ^+ data and (3.54 ± 0.06) G for the σ^- data and the calculated widths were $2\pi \times (6.0 \pm 0.2)$ MHz and $2\pi \times (6.1 \pm 0.2)$ MHz respectively. Thus the bias field that was applied here is calculated to be (2.12 ± 0.05) G, using the theoretical Zeeman shift at low-fields of 1.40 MHz G^{-1}. The reason that the σ^- plot is shifted more than the σ^+ plot is that at the time the cancellation fields required for the shim coils were not well known, hence the quantisation field may not have been purely in the correct direction. The widths were in agreement with each other but not with the theoretical ^{133}Cs linewidth of $2\pi \times 5.2340$ MHz. Similarly this is potentially due to the quantisation field not purely being in the direction of propagation of the probe beam. Imaging of different m_F states is performed experimentally by the Stern-Gerlach method, described in detail in section 2.4.3.

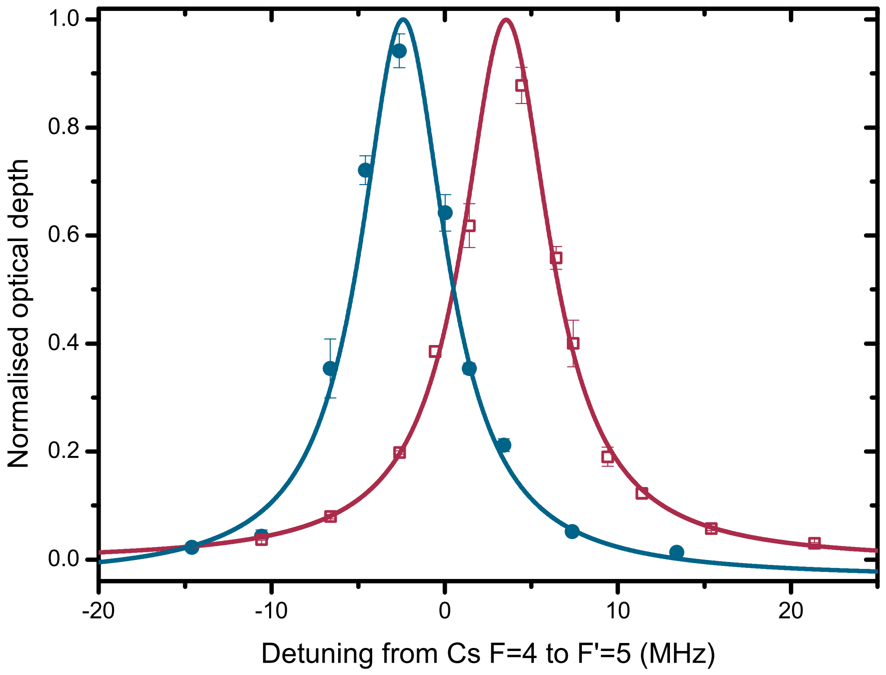

Figure 3.11: Optical depth of a cloud of ^{133}Cs atoms imaged after a 2 s hold in the magnetic trap and a 3 ms free time-of-flight as a function of the probe beam detuning from the zero field resonant frequency. A 50 μs probe pulse was used with 1 ms of repumping light applied prior to the probe pulse. The two plots correspond to a bias field being applied that drives σ^+ transitions (blue) and then reversing the bias field such that σ^- transitions are driven (red). A Lorentzian fit to the data, weighted to the error bars calculates linewidths of $2\pi \times (6.0 \pm 0.2)$ MHz for the σ^+ data and $2\pi \times (6.1 \pm 0.2)$ MHz for the σ^- data. These values agree with each other, however are not in agreement with the natural linewidth of ^{133}Cs (see table A.1). The detuning at the peak in the optical depth is (-2.41 ± 0.07) G for σ^+ transitions and (3.54 ± 0.06) G for the σ^- data. For clarity the values are normalised to the maximum optical depth obtained from a fit to the raw data.

3.8.3 Imaging lens positioning

The approximate alignment of the telescope was discussed in the previous section however the first lens in the telescope has been mounted on a translation stage such that the exact position can be optimised. Exact positioning was not immediately possible due to the atomic density not being very large. Imperfect focussing on the atom cloud results in distortion of the image as discussed in the following.

The model for calculating atom number in appendix D only considers absorption and scattering of photons from the probe beam, it does not include the effects that the cloud may have on the spatial profile of the probe beam. For a dense atomic cloud the refractive index is not unity as the atomic susceptibility is non-zero [194]. The refractive index of the atomic medium will be greater than 1 for a red detuned probe beam and less than 1 for a blue detuned probe beam [195]. The spatial density profile within the cloud and its curvature at the edges therefore lead to lensing of the probe beam.

Modelling the cloud as a sphere of radius R and refractive index n its focal length is [196]

$$f = \frac{R}{2(n-1)}. \tag{3.11}$$

Due to this lensing of the probe beam the image will not reflect the true spatial profile of the atomic cloud. To remove the effect the probe beam may be tuned to resonance, however the high optical depth of the dense cloud would limit number calculation. Alternatively, accurate focussing of the cloud means the effect is removed, as described below.

Consider the case of a blue detuned beam where $n < 1$. For $n < 1$ the cloud will act as a diverging lens. Therefore as the beam diverges the light in the imaging sequence's first shot is refracted and its new path is incident on outlying parts of the CCD camera, where light otherwise wouldn't reach. Resultantly the amount of light in the centre of the image is reduced. As the cloud is then 'destroyed' the second shot in the imaging sequence is unaffected. If the focussing lens is placed too far away from the atom cloud, the optical depth calculated is higher in the centre of the image and becomes negative at the edges of the image. If the imaging lens is placed too close to the cloud we record a virtual image of the clouds, and one must consider the virtual rays of the probe beam. In this situation more light is incident at the centre of the cloud, resulting in a sharp dip in the optical depth here. Conversely for red detuned beams $n > 1$ and the cloud acts as a converging lens, hence the process described above is reversed.

A schematic of this lensing effect is presented in figure 3.12(a). When the imaging lens is positioned too close to the atoms such that it is focussed at the side of the probe beam source (position 1 in the figure highlighted by the dashed lines) a region of negative optical depth occurs at the centre of the image for blue detuned light, or at the edge of the image for red detuned light. For this location one must consider the virtual imaging rays, represented by dotted lines. For the case where the imaging lens is positioned too far from the atoms such that it is focussing on position 2 in the figure, we obtain more light at the edges for blue detuned light and more light at the centre for red detuned light. The optical depth thus calculated as a function of position is presented in figure 3.12(b) for the case where there is more light at the edges (left), an ideal image (centre) and more probe light at the centre (right). Where more probe light is observed at the edges, this creates a dip in the optical depth here, which is observed on either wing of the graph, and a slight enhancement of optical depth can also be seen at the centre, as there would be less light in the first probe shot here. When there is more light at the centre we get a sharp dip in optical depth here. A clean Gaussian profile is observed if the imaging telescope is well focussed. Corresponding experimental data for a ^{87}Rb condensate can be seen in figure 3.12(c). For both the profiles on the left and right the imaging system was focussed too far away from the atoms, with the probe light blue and red detuned, respectively. For the blue detuned image a dip in optical depth can be observed at the edge of the cloud. Conversely for the red detuned profile at the centre of the cloud a region of lower optical depth can be observed. The profile in the centre was taken with blue detuned light, however the imaging system was well focussed on the atoms.

To accurately focus onto the atoms a sequence of images were taken for different positions of the focussing lens. For each position a red and a blue detuned image were taken. Starting with the lens focussed too far from the atoms, one could observe the effects of the lensing becoming less pronounced the closer the system became to being in focus, and then once past the optimum position the opposite effect begins to manifest itself. Additionally it is possible to reduce the effects of lensing by performing a large time-of-flight such that the density at the time of imaging decreases. This is preferable to detuning the beam as the lensing effect will become less pronounced for large detunings as it is inversely proportional to Δ, however the strength of

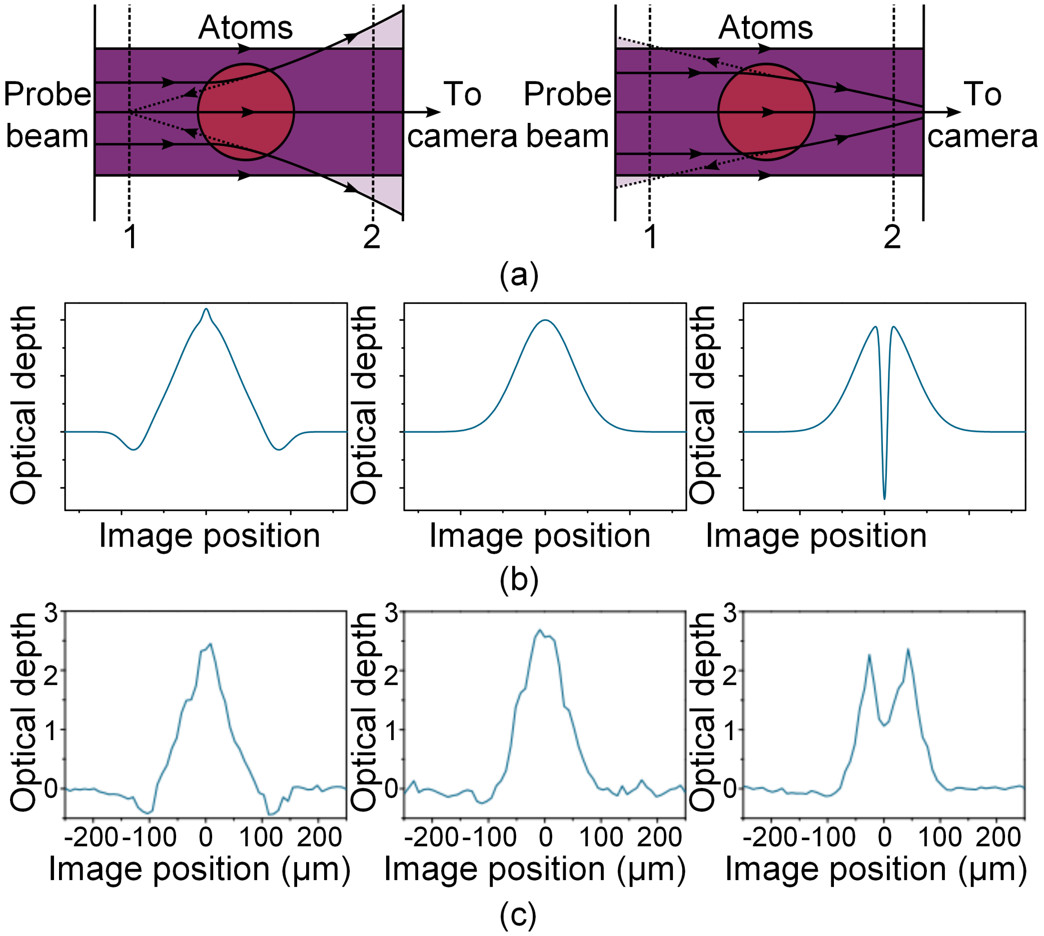

Figure 3.12: Schematic of the imaging lensing effect (a) for blue detuned (left) and red detuned (right) probe light, theoretical density profiles observed for the different imaging cases (b) and experimentally obtained density profiles of the atom cloud for these cases (c). In the schematics regions where probe light intensity is increased are highlighted by the transparent purple shade and virtual focussing rays are represented by dotted lines. The dashed lines at location 1 and 2 indicate the two focussing locations discussed in the text. In (b) the optical depth is represented as a function of position in the image for the case of (left to right) more probe light at the wings of the image, an ideal image and more probe light at the centre of the image. In (c) the $x-$axis refers to the horizontal distance from the cloud's centre.

the signal at high detunings is inversely proportional to Δ^2 so the signal to noise ratio will decrease.

3.9 Bias field stabilisation

The methods used in the work to detect Feshbach resonances require the application of a stable bias field. Various resonances are located at high magnetic fields, hence the ability to generate these high-fields in a stable manner must be achieved. The bias field coils used in this experiment are set up such that one is used for making small, fast changes to the magnetic field, known as 'Bias 3' and the other two coils ('Bias 1 and 2') are run in series. These are used to generate fields in excess of 1000 G. To generate the fields a current is driven through the coils, the calculation of the field at the centre of the coils is given by equation 2.59. Approximate calibrations for the magnetic field generated by driving current through the coils are (2.761 ± 0.004) G A^{-1} for Bias 1 and 2 and (0.261 ± 0.002) G A^{-1} for Bias 3 [127]. To achieve an accuracy of ± 10 mG in our experiments this requires stabilisation of the current driven through the coils to 1 part in 10^5 for measurements at 1000 G.

3.9.1 Magnetic field generation

The current is drawn from two power supplies (Agilent 6681A and Agilent 6690A), the amount of which is stabilised via a series of four field-effect transistors (FETs) (IXYS Semiconductor 230N10) which are water cooled. A distinct power supply and FET bank are utilised for Bias 3, and Bias 1 and 2. Each set are connected in parallel such that they have a common source, drain and ground [126]. The current flowing through the coils is measured using a Hall effect sensor (Honeywell CSNL181). The Hall effect sensor generates a current 2000 times smaller than that in the coil. The current drawn by the Hall sensor is detected as a voltage dropped across a sense resistor on a 'feedback board' (Oxford University Deparment of Physics EW1282) and this voltage is compared with a voltage from a 'reference board' (Oxford University Deparment of Physics EW1285). The reference voltage is set in the LabVIEW computer control program.

The circuit works by varying the current in the coils such that the Hall voltage dropped over the sense resistor is equal to the reference voltage. A TTL switch controls by-passing of capacitors which when switched in provide higher stability to an initial amplification stage. The values of the capacitors chosen have been selected to minimise current instability at all currents, and is specific to the individual coils which have different resonant frequencies. When switching the currents through the coils on and off the capacitors are bypassed by the switch and fast ramping is achievable. A second stage of amplification allows the current to be switched to high values quickly without oscillation of the current at the final value. A tunable offset is set such that the current oscillates about the final current value.

In optimising the feedback boards two main changes have been made to the existing design. First, the level of variable gain on the second amplification stage is set to reduce the stabilisation time. The combination of capacitors used for each board was then changed to reduce current noise and thus increase stability. The combination of the capacitors required is dependent on the level of variable gain set. The second change was undertaken for the feedback boards of both Bias 1 and 2 and Bias 3. Previously the Hall voltage was measured over a 1 Ω resistor, however this has since been changed to a 20 Ω (Isabellenhütte A-H2-20R0-F1-K2-0.1) power resistor. The increase in the voltage of the sense resistor means a larger voltage will be dropped over the resistor, hence stabilisation is more sensitive. The power dropped over the resistor is larger, however the load capacity of the resistor is 10 W and the temperature coefficient is ±10 ppm K^{-1}. The resistor is mounted on a heatsink to further reduce any change in resistance if the magnetic field remains on for a long period of time. Indeed, a marked improvement in bias field stability has been observed, examples of which will be demonstrated in figures 6.5 and 6.6.

3.9.2 Magnetic field calibration

The bias fields used in this experiment have previously been calibrated by driving RF transitions between the excited states [127]. To obtain a more precise calibration by observing a narrower feature we are able to drive microwave transitions between the ground states in the atoms. The field axis for each individual feature observed in this work is calibrated by driving either RF or microwave transitions as presented in figure 3.13. The central frequency at which transitions are driven for each field are then used to calculate the magnetic field using the Breit-Rabi equation (equation A.1). A set of measurements are performed at a minimum of two points off resonance with the feature. The same experimental routine is performed, for example all MOT load, RF evaporation and forced dipole trap evaporation timings are identical, however the RF or microwave field is applied during the final hold at the final magnetic field. The different ground or m_F states are then separated using the Stern-Gerlach method and imaged.

The microwave frequencies are generated using an Agilent E8257D frequency generator as the source. When we calibrate the fields the output from the source remains on and a Mini-Circuits MSP2T-18-12 switch controlled by a TTL signal from LabVIEW determines whether the signal is applied to the atoms. The microwave frequencies are delivered using an AtlanTecRF AS 6186 waveguide-coaxial adapter. The output of the adapter is positioned (118 ± 2) mm from the centre of the glass cell.

A similar scheme is utilised to deliver RF frequencies to drive transitions between different m_F states. An Agilent E4400B is used as the RF source and once again the output remains constantly on. A TTL controlled Mini-Circuits ZYSW-2-50DR switches the signal on and off. The signal is then amplified by a Mini-Circuits TIA-1000-1R8-2 35 dB gain amplifier. A (25 ± 1) mm diameter single turn copper coil of thickness (0.8 ± 0.1) mm, which is positioned (80 ± 5) mm from the centre of the glass cell delivers the RF field to the atoms.

Figure 3.13 presents a sample bias field calibration taken at ≈ 31.5 G. Here the dipole trap beams are ramped to powers of 630 mW and the bias field from Bias 3 is ramped in 5 ms to its final value and held at this value for 100 ms. The microwave frequencies are then applied in this holding period. Note that the magnetic trap is also switched on to a field gradient of 28 G cm^{-1} for this measurement, hence the bias field at the atoms is approximately 0.6 G lower than the bias field produced by the coils as the atoms are positioned

$\sim$ 200 μm below the magnetic trap centre (see chapter 4). The magnetic field gradient was kept on during this measurement in order to maintain the same experimental procedure as described above.

Lorentzian fits to the data in figure 3.13 reveal that the central transition frequencies (widths of transitions) are (6.90109 ± 0.00001) GHz ((0.20 ± 0.04) MHz), (6.879262 ± 0.000003) GHz ((0.070 ± 0.009) MHz) and (6.857288 ± 0.000002) GHz ((0.05 ± 0.01) MHz) for σ^+, π and σ^- transitions, respectively. The magnetic fields required to drive these specific transitions at these frequencies were then determined from the Breit-Rabi equation. Combining these values represents a magnetic field of (31.490 ± 0.007) G and at this field a 10 mG change in field results in approximately 0.021, 0.007, or 0.014 MHz changes in frequency for the σ^+, π, and σ^- transitions respectively. Experimentally to calibrate fields we drive σ^+ transitions as the signature of atom loss from the $|1, +1\rangle$ state is most pronounced.

Most experiments in this work are performed by switching on the field from Bias coils 1 and 2 to the lower extreme of the region of interest, and then using the setting of Bias coil 3 the field is quickly ramped to the final field. The range we typically run with Bias 3 is 50 G, hence many experiments explore a 50 G window. To calibrate we set the voltage to which the feedback board will servo to in LabVIEW and obtain a plot similar to figure 3.13(a). This is repeated for a minimum of one other point in the window, and after calculating the field for each voltage a linear fit is made to the data. The bias field of each experimental point can then be calculated from this fit. A series of these fits at various bias fields is presented in figure 3.14.

Figure 3.14 highlights that although the calibration of the field provided by Bias 3 remains very similar over the entire field range, there is still a change at the highest fields. There is a tendency for Bias 3 to provide a smaller field as a function of LabVIEW control voltage at higher bias fields. This is potentially due to an offset picked up on the different Hall effect sensors and feedback electronics inherent when high currents are being driven through the coils. We also note that when the magnetic trap is switched off the bias field at the atoms with Bias 3 also switched off is (153.87 ± 0.01) mG. In section 3.6 the errors involved with nullifying the shim field were typically ±200 mG, which is consistent with the field seen at the atoms.

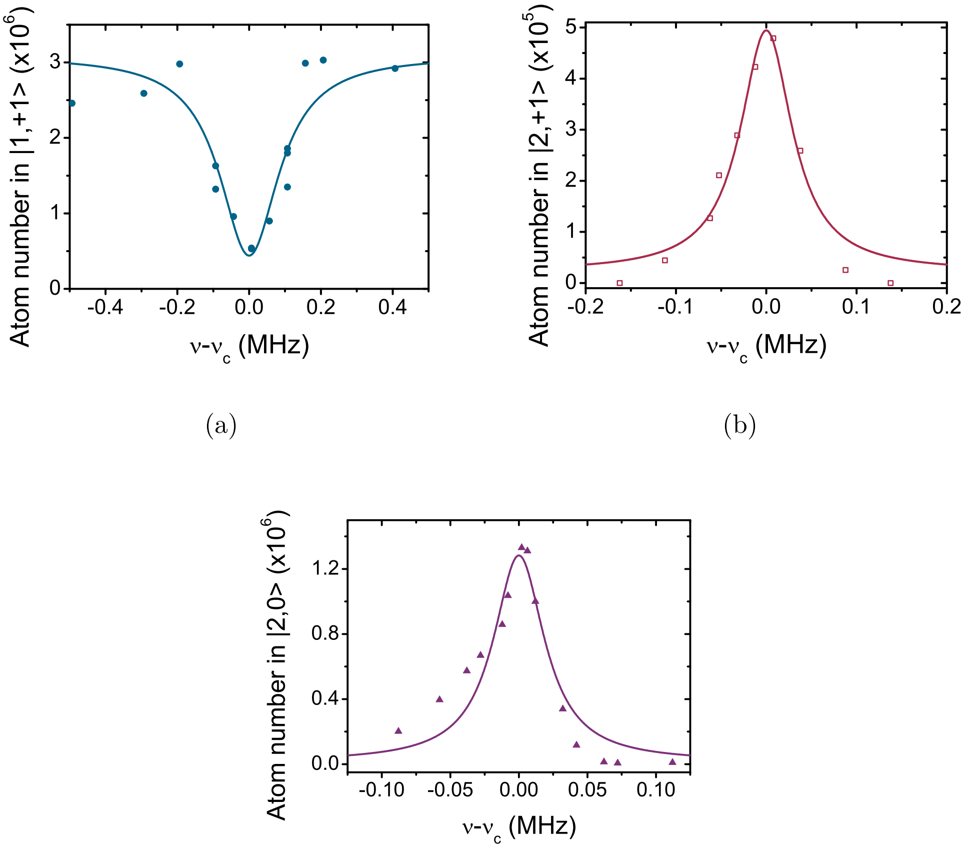

(a)

(b)

(c)

Figure 3.13: Number of ^{87}Rb atoms in different ground and magnetic states remaining after a 100 ms pulse of a microwave frequency field drives σ^+ (a), π (b) and σ^- (c) transitions. The same bias magnetic field is used for each case. The lines represent Lorentzian fits to the data and are used to calculate the central frequency of the transitions. In (a) the number of atoms remaining in $|1,+1\rangle$ is displayed as the $|2,+2\rangle$ atoms are not trapped. In (b) and (c) the number of atoms transferred to the $|2,+1\rangle$ and $|2,0\rangle$ states are displayed, respectively. The $x-$axes are centred on (6.90109 ± 0.00001) GHz (a), (6.879262 ± 0.000003) GHz (b) and (6.857288 ± 0.000002) GHz (c).

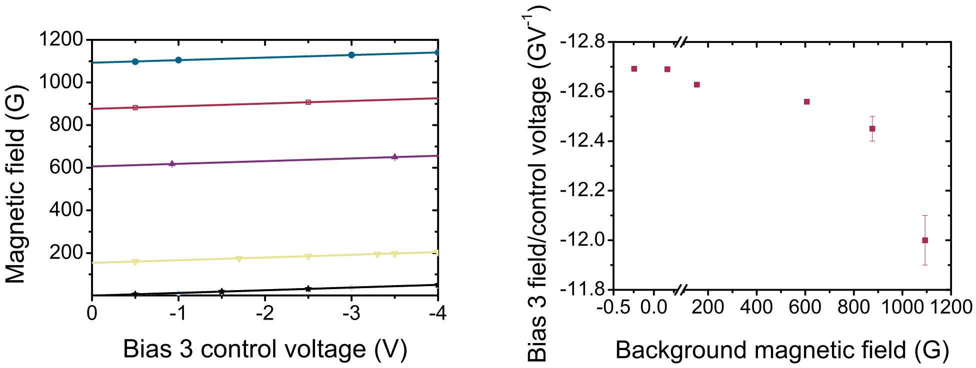

(a) (b)

Figure 3.14: Bias field as a function of LabVIEW control voltage (a) for a series of different bias fields produced by Bias 1 and 2 and the corresponding calibration of bias field as a function of the bias field at the atoms produced by Bias 1 and 2 (b). Note there are two plots where Bias 1 and 2 are switched off which can't be resolved due to the scale. The different bias fields without Bias 3 switched on are approximately 1093 G (blue circles), 876 G (red squares), 606 G (purple triangles), 154 G (yellow inverted triangles), 0 G (blue diamonds) and 0 G without the magnetic trap switched on (black stars).

3.10 Experimental control

To control the experimental timings down to small (ms-μs) timescales computer control of the apparatus is necessary. The necessity of computer control of the experiment is outlined in reference [125] hence a brief description is given here. The program used to control the system is 'LabVIEW' which allows precise timings to be pre-programmed and takes account of the delays involved when switching different hardware on or off.

A recent upgrade of the computer control systems has been implemented to both improve and simplify the computer control of the experiment. The LabVIEW program is still utilised, however a 'Field Programmable Gate Array' (FPGA) module has been installed. This has increased the resolution of the timing sequence and made the graphical user interface more intuitive. To control the experiment an NI PCI-7833R 'Reconfigurable Input/Output' (RIO) control board is used which allows independent control of 56 'Digital Input/Output' (DIO) channels, 8 'Analogue Input' (AI) and 8 'Analogue

Output' (AO) channels. The DIO channels are used for various functions such as the control of shutters and switching the magnetic field coils on and off. They are also required to receive input as a trigger to continue the imaging sequence [125]. The AO channels are used to control analogue parameters such as the magnetic field coil currents. Currently no AI channels are in use.

The control computer also communicates with a separate computer that controls external hardware using a PCI-GPIB card. The GPIB computer also has a PCI-DIO-32-HS DIO installed, which was used in the experiment previously. The main control computer outputs a series of digital signals which are read using the DIO channels on the GPIB computer. Depending on the input, the GPIB computer interfaces with different hardware. The frequencies applied during RF evaporation in the magnetic trap and rapid adiabatic passage are controlled in this way.

To reduce the number of DIO channels used on the control board two DIO channels can be combined to produce four possible outputs using a 'Voltage Level Multiplexer' designed by Oxford University Department of Physics. This is used to control shim coil currents, the MOT magnetic field gradient and the level of attenuation to apply to the cooling and repump AOMs for both Rb and Cs. The multiplexer works on a principle of setting analogue voltages assigned to the four output channels, and then selecting which one is used depending on the TTL input. Additionally control boards developed in the Durham University Department of Physics Electronics Workshop are used to control the driving frequency and RF power applied to the AOMs. Through TTL input from the control board or analogue input from the multiplexer it is possible to adequately time the switching of all frequencies.

Chapter 4

Bose-Einstein condensation of ^{87}Rb in an optical dipole trap

The following chapter discusses modelling of the experimental potentials encountered in this work and characterisation of the dipole trapping beam. The criteria that were required to be met by the final design of the experiments are discussed in detail, and this final design is presented in section 4.3.2. Finally data on loading the trap is reported in section 4.4 and data on improved evaporation within the trap is presented in section 4.5. This culminates in the the production of large ^{87}Rb BECs, which can be thought of as the ultimate test of evaporation within the system.

4.1 Modelling the optical trap

To model the experimental potentials it is possible to calculate the different contributions to the overall potential and superpose each one. In this section a model of the optical trap is developed sequentially by adding the individual building blocks in turn.

Species	$\alpha\,(a_0^3)$
Rb	(424.7 ± 0.7)
Cs	(572.2 ± 1.2)

Table 4.1: Polarisability of Rb and Cs at a wavelength of 1550 nm, in atomic units of a_0^3 [175].

4.1.1 The optical potential

The optical potential is calculated using the values in table 4.1 and

$$U_{\mathrm{dip}} = -\frac{\Re\left(\alpha\right) I}{2\epsilon_0 c}, \tag{4.1}$$

where I is the intensity of the light and α is the complex polarisability. For a crossed optical dipole trap consisting of two identical beams we sum the contribution from each beam. Given the linear relationship between intensity and beam power, and thus dipole potential and beam power, the trap depth of the lone optical potential trivially increases linearly with beam power (see figure 4.2(b)). The other parameter affecting the trap depth and frequencies is the beam waist, this dependence is displayed in figure 4.1. The trap frequencies in each direction are calculated by fitting a quadratic function to a slice through the potential, and approximating this potential with a harmonic oscillator potential, for example

$$U_z = \frac{1}{2} m \omega_z^2 z^2. \tag{4.2}$$

4.1.2 The gravitational potential

The gravitational potential is simply given by

$$U_{\mathrm{g}} = mgz \tag{4.3}$$

where m is the mass of the atom.

The gravitational potential effectively tilts the total potential, reducing the height of the potential barrier on one side of the trap, hence reducing the trap

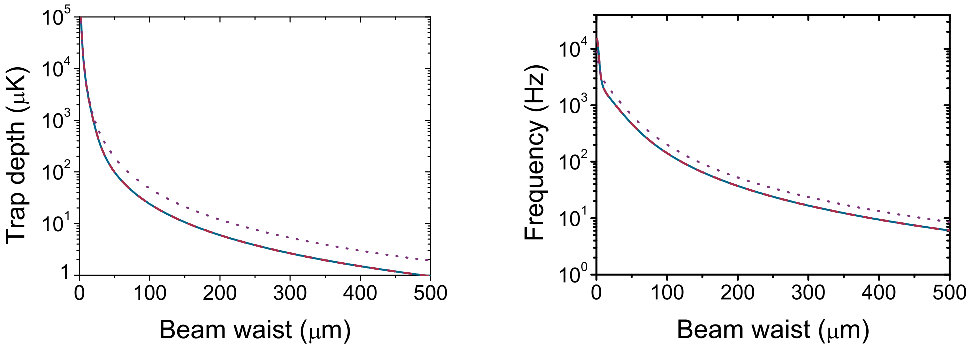

(a)

(b)

Figure 4.1: Trap depth (a) and frequencies (b) in the $x-$ (blue solid), $y-$ (red dashed) and $z-$ (purple dotted) directions, as functions of the beam waist for ^{87}Rb atoms in the $|1,-1\rangle$ state. These values are calculated for a purely optical potential created by two beams of power 4.05 W and wavelength 1550 nm, crossing at right angles to each other.

depth. This effect can be seen in figure 4.2(a). For a crossed optical dipole trap at high beam powers the evaporation surface is initially along the beams as the trap depth along the beams is approximately half that in the vertical direction, however as beam power is reduced the gravitational tilting of the trap becomes more pronounced until the trap depth in the vertical direction becomes smaller than in the horizontal direction. When this happens the evaporation surface changes which can be seen in figure 4.2(b).

4.1.3 The magnetic potential

As discussed in chapter 2 the Biot-Savart law can be used to calculate the magnetic field due to a pair of coils at a particular point in space. However the analytic equations 2.57 and 2.59 are only valid for a point on the axes of the coils. To perform the integral over many points in space is computationally slow, however a different method exists [197]. The field produced by a pair of coils can be expressed in terms of elliptic integrals, functions which are in-built into many computational programs. Our simulation of the magnetic field thus calculates the field at a particular point using these functions and knowledge of the coil pair's radius and separation.

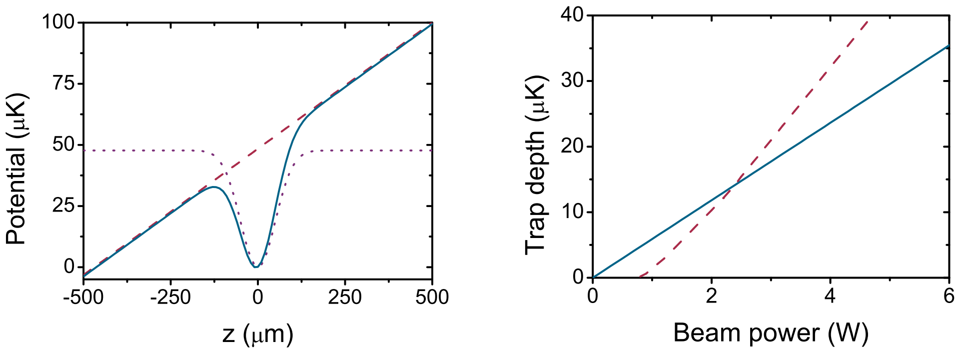

(a) (b)

Figure 4.2: Potentials as functions of vertical position (a) and trap depth as a function of beam power (b), when considering ^{87}Rb atoms in the $|1, -1\rangle$ state in a combined opto-gravitational potential. In (a) the three potentials displayed are the combined (blue solid), the gravitational (red dashed) and the optical (purple dotted), for two beams of 4.05 W optical power and 100 μm waist crossed at right-angles. In (b) the trap depth along the beams (blue solid) and in the $z-$direction (red dashed) are displayed as functions of beam power. For the combined potential the dimension in which the trap depth is smallest switches from the horizontal direction to the vertical at smaller beam powers. The optical trapping beams in (b) are crossed at right angles to each other and have a waist of 100 μm.

The magnetic field gradient created by the anti-Helmholtz coil can be utilised to cancel the effects of gravity on one side of the magnetic trap. This is the case if the current driven through the coil is stabilised to a value such that the field gradient is that which levitates against gravity (see table 2.2). The levitation gradient is dependent on the magnetic bias field however due to the $\mu\left(B\right)$ term in equation 2.55. The effect that this has on the trap depth must be taken into account at high bias fields. The magnetic field dependence of the magnetic moment and the magnetic field gradients required to levitate ^{87}Rb and ^{133}Cs atoms are displayed in figure 4.3.

4.1.4 The combined potential

The total potential that an atom experiences at a particular point in space is the summation of the optical, magnetic and gravitational potentials. For a hybrid trap where a single dipole trapping beam's waist is displaced a

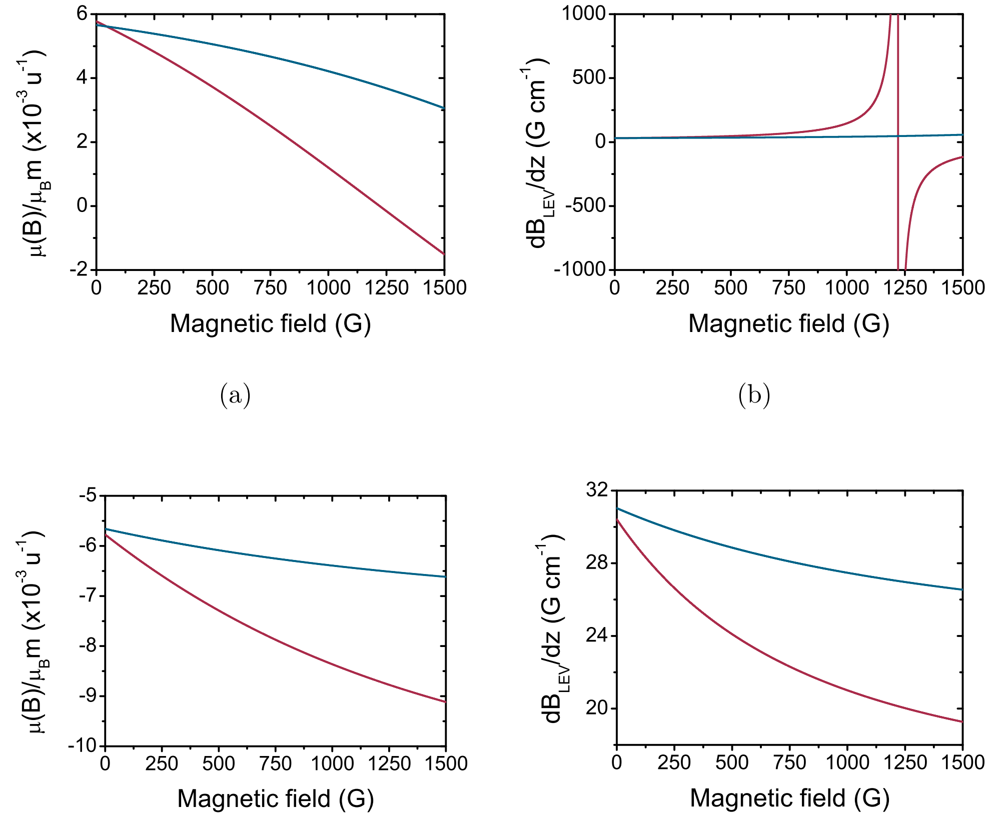

(a) (b)

(c) (d)

Figure 4.3: Magnetic moment to mass ratio (a,c) and levitation gradients (b,d) for ^{87}Rb atoms (red) and ^{133}Cs atoms (blue) as functions of bias field. Data for both stretched weak-field seeking (a, b) and high-field seeking (c, d) states in the lower hyperfine levels are shown.

distance z_0 from the magnetic field zero (at $x = y = z = 0$), and the beam propagates in the $x-$direction, the potential is given by [165]

$$\begin{aligned} U_{\text{Tot}}\left(\vec{r}\right) =& \mu\left(B\right)\frac{dB}{dz}\sqrt{\left(\frac{x^2}{4}+\frac{y^2}{4}+z^2\right)}- \\ & U_0 \exp\left(-2\left(y^2+\left(z-z_0\right)^2\right)/w_0^2\right)+mgz+E_0. \end{aligned} \tag{4.4}$$

Here U_0 is the trap depth of the optical potential and E_0 is the calculated energy difference between the total potential trap minimum, and the potential

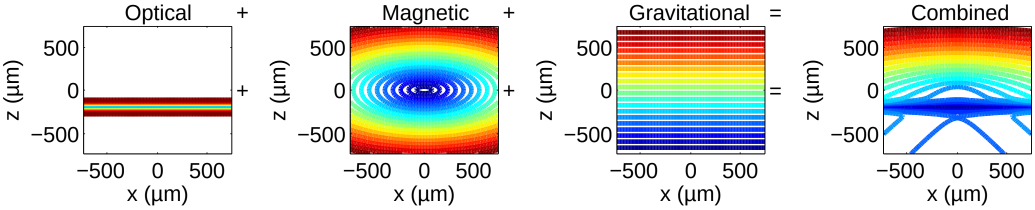

Figure 4.4: Contour plots of the optical, magnetic, gravitational and combined potentials experienced by ^{87}Rb in the $|1,-1\rangle$ state. The graphs indicate the potential experienced as a function of position. The combined potential is a linear sum of the three constituent potentials. The optical potential is generated by 4.05 W of 1550 nm light, focussed to a waist of 68 μm, 200 μm below the magnetic field zero. The magnetic potential is produced by a field gradient of 28 G cm^{-1}.

at this point without the dipole potential present

$$E_0 = U_0 \exp\left(-2z_0^2/w_0^2\right). \tag{4.5}$$

The inclusion of E_0 in equation 4.4 sets the total potential at the trap minimum to zero.

Consider one experimental situation that this work is concerned with (see section 4.3). The $|1,-1\rangle$ state in ^{87}Rb in an optical potential generated by a single 4.05 W beam of light of wavelength 1550 nm and a waist of 68 μm, focussed 200 μm below the magnetic field zero, and a magnetic potential produced by a field gradient of 28 G cm^{-1} experiences the total potential (in the x-$z-$plane) presented in figure 4.4.

In previous work [12, 127, 162, 167] the dipole trapping beam was located approximately one beam waist below the magnetic trap centre. This was to take advantage of the increased trap depth here (see figure 4.5(a)) resulting in a larger load into the trap, as well as the increase in trap frequency at this location for a single beam trap, as displayed in figure 4.5(b). Condensates of up to 2×10^5 atoms were produced in this potential, and an investigation of evaporation efficiency at different beam positions revealed that positioning the beam (of 60 μm 1/e^2 radius) 80 μm below the magnetic trap centre was optimum. However, figure 4.21 indicates that in the crossed-beam trap the optimum loading position is approximately three beam waists below the magnetic trap centre. Therefore the crossed beam trap was located there. The trap depth and frequencies for the crossed beam trap are independent of beam location at high beam powers as axial confinement is provided by the optical potential and the magnetic field gradient only increases the confinement slightly.

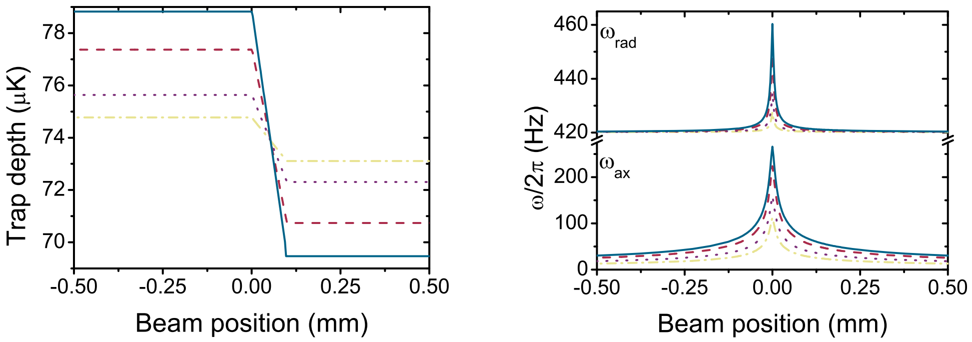

(a) (b)

Figure 4.5: Trap depth (a) and frequencies (b) for the single beam dipole trap versus beam position calculated for different magnetic field gradients for ^{87}Rb in the $|1,-1\rangle$ state. In (a) the trap depth is increased below the magnetic trap centre hence larger dipole trap loads can be expected here. In (b) the data above the break represents radial frequencies and the data below the break represents axial frequencies. It can be seen that the radial frequency is nearly independent of beam position, however as the axial confinement is provided by the magnetic field gradient, the axial frequency shows strong dependence on position. The different magnetic field gradients used are 28 G cm^{-1} (blue solid), 20 G cm^{-1} (red dashed), 10 G cm^{-1}(purple dotted) and 5 G cm^{-1} (yellow dash-dotted). Parameters used are $P = 6.70$ W, $w_0 = 68$ μm, $\lambda =$ 1550 nm.

4.1.5 The loading trap

Atoms in the weak-field seeking $|1,-1\rangle$ state are loaded into the hybrid loading trap from the magnetic trap after pre-cooling using forced RF evaporation (see section 3.7 for more details). Initial loading is performed at a power of 4.05 W in each beam with a gradient of 28.2 G cm^{-1} and zero bias field. The magnetic field gradient is set slightly below the value which cancels gravity for the $|1,-1\rangle$ state (i.e. levitates it) and provides an attractive confining potential that adds to the existing optical confinement along the beam. The essential features of the trapping potential are presented in figure 4.6. Along the beam the trap potential is the sum of the harmonic trap obtained from a quadrupole trap offset by a bias field (due to the beam being positioned below the magnetic trap centre) and the dimple optical potential superimposed in the centre. In the horizontal plane, outside the dimple region, the trap potential increases linearly in all directions to values $> 1000\ \mu$K. The trap depth of 101 μK is thus entirely determined by the potential in the $z-$direction, which is nearly constant on the lower side of the trap owing to the near cancellation of gravity. On the upper side of the trap a potential gradient of $\approx 2g$ exists owing to the addition of magnetic and gravitational potentials. Hotter atoms are lost vertically downwards in the direction with the lowest trap depth. The frequencies of the loading trap for ^{87}Rb atoms in the $|1,-1\rangle$ state are $\omega_{\mathrm{rad}} = 2\pi \times 448.3$ Hz and $\omega_{\mathrm{ax}} = 2\pi \times 90.4$ Hz.

4.1.6 Trap tilting

The trapping potential can be tilted by varying the magnetic field gradient. By applying the field gradient required to levitate the weak-field atoms, gravity is cancelled on one side of the trap and effectively doubled on the other side. If we apply a magnetic bias field such that the high-field seeking states are levitated it is then possible to increase $\partial B/\partial z$ such that we 'overcompensate' for gravity, and the potential is reduced on one side of the trap. This gravito-magnetic trap tilting has been utilised in order to bring ^{133}Cs to degeneracy [11]. The evaporation surface depends on the quadrupole tilt applied, as the lowest trap depth is generally in the direction along the beams, unless beam powers are low or the amount of tilting is large. This is displayed in figure 4.7

It can be seen in figure 4.7 that the trap depth along the beam (which is the shallowest part of the trap potential in the horizontal plane) is almost constant, whereas the vertical trap depth may be either greater or less than the horizontal depth. Thus the figure divides into two regions, with an approximate crossover gradient for this example of 37 G cm^{-1}. The usefulness of this levitated trap stems from the existence of both regions. For gradients less

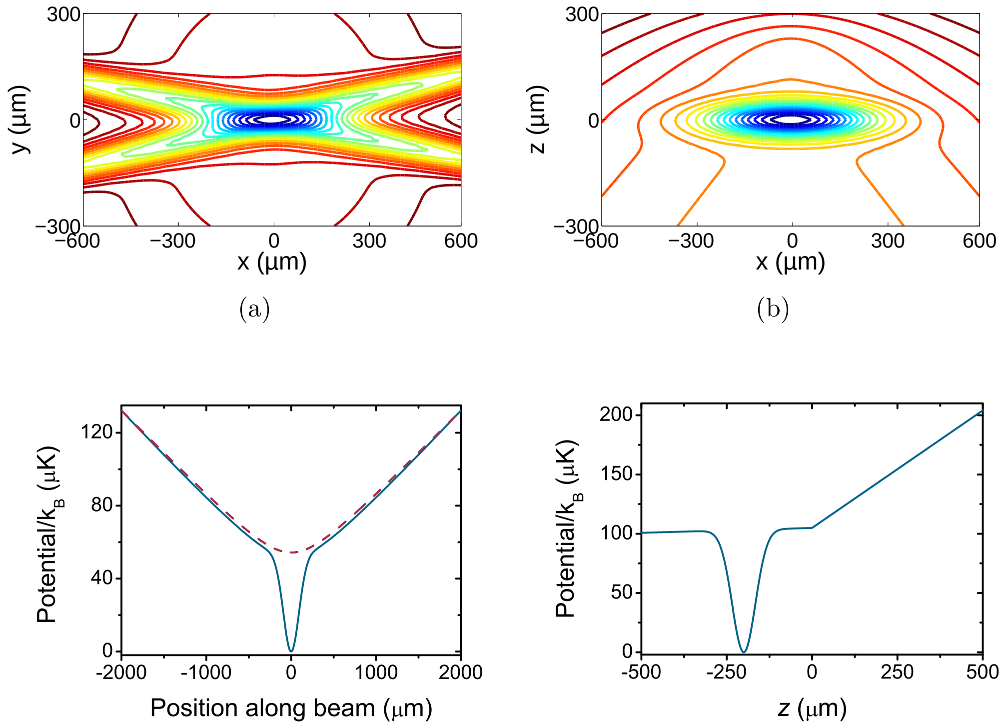

(a) (b)

(c) (d)

Figure 4.6: The loading trap potential for ^{87}Rb atoms in the $|1, -1\rangle$ state created with 4.05 W in each 68 μm dipole beam and a magnetic field gradient of 28.2 G cm^{-1}. Contour plots of the trap potential in the x-y−plane (a) intersecting the potential minimum and the x-z−plane (b). Cross-sections through the potential minimum along one of the beams (c) and vertically (d). The crossed dipole trap is positioned 200 μm below the field zero of the quadrupole potential resulting in additional magnetic harmonic confinement along the beams. The purely magnetic contribution is shown as the dashed line in (c).

than the crossover gradient evaporation occurs horizontally along the beams and can be achieved by decreasing the beam powers. This method also causes a consequent decrease in trap frequencies and hence the collision rate, which is generally detrimental to evaporative cooling, although we note that it may be useful in some circumstances where three-body loss rates are high. For gradients greater than the crossover gradient evaporation occurs in the vertical direction owing to the lower trap depth (see figure 4.7(c)). Physically this occurs because, as the gradient is increased, gravity is overcompensated and the residual upwards force (magnetic minus gravity) eventually overcomes the downwards confinement of the optical potential. The atoms escape up-

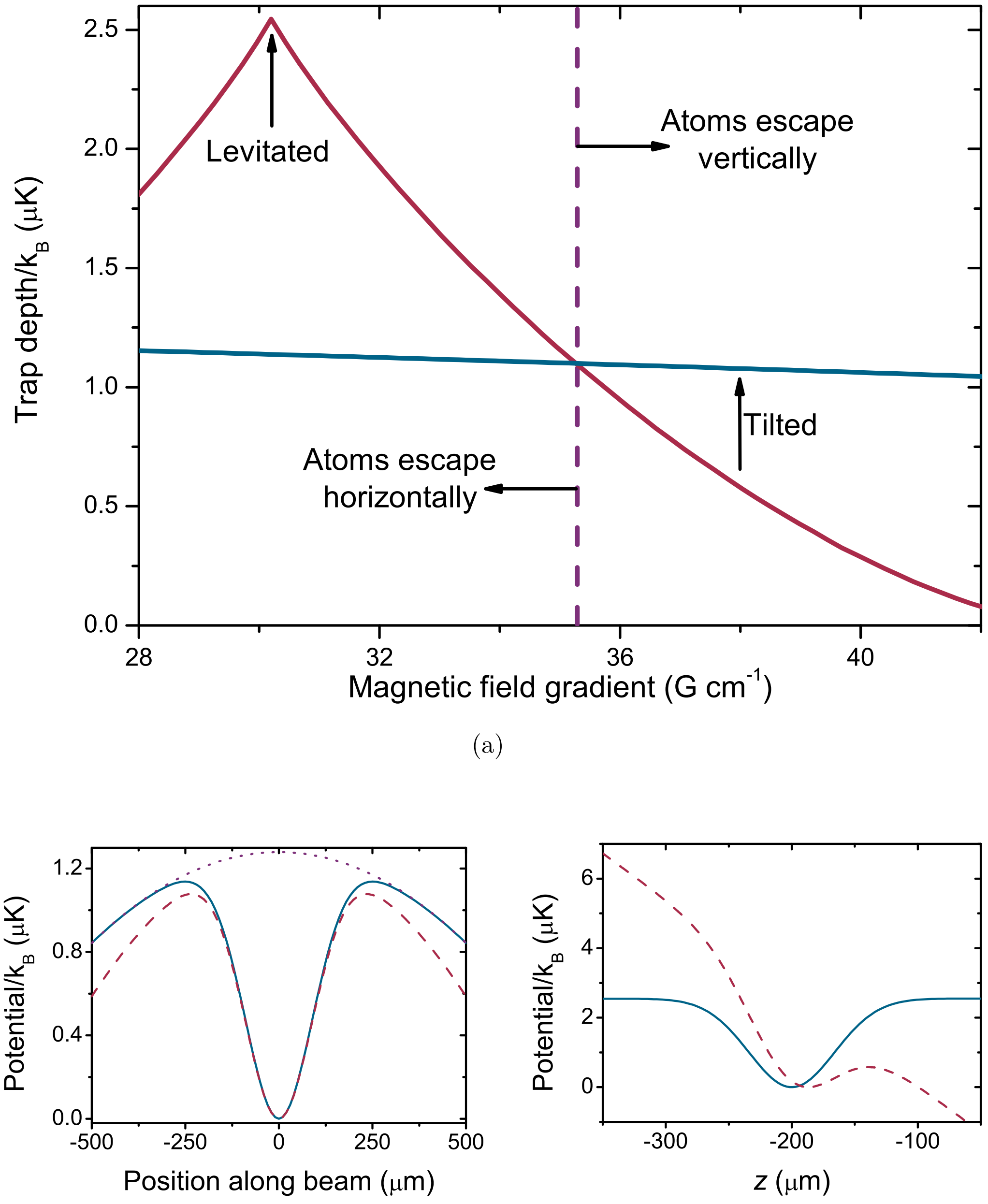

(a)

(b)

(c)

Figure 4.7: Trap depth of the levitated trap as a function of magnetic field gradient (a), a cross-section through the potential along one of the beams (b) and vertically (c). The trap depth is calculated for ^{87}Rb atoms in the $|1, +1\rangle$ state in the $z-$direction (red) and along the beams (blue). Cross-sections through the potential are shown for the levitated (blue solid) and the tilted (red dashed) potentials indicated by the arrows in (a). The purple dotted line in (b) indicates the magnetic potential due to a gradient of 30.2 G cm^{-1} with no optical potential present. The beam powers are both 100 mW, the beam waist is 68 μm and the bias field is 22.4 G.

wards; an effect referred to as 'tilting' the trap as it is analagous to tilting a cup full of water. For gradients greater than the crossover gradient evaporation may be implemented by either reducing the beam power or by simply increasing the magnetic field gradient. In the latter case the trap frequencies do not change appreciably as the evaporation proceeds.

4.2 Development of the optical trap

4.2.1 Characterisation of the dipole trapping beam

The location of the beam's waist can be determined by measuring the radius of the beam as a function of position along its path, and using equation 2.74.

The location of the beam's waist in terms of distance from the fibre laser's output was inferred from figure 4.8 by a fit to equation 2.74. The location of the waist in the horizontal direction was found to be (0.20 ± 0.07) m and in the vertical direction it was found to be (0.13 ± 0.05) m from the fibre laser's output. As the Rayleigh range of the beam is also explicit in equation 2.74 the data returns values for Z_{R} of (0.69 ± 0.07) m and (0.61 ± 0.04) m in the horizontal and vertical directions respectively. Hence in the horizontal direction we have a q of -200 mm $+$ i690 mm and -130 mm $+$ i610 mm in the vertical direction.

Considering equation 2.77 and the data in figure 4.8 values of $M^2 = (1.1 \pm 0.1)$ and $M^2 = (1.08 \pm 0.08)$ are obtained for the horizontal and vertical directions respectively. Both values are in excellent agreement with each other. The close proximity of these values to 1 indicated that the output of the laser is close to an ideal Gaussian.

4.2.2 Sources of heating in the optical trap

Heating of the atoms due to effects of the dipole trapping beam will be considered in this section. Note that other sources of heating such as Majorana spin flips [163, 198, 199] and the spontaneous scattering of trap photons are also present [174].

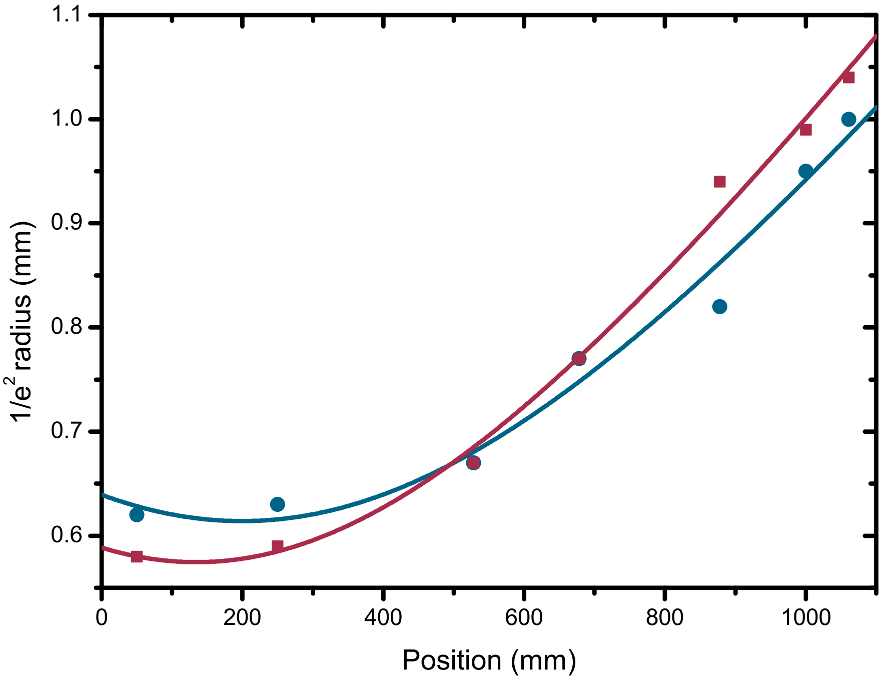

Figure 4.8: $1/e^2$ radius of the dipole trapping beam as a function of displacement from the laser's output, in the horizontal (blue circles) and vertical (red squares) directions. The lines are fits to the data using equation 2.74.

Relative intensity noise

Relative intensity noise (RIN) is defined as the relative change in the intensity of a laser beam compared to the average power of the beam. Heating due to RIN can be quantified using a harmonic oscillator model [200] where the spring constant k is dependent on the laser intensity, hence k varies with time. Exponential heating occurs as a result of this fluctuation [200, 201]. Transition rates between the available states can be calculated using time-dependent perturbation theory, revealing that the average energy increases exponentially

$$\left\langle \dot{E} \right\rangle = \Gamma_\epsilon \left\langle E \right\rangle , \tag{4.6}$$

where Γ_ϵ is the time constant of the heating

$$\Gamma_\epsilon = \frac{1}{T_\mathrm{I}} = \pi^2 \nu_\mathrm{tr}^2 S_\epsilon(2\nu_\mathrm{tr}) \tag{4.7}$$

where T_{I} is the time taken for $\langle E\rangle$ to increase by a factor e, ν_{tr} is the frequency of the trap, $\epsilon = (I(t) - I_0)/I_0$ is the laser intensity's fractional fluctuation and S_ϵ is the power spectrum of the RIN

$$S_\epsilon(\nu_{\mathrm{tr}}) = \frac{2}{\pi}\int_0^\infty \cos(\nu_{\mathrm{tr}}\tau)\,\langle\epsilon(t)\epsilon(t+\tau)\rangle\,d\tau. \tag{4.8}$$

Due to the trap's oscillation frequency the heating rate is dependent on the laser intensity, and when $E \approx V$ the atoms will be lost from the trap. The dependence on the trap frequency's second harmonic indicates that the heating is parametric.

Although measurement of the RIN on a laser is a reasonably involved measurement to undertake [202] it is possible to predict the level of RIN using simple techniques. By focussing the light directly from a laser beam onto a photodiode and measuring the AC component of the photodiode output the frequency spectrum of the noise can be observed if a Fourier transform of the signal is taken. It is worth noting that there is noise present on the photodiode circuit when no light is present on the diode. The noise due to the circuit is generally of a higher frequency than the noise due to the laser hence it can be removed with a low pass filter. Of the remaining noise, comparing the Fourier transform of the photodiode signal with and without laser light present the frequency components that laser noise is responsible for can be determined. Figure 4.9 displays the output of the photodiode in the two cases.

Considering figures 4.9(b) and 4.9(d) it is possible to see that noise is present on the circuit at frequencies of 0.92 kHz, 1.95 kHz, 2.18 kHz, 2.27 kHz, 2.47 kHz. Hence in figure 4.9(a) peaks at these frequencies can be discarded and the remaining peaks relate to the noise from the laser. Much of the remaining noise is at a frequency of 50 Hz and this frequency's harmonics. These frequencies are present on the photodiode when no light is present, but it is possible to see that the depth of the noise is increased when the light is present. The source of this noise has been attributed to the 50 Hz frequency of the mains voltage. There are also noise peaks at 2 Hz and three peaks at approximately 1.75 kHz. Since the frequencies of the dipole trap are in the $20 - 500$ Hz range we are not concerned with these noise peaks

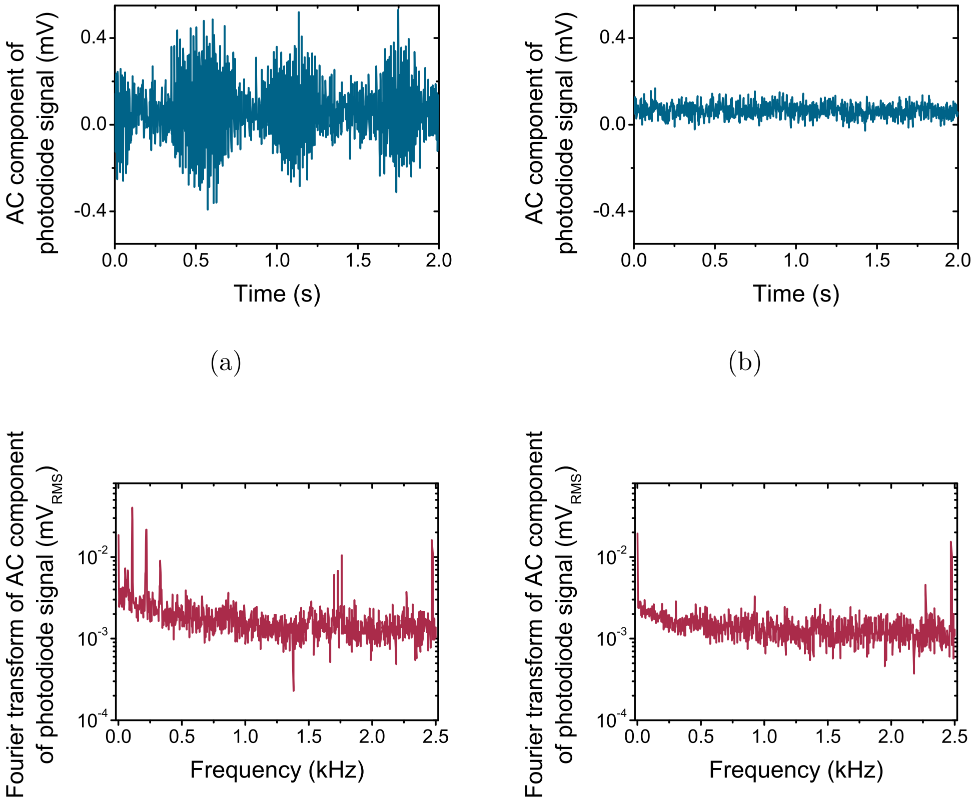

(a)

(b)

(c)

(d)

Figure 4.9: AC component of photodiode signal versus time (a,b) and its Fourier transform (c,d) with light present (a,c), and just for the bare photodiode (b,d). Electronic noise on the photodiode accounts for peaks at 0.92 kHz, 1.95 kHz, 2.18 kHz, 2.27 kHz, 2.47 kHz and values which are multiples of 50 Hz are attributed to the frequency of the mains supply. For this data $\epsilon = 0.12$ %.

as they are not close to the trapping frequencies, where parametric heating would be a large problem. Additionally, as will be described in the following section, the relative intensity noise can be removed via the use of feedback to a servo-mechanical circuit.

Reduction of relative intensity noise

Equation 4.6 indicates that intensity noise on the laser induces heating of atoms. To reduce this heating the intensity of the laser beam can be servo-mechanically controlled using feedback about the intensity from a photodiode and an AOM to control the intensity. In this experiment the two beams are monitored separately as discussed in section 4.3. The photodiode signals are then separately stabilised via feedback to the AOMs provided by a servo-mechanical circuit which is documented elsewhere [127].

Figure 4.10 presents the removal of intensity noise on the fibre laser beam. The output signal of the servo circuit is presented, as are the incident powers on two different photodiodes. The two photodiodes measure the beam intensity before and after stabilisation via an AOM. The signals shown are the AC components to highlight the noise, and have been displaced for clarity. The servo circuit's output signal is displayed to indicate the varying RF power applied to the AOM required to remove the intensity noise. It can be seen that the noise on the photodiode signal measuring the stabilised beam is approximately 4 times lower than that on the photodiode measuring the unstabilised beam, indicating the gain in beam power stability that can be achieved by intensity stabilising the dipole trapping beams. The servo circuit has been set to stabilise the beam power at the trap to be $\sim 100\ \mu$W.

Beam pointing stability

We have seen previously that the use of an AOM is imperative in producing a beam of stable intensity as well as achieving modulation of that intensity such that the desired evaporation routine can be performed. The drawback to using this method is that to reduce the beam intensity the RF power to the AOM must be reduced. Due to thermal effects when the RF power is varied the diffracted beam is displaced. This displacement is known to cause heating of the atoms [200–202] in addition to the changes in trap depth and frequency that result from a displacement of the trap centre (see section 4.1). The AOM used in this work is driven by an external AOM driver, which is controlled via a control voltage input, between 0 and 1 V. The larger this input, the more RF power is applied to the AOM. More detail about the AOM is given in section 4.3.2.

In contrast to heating due to RIN (equation 4.6), for fluctuations of trap

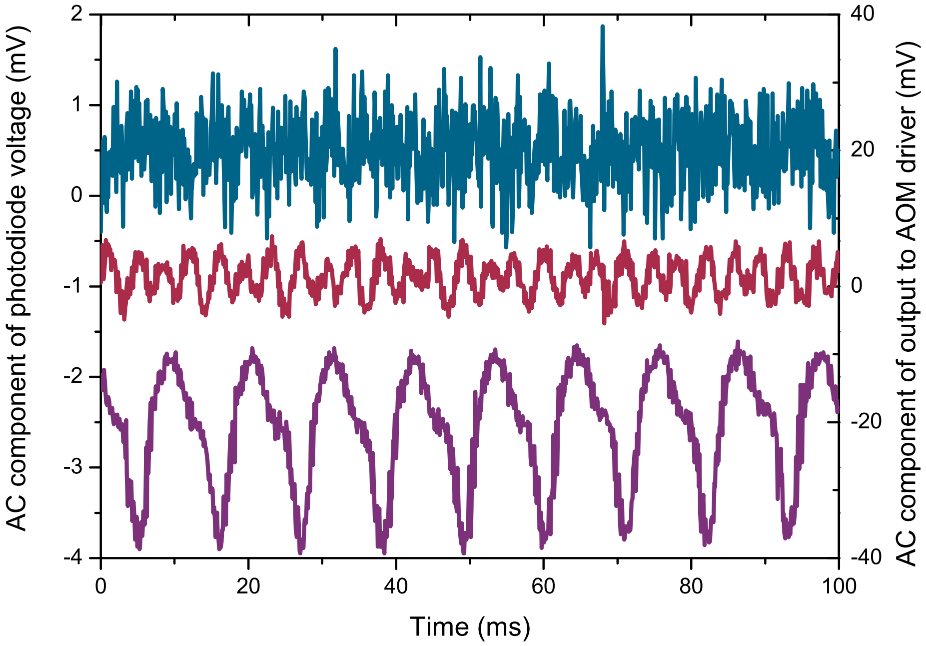

Figure 4.10: AC components of the signal of a photodiode measuring the beam prior to stabilisation (blue), the signal of a photodiode measuring the stabilised beam (red) and the output signal from the servo circuit (purple) over 100 ms. Note the reduction in noise that is evident when removing the noise via the servo circuit. A ten point average has been applied and the output signals have been displaced for clarity.

position the resultant heating is independent of the trap energy [201]

$$\left\langle \dot{E} \right\rangle = 4\pi^4 \nu_{\mathrm{tr}}^4 m S_{\epsilon_x}(\nu_{\mathrm{tr}}) \tag{4.9}$$

where $S_{\epsilon_x}(\omega)$ is the power spectrum of the position fluctuations, ϵ_x. At first inspection equation 4.9 suggests that as the beam powers are reduced, which would reduce the trap frequencies, the rate of heating would also reduce. However it is likely that for lower beam powers the position fluctuations would increase as this involves a larger change in RF power applied to the AOM.

Techniques exist to reduce the level of beam pointing fluctuations in an experiment. Simply water cooling the AOM will reduce the thermal effect of changing the RF power applied to the AOM, however this solution does not remove pointing instability to a sufficient degree, and is already in place in many AOMs that deliver large RF powers. A method already employed in this work in the optical setup of the cooling and repumping lasers is to pass the beam through the AOM twice. On the second pass through the AOM the deviation caused by thermal effects is reversed, thus the beam travels along its original path, in the opposite direction. In the case of an optical dipole trap this technique has been utilised previously [203] resulting in a 92% reduction of pointing instability. The disadvantage of this technique is that passing a beam through an AOM twice results in a reduction of available beam power. Another technique involves driving the AOM with a second frequency and varying the power of this frequency as the main frequency's power is changed such that the total power transmitted to the AOM remains constant [204]. For constant RF power the thermal effects and hence beam pointing changes are removed. This technique has reportedly reduced the angular deviation of an AOM to a maximum of 0.03 mrad, a 95% reduction in pointing instability. One final technique that removes the pointing issue completely is to fibre couple the dipole trapping beams into the experiment. Any pointing instability is then only detectable by a reduction in efficiency of coupling to the fibre. It would then be possible to reduce the intensity noise with feedback to the AOM. The drawback to this technique is that the total available power is reduced due to imperfect coupling into the fibre, and production of optical fibres that will adequately transmit the magnitude of optical power required for this work is non-trivial.

The beam pointing stability of the apparatus used in this experiment was measured using three techniques, which are discussed later. Figure 4.11 displays the deflection angle out of the AOM measured after the RF power to the AOM is varied. The maximum deflection measured was (0.2 ± 0.1) mrad. This value was obtained using the first method. The direct measurement via the razor blade position (the third method) is the most accurate, hence we believe the maximum deflection angle to actually be (94 ± 3) μrad. Since the values returned using the first and second method are consistently larger than the direct measurement it appears there is a systematic error in converting the difference in the photodiode signals into a beam displacement.

Realistically the maximum change in the control voltage applied to the AOM during an experimental sequence would be $\sim$ 0.5 V. Figure 4.11 indicates that the deflection angle expected for this change in control voltage would be $\sim$ 60 μrad. This is likely to be satisfactory as previous work reports a deflection angle of 2 mrad to be sufficient for all-optical production of a BEC [203], hence other removal techniques are not deemed to be necessary.

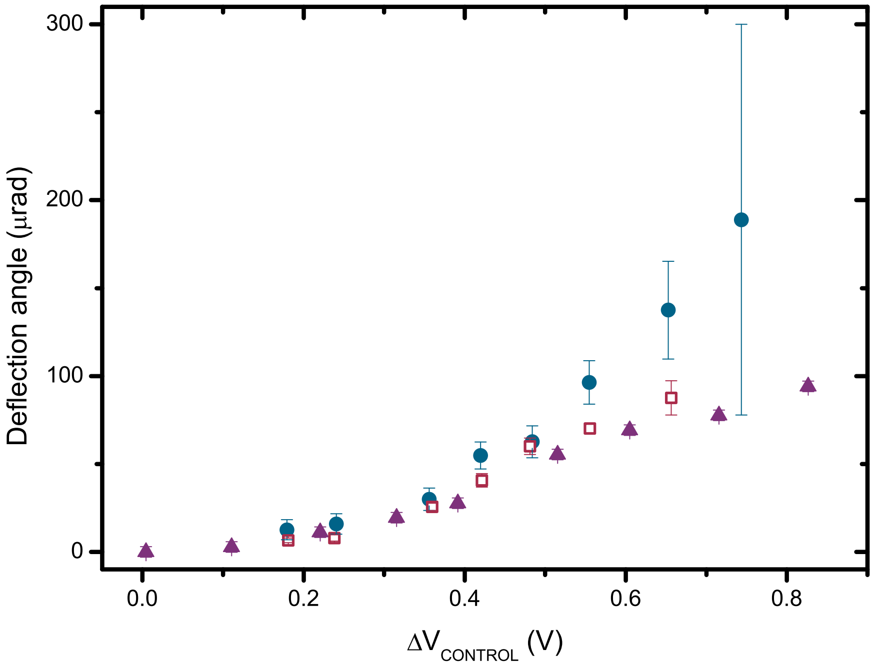

Figure 4.11: Angular deviation of the dipole trapping beam from the AOM as a function of the change in control voltage applied to the AOM, measured using the two photodiode technique and a razor blade at the focus of a beam (solid blue circles), the two photodiode technique without focussing the beam (hollow red squares) and a direct measurement with a razor blade and translation stage (solid purple triangles). There is a clear systematic error in converting the difference in photodiode signals into a displacement, potentially due to a non-linear relation between displacement and difference in signal.

Various tests have been devised in order to determine the amount of deflection experienced by the beam in this work [201, 202]. In this work the first order diffracted beam was split using a PBS cube as in figure 4.12. Both

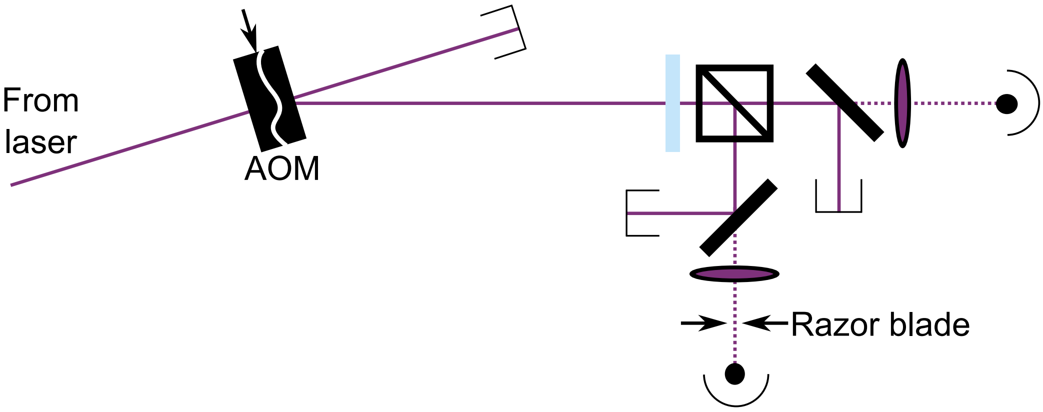

Figure 4.12: The experimental setup designed to calculate the beam pointing stability of the AOM. See appendix B for a key to the different components.

transmitted and reflected beams were focussed onto photodiodes (after the beam power was attenuated to reduce it to a suitable value). A razor blade was used to block half of the reflected beam, and finally the half-wave plate was used to equalise the signal on each photodiode. The beam transmitted through the PBS allows any changes in laser intensity to be discriminated. Any deviation in the beam pointing results in a change in the signal detected by the beam with the razor blade cutting it, however the other beam would remain unchanged. The difference in the two signals can then be converted into a beam deflection. The angular deviation of the beam is then calculated given the distance of the knife edge from the AOM (3.6 m) and using ABCD matrices as described in section 2.5.1 to account for the refraction at the lens.

Three similar methods were employed to determine the beam pointing stability. The exact method explained above was utilised, a slight variation on this technique was also used, however the beam was focussed after the razor blade so a direct deflection of the beam was determined without need to remove the effect of the lens. Finally the deflection was directly measured using the razor blade on a translation stage to measure the difference in position of the beam's centre.

Prior to each measurement the AOM was stabilised by applying a control voltage to the AOM driver such that the diffraction efficiency was maximised, which is representive of how the AOM would be powered during loading of the dipole trap. The control voltage was then changed to one that would result in a lower RF power being applied to the AOM. The magnitude of the largest difference between the two photodiode signals was then recorded, or in the case of the direct measurement with the translation stage the blade was positioned at the new beam centre and the displacement noted. For the technique utilising the difference between the two photodiode signals the magnitude of the signal on the photodiode measuring the unblocked beam was also recorded as this would be reduced for lower RF powers, hence was required in calibrating the beam displacement. Results are displayed in figure 4.11. There is a systematic error involved in converting the difference in the photodiode signal into a deflection angle and the errors propagate accordingly resulting in the large error bars observed, however this is not an issue with the direct measurement. Likewise due to the small signal when the control voltage is low, relative errors in the measurement are large. Another source of error is potentially a deviation from a linear relationship between the distance the beam moves and the difference in the photodiode signals.

The conclusion drawn from this test is that the maximum realistic deflection of the beam is likely to be $\sim 60\ \mu$rad. In section 4.3.2 we will discuss the corresponding deviation at the trap centre. Without utilising any special techniques to reduce beam pointing instability such as the two RF technique or double passing the AOM the deflection angle observed is favourable compared to values reported in previous work [203, 204]. If these techniques were implemented the gain to be expected may not be necessary as a stability of approximately 2 mrad was reported to be sufficient for all-optical production of a BEC [203]. We therefore determine that no corrective techniques are required and in the following a solution to reducing the beam pointing instability will be discussed in the context of this work.

Consider the situation in figure 4.13. A beam originating from position z_1 which in the current context would be at the AOM, is translated to position z_2, at the surface of a lens. The angle the beam makes with the origin is θ_1. The beam is refracted at the lens, hence the propagation angle changes to θ_3. Consider the location of the beam to now be (z_3, y_3). The beam then undergoes a final translation to z_4. The displacement between y_3 and the beam's new $y-$position is defined as y_4. When the RF power applied to the AOM is changed angle θ_1 and hence θ_3 and y_4 are changed (thus the change in y_4 is what is measured in figure 4.11). This situation resembles the setup

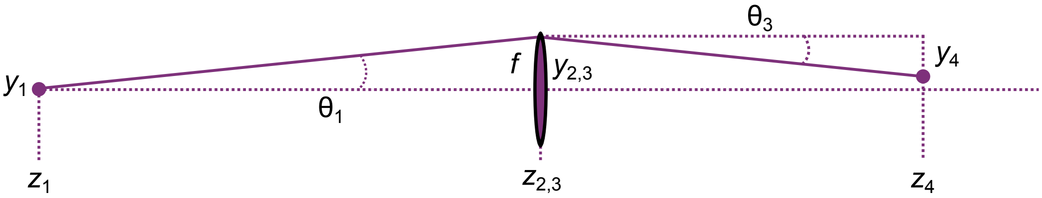

Figure 4.13: Diagram defining positions, displacements and angles required in the discussion of beam pointing instability minimisation. The solid purple line is the actual beam path, dashed lines indicate lines used for construction purposes only.

of the experiment in this work (see figure 4.16).

Using the method of ray transfer, we can see the situation is described by

$$\begin{pmatrix} y_4 \\ n_4\theta_4 \end{pmatrix}_{z=Z_4} = \begin{pmatrix} 1 & (z_4 - z_3) \\ 0 & 1 \end{pmatrix} \begin{pmatrix} 1 & 0 \\ -1/f & 1 \end{pmatrix} \times \begin{pmatrix} 1 & (z_2 - z_1) \\ 0 & 1 \end{pmatrix} \begin{pmatrix} y_1 \\ n_1\theta_1 \end{pmatrix}_{z=Z_1} . \tag{4.10}$$

For simplicity we may assume that $n_{1,2,3,4} = 1$. Expanding out the matrices we find

$$y_4 = (1 - (z_4 - z_3)/f)\, y_1 + \theta_1 \left((z_2 - z_1)(1 - (z_4 - z_3)/f) + z_4 - z_3\right) \tag{4.11}$$

If we set $y_1 = 0$ and given that $z_4 - z_3 + z_2 - z_1 = z_4 - z_1$

$$y_4 = \theta_1 \left((z_4 - z_1) - (z_4 - z_3)(z_2 - z_1)/f\right) \tag{4.12}$$

Thus we can minimise any change in y_4 by reducing θ_1 or by ensuring that $(z_4 - z_3)(z_2 - z_1)/f$ is equal to the total path length $z_4 - z_1$. Note that this condition is always satisfied if the waist is located at z_1 and z_4, which can be seen using the lens equation. This means that if the waist is aligned to the atomic cloud, and there is a waist at the AOM, then any beam deviation is purely angular.

4.3 Experimental design

4.3.1 Design criteria

The optical setup of the dipole trap was designed with various criteria imposing restrictions on the beam size and path. Fulfilment of five main criteria was required of the final design:

1. The beam path should be as small as possible such that optics fit within the limited space. A smaller beam path after the AOM will also reduce beam pointing instability.
2. Beam pointing instabilities should be reduced as much as possible (see section 4.2.2).
3. The number of optics used should be minimised to reduce loss of beam power (for example transmission through mirrors), to avoid burning pollutants from the air onto optics and to reduce distortion of the beam at optical surfaces.
4. The $1/e^2$ radius of the beam at the AOM should be favourable to achieve good diffraction efficiency (see figure 4.15).
5. The waist of the trap should be (80 ± 20) μm to produce the trap depths desired (see calculations below).

Other trivial criteria such as avoiding placing optics in the already existing MOT beams were also required of the final design.

The required waist is determined by the desired loading trap depth and the amount of available power. With the available power it is possible to achieve an initial trap depth of 100 μK for ^{87}Rb in the $|1, -1\rangle$ state in a crossed beam trap for beam waists between 60 and 100 μm. For example two beams of waist 60 μm intersecting 200 μm below the magnetic trap centre generate a trap depth of ≈ 97 μK for a beam power of 3 W. Similarly for beam waists of 100 μm a trap depth of 93 μK is achievable with 8 W in each beam. There are advantages in using larger or smaller beams - given a limited laser power the trapping volume requires maximising, whilst matching the trap depth to the temperature after pre-dipole trap loading evaporation. Larger beams have the advantage of a larger capture volume and reduced trap frequencies, which reduce three-body collision rates and hence losses within the atomic mixture, however larger laser powers are required to generate the same trap depth. Conversely beams of a tighter waist suffer from increased three-body losses, and additionally the trapping volume is reduced owing to the smaller size of the beams. The advantage of the smaller beam size is that less laser power is required.

The diffraction efficiency of the AOMs is dependent on beam size. Diffraction efficiency is defined as the beam power in the first-order diffracted beam when the AOM is switched on as a percentage of the beam power that is transmitted through the AOM when it is switched off (P_3/P_2). The total efficiency of the AOM is simply the percentage of the total beam power incident on the AOM available in the first order diffracted beam (P_3/P_1). The definition of each beam is displayed in figure 4.14. To determine the optimum $1/e^2$ radius the diffraction efficiency and total efficiency as functions of beam size were recorded (figure 4.15). The optimum beam size was found to be approximately 1.25 mm hence to satisfy the fourth criteria the beam size at the AOM should be this size. The total efficiency is dependent on the beam size for two reasons. Firstly, the insertion losses decrease for smaller beam sizes, however, the diffraction efficiency increases for larger beam sizes as the volume of the interaction medium is increased. Hence an intermediate beam size is optimum. The active area of the AOMs used for dipole trapping is 3 mm, which gives rise to the optimum beam size measured.

A scheme that satisfied the above criteria was devised utilising the knowledge of the Gaussian nature of the beam. Lenses L_1 and L_2 were chosen to achieve the correct beam size at the AOM and the lenses used to focus the beam at the trap centre. Coupled into this decision was the fact that using a 200 mm focal length lens to focus onto the atoms would create a scenario where the beam pointing stability was reduced. Unnecessary use of optics has been avoided to achieve the third criteria. A waist of $\approx 70\ \mu$m was predicted, which agrees with values measured from parametric heating experiments (figure 4.22).

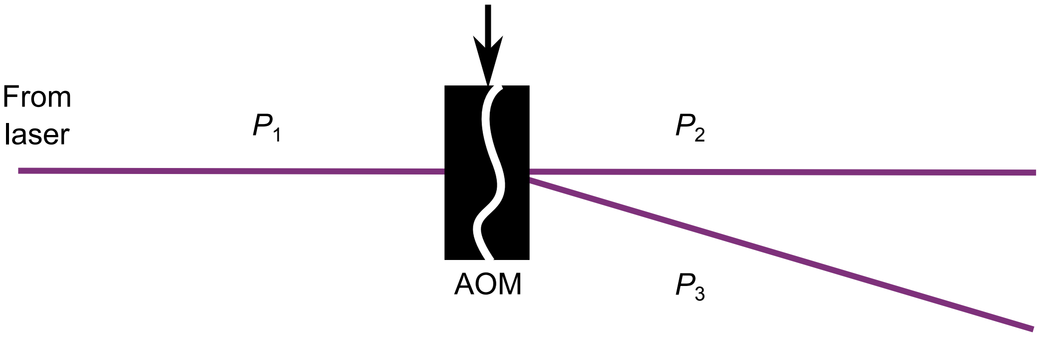

Figure 4.14: Definition of the beam power incident on an AOM (P_1), the beam power transmitted through the AOM (P_2) and the beam power in the first order diffracted beam (P_3). P_2 and P_3 differ when the AOM is switched on or off. In practice higher diffraction orders are present with negligible power in those beams.

4.3.2 The experimental design

In this experiment the light used for optical trapping is derived from an IPG Photonics ELR-30LP-SF fibre laser, which provides a maximum power of 30 W at 1550 nm. The light output is of a single-frequency. A PBS cube is used to ensure only light of a pure polarisation is used in the remainder of the dipole trapping setup. The servo-mechanical circuits (which were discussed in section 4.2.2) are unable to stabilise the beam power effectively without the presence of this cube as the power transmitted and reflected by the second PBS in the optical setup varies too much otherwise. Two lenses, L_1 and L_2 (of focal length -50 mm and 100 mm, respectively) are used in a standard telescope configuration. Their separation is 42.5 mm in order to achieve the required beam widths as discussed in section 4.3.2. PBS_2 splits the beam power approximately in two to derive a crossed-beam dipole trap. The reflected beam's polarisation is vertically polarised, which is required to assure maximum transmission through an acousto-optic modulator (AOM). The beam transmitted through PBS_2 is polarised horizontally, hence a half-wave plate (Thorlabs WPH502) is used to rotate the polarisation to vertical.

The two aforementioned beams impinge on separate AOMs, both of which are water cooled Isomet M1135-T50L-H-1550 anti-reflection coated AOMs. The AOMs are driven by Isomet 531B RF drivers, which provide a signal at a fixed modulation frequency of 50 MHz. Light in the 1st order diffracted

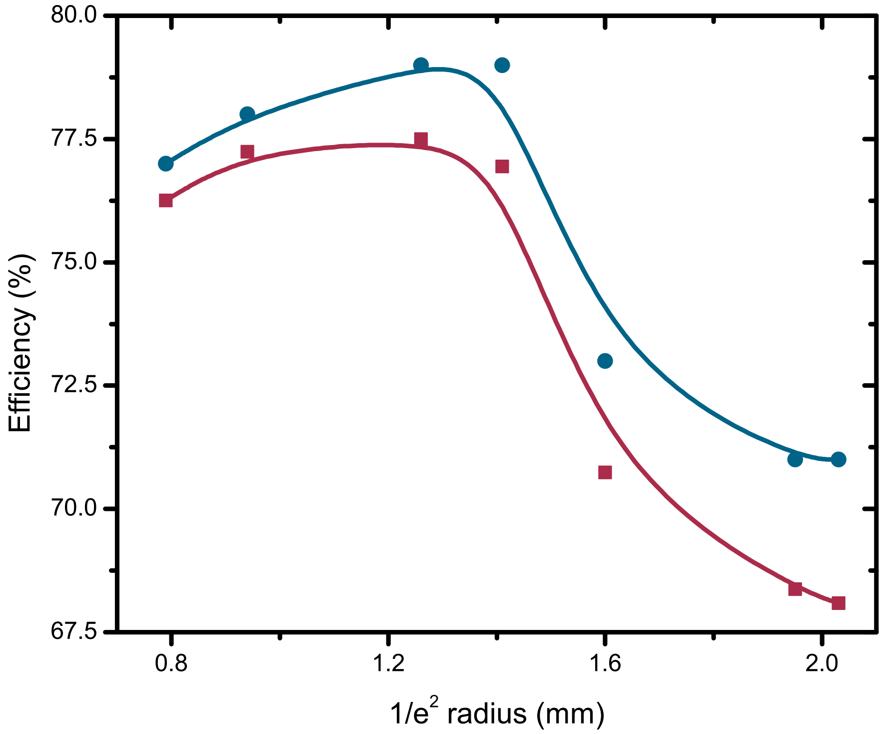

Figure 4.15: Diffraction efficiency (blue circles) and total AOM efficiency (red squares) as defined in the text, as functions of beam size. Maximum efficiency is obtained for a $1/e^2$ radius of ≈ 1.25 mm. Lines are intended solely to guide the eye.

beam is therefore 50 MHz detuned from the light in the 0th order. The beam of increased frequency is used in beam 1 (as denoted in figure 4.16) whereas the light in beam 2 is of a decreased frequency. The reason for this difference is to avoid standing wave effects in the crossed-beam region. A more detailed diagram higlighting the position of the beam and the coils can be observed in figure 4.17. The AOMs allow fast switching of the light as well as servo-mechanical reduction of relative intensity noise (RIN) as discussed in section 4.2.2. During the earlier phases of the experiment, such as MOT loading and magnetic trapping where the dipole trap is not required, the AOMs remain switched on such that displacement of the beam due to thermal effects in the AOM are not observed when the RF power changes. To deflect the beams from the cell during these phases mirrors mounted in Thorlabs MFF001/M motorised flipper mounts are used. Two steering mirrors are utilised to position the beams within the cell. The vertical and horizontal positioning of these beams is discussed in section 4.4. The light is focussed to a waist of 68 μm.

The beams are transmitted through the cell at an angle of approximately 11° to the normal. The reflection coefficient for vertically polarised light incident on glass at this angle is approximately 4%, which is in agreement with what is measured. The reflected beams have therefore been blocked to avoid potentially hazardous reflections. The light transmitted through the far side of the cell is blocked directly for beam 2. For beam 1 two successive beam samplers (Thorlabs BSF-10-C) are used to pick off approximately 0.01% of the total beam power. This is focussed onto the photodiode which provides the signal for the servo-mechanical circuit. For beam 2 the light used as the signal for the servo-mechanical circuit is that which is transmitted through the steering mirror M_4, focussed onto a photodetector. Neutral density filters reduce the beam power incident on both photodetectors to a safe level. Both photodetectors are Thorlabs FGA10 InGaAs photodiodes.

A schematic of the setup used to remove relative intensity noise is displayed in figure 4.18. A control voltage is set by the user which corresponds to a trapping beam power. When the 'On/Off' TTL is true the circuit attempts to stabilise the photodiode signal (V_{PD}) by varying the output to the AOM driver, which in turn outputs a corresponding RF signal to the AOM. In between experimental runs a pair of mirrors in motorised flipping mounts block the dipole trapping beams for three reasons. If they weren't utilised, in between experimental runs, and during the phases of the experiment where dipole trapping light isn't required (or indeed would be detrimental), it would be necessary to apply zero RF power to the AOM, thus the majority of light would be present in the zeroth order diffracted beam. The light in this beam is blocked by a beam dump which is necessarily small to avoid clipping the first order diffracted beam, and would rapidly heat this beam dump. Secondly it is important for the RF power applied to the AOM to be as stable as possible to reduce beam pointing instabilities as discussed in section 4.2.2. Finally there is still a small amount of diffraction into the first order diffracted beam when zero RF power is applied, which would then

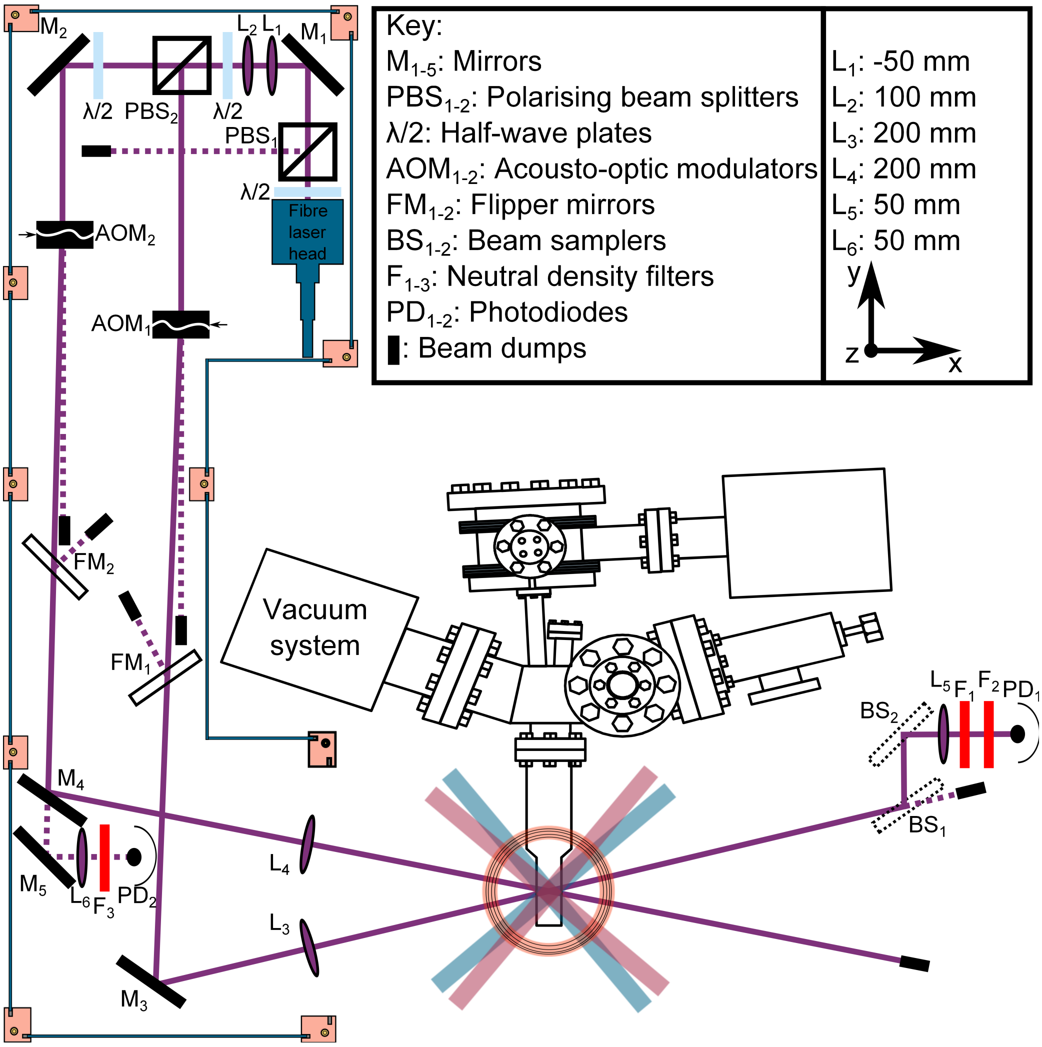

Figure 4.16: Schematic diagram of the optical setup of the dipole trap. The two dipole trapping beams intersect in the region of the centre of the magnetic trapping coils, at an angle of ∼ 22° to one another. The MOT chamber and vacuum apparatus are also pictured for reference. The blue panels shown surrounding the optics are the safety enclosure. A key to the symbols used can be found in the top right of the diagram.

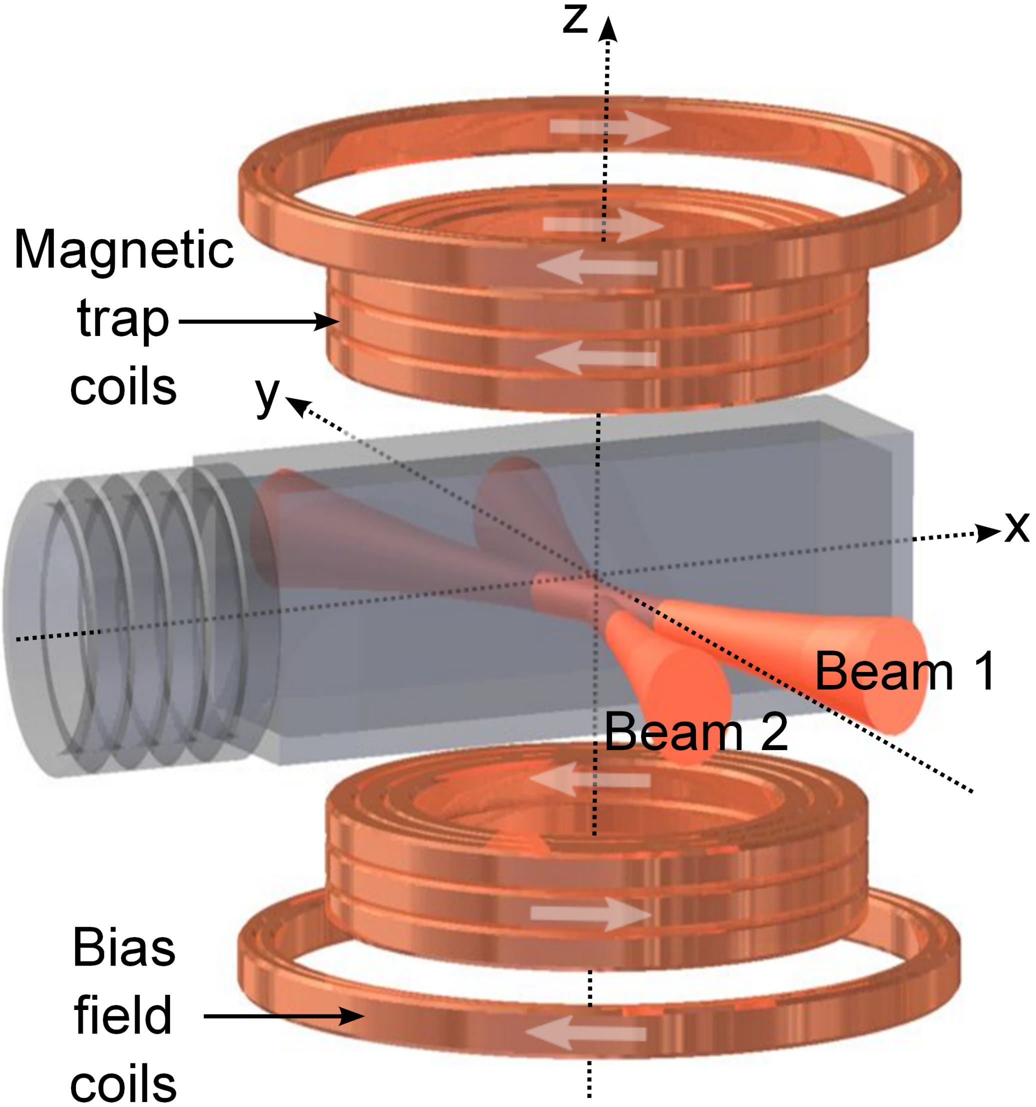

Figure 4.17: Diagram of the dipole trapping beams and their positions as they intersect the glass cell. The beams are angled at approximately 22° to each other. Also shown are the coils used to generate the magnetic field gradient for magnetic trapping and for the MOT, as well as those used for applying a magnetic bias field. The assignment of the axes used throughout this work are labelled.

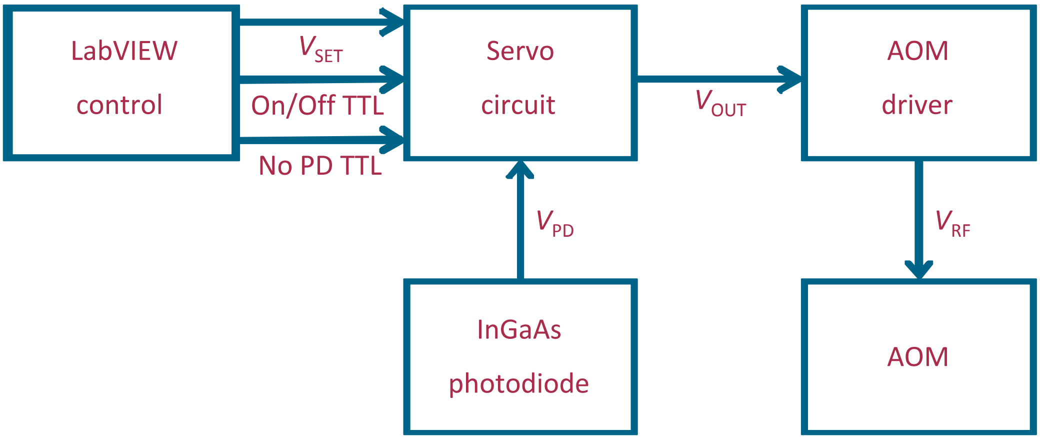

Figure 4.18: Schematic of the integration of the servo-mechanical circuit in the experiment.

be incident on the atoms during other experimental phases, a potentially detrimental consequence. During the time in which the mirrors block the beam a TTL (‘No PD TTL’) is output by the control system. When the servo-mechanical board receives this signal the output to the AOM is set to a constant voltage, nominally that which is used to generate the correct beam power for dipole trap loading.

Experimentally the servo-mechanical circuit is also used during the evaporation procedures described in section 4.5. The evaporation ramps are programmed into the experimental control procedure resulting in the desired beam powers being output from the AOM.

4.4 Loading the optical trap

Atoms are pre-cooled via RF evaporation, which is described in section 3.7.2, prior to dipole trapping the atoms. During the RF evaporation the dipole trapping beam impinges on the magnetically trapped atom cloud and is loaded continuously throughout the process by atoms which fall into the potential. The vast majority of atoms are loaded after the RF evaporation where $\partial B/\partial z$ is reduced from 187 G cm^{-1} to 28 G cm^{-1}, a value just below that which levitates ^{87}Rb and ^{133}Cs. Hence as the atoms are no longer levitated the cloud will expand into the region where the dipole trapping beam is located (200 μm below the magnetic trap centre). These atoms may then collisionally load the dipole trap's potential.

Positioning of the dipole trapping beam was performed by exploiting the fact that each individual beam can be used to form a hybrid trap with the magnetic field gradient providing the axial confinement. In this manner each beam could be aligned separately. The beams were aligned independently in each direction. Good alignment in the axial plane is essential as the beam size determines trap depth and frequency. Given the beam waist is 68 μm (see figure 4.22) the Rayleigh range is $\sim$ 9 mm. Hence if the beam waist is axially misaligned by 1 cm, the beam radius at the trap centre would be $\sim$ 100 μm. Typically the trap depth and frequency would then decrease by approximately a factor of 2.

4.4.1 Longitudinal alignment

To achieve good axial alignment two techniques were used. After RF evaporation the dipole trap was loaded by reducing the magnetic field gradient to 28 G cm^{-1} in 6 s for a beam power of 5.20 W. The atoms were then held in this potential for 20 s. As the atoms would be in equilibrium with the trap after this hold we expect their temperature to be approximately 1/10 of the trap depth. Imaging the atoms after a long time-of-flight ensures that the cloud's width is independent of trap frequency, hence we can be confident that the temperature determined in this manner would be accurate, even if the trap frequency wasn't precisely known. The trap depth calculated can then be used to determine the beam size at the atoms if the beam power is known. Plotting this for various lens positions (assuming the waist's position varies linearly with the lens position) allows correct positioning of the lens using equation 2.74. To aid the measurement a second technique was used, where the atoms were loaded into the dipole potential only, as the magnetic field gradient was reduced to 0 G cm^{-1} in 7 s, removing confinement along the beam. If the atoms were then imaged immediately one observes the atoms positioned precisely over the magnetic trap centre. We then imaged the atoms after a 1 s hold in the single beam potential and after a 5 s hold. If the beam waist doesn't coincide with the magnetic trap centre the atoms can be seen moving away from the focus of the imaging system, however if the beam is well positioned they do not move. This technique was used to determine in which direction the beam was axially mis-aligned. Three such images taken for this purpose are displayed in figure 4.19.

The beam waist calculated from the temperature and trap depth as a function of lens displacement from an arbitrary reference point are presented in figure 4.20. Using equation 2.74 we find that for beam 1 $w_0 = (65.6 \pm 0.8)$ μm, $z_0 = (12.19 \pm 0.02)$ cm and $z_{\mathrm{R}} = (0.79 \pm 0.02)$ cm. For beam 2 we find $w_0 = (69.8 \pm 0.3)$ μm, $z_0 = (12.19 \pm 0.01)$ cm and $z_{\mathrm{R}} = (0.87 \pm 0.01)$ cm. These values are not in agreement, however the horizontal and vertical alignment had not been performed at this stage, hence, as trap depth and frequency depend on position any small dependencies may change the temperature calculated. M^2 can also be calculated for each beam from these values, for beam 1 we find $M^2 = (1.1 \pm 0.2)$ and for beam 2 we find $M^2 = (1.14 \pm 0.01)$. These values are in excellent agreement with each other, however they are larger than the values calculated for the direct beam output as every extra optic in the path distorts the beam a finite amount.

4.4.2 Horizontal and vertical alignment

Horizontal alignment

To locate the optimum horizontal and vertical positions for loading, which we believe to be approximately three beam waists below the magnetic trap centre (see section 4.1), ^{87}Rb atoms were prepared in the magnetic trap as above. Again the hybrid potential was used with a beam power of 5.20 W. The magnetic field was ramped to 28 G cm^{-1} in 6 s and atoms were held in this potential for a further 6 s. An image of the ^{87}Rb atoms was then taken after 19.92 ms time-of-flight. The number of atoms loaded into the potential was recorded as a function of the beam's horizontal position, with the beam's vertical position set 'by eye' at the magnetic trap centre. Figure 4.21(a) presents the results of this experiment. The beams' horizontal positions were then set at the trap's centre, where the dip occurs in figure 4.21(a).

Horizontally the beam was located at the centre, where the profile dips in figure 4.21(a). The atom number dips at this point as the trap was close

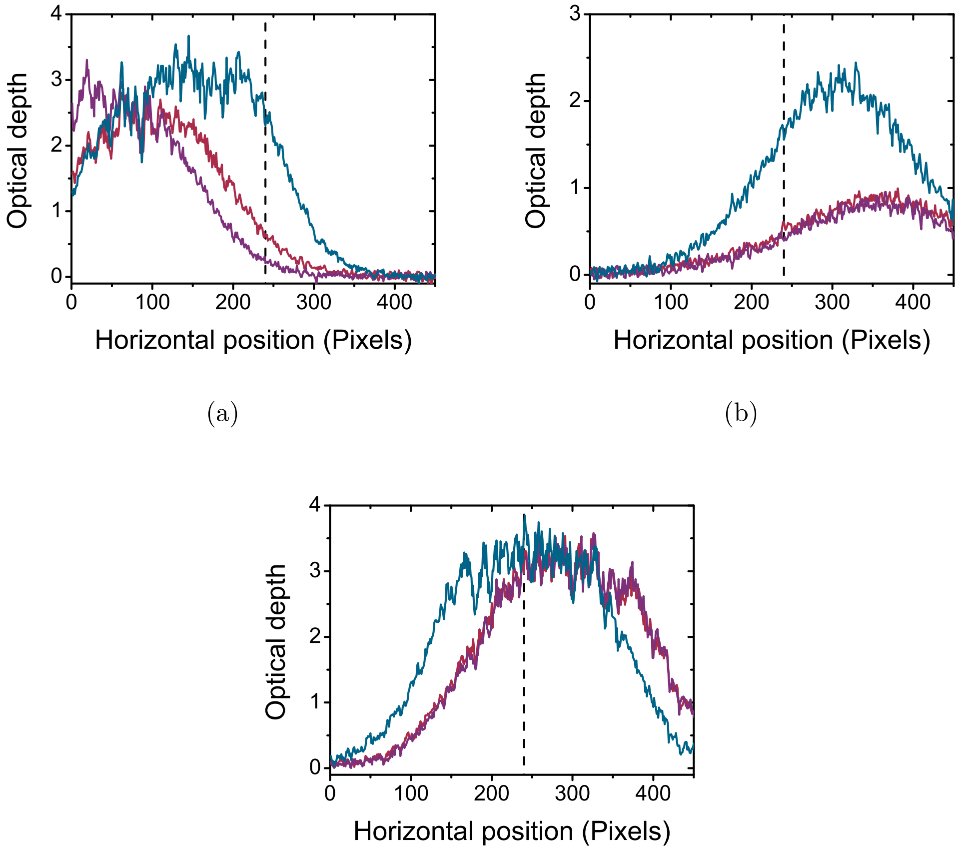

(a)

(b)

(c)

Figure 4.19: Cloud profiles taken immediately after $\partial B/\partial z$ is reduced to 0 G cm^{-1} (blue), 1 s after (red) and 5 s after (purple) for three different waist locations. The three lens positions (explained in the text as arbitrary) are 11.73 cm (a), 12.69 cm (b) and 12.13 cm (c). The black dashed line highlights the magnetic trap's horizontal centre at 240 pixels. In (a) and (b) the lens is too far from and too close to the centre of the magnetic trap respectively, and the atoms can be seen moving along the beam, and away from the edge of the CCD camera. This data was used to aid axial alignment of the dipole trapping beam.

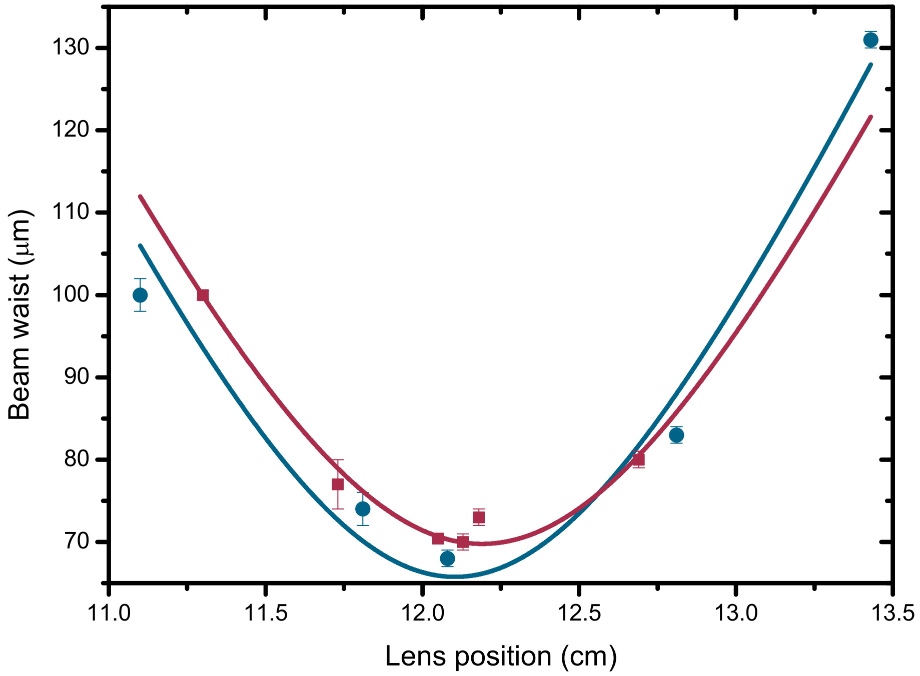

Figure 4.20: Beam size at the magnetic trap centre calculated from the cloud temperature after a 20 s hold in a hybrid potential comprised of a 5.20 W beam and a 28 G cm^{-1} magnetic field gradient, for beam 1 (blue circles) and beam 2 (red squares). The solid lines are fits to the data using equation 2.74.

to the magnetic field zero where Majorana spin flips limit the lifetime of the atoms and hence few atoms are loaded into the trap. We would expect the reduction in number to precisely reach zero, however the vertical trap position had only been set ‘by eye’ hence the beam was not perfectly located at the trap zero.

Vertical alignment

An identical experiment was then performed for different vertical positions, the results of which are displayed in figure 4.21(b). When the experiment was performed in the vertical direction the number dropped to zero at the trap centre. We see optimum trap loading approximately 200 μm below the trap centre. For the single beam trap this location represents a lower trap frequency region [165] however in the crossed beam trap the trap frequency is nearly independent of location. The beams were therefore located 200 μm below the magnetic field zero, avoiding the region of spin flip losses. The profiles of the magnetically trapped atoms demonstrate how atoms 'sag' into the trapping region as the magnetic field is reduced.

4.4.3 Parametric heating

To determine the size of each beam at the centre of the magnetic trap the frequency of the hybrid traps were measured by observing parametric heating. The single beams were loaded by reducing $\partial B/\partial z$ at a beam power of 5.20 W. The power of beam 1 (beam 2) was then reduced to 1.54 W (1.70 W) in 10 s and to ensure atoms were in equilibrium with the trap they were held in this potential for 10 s. The beam power was then modulated sinusoidally by sending an oscillating control signal to the AOM for 3 s at different frequencies. When the modulation frequency (ω_{mod}) matches the second harmonic of the trap frequency ($\omega_{\text{mod}} = 2\omega_{\text{trap}}$) parametric heating of the atoms was observed in addition to a loss of atoms from the trap. Heating and loss can also be observed at subharmonic frequencies ($\omega_{\text{mod}} = 2\omega_{\text{trap}}/n$, where n is an integer) [205]. The depth of the modulation was changed when searching for the fundamental trap frequency where a depth of 18% (18%) of the total beam 1 (2) power was used. When searching for the second harmonic the modulation depth used was 5% (7%) of the total beam power. Figure 4.22 presents the increase in temperature observed when the beam was modulated at the trap frequency.

The fundamental trap frequencies measured were (188 ± 2) Hz for beam 1 and (197.1 ± 0.5) Hz for beam 2, as determined by Gaussian fits to the temperature (the solid lines in figure 4.22). The second harmonic frequencies measured were (392 ± 3) Hz for beam 1 and (378 ± 2) Hz for beam 2 (the dashed lines). Similar frequencies were obtained for fits to the loss of atom number. Assuming the beam to be displaced 200 μm below the trap centre we calculate the 1/e^2 radius of both beams to be (68 ± 1) μm. Similar measurements have been performed for various beam powers, all agreeing with a 68 μm beam waist. The same experiment was also performed in the

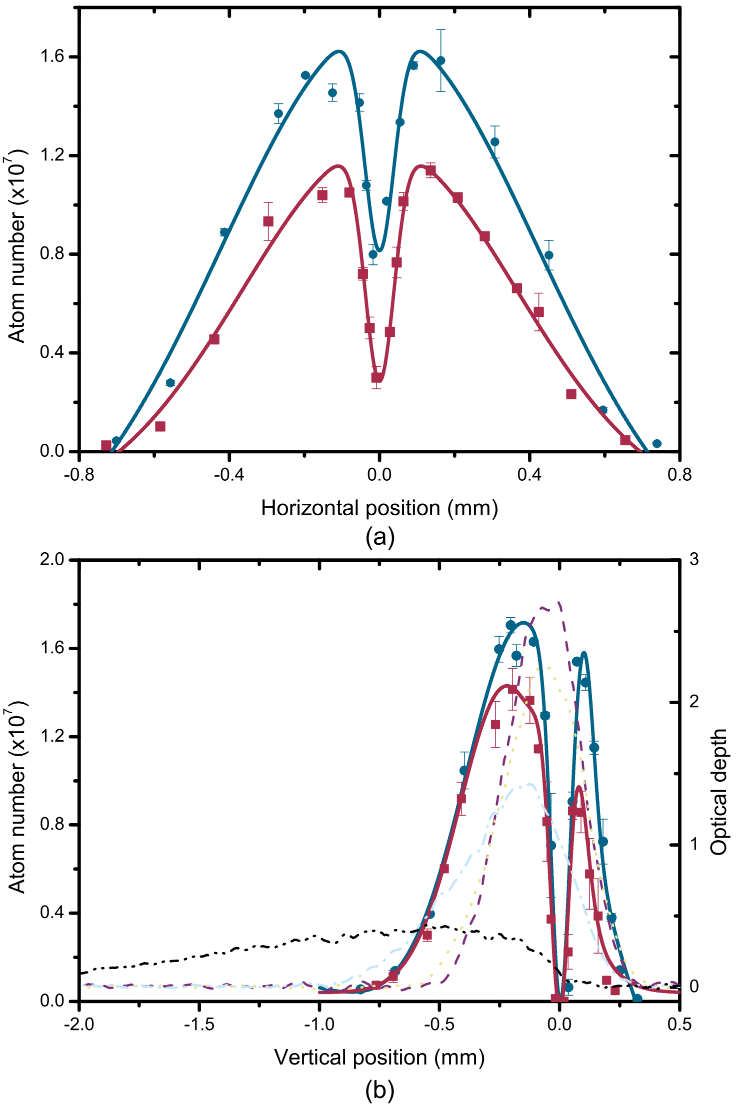

Figure 4.21: Number of ^{87}Rb atoms loaded into the dipole trap after a 6 s hold for different horizontal (a) and vertical (b) beam positions for beam 1 (blue circles) and beam 2 (red squares). Positions are relative to the magnetic trap centre. Lines are included to guide the eye. The profiles in (b) show the evolution of the cloud density profile as the magnetic field gradient is adiabatically ramped from 187 G cm^{-1} (purple dashed) to the final 28 G cm^{-1} (black dash-dot-dotted). A five point moving average has been applied to these profiles. The dips in (a) and (b) strikingly reveal the magnetic trap's centre as Majorana losses limit dipole trap loading.

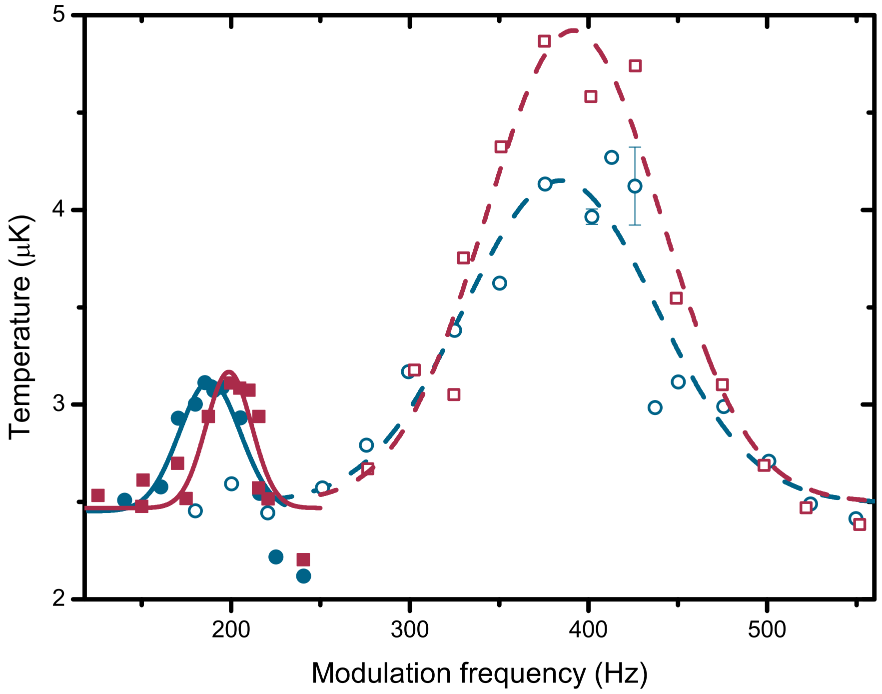

Figure 4.22: Temperature of the atoms trapped in the hybrid potential of beam 1 (blue circles) and beam 2 (red squares) when the beams are being modulated. Heating is observed when the beam power is modulated at the trap frequency. Modulation depths are 18% for the fundamental frequency data (solid data points), 5% for the second harmonic frequency for beam 1 and 7% for the second harmonic frequency for beam 2 (hollow data points). Gaussian fits to the fundamental frequencies (solid lines) are centred on (188 ± 2) Hz and (197.1 ± 0.5) Hz, and to the second harmonics (dashed lines) they are centred on (378 ± 2) Hz and (392 ± 3) Hz for beam 1 and beam 2 respectively.

crossed beam potential. It is then possible to observe the harmonic and sub-harmonic frequencies of the crossed beam trap's frequencies in all three dimensions. Note that it is also possible to observe loss from the trap as a way of measuring the trap frequency, however more modulation is required. The fitting of the data is generally more accurate for lower modulation depths.

4.4.4 The loading process

To load the hybrid trap the dipole trap beam power is held at 6.70 W throughout the RF evaporation. $\partial B/\partial z$ is reduced to 28 G cm^{-1} in 6 s whilst the radio-frequency is simultaneously reduced to 3.50 MHz. The single beam trap is typically loaded with $(2.88 \pm 0.02) \times 10^7$ ^{87}Rb atoms in the $|1, -1\rangle$ state at a temperature of (13.80 ± 0.02) μK and a PSD of $(2.77 \pm 0.02) \times 10^{-3}$. The trap depth here is 83 μK and the trap frequencies are $\omega_{\text{rad}} = 2\pi \times 411.2$ Hz and $\omega_{\text{ax}} = 2\pi \times 17.0$ Hz. In single beam experiments the magnetic field gradient is never switched off completely such that atoms are confined in the axial beam direction. Without the magnetic confinement the axial frequency would be $\omega_{\text{ax}} = 2\pi \times 2.2$ Hz

Atoms are loaded into the crossed dipole trap by reducing the magnetic field gradient from 187 G cm^{-1} to 28 G cm^{-1}. This is done in two stages, first the gradient is reduced to 94 G cm^{-1} in 200 ms. The RF cut into the atoms continues during this time to a frequency of 5.05 MHz. The field gradient and RF frequency are held at these values for 500 ms before the field gradient is reduced to 28 G cm^{-1} in 1 s. The RF cut continues down to a frequency of 3.50 MHz during this time. The dipole trapping beam is stabilised to a power of 4.05 W during the RF evaporation and dipole trap loading sequences. Typically $(1.45 \pm 0.06) \times 10^7$ ^{87}Rb atoms are loaded into the crossed beam potential at a temperature of (11.7 ± 0.1) μK and PSD of $(1.39 \pm 0.03) \times 10^{-2}$. In this configuration the atoms are evaporated in the vertical direction.

The dipole trap potential is the same for all magnetic sublevels of the atoms, hence once atoms are loaded into the crossed beam dipole trap we transfer the atoms into the absolute ground states. In this state two-body loss is suppressed for energetic reasons [137] thus removing the potential for high two-body losses in ^{133}Cs [117, 136]. This is done via rapid adiabatic passage [170]. Experimentally the state transfer is performed by applying a fixed RF field to the atoms. This field dresses the atoms, and the magnetic field is ramped which causes the atoms to sweep through a resonance (alternatively a fixed magnetic field may be applied and the RF frequency swept). The atoms are transferred to the absolute ground state. Full details of the experimental setup exist elsewhere [127].

In this work, to perform rapid adiabatic passage the frequency applied to the atoms is 1.64 MHz. This is achieved via a small 3 turn coil of copper wire of 26×26 mm^2 square cross-section, which is placed a few centimetres from the trap centre. The power applied to the coil is +29 dBm. The bias field is then switched on in three stages. The Helmholtz coil pair are switched on in 10 ms to a low current via a TTL. The current in the coil is then increased linearly in 20 ms to 5.35 A, which generates a field of (0.93 ± 0.04) G at the atoms. This sweeps the atoms through the resonance and the atoms are transferred into the absolute ground states. From here the current in the coils is ramped in 5 ms to the final experimental value, generally 89 A which generates a bias field of (22.91 ± 0.02) G, the optimum field for evaporation of ^{133}Cs (see figure 5.4). Considering the inclusion of the 28 G cm^{-1} magnetic field gradient the high-field seeking states are levitated against gravity in this potential.

For single-species loading of ^{87}Rb $(1.05 \pm 0.01) \times 10^7$ atoms remain after the spin flip at a temperature of (7.16 ± 0.06) μK and a PSD of $(4.31\pm0.08)\times10^{-2}$. Since atoms are now levitated against gravity the trap depth is reduced by a factor of 2. The evaporation surface is now along the beams, as the trap depth in the vertical direction remains the same as it was before the bias field ramp and spin flip were performed. The new trap depth and frequencies are 52 μK, $\omega_{\text{rad}} = 2\pi \times 448.1$ Hz and $\omega_{\text{ax}} = 2\pi \times 88.8$ Hz.

4.5 Evaporation within an optical trap

Evaporation within the dipole trap is performed via two distinct methods. The first method is plain evaporation of the atoms by reducing the trap depth of the dipole trap, in practice this is performed by reducing the beam power. This method takes advantage of the high trapping frequency of an optical trap, resulting in fast, efficient evaporation [159, 165, 166, 206–208]. Due to the harmonic trapping potential, at low beam powers the trapping frequencies are reduced, resulting in fewer atomic collisions. At this stage we sometimes apply a magnetic field gradient which 'tilts' the potential, reducing the trap depth in the vertical direction and allowing evaporation to take place with little reduction in the trap frequencies [11, 162].

4.5.1 Evaporation within the optical trap

Due to the improvements outlined in section 3.7 the increased number and PSD at the end of the RF evaporation sequence resulted in larger dipole trap loads. This resulted in faster optimum dipole trap evaporation ramps than observed previously, as well as an increase in condensate number upon evaporation in the single beam trap. Optimised evaporation in the single beam trap consists of three plain evaporation ramps. We first ramp to a power of 1.69 W in 2 s. Here $(1.16\pm0.02)\times10^7$ atoms remain at a temperature of (3.10 ± 0.02) μK. After the second ramp which lasts 3 s to a power of 420 mW the cloud temperature is (0.624 ± 0.005) μK with $(6.57\pm0.02)\times10^6$ atoms remaining. A final ramp to 68 mW in 3 s increases the PSD to (1.37 ± 0.05). Thus the $(5.37\pm0.10)\times10^6$ atoms retained by the potential are close to degeneracy. Holding in this potential for 1 s results in the production of a pure BEC of $(1.31\pm0.02)\times10^6$ atoms after rethermalisation. These ramps are summarised in tables 4.2 and 4.3. The trajectory to BEC of ^{87}Rb in both the single beam and crossed beam traps can be observed in figure 4.23.

In the crossed beam dipole trap three linear evaporation ramps to BEC are utilised. From the loading beam power of 4.05 W the beam power is ramped to 1.01 W in 0.5 s. Immediately after this ramp the power is reduced to 250 mW in 0.4 s and finally the power is ramped down to 90 mW in 1 s. After the first evaporation ramp $(5.8\pm0.4)\times10^6$ atoms remain at a temperature of (1.82 ± 0.01) μK. $(4.5\pm0.1)\times10^6$ ^{87}Rb atoms remain at a temperature of (0.85 ± 0.04) μK after the second evaporation ramp and the PSD here is (0.51 ± 0.09). After the third evaporation ramp a condensate can be observed

Ramp	P_1 (W)	P_2 (W)	t (s)	Trap depth (μK)	f_{rad} (Hz)	f_{ax} (Hz)
Load	-	6.700	-	83.1	411.2	17.0
1	6.700	1.690	2	20.5	210.8	17.0
2	1.690	0.420	3	4.5	105.6	16.9
3	0.420	0.068	3	0.2	41.9	16.9
4	0.068	0.068	1	0.2	41.9	16.9

Table 4.2: Hybrid magnetic and optical trap evaporation ramps used for evaporation of ^{87}Rb. Trap depths and frequencies quoted are for the power P_2 in each ramp, for the $|1,-1\rangle$ state.

Ramp	N	T (μK)	PSD
Load	$(2.88 \pm 0.02) \times 10^7$	(13.80 ± 0.02)	$(2.77 \pm 0.02) \times 10^{-3}$
1	$(1.16 \pm 0.02) \times 10^7$	(3.10 ± 0.02)	$(2.56 \pm 0.02) \times 10^{-2}$
2	$(6.57 \pm 0.02) \times 10^6$	(0.624 ± 0.005)	$(4.6 \pm 0.1) \times 10^{-1}$
3	$(5.37 \pm 0.10) \times 10^6$	(0.024 ± 0.003)	(1.37 ± 0.05)
4	$(1.31 \pm 0.02) \times 10^6$	-	> 2.612

Table 4.3: Number, temperature and PSD after each hybrid magnetic and optical trap evaporation ramp for ^{87}Rb. The ramp numbers correspond to those in table 4.2.

along with thermal atoms and a pure BEC of $(1.10 \pm 0.08) \times 10^6$ is formed after a 1 s hold in the potential. The ramps are summarised in tables 4.4 and 4.5.

Figure 4.23 displays that overall the evaporation procedure in the dipole trap produces larger BECs now than previously. This is largely due to the increased load into the dipole trap however. The lines of best fit represent more efficient cooling if they are steeper as a lower temperature or higher PSD is achieved with a lower loss of atom number. In the single beam dipole trap the evaporation efficiency is similar to the previous results, however the time taken to reach degeneracy is much faster as the larger density throughout the evaporation results in a higher collision frequency. In the crossed beam trap the efficiency is lower, despite larger condensates being produced. This has been attributed to a larger three-body loss coefficient being observed due to the higher density [138]. When the elastic collisions required for good evaporation are competing with the three-body losses the efficiency

Ramp	P_1 (W)	P_2 (W)	t (s)	Trap depth (μK)	f_{rad} (Hz)	f_{ax} (Hz)
Load	-	4.050	-	101.0	448.3	90.4
Spin flip	4.050	4.050	0.02	52.0	448.1	88.8
1	4.050	1.010	0.50	13.0	210.8	44.3
2	1.010	0.250	0.40	3.1	112.0	22.0
3	0.250	0.090	1.00	0.2	66.8	13.0
4	0.090	0.090	1.00	0.2	66.8	13.0

Table 4.4: Crossed dipole trap evaporation ramps used for evaporation of ^{87}Rb. Trap depths and frequencies quoted are for the power P_2 in each ramp, for the $|1, +1\rangle$ state.

Ramp	N	T (μK)	PSD
Load	$(1.45 \pm 0.06) \times 10^7$	(11.7 ± 0.1)	$(1.39 \pm 0.03) \times 10^{-2}$
Spin flip	$(1.05 \pm 0.01) \times 10^7$	(7.16 ± 0.06)	$(4.31 \pm 0.08) \times 10^{-2}$
1	$(5.8 \pm 0.4) \times 10^6$	(1.82 ± 0.01)	$(1.9 \pm 0.2) \times 10^{-1}$
2	$(4.5 \pm 0.1) \times 10^6$	(0.85 ± 0.04)	$(5.1 \pm 0.9) \times 10^{-1}$
3	$(1.7 \pm 0.2) \times 10^6$	-	~ 2.612
4	$(1.10 \pm 0.08) \times 10^6$	-	> 2.612

Table 4.5: Number, temperature and PSD after each crossed dipole trap evaporation ramp for ^{87}Rb. The ramp numbers correspond to those in table 4.4.

of evaporation is reduced. However, an efficiency of $\gamma = (3.0 \pm 0.2)$ still represents highly efficient evaporation.

4.5.2 Expansion of the condensate

A characteristic signature of the production of a BEC is the anisotropic expansion of the condensate upon release from the trapping potential, in contrast to the expansion of a thermal cloud where the aspect ratio approaches unity, independent of the trap frequency. As discussed in section 2.3.5 at long time-of-flights the aspect ratio of a thermal cloud tends to one in contrast with the anisotropic expansion of the condensate, described by equations 2.53.

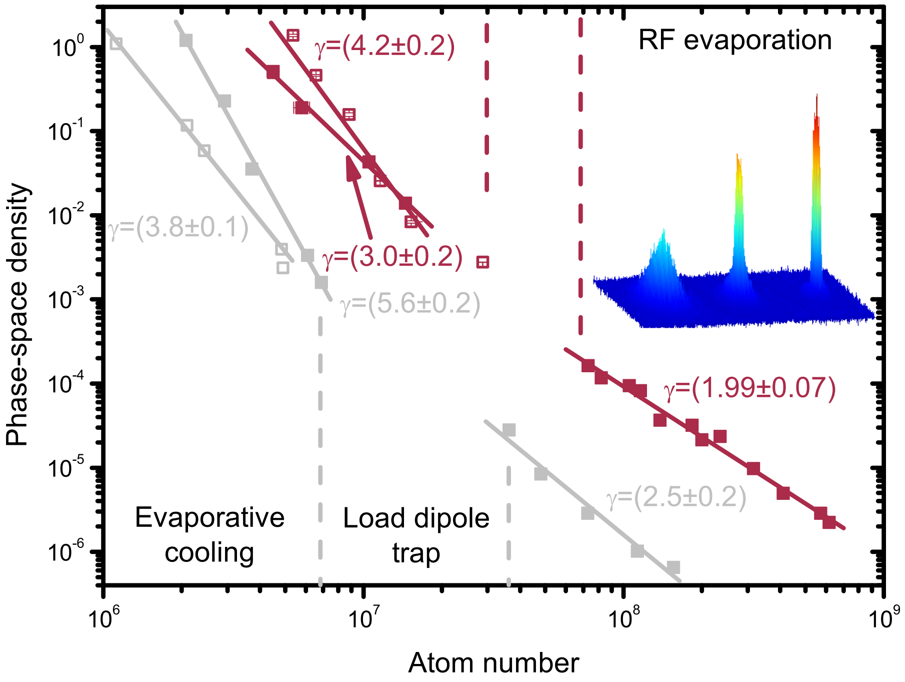

Figure 4.23: ^{87}Rb PSD as a function of atom number throughout the experimental evaporation sequences. Atom numbers after the improvements were made to the system (red) consistently exhibit higher PSDs than previous data (grey). Both single beam data (hollow squares) and crossed beam trap data (solid squares) are presented. The lines correspond to linear fits to the logs of the data points, and the gradient of these fits are the reported values of γ. More efficient evaporation is represented by a steeper line of best fit. Note some points aren't included in these fits, such as the first points after loading the dipole trap, as some of the atoms are still being evaporated at this point. A characteristic signature of the BEC transition is shown in the form of absorption images which highlight the evolution of the density distribution as the gas is cooled through the critical temperature (top right). Data in the RF evaporation sequence is identical to that presented in figure 3.7.

The anisotropic expansion of the BEC produced in the hybrid trap was observed by switching off the potential and measuring the horizontal and vertical cloud widths for various time-of-flights, this is displayed in figure 4.24. For comparison the expansion of a thermal cloud is also presented, the aspect ratio of which converges to one at long time-of-flights as expected. The BEC in the hybrid trap is cigar shaped due to the anisotropic confining potential where the radial trapping frequency is larger than the axial trapping frequency. Upon release the condensate's internal energy is converted into kinetic expansion energy in an anisotropic way such that the acceleration is larger in the radial direction, leading to an inversion of the aspect ratio. This can be seen in the false colour absorption images in figure 4.24.

4.5.3 Condensate fraction

The temperature dependence of the occupancy of the condensate has been measured below the critical temperature, T_c, which is described by equation 2.30. Measurement of the condensate occupancy was performed by taking two measurements for different final cloud temperatures, one with the probe beam close to resonance to image the thermal atoms, and one far detuned to image the condensate. Depending on the final temperature the cloud consists of purely thermal atoms, a bimodal distribution or a near pure condensate. Thermal clouds were fit using a Gaussian distribution and bimodal clouds were fit using a double Gaussian. The fits to the data can be seen in the inset of figure 4.25.

Figure 4.25 displays the condensate fraction as a function of the temperature, normalised to T_c, plotted with the theoretical prediction, resulting in reasonable agreement between experiment and theory. The accuracy of measuring condensate fractions > 0.8 render measurements at very low temperature unreliable due to the requirement of highly reproducible condensate numbers and imaging of dense condensates. Note that this data was obtained prior to the improvements to the evaporation in the magnetic trap were made.

The ability to produce large BECs is the ultimate test of all technical aspects of the dipole trap setup, such as the alignment, beam pointing stability, intensity stabilisation and experimental control, hence the performance of

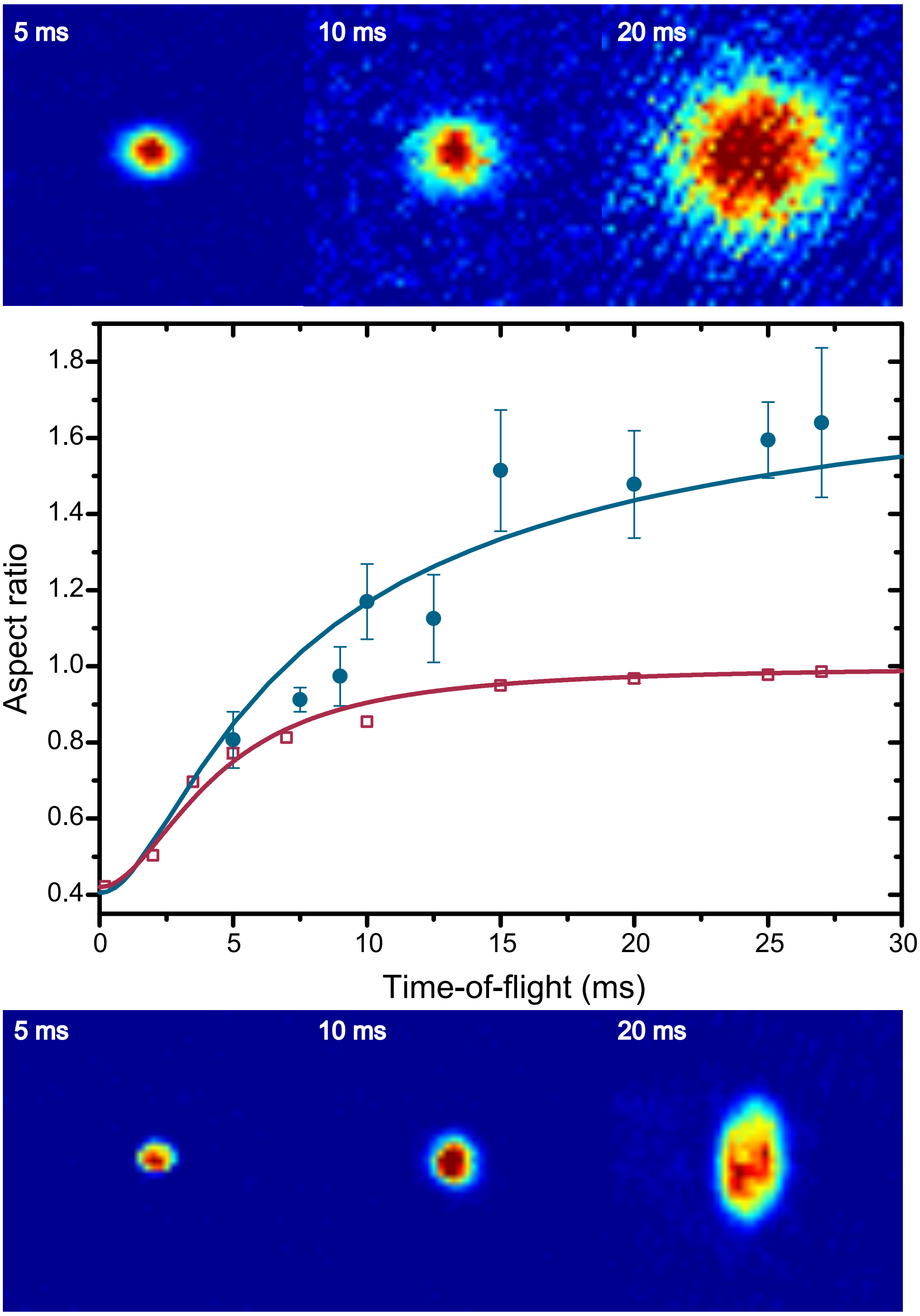

Figure 4.24: Aspect ratio ($\sigma_\mathrm{v}/\sigma_\mathrm{h}$) of a BEC (blue circles) and a thermal cloud (red squares) after being released from the hybrid potential for different time-of-flights. At long time-of-flight the aspect ratio of the thermal cloud tends to unity, however the BEC becomes elongated in the vertical direction, a characteristic signature of a BEC. The lines indicate the predicted expansion of the BEC and the thermal atoms using equations 2.53 and 2.54, respectively. Absorption images of a thermal cloud (top) and a BEC (bottom) highlight the evolution pictorially.

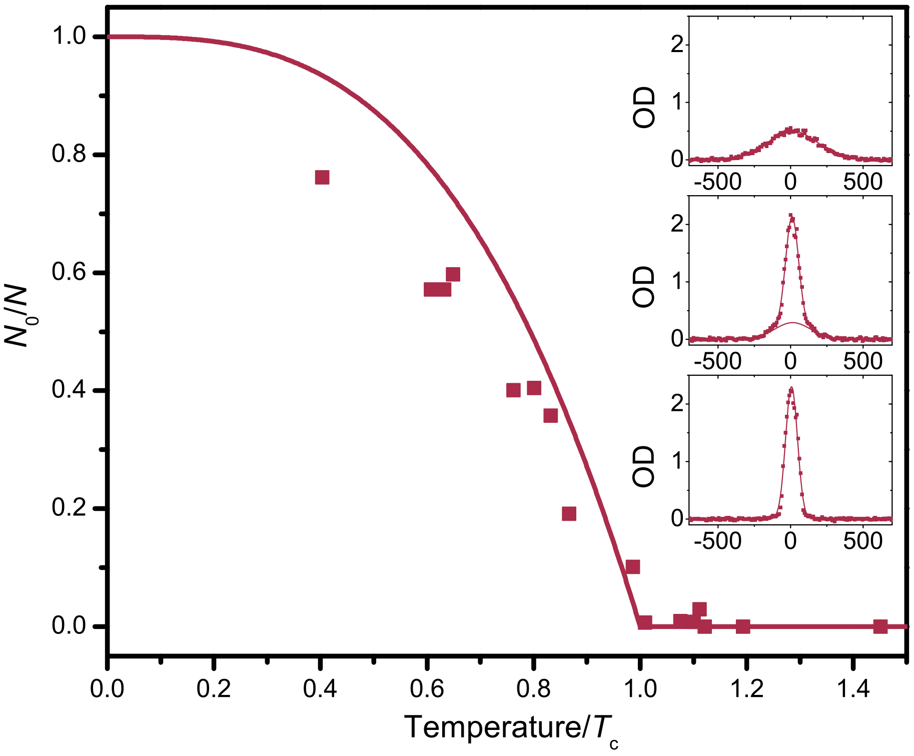

Figure 4.25: Condensate fraction as a function of temperature normalised to T_c. The line is the theoretical prediction given by equation 2.30. At the critical temperature $(1.2 \pm 0.1) \times 10^6$ atoms remain. On the right statistical fits to the data are displayed for a thermal cloud (top), a bimodal distribution (middle) and a near pure condensate (bottom).

the system has proved to be more than adequate when applied to ^{87}Rb.

Chapter 5

An ultracold mixture of ^{87}Rb and ^{133}Cs

So far we have only considered single-species cooling of ^{87}Rb. We now move on to study a mixture of ^{87}Rb and ^{133}Cs, starting with a study of sympathetic cooling of ^{133}Cs. In section 3.7 improvements made to the RF evaporation of ^{87}Rb were discussed, which has implications for sympathetic cooling of ^{133}Cs. Subsequent dipole trap loading and evaporation of ^{133}Cs alone is discussed in section 5.2 followed by a discussion of the ^{133}Cs scattering properties at low magnetic field and optimisation of the bias field used for cooling. The production of a ^{133}Cs BEC is then presented in sections 5.3 and 5.4.

5.1 Improved sympathetic cooling within the magnetic trap

The evaporation sequence described in section 3.7.2 was optimised for evaporation of ^{87}Rb alone, however when ^{133}Cs was added to the potential the evaporation sequence was not changed. This is because the ^{87}Rb atom number is approximately an order of magnitude larger than the ^{133}Cs number throughout the evaporation hence the optimum ramp should not be vastly affected by the presence of the small amount of ^{133}Cs. This is demonstrated in figures 5.1 and 5.3. With the addition of the ^{133}Cs we are able to load

$(5.6 \pm 0.2) \times 10^8$ ^{87}Rb atoms into the magnetic trap at a temperature of (130 ± 10) μK and a PSD of $(3 \pm 1) \times 10^{-6}$, and $(1.7 \pm 0.1) \times 10^7$ ^{133}Cs atoms at a temperature of (160 ± 10) μK and PSD of $(6 \pm 2) \times 10^{-8}$.

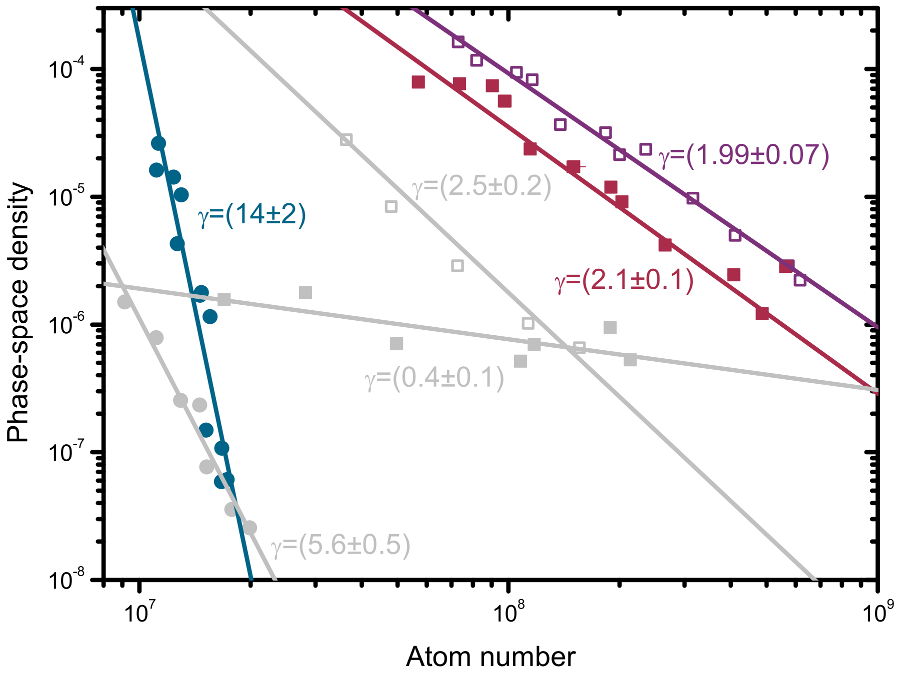

Figure 5.1: PSD as a function of atom number in the quadrupole trap. Solid blue circles and red squares correspond to data for ^{133}Cs and ^{87}Rb respectively, when ^{87}Rb is cooling ^{133}Cs. Open purple squares correspond to the ^{87}Rb PSD when not in the presence of ^{133}Cs. The lines have been added to guide the eye. The grey data points and lines represent data taken before improvements to the magnetic trap loading were made [12].

Figure 5.1 indicates that in the two-species case the presence of ^{133}Cs hardly affects the evaporation of ^{87}Rb. This is because the number of ^{87}Rb atoms is so large that any collisional loss with ^{133}Cs atoms does not remove a significant proportion of the ^{87}Rb atoms from the trap. The final number of ^{87}Rb atoms remaining is $(5.7 \pm 0.1) \times 10^7$ when ^{133}Cs is also present, however this is not due to a decrease in evaporation efficiency as the initial magnetic trap load is lower due to light assisted interspecies collisions within the MOT. The evaporation efficiency of ^{87}Rb when cooling ^{133}Cs is (2.1 ± 0.1). This is within error of the efficiency when ^{133}Cs is not present, and the slight increase in

Ramp	Species	N ($\times 10^7$)	T (μK)	PSD
Load	^{87}Rb alone	(62 ± 2)	(140 ± 10)	$(2.2 \pm 0.6) \times 10^{-6}$
	^{87}Rb(+Cs)	(56 ± 2)	(130 ± 10)	$(3 \pm 1) \times 10^{-6}$
	^{133}Cs	(1.7 ± 0.1)	(160 ± 10)	$(6 \pm 2) \times 10^{-8}$
1	^{87}Rb alone	(7.3 ± 0.3)	(33.6 ± 0.3)	$(1.6 \pm 0.2) \times 10^{-4}$
	^{87}Rb(+Cs)	(5.7 ± 0.1)	(37.3 ± 0.8)	$(7.9 \pm 0.9) \times 10^{-5}$
	^{133}Cs	(0.113 ± 0.006)	(37.8 ± 0.6)	$(2.6 \pm 0.3) \times 10^{-5}$

Table 5.1: Number, temperature and PSD after each RF evaporation ramp for ^{87}Rb and ^{133}Cs. The ramp labels correspond to those in table 3.2.

the efficiency may be explained by the fact that the initial atomic density is lower, leading to lower three-body intraspecies losses, which would otherwise reduce the final efficiency calculated. Previously the RF evaporation of ^{87}Rb with ^{133}Cs present in the trap was massively impacted by the presence of ^{133}Cs, as highlighted by the much lower gradient of the fit to the old data in figure 5.1. The efficiency in this case was (0.4 ± 0.1). This improved ^{87}Rb number has implications later in the experiment as collisional loading of ^{133}Cs into the dipole trap should be improved with increased collisions with ^{87}Rb.

The atom numbers and temperatures before and after the RF evaporation are listed in table 5.1. The ^{133}Cs number post evaporation is slightly larger than the old value of $(9.1 \pm 0.3) \times 10^6$. However the main difference is that due to the improved ^{87}Rb cooling the temperature after evaporation is now almost a factor of two lower than the (68 ± 3) μK achieved previously, resulting in a maximum ^{133}Cs PSD of $(2.6 \pm 0.3) \times 10^{-5}$, which is more than an order of magnitude larger than the previous data. Hence when loading the dipole trap, which has a set trap depth, the trap would be able to confine a larger number of ^{133}Cs atoms. The efficiency of ^{133}Cs cooling now is (14 ± 2), a huge improvement on the previous efficiency of (5.6 ± 0.5). Clearly the ^{133}Cs evaporation is more efficient than the ^{87}Rb evaporation, which is because the trap depth of ^{87}Rb is smaller than that of ^{133}Cs, hence, after ^{133}Cs atoms collide with atoms in the collisional bath of ^{87}Rb, they rethermalise to the lower temperature. This sympathetic cooling is efficient for ^{133}Cs, reflected in the high value of γ. The sympathetic cooling is highlighted further in figure 5.2.

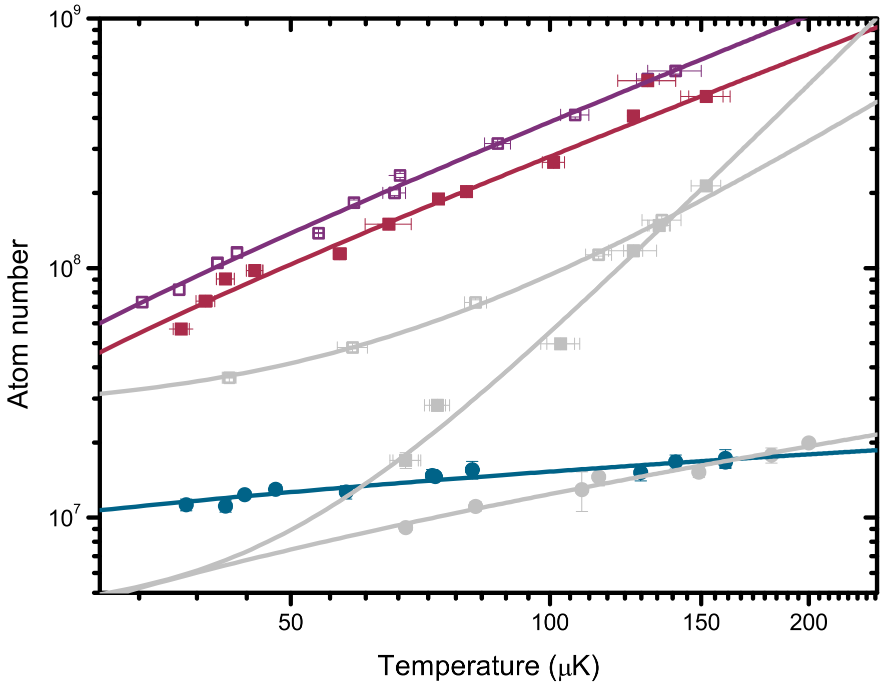

Figure 5.2: Atom number as a function of temperature in the quadrupole trap. Solid blue circles and red squares correspond to data for ^{133}Cs and ^{87}Rb respectively, when ^{87}Rb is cooling ^{133}Cs. Open purple squares correspond to the ^{87}Rb number when not in the presence of ^{133}Cs. The lines have been added to guide the eye. The grey data points and lines represent data taken before improvements to the magnetic trap loading were made [12].

Figure 5.2 highlights the fact that the sympathetic cooling of ^{133}Cs is efficient with little drop in atom number. This is demonstrated by the fact that the ^{133}Cs data are almost a flat line, which would indicate perfect sympathetic cooling where all rethermalisation of ^{133}Cs is performed via collisions with ^{87}Rb. In comparison with the previous ^{133}Cs data it is clear that there is a much smaller loss of ^{133}Cs atoms. The figure also highlights that the temperatures reached now are much lower than the previous values due to the increased Rb:Cs ratio. Previously the ^{87}Rb cloud rapidly heated as the collisional bath of ^{87}Rb atoms was depleted. However, as we now load more ^{87}Rb into the magnetic trap the heat load of ^{133}Cs does not have as much of a pronounced effect on the ^{87}Rb, which also correspondingly affects the final atom numbers, as discussed above, as is evident in the figure. Similarly, one can also see in figure 5.2 that the number of ^{87}Rb atoms is not affected by the presence of ^{133}Cs in the magnetic trap, the reduction in atom number is simply due to light assisted collisions in the MOT.

To investigate the effect that the presence of ^{133}Cs has on the efficiency of the ^{87}Rb cooling the full 15.1 s RF evaporation sequence was performed with different initial ^{133}Cs atom numbers within the magnetic trap. The ^{133}Cs load was controlled using the servo control circuit to stabilise the number of ^{133}Cs atoms within the MOT, and for the different MOT loads the two-species clouds were imaged both immediately after loading the magnetic trap and after the entire RF evaporation sequence. The final atom numbers, temperatures and cooling efficiencies are displayed in figure 5.3. The final atom number is displayed as a fraction of the initial load number. The experiment was performed for as high a ^{133}Cs MOT load as possible with ^{87}Rb present. We find that even though the push beam is being utilised, there are still some interspecies collisions that reduce the maximum ^{133}Cs MOT number trappable.

Figure 5.3(a) indicates that the final fractional ^{133}Cs atom number remaining is largely independent of the intial load, although there is a slight trend for the number to increase with initial load number. This increase is not significant in terms of the uncertainty of the data however. Indeed, considering the absolute final number remaining as a function of the initial magnetic trap load there is a strong linear relationship between the two, as would be expected. The fact that this relationship is linear indicates that up to the magnetic trap loads possible there is no effect on the ^{87}Rb evaporation. Likewise for the fractional ^{133}Cs number data. On average $\approx 63\%$ of ^{133}Cs atoms remain after the evaporation, in comparison to $\approx 13\%$ of ^{87}Rb atoms, which is consistent with good sympathetic cooling as the remaining fraction of ^{133}Cs atoms is much higher than that for ^{87}Rb. The fraction of ^{87}Rb remaining decreases by only $\approx 2\%$ from the zero ^{133}Cs case to the full ^{133}Cs load case, hence the presence of ^{133}Cs does affect the ^{87}Rb evaporation a small amount, however it isn't significant. The absolute ^{87}Rb number remaining does show a decrease of $\approx 30\%$ with ^{133}Cs load, however as the fractional number remaining doesn't vary by this amount we attribute the difference to the lower ^{87}Rb load into the magnetic trap as a result of interspecies collisions in the MOT.

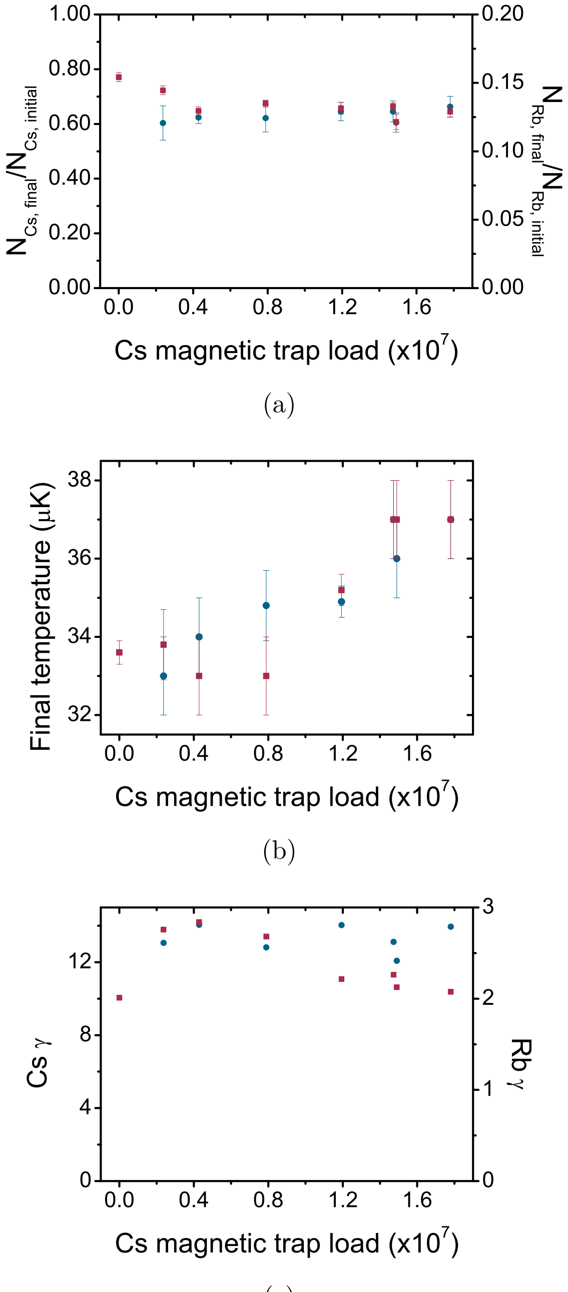

(a)

(b)

(c)

Figure 5.3: Fractional number of the magnetic trap load remaining (a), evaporation efficiency (b) and final temperature (c) of ^{133}Cs (blue circles) and ^{87}Rb (red squares) after the evaporation sequence in the magnetic trap, as a function of the number of Cs atoms loaded into the magnetic trap. Evaporation efficiency is calculated considering the numbers and PDSs immediately after loading the magnetic trap and after RF evaporation.

Figure 5.3(b) shows that as the ^{133}Cs magnetic trap load increases the ultimate temperature that we can reach when evaporating ^{87}Rb increases because of the extra heat load that ^{133}Cs imposes on the refrigerant ^{87}Rb atoms. The consequence of having a higher ^{87}Rb temperature is that the ^{133}Cs atoms rethermalise to a higher temperature, which is shown in the figure. We also observe corresponding patterns in the PSD. The final ^{133}Cs PSD is understandably dependent on the initial ^{133}Cs load, and little effect of stagnation of evaporation can be seen in the ^{133}Cs PSD data, even at higher loads. For higher ^{133}Cs loads the ^{87}Rb PSD density drops to about one-third of the value when ^{133}Cs is not present. This is a manifestation of both reduced efficiency of evaporation due to the heat load of the ^{133}Cs atoms, and a reduction in initial PSD density as the MOT load is reduced.

The evaporation efficiency of ^{133}Cs does not decrease as a function of the ^{133}Cs magnetic trap load, taking the uncertainties into account. This is to be expected given the trends in the number, temperature and PSD as explained above. The ^{87}Rb efficiency does decrease slightly, which suggests that if it were possible to load more ^{133}Cs than we can currently that the sympathetic cooling would be limited for higher ^{133}Cs numbers. The initial efficiency of ^{87}Rb evaporation is slightly lower than the other points, which is attributed to the fact that without the presence of ^{133}Cs atoms in the MOT the ^{87}Rb number is larger, hence the magnetic trap load is too. The three-body loss rate would then increase due to the higher atomic density, resulting in a lower number and heating which competes with the evaporation.

5.2 Optimisation of ^{133}Cs evaporation in the dipole trap

To load the dipole trap the magnetic field gradient and RF frequency are reduced in the same way they were for single species ^{87}Rb trap loading, as described in section 4.4. The dipole trapping beam is stabilised to a power of 4.05 W throughout the RF evaporation. For experiments involving Cs alone the ^{87}Rb atoms are removed from the trap via a blast of resonant light from the MOT cooling beam. We then load $(3.9 \pm 0.2) \times 10^6$ ^{133}Cs atoms into the trap at a temperature of (20.1 ± 0.1) μK and a PSD of $(6.5 \pm 0.5) \times 10^{-4}$. For two-species experiments the ^{87}Rb atoms aren't removed from the trap, however the exact number of each species remaining varies depending on the exact experiment being performed. Trap depths and frequencies are listed for all stages of the loading and evaporation process for ^{133}Cs in tables 5.3 and 5.4. For ^{87}Rb the values can be found in table 4.4.

After the spin flip $(2.4 \pm 0.3) \times 10^6$ ^{133}Cs atoms remain in the $|3, +3\rangle$ state. Their temperature and PSD at this stage are (15.04 ± 0.04) μK and $(1.03 \pm 0.02) \times 10^{-3}$ respectively. Since atoms are now levitated against gravity the trap depth is reduced by a factor of 2. The evaporation surface is now along the beams, as the trap depth in the vertical direction remains the same as it was before the bias field and spin flip were performed. Again, for two-species experiments the ratio of the two atom numbers differs depending on the measurement that is being taken.

Cooling of ^{133}Cs is more complicated than a 'simple' atomic species such as ^{87}Rb. Previous experiments have found that there is a small window of 21-25 G where ^{133}Cs can be condensed due to its rich Feshbach structure in addition to a large background scattering length [10, 151]. In this 4 G wide window the scattering length varies between approximately 200-400 a_0 [209], and there is a minimum in the recombination rate (see equation 5.1) due to the existence of Efimov physics when $a \approx 210$ a_0 [154], which occurs when $B \approx 21$ G [209]. This scattering length allows three-body losses to be minimised whilst still ensuring efficient rethermalisation of the atoms. We find the optimum magnetic field for evaporation to be (22.91 ± 0.02) G, which is in reasonable agreement with previous experiments [10]. To determine the optimum field for evaporation ^{133}Cs atoms were loaded into the dipole trap, and following the spin flip the beam power was reduced to 1.01 W in 0.6 s, and then to 250 mW in 1 s. The trap depth and frequencies in this trap are listed in table 5.3. The number after the spin flip was recorded and the final number and PSD after the evaporation ramps were used to calculate γ. The evaporation was performed at different magnetic fields in the 8-57 G region. The results of the experiment are displayed in figures 5.4 and 5.5.

Although this experiment doesn't provide a complete exploration of the optimum method with which to evaporate to BEC it does provide a good way to locate Feshbach resonances, regions of zero scattering length and the optimum location to evaporate for a given set of dipole trap ramps. It is worth

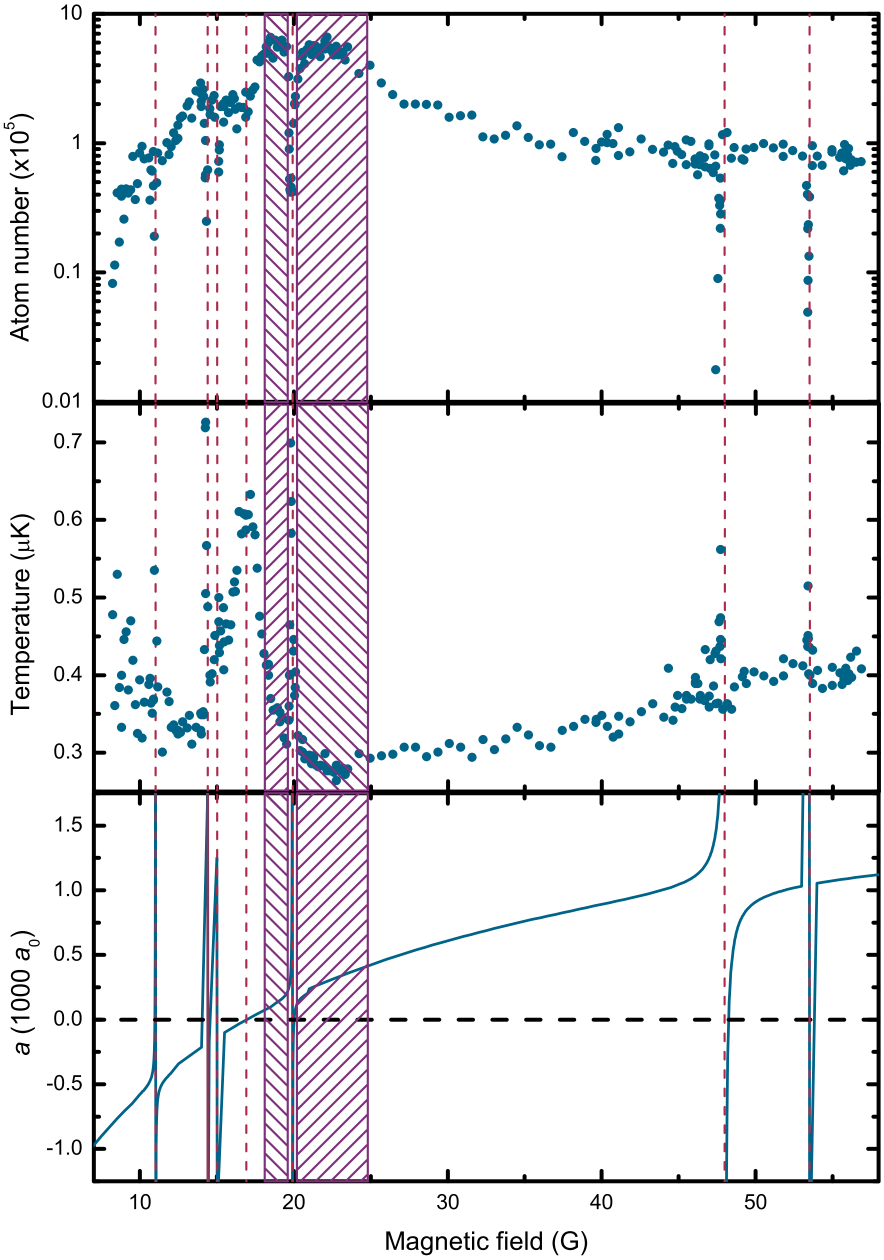

Figure 5.4: ^{133}Cs number remaining and temperature after two plain dipole trap evaporation ramps to beam powers of 250 mW at different magnetic fields. The scattering length is displayed below for reference. Feshbach resonances are highlighted by regions of number loss and high temperature. Red lines indicate the locations of known Feshbach resonances and the zero in scattering length [151]. The purple boxes span the two regions where ^{133}Cs has been condensed in the current apparatus, the previously used 21-25 G region [10] and the new region of 18.1-19.6 G.

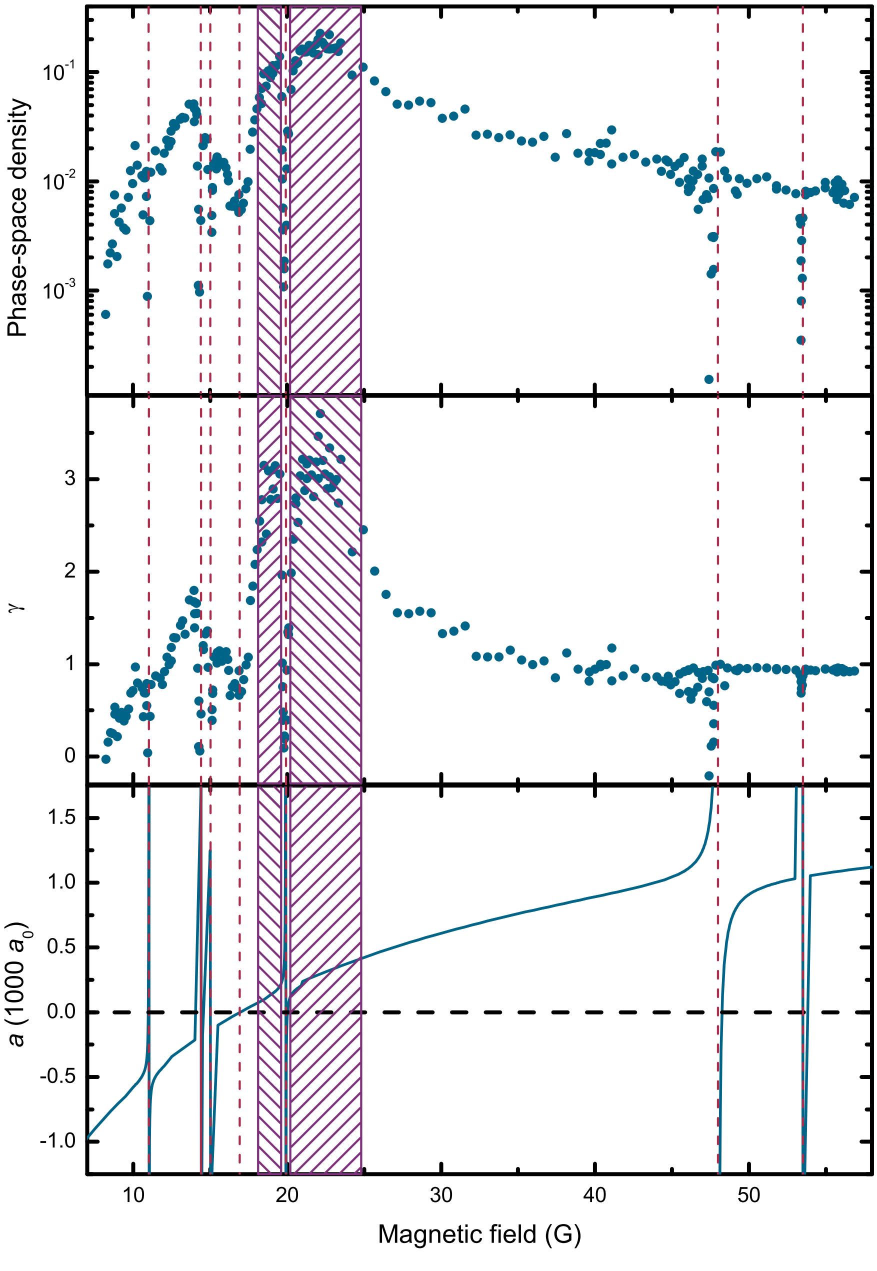

Figure 5.5: PSD of ^{133}Cs and the evaporation efficiency after two plain dipole trap evaporation ramps to beam powers of 250 mW at different magnetic fields. The scattering length is displayed below for reference. Feshbach resonances are highlighted by regions of lower PSDs and efficiencies. Red lines indicate the locations of known Feshbach resonances and the zero in scattering length [151]. The purple boxes span the two regions where ^{133}Cs has been condensed in the current apparatus, the previously used 21-25 G region [10] and the new region of 18.1-19.6 G.

This experiment B (G)	Literature B (G)	Theory B (G)
(10.97 ± 0.07)	(11.02 ± 0.03)	(11.2 ± 0.2)
(14.34 ± 0.06)	(14.37 ± 0.03)	(14.6 ± 0.2)
(15.1 ± 0.1)	(15.06 ± 0.03)	(15.1 ± 0.2)
(19.89 ± 0.09)	(19.90 ± 0.03)	(20.1 ± 0.2)
(47.7 ± 0.1)	(47.97 ± 0.03)	(47.7 ± 0.2)
(53.43 ± 0.04)	(53.50 ± 0.03)	(54.3 ± 0.2)

Table 5.2: Feshbach resonances observed due to collisions between ^{133}Cs atoms in the $|3, +3\rangle$ state. Positions have been determined using Lorentzian fits to the atom number. Experimental and theoretical values have been taken from the literature for comparison [210].

noting that if different ramp timings or depths are used the optimum bias field may change (indeed to reach degeneracy in the lower field region the ramps require modification). The process of locating the resonances also provides an additional tool with which to check operation of the system.

Feshbach resonances (see table 5.2) can be observed as regions of low atom number, PSD and efficiency, and of high temperature. The number decreases as the three-body recombination rate scales with a^4 [138, 141, 142]

$$K_3 = n_l C \hbar a^4 / m, \tag{5.1}$$

where n_l depends on the atom loss per recombination event and C is a dimensionless factor. This results in a consequent decrease of PSD and efficiency. The temperature is seen to increase as the energy released during three-body recombination processes is absorbed by the atom cloud [138].

At approximately 17 G the scattering length is zero, hence rethermalisation of the atoms is poor here, and atom cloud isn't cooled. This is seen as a large peak in the temperature. A Gaussian fit to the temperature in this region suggests the zero in scattering length is at (16.9 ± 0.1) G, in reasonable agreement with the theoretical value [151] and the experimental value of (17.119 ± 0.002) G, measured via Bloch oscillations [150]. The atom number remaining here is high due to the low number of collisions. The cooling is poor over a range of approximately 3 G due to this feature. Either side of the zero in the scattering length the cooling can be seen to quickly become more efficient as interactions between the atoms increase, resulting in a rise in rethermalisation also. Towards more negative scattering lengths the atom number again begins to drop at fields lower than 12.5 G as the interactions increase, and likewise in the positive scattering length regime, the number begins to drop for fields above 25 G. It is also possible to see that above 25 G the temperature increases in accordance with the scattering length, as the ratio of elastic-inelastic collisions decreases.

5.3 Bose-Einstein condensation of ^{133}Cs

The overall efficiency of cooling is maximised between 20.2-24.8 G, a region highlighted by the purple boxes in figures 5.4 and 5.5. Here the scattering length is optimum for efficient cooling, and we find that producing a BEC is possible in this window if evaporation continues. BECs of up to 2×10^5 atoms may be produced in this region if evaporation continues via trap tilting. There is also a region of slightly less efficient cooling at lower bias fields between 18.1-19.6 G, separated from the main region by the Feshbach resonance at 19.90 G, a region also highlighted in the figures. In this region we find that we are able to produce a BEC if the experiment is modified in the dipole trap evaporation stage. Two plain evaporation ramps are performed, to 1.01 W and 250 mW in 1 s and 800 ms respectively. The magnetic field gradient is then increased to 42.3 G cm^{-1} at which point the trap depths in the vertical direction and along the beams are equal. Over the course of 17.5 s $\partial B/\partial z$ is increased to a value of 62 G cm^{-1} tilting the trap further. At this stage we are able to produce a BEC of up to 3×10^4 atoms. To present knowledge a BEC of ^{133}Cs has not been produced in this field range before. The plain evaporation ramps used to produce a BEC in this field range are summarised in table 5.3, and the trap tilting ramps are summarised in table 5.4.

In the optimal experimental configuration, performing evaporation at a B-field of (22.91 ± 0.02) G, we continue our evaporation using another plain evaporation ramp to a power of 130 mW in 1 s. The trap and frequencies in this trap are listed in table 5.5. At this stage if we continue to evaporate

Ramp	P_1 (W)	P_2 (W)	t (s)	Trap depth (μK)	$f_{\rm rad}$ (Hz)	$f_{\rm ax}$ (Hz)
Load	-	4.050	-	136.0	422.3	85.3
Spin flip	4.050	4.050	0.02	69.0	422.0	82.0
1	4.050	1.010	1.00	16.5	211.0	41.7
2	1.010	0.250	0.80	4.2	105.5	20.7

Table 5.3: Crossed dipole trap plain evaporation ramps used for evaporation of ^{133}Cs in the lower field 18.1-19.6 G region, performed by simply reducing the beam power. The magnetic field gradient used is 28.2 G cm^{-1}. A condensate is produced using a bias field in the range of 18.1-19.6 G throughout the plain evaporation. Trap depths and frequencies quoted are for the power P_2 in each ramp, for the $|3,+3\rangle$ state, except for the loading trap, where values are calculated for the $|3,-3\rangle$ state.

Ramp	$\partial B/\partial z_1$ (G cm^{-1})	$\partial B/\partial z_2$ (G cm^{-1})	t (s)	Trap depth (μK)	$f_{\rm rad}$ (Hz)	$f_{\rm ax}$ (Hz)
1	28.2	42.3	0.05	3.9	105.5	20.6
2	42.3	53.5	9.50	0.9	100.8	20.5
3	53.5	57.0	4.00	0.4	96.9	20.5
4	57.0	62.0	4.00	0.1	96.6	20.5

Table 5.4: Crossed dipole trap tilting ramps used for evaporation of ^{133}Cs in the lower field 18.1-19.6 G region, performed by tilting the trap by increasing the magnetic field gradient. The beam power used is 250 mW. A condensate is produced using a bias field in the range of 18.1-19.6 G throughout the evaporation. Trap depths and frequencies quoted are for the field gradient $\partial B/\partial z_2$ in each ramp, for the $|3,+3\rangle$ state.

by simply reducing the beam power the evaporation stagnates, and we are unable to reach the BEC phase transition. We instead increase $\partial B/\partial z$ to 37.0 G cm^{-1} in 10 ms, as this now balances the trap depths along the beams and in the vertical direction (note the lower value than in the case for the lower field region, where the beam power is higher). The trap is then tilted by increasing $\partial B/\partial z$ to 40.0 G cm^{-1} in 1 s, and then to 42.5 G cm^{-1} in 0.2 s. The atoms are held in this potential for 1 s where the trap depth is 0.5 μK deep. A pure BEC of up to 1×10^5 ^{133}Cs atoms is produced via this method, as presented in figure 5.7. The plain evaporation ramps used to produce an optimised BEC are summarised in table 5.5 and the trap tilting ramps are

Ramp	P_1 (W)	P_2 (W)	t (s)	Trap depth (μK)	f_{rad} (Hz)	f_{ax} (Hz)
Load	-	4.050	-	136.0	422.3	85.3
Spin flip	4.050	4.050	0.02	69.0	422.0	82.0
1	4.050	1.010	0.60	16.5	211.0	41.7
2	1.010	0.250	1.00	4.2	105.5	20.7
3	0.250	0.130	1.00	1.9	72.7	14.6

Table 5.5: Optimised crossed dipole trap plain evaporation ramps used for evaporation of ^{133}Cs, performed by simply reducing the beam power. The magnetic field gradient used is 28.2 G cm^{-1} and the bias field is 22.91 G throughout the plain evaporation. Trap depths and frequencies quoted are for the power P_2 in each ramp, for the $|3,+3\rangle$ state, except for the loading trap, where values are calculated for the $|3,-3\rangle$ state.

Ramp	$\partial B/\partial z_1$ (G cm^{-1})	$\partial B/\partial z_2$ (G cm^{-1})	t (s)	Trap depth (μK)	f_{rad} (Hz)	f_{ax} (Hz)
1	28.2	37.0	0.01	1.9	72.7	14.3
2	37.0	40.0	1.00	1.1	69.5	14.3
3	40.0	42.5	0.20	0.5	69.5	14.2
4	42.5	42.5	1.00	0.5	69.5	14.2

Table 5.6: Optimised crossed dipole trap tilting ramps used for evaporation of ^{133}Cs, performed by tilting the trap by increasing the magnetic field gradient. The beam power used is 130 mW and the bias field is 22.91 G throughout the evaporation. Trap depths and frequencies quoted are for the field gradient $\partial B/\partial z_2$ in each ramp, for the $|3,+3\rangle$ state.

summarised in table 5.6. The number, temperature and PSD after each stage of evaporation are summarised in table 5.7.

5.4 Tuning interactions in a Cs Bose-Einstein condensate

Figures 5.4 and 5.5 demonstrate the rich Feshbach structure exhibited by ^{133}Cs in the 0-50 G field range. These broad resonances allow control of the scattering length and thus the mean field interactions within the BEC can

Ramp	N	T (μK)	PSD
Load	$(3.9 \pm 0.2) \times 10^6$	(20.1 ± 0.1)	$(6.5 \pm 0.5) \times 10^{-4}$
Spin flip	$(2.4 \pm 0.3) \times 10^6$	(15.04 ± 0.04)	$(1.03 \pm 0.02) \times 10^{-3}$
Plain 1	$(1.22 \pm 0.03) \times 10^6$	(2.91 ± 0.04)	$(8.2 \pm 0.1) \times 10^{-3}$
Plain 2	$(8.5 \pm 0.2) \times 10^5$	(0.861 ± 0.005)	$(3.4 \pm 0.1) \times 10^{-2}$
Plain 3	$(3.77 \pm 0.06) \times 10^5$	(0.3423 ± 0.0003)	$(2.34 \pm 0.003) \times 10^{-1}$
Tilt 1	$(2.8 \pm 0.1) \times 10^5$	(0.247 ± 0.001)	$(4.6 \pm 0.3) \times 10^{-1}$
Tilt 2	$(2.2 \pm 0.2) \times 10^5$	(0.224 ± 0.005)	$(5.1 \pm 0.7) \times 10^{-1}$
Tilt 3	$(1.77 \pm 0.07) \times 10^5$	-	≈ 2.612
Tilt 4	$\sim 1 \times 10^5$	-	> 2.612

Table 5.7: Number, temperature and PSD after each crossed dipole trap evaporation ramp for ^{133}Cs. The ramp numbers correspond to those in tables 5.5 and 5.6.

be tuned due to the interaction term in the Gross-Pitaevski equation

$$\left(-\frac{\hbar^2\nabla^2}{2m} + U_{\mathrm{ext}}(\vec{r}) + g\left|\psi(\vec{r})\right|^2\right)\psi(\vec{r}) = \mu\psi(\vec{r}). \tag{5.2}$$

A resonance exists between a pair of atoms initially in the $|3,-3\rangle$ state at approximately 8 G, which derives from an avoided crossing in the $6(s)$ molecular bound state. Being the last bound state for fields >20 G the avoided crossing results in a broad resonance where the scattering length increases from negative to positive values at a steady rate [210]. The width of the resonance allows precise control of the scattering length and thus the interactions.

Experimentally the tunability of intraspecies interactions is observed by creating a condensate and allowing the cloud to evolve at various bias fields for a free time-of-flight. The BEC was prepared as discussed previously, and the bias field was then non-adiabatically jumped in 100 μs to a value in the 14-29 G range. The number of condensed atoms was kept constant at $(9 \pm 1) \times 10^4$ as the release energy of the BEC is the sum of the kinetic energy and the interaction energy. Assuming the condensate is large enough such that the kinetic term can be neglected, we can see that the release energy is proportional to the chemical potential, which is in turn proportional to $(Na)^{2/5}$, hence $E_{\mathrm{rel}} \propto (Na)^{2/5}$ (see section 2.3.4). The atoms were levitated

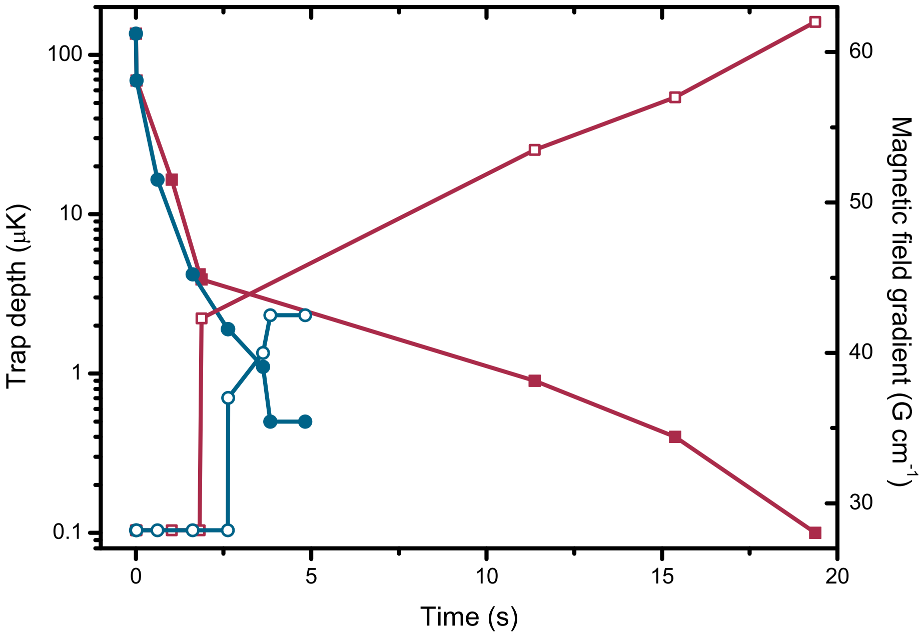

Figure 5.6: Graphical representation of the optimised (blue) and lower field region (red) crossed dipole trap ramps for Bose-Einstein condensation of ^{133}Cs. The trap depth (solid symbols) and the magnetic field gradient (hollow symbols) are presented as functions of time after loading the dipole trap. The trap depths are given for the $|3,+3\rangle$ state, except for the first points, where it is given for the $|3,-3\rangle$ state. The ramps correspond to those in tables 5.3-5.6

for 30 ms at the measurement field, prior to a free time-of-flight expansion of 10 ms. An absorption image of the cloud was then taken. The results of this experiment are presented in figure 5.8.

Figure 5.8 exhibits three distinct regimes of interaction. For negative scattering lengths (fields below the zero-crossing at ∼ 16.9 G) the interactions are attractive, which causes the condensate to collapse [44, 211]. In the collapse process many atoms are lost and the large spread in momentum results in larger vertical widths being observed [10]. At the zero in scattering length the interactions are 'switched off' (an ideal Bose gas) and there is little or no expansion of the cloud, as seen in figure 5.8. The condensate is generally referred to as being 'frozen'. The final regime is in the positive scattering length region between 17 G and 29 G, where the scattering length increases almost linearly up to 600 a_0 (with exception of the narrow resonance at

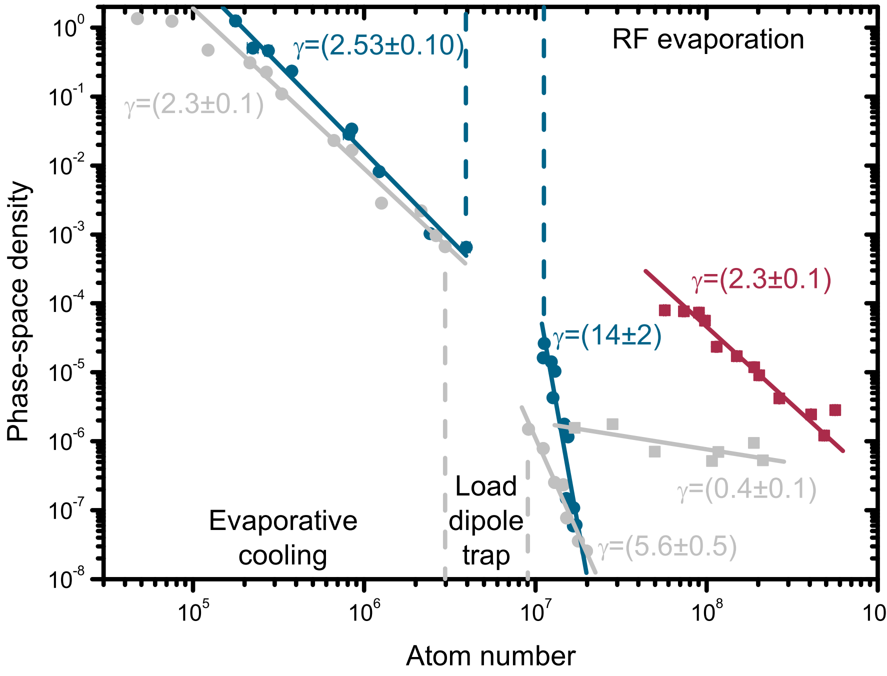

Figure 5.7: ^{133}Cs and ^{87}Rb PSD as a function of atom number throughout the experimental evaporation sequences in the crossed dipole trap. Atom numbers after the improvements were made to the system (blue and red for ^{133}Cs and ^{87}Rb repectively) consistently exhibit higher PSDs than previous data (grey circles and squares for ^{133}Cs and ^{87}Rb respectively). The lines correspond to linear fits to the logs of the data points, and the gradient of these fits are the reported values of γ. More efficient evaporation is represented by a steeper line of best fit. In the past it was observed that the evaporation during trap tilting wasn't as efficient as plain evaporation, however the new data indicates that the efficiency is the same using both methods. Note that some points aren't included in these fits, such as the first points after loading the dipole trap, as some of the atoms are still being evaporated at this point. Data in the RF evaporation sequence is identical to that presented in figure 5.1.

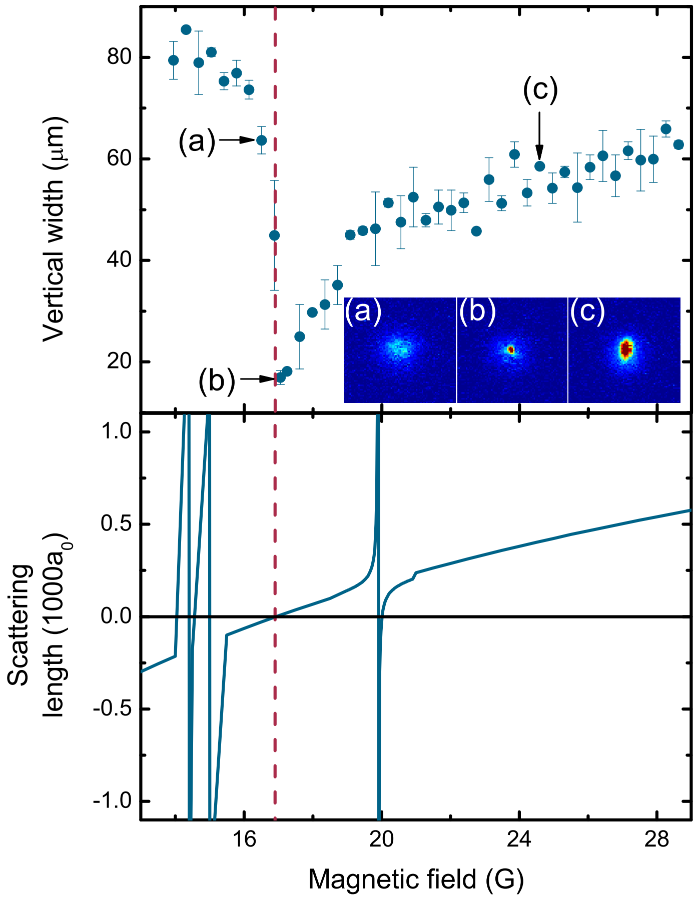

Figure 5.8: The vertical width ($1/\sqrt{e}$ half width) of the ^{133}Cs BEC after a time-of-flight expansion for a series of magnetic fields applied during levitation and the free time-of-flight. The $(9 \pm 1) \times 10^4$ condensed atoms are levitated for 30 ms prior to the 10 ms free time-of-flight. Three particular regions of interest are highlighted by the false colour absorption images (of dimension 600×600 μm^2): (a) negative scattering length, (b) zero scattering length and (c) positive scattering length. The ^{133}Cs scattering length is included for comparison [151], and the location of the zero in scattering length is highlighted by the red dashed line.

19.90 G). Here the interaction is repulsive, hence the condensate is stable, and the mean field interaction causes the width to increase. The false colour images in figure 5.8 demonstrate the size of the condensate pictorially.

Chapter 6

Observation of ^{87}Rb and ^{133}Cs Feshbach resonances

The ability to condense both ^{87}Rb and ^{133}Cs within the same apparatus is a useful step in the process of preparing a sample of ultracold atoms with which a Feshbach resonance can be measured. Before measuring interspecies Feshbach resonances at high-fields there remain a few tests such as measuring sensitivity via intraspecies Feshbach resonances and exploring the behaviour of ^{133}Cs at high-fields where comparatively little work has been undertaken previously. In this section the preliminary single-species tests are covered, before a discussion of the various interspecies Feshbach resonances that have been observed. Magnetic fields for all results are calibrated using either RF signals to drive transitions between different m_F levels, or microwaves to drive transitions between the $F = 1$ and $F = 2$ ground states in ^{87}Rb. The procedure used to determine the locations of the resonances and the errors on these fields is described in appendix E.

6.1 Single-species results

6.1.1 Single species Feshbach resonances

Single-species dipole trap loading has been discussed in sections 4.4.4 and 5.2, we use the same procedures for the following single-species experiments. To test the stability of the system at high-fields two known resonances were measured, one in ^{133}Cs and one in ^{87}Rb. Our detection methods included detection of increased atom losses [51] which arise due to the a^4 dependence of the three-body loss coefficient on scattering length [138], and an observation of an increase in temperature, due to the recombination energy of the atoms involved in such three-body processes. However, the situation becomes more complicated in two-species experiments, where the intra- and interspecies scattering lengths must be considered.

A high-field ^{133}Cs Feshbach resonance

In ^{133}Cs, Feshbach resonances and Efimov features exist in the region around 550 G [152], making this region ideal to test the sensitivity of the apparatus. In addition to the large *s*-wave resonance in ^{133}Cs at 548.8 G where the scattering length is zero at 556.19 G three other resonances are present in the window from 540-590 G [153, 209].

Once ^{133}Cs atoms were loaded into the dipole trap the beam power was reduced as standard to 1.01 W in 0.6 s and then to 250 mW in 1 s at a bias field of (22.91 ± 0.02) G. The bias field was then increased to (537.23 ± 0.04) G in 10 ms before a final small jump was made in a further 10 ms to the measurement field. At the high-field the trap depth is 4.4 μK and the trap frequencies are $\omega_{\mathrm{rad}} = 2\pi \times 105.5$ Hz and $\omega_{\mathrm{ax}} = 2\pi \times 20.8$ Hz. At this stage there are $(5.6 \pm 0.6) \times 10^5$ atoms in the trap at a temperature of (1.83 ± 0.02) μK and a PSD of $(1.8 \pm 0.2) \times 10^{-3}$. The atoms were allowed to evolve in the trap at the measurement field for 100 ms. The atom number remaining, temperature and density were recorded. These can be seen in figure 6.1.

The large *s*-wave resonance at 548.8 G is only detectable through the loss minimum where the scattering length and the collision cross section are zero (the Ramsauer-Townsend minimum [212]). The scattering length at 540 G is 4500 a_0 where it begins to diverge due to the resonance. From this unitarity the scattering length increases (becomes less negative) until 556.19 G where the scattering length is 0 a_0. The scattering length then increases to 2500 a_0 at 590 G. From equation 2.12 we can see that the elastic cross section becomes

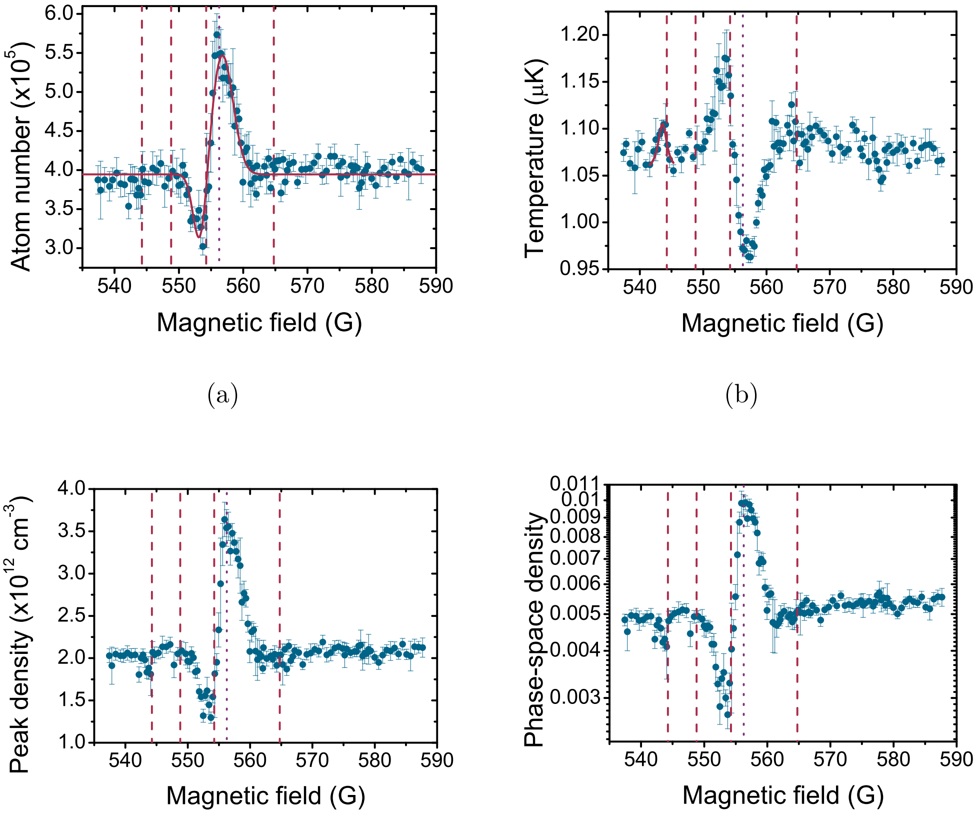

(a)

(b)

(c)

(d)

Figure 6.1: ^{133}Cs atom number (a), temperature (b), peak-density (c) and PSD (d) after a 100 ms hold at various B-fields in the 540-590 G region. The resonance predicted to be at 554.3 G can be observed as a minimum in the number, and the zero in scattering length due to the large s-wave resonance at 548.8 G can be observed as a peak in the number. The pole of the large $s-$wave resonance is not observed due to the measurement being unitarity limited as described in the text. Additionally the temperature increases due to the resonances at 544.3 G and 554.3 G. The theoretical position of the zero in scattering length is highlighted by the purple dotted line and the poles of the local resonances are indicated by the red dashed lines. The solid red lines in the number and temperature plots display the fits to the data used to measure the locations of the resonances and zero in scattering length.

limited when $ka \approx 1$. For a cloud of ^{133}Cs with a temperature of 1 μK the elastic cross section becomes unitarity limited approximately when $a = 1000\ a_0$. Clearly this value is smaller than the scattering length is in a large portion of this window. Thus we expect only to be able to detect the resonances at 544.3 G and 554.3 G and the Ramsauer-Townsend transmission at 556.19 G with the current experiment. Previous work has observed other resonances in this region at temperatures of (200 ± 50) nK where the cross section is unitarity limited at scattering lengths of $\sim 2250\ a_0$, however colder temperatures still would be required to observe the large s-wave resonance in this window [153].

The drop in number in figure 6.1(a) displays the atom loss after the 100 ms hold. Fitting the number data with a double Gaussian function we find the resonance position is (553.3 ± 0.7) G, in reasonable agreement with the previous experimental value of (554.06 ± 0.02) G [213]. There is also a peak in the temperature here due to three-body recombination. The peak in number and the minimum in temperature represents the zero in scattering length, where the cross section is zero and hence atom loss and rethermalisation are reduced. From the same fit as above we find that this occurs at (557 ± 1) G, in excellent agreement with the previous measurement of (556.26 ± 0.10) G [153]. We are also able to measure the resonance at (543.6 ± 0.4) G as a small peak in the temperature that has been fit with a Lorentzian function, which is in reasonable agreement with the theoretical value of 544.3 G [209]. The experiment's sensitivity to measure ^{133}Cs resonances at high-field was determined to be sufficient enough for measurement of resonances of similar sizes.

A high-field ^{87}Rb Feshbach resonance

Better confidence in the field stability was achieved by measuring a previously observed Feshbach resonance at the highest fields achievable with the current setup. Although the scattering length of ^{87}Rb is $(102 \pm 6)\ a_0$ at low-fields [214], narrow resonances in the $|1,1\rangle \otimes |1,1\rangle$ entrance channel have previously been measured between 400-1300 G [118]. The resonance at 1007.4 G [215] has a width of (0.21 ± 0.02) G [216] hence proves an excellent resonance to test sensitivity.

To observe the resonance ^{87}Rb in the $|1, +1\rangle$ state was trapped in the dipole trap as discussed in section 4.4.4. Atoms were then evaporated in two linear evaporation ramps, first to 1.013 W in 0.6 s and finally to 630 mW in 1 s. In this potential the trap depth is 7.9 μK and the trap frequencies are $\omega_{\mathrm{rad}} = 2\pi \times 177.2$ Hz and $\omega_{\mathrm{ax}} = 2\pi \times 35.1$ Hz. As the inelastic scattering in ^{87}Rb is much smaller than in ^{133}Cs the background lifetime is longer, hence the atoms can be held in the trap for longer. Here we hold the atoms for 5 s to allow the atoms to come into equilibrium with the potential. The bias field is then switched on in two stages. We first switch on to (1003.17 ± 0.04) G in 10 ms, and then ramp to the field in question in 10 ms. The atoms are allowed to evolve at this field for 100 ms before imaging the atom cloud. Figure 6.2 displays the results of this experiment.

Atom loss and three-body heating of the atom cloud can be used to detect the Feshbach resonance, and the peak density and PSD of the cloud evolve accordingly. A Lorentzian fit to the number data reveals that the resonance position is (1007.6 ± 0.2) G, which is in excellent agreement with the published value of (1007.40 ± 0.04) G. The width of the resonance, obtained from the Lorentzian fit to the data, is measured to be (0.3 ± 0.1) G which is in excellent agreement with the published value of (210 ± 20) mG. It may be noted that the shape of the resonance in figure 6.2 is not Lorentzian in nature however, hence the centre and width measured in this way have a systematic error associated with the calculation. The potential cause of the distortion of the lineshape is due to ramping from low-field to high-field in 10 ms, while at a high PSD. The success of this measurement provided ample confidence in the sensitivity of the experiment to measurements at high-field on Feshbach resonances of a similar width.

6.1.2 Optimisation of high-field ^{133}Cs evaporation

As an extension to the investigation of the efficiency of the evaporation of ^{133}Cs as a function of field in the low-field region we have performed a similar experiment at high bias fields. At low-field it is possible to produce a BEC between 18.1-19.6 G and 20.2-24.8 G. The scattering length in these regions

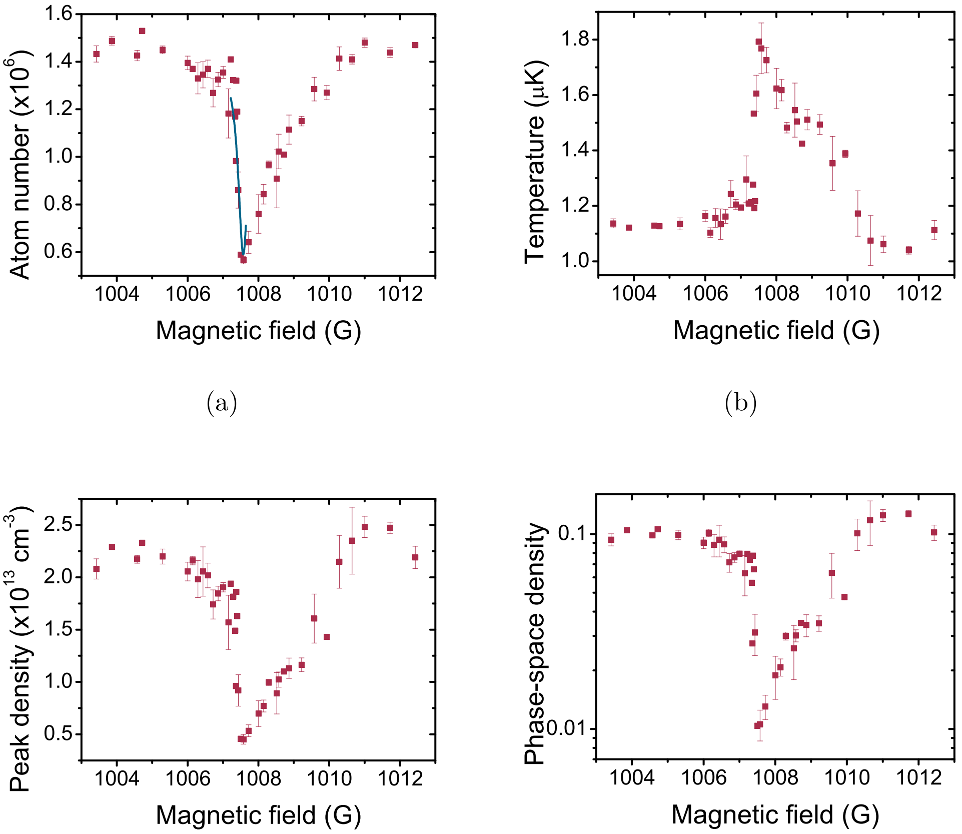

(a) (b)

(c) (d)

Figure 6.2: ^{87}Rb atom number (a), temperature (b), peak-density (c) and PSD (d) after a 100 ms hold at various B-fields between 1003-1013 G. The Feshbach resonance can be observed as a minimum in the number, peak density and PSD, and a maximum in the temperature. A Lorentzian fit to a portion of the data highlighted by the blue line returns a resonance position of (1007.6 ± 0.2) G and a width of (0.3 ± 0.1) G.

varies between 55-400 a_0 [209]. Due to the broad s-wave Feshbach resonance at 786.84 G which is 93.82 G [153] wide the interactions are tunable with a high precision possible. The same range of scattering lengths are present between 883.0-900.5 G, hence a similar precision should be possible as at low-field.

After the ^{133}Cs dipole trap load the bias field is ramped up in 10 ms to (869.76 ± 0.07) G, before the field is ramped in 5 ms to a final value in the range of 860-910 G. At this stage $(2.7 \pm 0.1) \times 10^6$ atoms remain at a temperature of (20.7 ± 0.5) μK and a PSD of $(4.2 \pm 0.8) \times 10^{-4}$. The efficiency of the evaporation is calculated using these values. We then perform three linear plain evaporation ramps, first in 1.9 s to 1.01 W, then to 280 mW in 1 s and to 170 mW in 1.5 s. In this final potential the trap depth is 2.7 μK and the trap frequencies are $\omega_{\text{rad}} = 2\pi \times 86.2$ Hz and $\omega_{\text{ax}} = 2\pi \times 17.0$ Hz. The number, temperature, PSD and evaporation efficiency are displayed in figures 6.3 and 6.4.

In contrast to the data presented in figures 5.4 and 5.5 there are no Feshbach resonances in the high field region, hence there is only one feature in the data which is due to the scattering length zero. The peak in the temperature data is due to the poor rethermalisation at this field. Fitting a Lorentzian function to this peak we find the scattering length zero occurs at a field of (880 ± 1) G, which is in excellent agreement with the theoretical value of 880.66 G. Due to the peak in the temperature a local minimum in the PSD and efficiency are also observed.

The performance of evaporation is observed to increase either side of the minimum as the interactions begin to increase again, at both lower fields where the scattering length is negative and at higher fields where the scattering length is positive. In the region where the scattering length is positive, the region of interest when evaporating to BEC, the optimum efficiency is achieved at (889 ± 1) G where the scattering length is ~ 200 a_0. Previous work reports an optimum field of 894 G where $a \sim 300$ a_0 [217]. Thus far attempts to condense ^{133}Cs at these fields have not yielded a condensate in this apparatus.

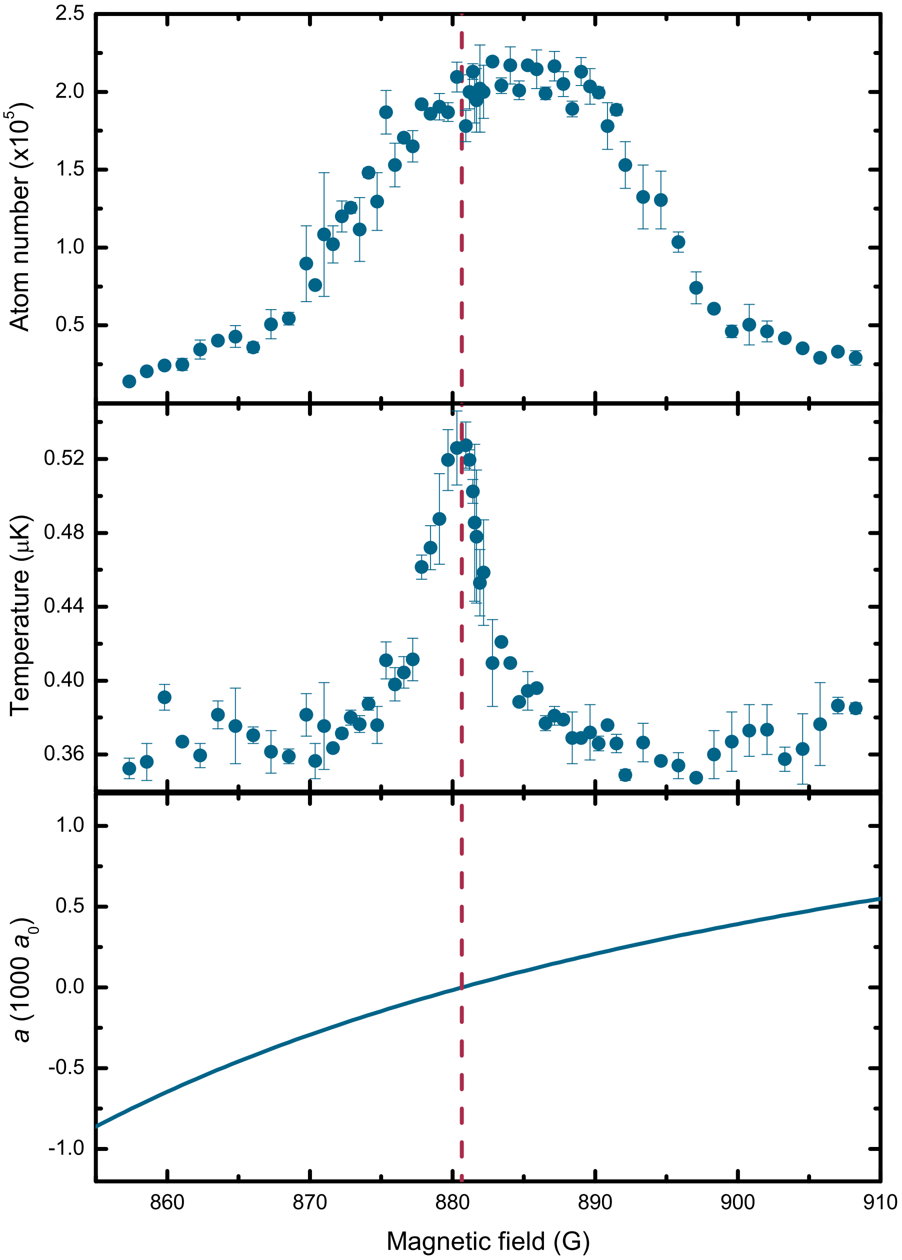

Figure 6.3: ^{133}Cs number remaining and temperature after three plain dipole trap evaporation ramps to beam powers of 170 mW at different magnetic fields between 860 and 910 G. The scattering length is displayed below for reference. The red dashed line indicates the location of the zero in scattering length [209]. There is a peak in the temperature at this field as there is little rethermalisation in the trap.

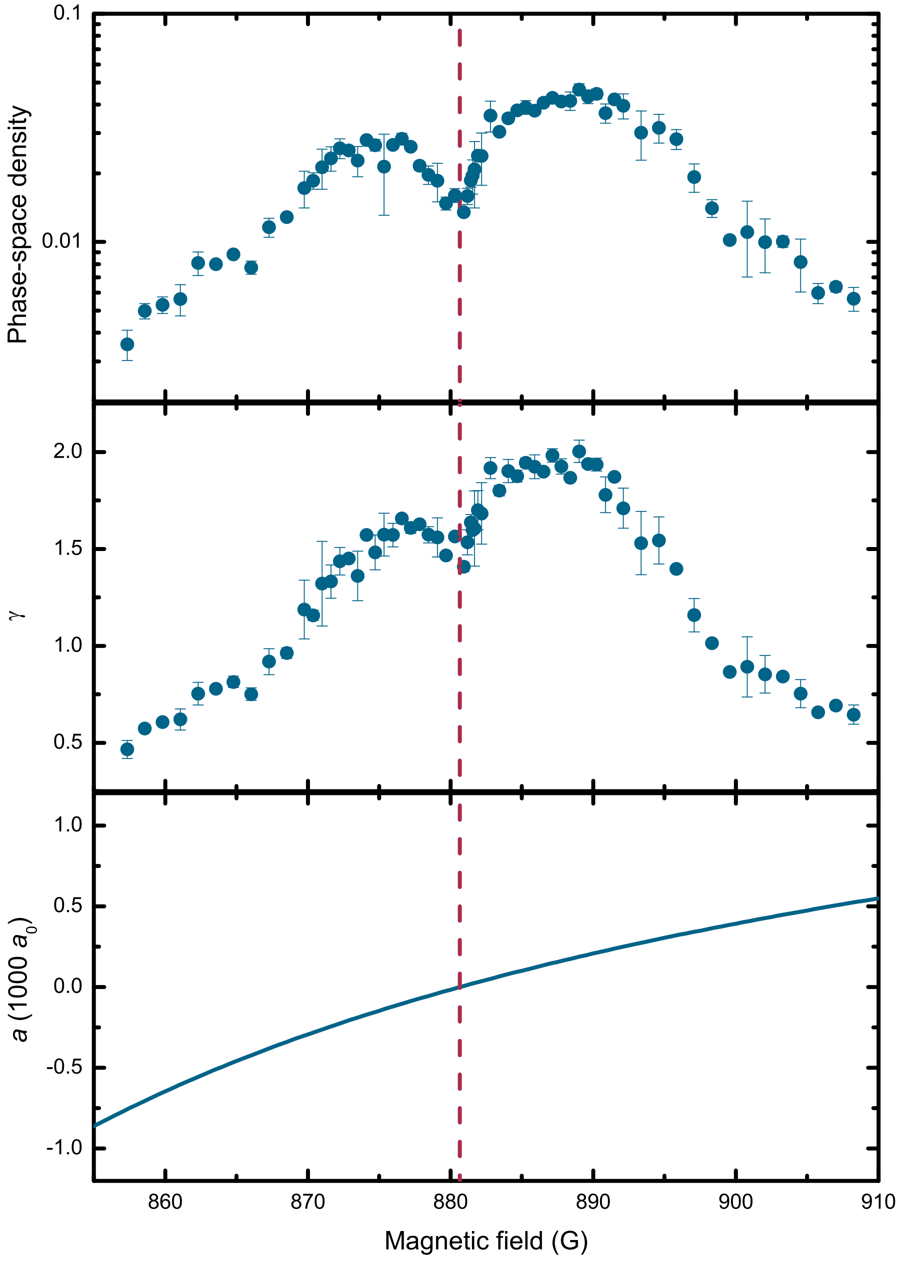

Figure 6.4: PSD of ^{133}Cs and the evaporation efficiency after three plain dipole trap evaporation ramps to beam powers of 170 mW at different magnetic fields between 860 and 910 G. The scattering length is displayed below for reference. The red dashed line indicates the location of the zero in scattering length [209]. At this field the rethermalisation is poor, hence the temperature is high, and conversely the PSD and γ are low here.

6.2 Two-species results

Here we discuss the observation of interspecies ^{87}Rb^{133}Cs Feshbach resonances. Initially the sensitivity of the system to the effects of the resonances was tested by observing resonances that have previously been observed in this apparatus [167] and in other work [72]. This is discussed in section 6.2.1, before observation of previously unmeasured resonances is discussed in section 6.2.2. Feshbach resonances in a ^{85}Rb^{133}Cs mixture are discussed in chapter 7.

In principle the procedure for observing interspecies Feshbach resonances is the same as for intraspecies resonances. A high PSD mixture is required, which can be achieved via the plain evaporation method, and interspecies three-body losses are enhanced around an interspecies Feshbach resonance, so a resonance generally manifests itself as a reduction in number in the system. The difference in the procedures utilised depends on the interaction of the two atoms and their relative numbers. A better signal-to-noise ratio is generally achieved if there is an imbalance in the number of each species present in the trap [218]. In this scenario the majority species (here we use ^{87}Rb as the majority species) acts as a collisional bath for the probe species (^{133}Cs in the case of this work). Thus in the vicinity of a Feshbach resonance the number of the buffer species is reasonably unchanged, whereas the probe species is depleted significantly. To achieve this imbalance in number the amount of ^{133}Cs loaded into the magnetic trap is controlled using the MOT repump light servo circuit. Another advantage to using ^{87}Rb as the majority species is that the trap depth at a given beam power is shallower for ^{87}Rb than ^{133}Cs as described in chapter 5, hence ^{87}Rb can sympathetically cool ^{133}Cs. Another feature of this system is the large background interspecies scattering length ($\sim 650\ a_0$), which is large, resulting in rapid loss of the minority species [12], hence we reduce the beam powers much faster when measuring ^{87}Rb^{133}Cs Feshbach resonances.

6.2.1 Low-field interspecies Feshbach resonances

Prior to the improvements made to the experiment as detailed in chapter 3 an interspecies ^{87}Rb^{133}Cs Feshbach resonance was observed in the current apparatus [167]. The effects that the improvements to the total atom number, the reproducibility of the atom number and the stability of the bias field have had on the system were possible to quantify by measuring the resonance again. After loading ^{87}Rb and ^{133}Cs into the dipole trap at beam powers of 4.05 W the power was decreased logarithmically in 500 ms to 250 mW. This evaporation took place at (22.91 ± 0.02) G. The field was then switched in 10 ms to (176.68 ± 0.01) G before ramping to the final field in 5 ms and holding in the potential at this field for 500 ms. The fraction of ^{133}Cs atom number remaining after the 500 ms hold in comparison to the number remaining off resonance as a function of field is displayed in figure 6.5. The temperatures away from the resonance are $T_{\mathrm{Rb}} = (0.79 \pm 0.01)$ μK and $T_{\mathrm{Cs}} = (0.78 \pm 0.02)$ μK, and the ^{133}Cs number here is $\approx 5 \times 10^4$ atoms, with approximately an order of magnitude more ^{87}Rb atoms.

Fitting a Lorentzian function to the data in figure 6.5 we measure the pole of the resonance to be at (181.55 ± 0.05) G. This is in reasonable agreement with other published values of (181.64 ± 0.08) G [72, 121]. The width of the fit is (0.45 ± 0.07) G, however the width is in general defined as the difference in field between the pole of the resonance and the zero in scattering length. At the pole the scattering length diverges, represented experimentally by a reduction in atom number, and at the zero in scattering length there is a maximum in atom number as the three-body losses are minimised. Hence the width of a Lorentzian fit is not a true representation of the width. No clear peak in atom number is visible in the data hence we cannot measure the zero in scattering length in this way.

This data represents a significant improvement in both number and magnetic field stability over previous measurements with this apparatus. The data points in figure 6.5 are averages of two shots, whereas previously five shots were required to allow similar confidence in precision. The previous measurement taken with this equipment is presented in figure 6.6. We also note that magnetic field noise has significantly decreased as the width of the

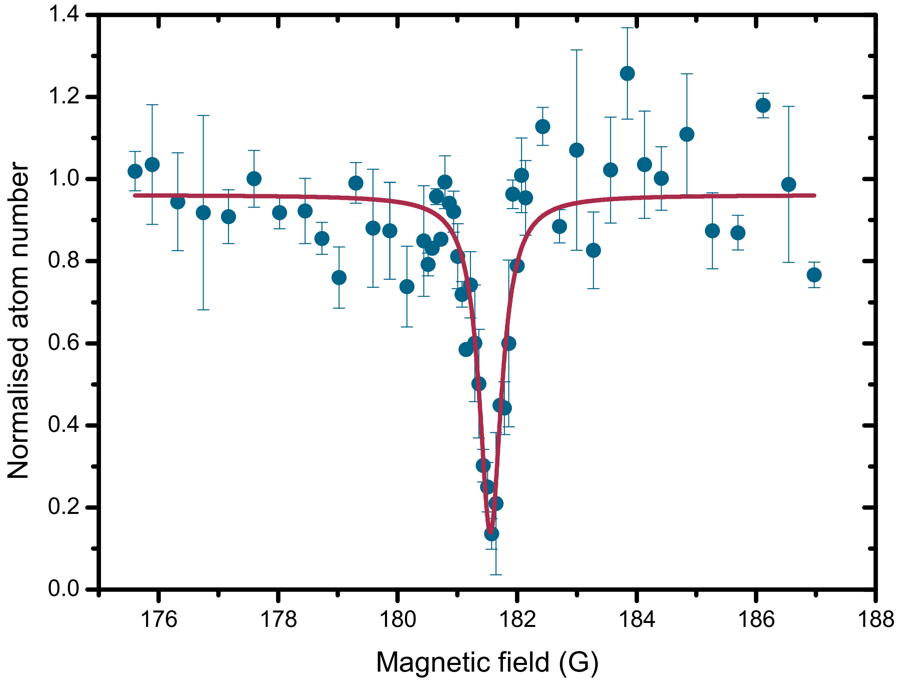

Figure 6.5: Fraction of ^{133}Cs atoms remaining after a 500 ms hold at different magnetic fields. The m_F states used are $|1,+1\rangle$ and $|3,+3\rangle$ for ^{87}Rb and ^{133}Cs respectively. The number remaining is normalised to the number remaining off resonance. The ^{133}Cs number off resonance is $\approx 5 \times 10^4$. The line indicates a Lorentzian fit to the data resulting in a resonance position of (181.55 ± 0.05) G and a width of (0.45 ± 0.07) G.

resonance has decreased from ≈ 3 G to ≈ 0.5 G.

The improvement in field and number stability is a significant advancement in the performance of the apparatus, hence an observation of a narrower resonance was made. Another published resonance exists nearby [121] at a magnetic field of (197.06 ± 0.05) G and with a width of (0.09 ± 0.01) G. The width is calculated as the difference in magnetic field between the loss maximum and minimum. Clearly with the resonance being narrower it allows a better determination of the bias field stability. The same experimental procedure was used to observe the resonance as detailed in the above. The normalised number of ^{133}Cs remaining after the 500 ms hold as a function of field is displayed in figure 6.7 for this field region.

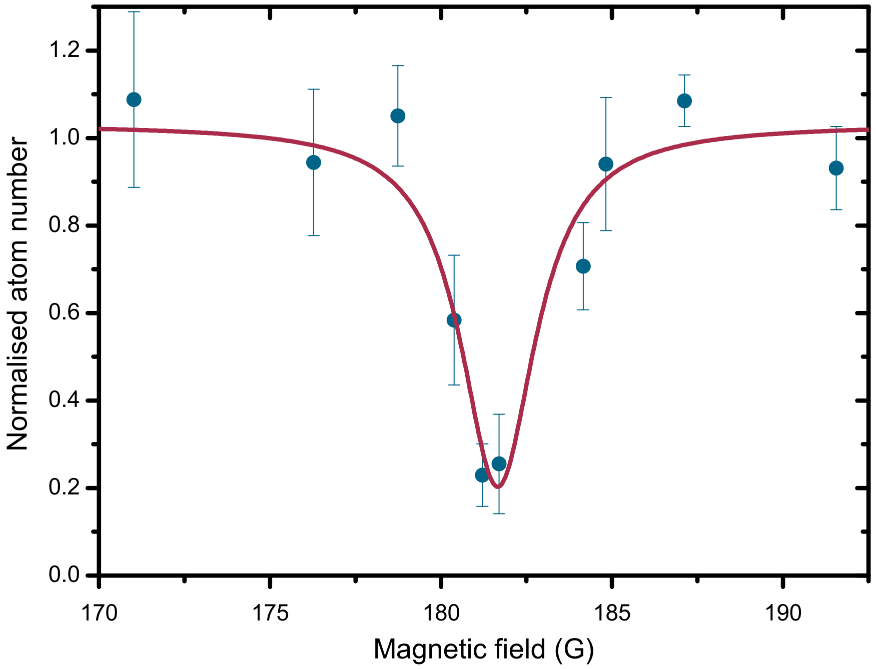

Figure 6.6: Previous measurement with this apparatus of the Feshbach resonance at ≈ 182 G, observed via atom loss measurements. Data points represent an average of 3-5 individual shots. The Lorentzian fit to the data returns a width of ≈ 3 G.

The data were fit with a double Gaussian function and the centre of the resonance is measured to be at (197.10 ± 0.03) G, in excellent agreement with the previously published value of (197.06 ± 0.05) G [121]. The width of the fit was (0.09 ± 0.01) G and is in excellent agreement with previous data. The zero in scattering length can be observed in this data as the small increase in normalised ^{133}Cs number at a slightly higher field than the decrease in number. The fit reveals the scattering length zero to be at (197.2 ± 0.1) G, also in excellent agreement with the past result of (197.15 ± 0.05) G. This value implies a width of (0.1 ± 0.1) G, in agreement with the value calculated by the fit. The ability to measure a feature of this width indicates that the bias field stability here is better than ≈ 0.01 G, however, in the trap $\sigma_{\mathrm{h}} \approx 6$ μm and $\sigma_{\mathrm{v}} \approx 1$ μm, which means the field spread sampled by the cloud is approximately 0.01 G and 0.003 G in the

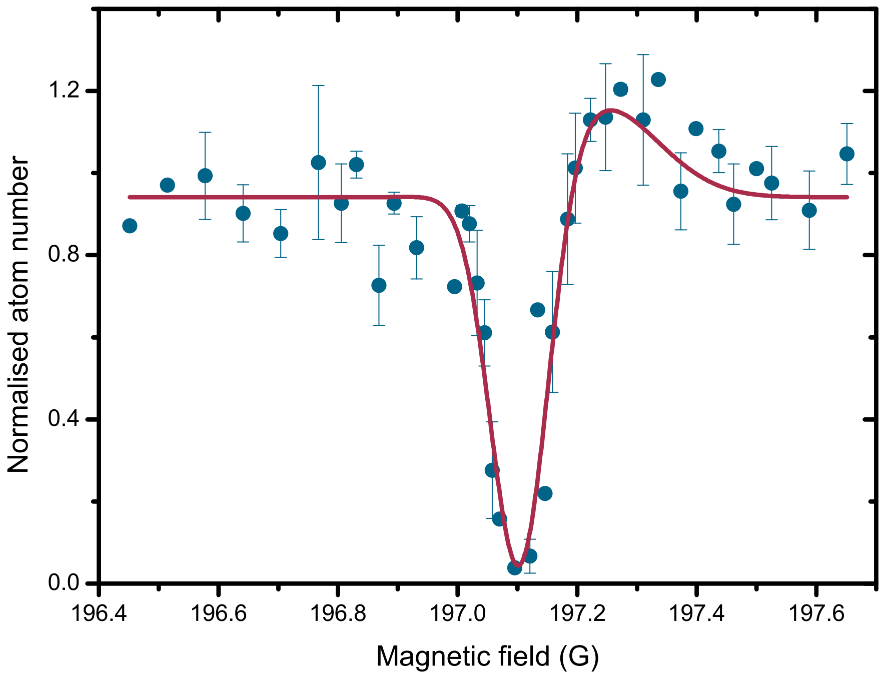

Figure 6.7: Fraction of ^{133}Cs atoms remaining after a 500 ms hold at different magnetic fields. The m_F states used are $|1, +1\rangle$ and $|3, +3\rangle$ for ^{87}Rb and ^{133}Cs respectively. The number remaining is normalised to the number remaining off resonance. The ^{133}Cs number off resonance is $\approx 5\times10^4$. The resonance position is measured to be at (197.10±0.03) G and has a width of (0.1±0.1) G. A small peak in the ^{133}Cs number can also be observed, the centre of which is measured to be (197.2 ± 0.1) G. These data were fit using a double Gaussian function (purple line).

horizontal and vertical directions, respectively. It is therefore impossible to tell whether the measurement of the width is limited by the bias field stability or the field spread. In principal any Feshbach resonance may be used to associate molecules via the magnetic field ramping technique [51], however the resonance at $\approx$ 182 G has previously been successfully used for Feshbach association of ^{87}Rb^{133}Cs molecules [109]. This resonance would be a good starting point for future association of Feshbach molecules.

The two interspecies Feshbach resonances already presented are reasonably narrow. Previously unobserved resonances of similar widths have been predicted to occur at high-field [209] however there are also two large resonances predicted at fields of ~ 792 G (width ~ 4 G) and ~ 1116 G (width ~ 9 G). As a precursor to measuring these resonances another previously reported resonance was observed, published as being located at (352.65 ± 0.34) G which has a width of (2.70 ± 0.47) G [121].

To measure this resonance a slightly different experimental method was applied. As the bias field is increased the atoms sample a range of magnetic fields and thus scattering lengths, hence potential for three-body recombination heating is increased. If the evaporation is performed at low-field in this system prior to increasing the field to the field range of interest, due to the reduced trap depths we find that atom loss on jumping to high-fields is increased. One method to combat this would be to adiabatically compress the trap, however we find the increase in cloud temperature detrimental to measurements. Thus we jump the magnetic field to (337.78 ± 0.01) G in 10 ms and then jump to the final field in 5 ms and evaporate at this field by reducing the beam powers logarithmically in 500 ms to powers of 250 mW. After a 500 ms hold the number of ^{133}Cs and ^{87}Rb atoms remaining was recorded, as displayed in figures 6.8(a) and (b) respectively, normalised to the off resonance numbers. Off resonance $(2.9 \pm 0.1) \times 10^5$ ^{87}Rb atoms remain at a temperature of (0.698 ± 0.003) μK and $(3.7 \pm 0.2) \times 10^4$ ^{133}Cs atoms remain at a temperature of (0.66 ± 0.01) μK.

The method of evaporating the atoms at various fields yields different information to experiments where the atoms are simply held in the same potential at various fields. We can see from figure 6.8 that the remaining number of ^{133}Cs atoms is reduced at the pole of the Feshbach resonance, a fit to the data reveals that the pole is located at (352.7 ± 0.4) G, in excellent agreement with the published value [121]. The zero in scattering length is noticeably highlighted by the peaks in both the ^{133}Cs and ^{87}Rb numbers, measured to be (355.7 ± 0.3) G using the ^{133}Cs number data, and (355.3 ± 0.3) G using the ^{87}Rb data. The ^{133}Cs data was fitted using a double Lorentzian function and the ^{87}Rb number was fitted using a Lorentzian function in the region highlighted by the blue line in figure 6.8(a). The reason the ^{87}Rb number shows a large increase where the interspecies scattering length is low is that ^{87}Rb is sympathetically cooling ^{133}Cs during the evaporation sequence, hence when there are no ^{87}Rb^{133}Cs interactions the heat load on the ^{87}Rb atoms is

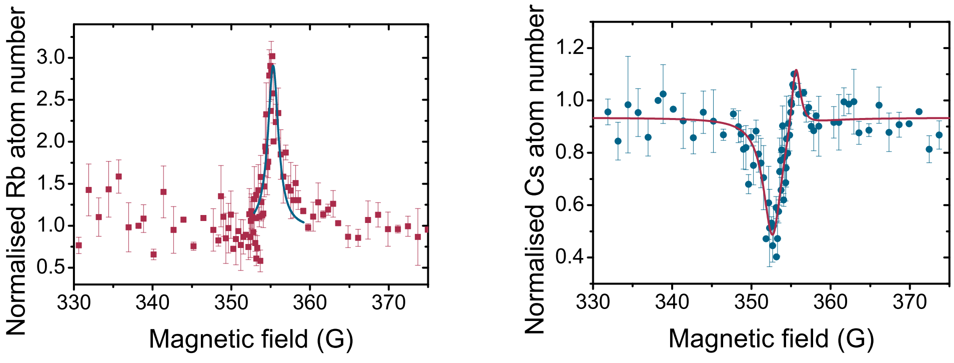

(a) (b)

Figure 6.8: Fraction of ^{87}Rb (a) and ^{133}Cs (b) atoms remaining after a 500 ms hold at different magnetic fields. The m_F states used are $|1, +1\rangle$ and $|3, +3\rangle$ for ^{87}Rb and ^{133}Cs respectively. The number remaining is normalised to the number remaining off resonance. The off resonance ^{87}Rb atom number is $(2.9 \pm 0.1) \times 10^5$ and the ^{133}Cs number off resonance is $(3.7 \pm 0.2) \times 10^4$. The pole of the resonance is measured to be at (352.7 ± 0.4) G, taken from the drop in the ^{133}Cs number, and the zero in scattering length, which can be seen as a peak in the ^{133}Cs and number, is measured at (355.7 ± 0.3) G. Alternatively, fitting the peak in the ^{87}Rb number reveals that the scattering length zero is located at (355.3 ± 0.3) G. The solid lines indicate fits to the data.

removed, resulting in more efficient cooling. The fit to the ^{133}Cs data yields a resonance width of (3.0 ± 0.5) G, in excellent agreement with the published value. The observation of this resonance indicated that performing a similar experimental routine would be adequate to measure the resonance at ~ 790 G.

6.2.2 High-field interspecies Feshbach resonances

The following results represent resonances that have not previously been measured, hence to locate them theoretical predictions were used to navigate the Feshbach resonance search [219]. Feshbach resonances in a ^{87}Rb^{133}Cs mixture have only been measured up to bias fields of ~ 670 G and the theory reports that there are six more resonances of widths larger than 1 mG within the operational range of the apparatus used here. These can be seen in figure 2.4. Three of the resonances are located within (800 ± 10) G, however observation of resonances in this region is complicated by the similarly rich ^{133}Cs Feshbach spectrum here, with the large s-wave resonance at 786.84 G and an additional d-wave resonance at 820.1 G. Figure 6.9 presents the intra- and interspecies scattering length in more detail.

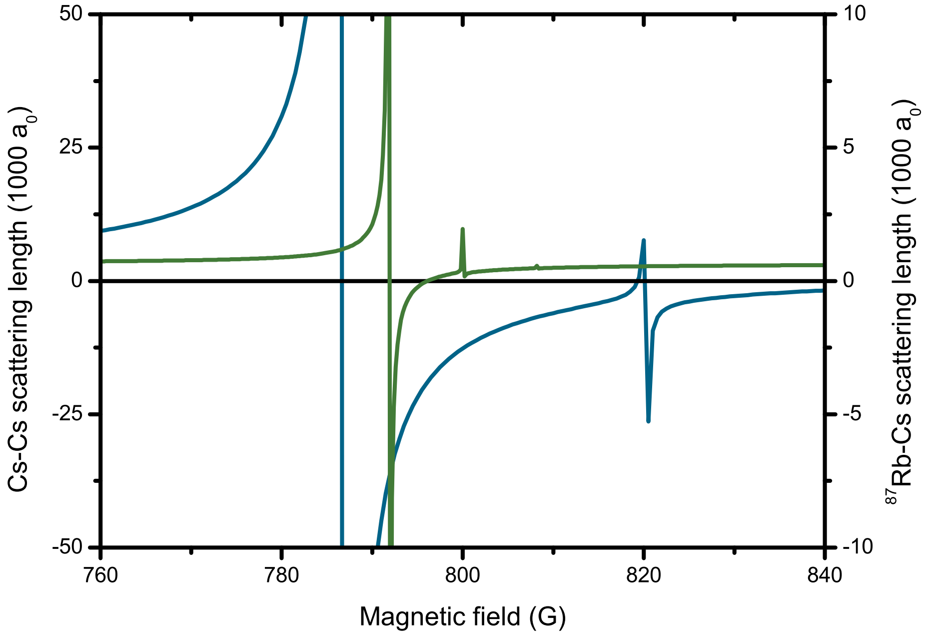

Figure 6.9: ^{133}Cs (blue) and ^{87}Rb^{133}Cs (green) scattering length between magnetic fields of 760 G and 840 G. Three interspecies resonances exist at fields of 791.7 G, 799.8 G and 808.0 G and two intraspecies ^{133}Cs resonances are located at 786.8 G and 820.1 G [209]. Note the difference in the vertical axes' scales.

To measure the interspecies resonances in this region the mixture was cooled in the dipole trap at a fixed magnetic field of (784.04 ± 0.09) G. One stage of evaporation was used, which involved a 500 ms logarithmic ramp to beam powers of 250 mW. In 5 ms the bias field was ramped to a final value and the atoms were held at this field for 500 ms. The number of ^{133}Cs atoms remaining after the hold at off resonance fields was $(1.64 \pm 0.07) \times 10^4$ and the number of ^{87}Rb atoms remaining was $(8.4 \pm 0.4) \times 10^4$. Off resonance the temperature of the ^{133}Cs atoms was (0.473 ± 0.004) μK and of the ^{87}Rb atoms it was (0.513 ± 0.002) μK. The results of this experiment are presented in figure 6.10.

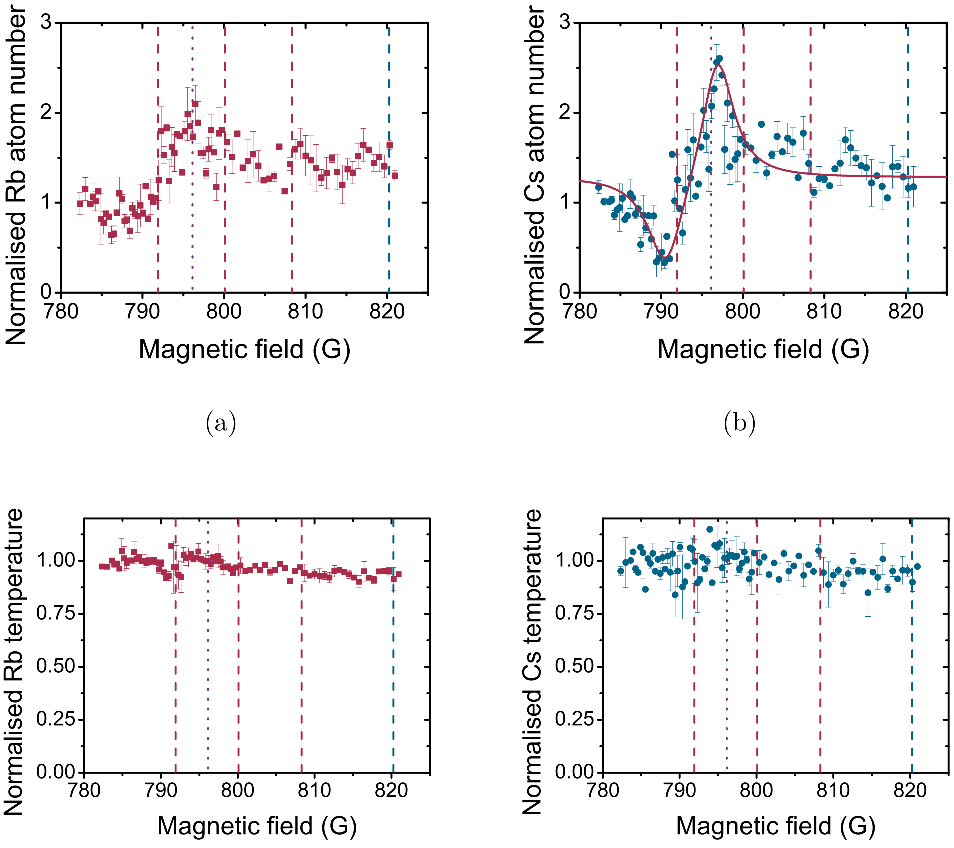

(a) (b)

(c) (d)

Figure 6.10: Atom number remaining (a,b) and temperature (c,d) after a 500 ms hold at various magnetic fields after dipole trap evaporation at (784.04 ± 0.09) G for ^{87}Rb (a,c) and ^{133}Cs (b,d). The red dashed lines indicate the theoretical locations of interspecies resonances, and the zero crossing in scattering length of the largest of these is marked by the purple dotted line. There is also a ^{133}Cs resonance located in this field range at 820.4 G which is highlighted by the blue dashed line. This resonance wasn't observed and likewise for two of the interspecies resonances. Both the pole and the zero scattering length position of the largest interspecies resonance can be observed. All values are normalised to an off resonant point. The red solid line indicates the fit used to determine the resonance and zero in scattering length.

Only two of the predicted features can be observed in figure 6.10, the pole and the zero crossing of the large resonance. The two smaller predicted resonances at 799.8 G and 808.0 G (of width 74 mG and 5 mG respectively) were not observed above the noise on the data. The detectable features can only be detected clearly in the number data for ^{133}Cs whereas the ^{87}Rb number data do indicate that a feature is present but not as clearly. The temperature data for each species also lack any clear evidence of a feature. A double Lorentzian fit to the peaks in the ^{133}Cs number data reveal that the pole of the resonance and the zero crossing of the scattering length are located at fields of (790.6 ± 0.8) G and (796.9 ± 0.4) G, respectively. The location of the pole of the resonance is in reasonable agreement with the theoretical value, however the location of the scattering length zero is in disagreement. The calculated width of the resonance is (6.3 ± 0.9) G which is 2.1 G wider than predicted.

Although the scattering length zero position is in disagreement with the theoretical prediction, there is scope for small changes to the theory as the prediction involves extrapolation based on lower field Feshbach resonance locations measured in other apparatus [72, 121]. Likewise, the fact that the narrower resonances weren't observed is not proof of non-existence, clearly the field step sizes are not small enough to rule out their existence as they are very narrow. It is also possible that they aren't distinguishable above the noise.

To rule out single-species effects being responsible for the features observed in figure 6.10 a single-species scan of ^{133}Cs in this region was performed. Note that the fact that the data for ^{87}Rb appear to indicate a feature confirms that the feature is a two-species effect, however better proof involves repeating the experiment with ^{133}Cs alone in the dipole trap. A near identical experiment was performed, however the dipole trap beams were ramped to lower powers in order for the final temperature to be the same as in the two-species case. The final power used was 200 mW where the ^{133}Cs trap depth is 3.4 μK and the trap frequencies are $\omega_{\text{rad}} = 2\pi \times 93.0$ Hz and $\omega_{\text{ax}} = 2\pi \times 19.4$ Hz. The temperature after the 500 ms hold off resonance was (0.497 ± 0.002) μK and the atom number remaining was typically $(5.95 \pm 0.04) \times 10^4$. The ^{133}Cs number remaining after the 500 ms hold is displayed in figure 6.11, normalised to an off resonant point.

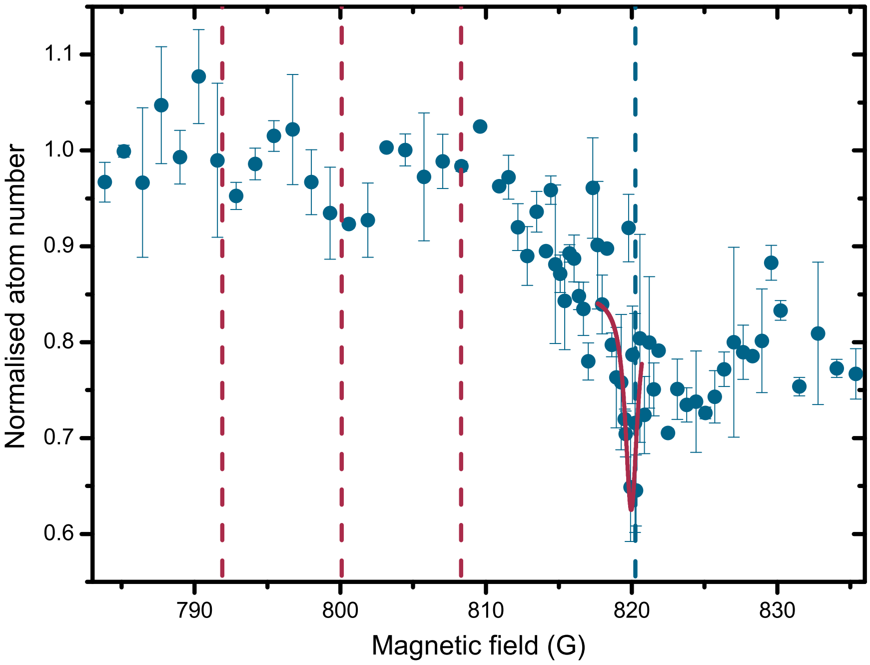

Figure 6.11: ^{133}Cs atom number remaining after a 500 ms hold at magnetic fields identical to those in figure 6.10 after dipole trap evaporation at (780.38 ± 0.04) G. The red dashed lines indicate the theoretical locations of interspecies resonances and the blue dashed line indicates the previous experimental value for the resonance's location [153]. No features can be observed where the two-species effects were observed. All values are normalised to an off resonant point. The number remaining off resonance is $(5.95 \pm 0.04) \times 10^4$. The solid red line indicates the Lorentzian fit used to determine the resonance location.

The data reveal the existence of the *d*-wave Feshbach resonance at a field of (820.0 ± 0.3) G. This is in excellent agreement with the theoretical and previous experimental values of 820.1 G [209] and (820.37 ± 0.22) G [213]. The presence of the resonance is indicated by the loss of atom number at the resonance location, no feature was revealed in the temperature data. It is also not possible to observe the zero crossing of the scattering length, where, in theory, there should be a larger atom number. The loss minimum has been measured before as being at (819.41 ± 0.02) G [153]. This is potentially because the atom number is comparatively low and accordingly the peak density will be also. This results in fewer collisions than the case where ^{87}Rb is present. Most importantly, there are no features present at lower magnetic fields than this resonance, hence we believe that the peaks in figure 6.10 are two-species related.

Locating the predicted ^{87}Rb^{133}Cs Feshbach resonance at 909 G perhaps provides a better confirmation of the theoretical model as it is narrower and hence easier to define its location. However since the predicted and measured values of the pole and zero of the resonance in the 790 G region were in disagreement by ≈ 2 G a search over a wide range for a narrow feature would possibly be required. To increase the possibility of observing the feature the bias field was sampled using ramps of (0.13 ± 0.01) G over a 2 s period. Prior to this field sampling the dipole trap beams were logarithmically ramped to powers of 370 mW in 500 ms at a bias field of (898.03 ± 0.01) G. The field was then jumped in 5 ms to the field in question and then the field was increased linearly by 0.13 G in 2 s as discussed. In the final potential the trap depth is 4.7 μK (6.4 μK) and the trap frequencies are $\omega_{\mathrm{rad}} = 2\pi \times 135.9$ Hz ($\omega_{\mathrm{rad}} = 2\pi \times 128.0$ Hz) and $\omega_{\mathrm{ax}} = 2\pi \times 26.9$ Hz ($\omega_{\mathrm{ax}} = 2\pi \times 23.8$ Hz) for ^{87}Rb (^{133}Cs).

A fit to the data in figure 6.12 reports a value of (910.3 ± 0.2) G for the pole of the resonance. This is in disagreement with the theoretical value as it is 1.06 G higher than predicted. A width can't be extracted from the data as the zero crossing of the scattering length can't be detected, and additionally we are scanning a range of fields. The temperature data for this measurement didn't reveal any information as only noise was visible, likewise for both the ^{87}Rb number and temperature data. Due to the nature of the width of this resonance and the detection method employed it is difficult to draw conclusions on the validity of the theoretical model. Similarly, for the predicted 39 mG wide resonance at 1033.6 G detection is difficult, and at present successful observation hasn't been achieved after a search of a 5 G window.

Of the predicted interspecies resonances the one at the highest field within range of the apparatus is predicted to be located at 1116.5 G. This is a large 8.9 G wide s-wave resonance, comparable to those at ~ 350 G and ~ 791 G,

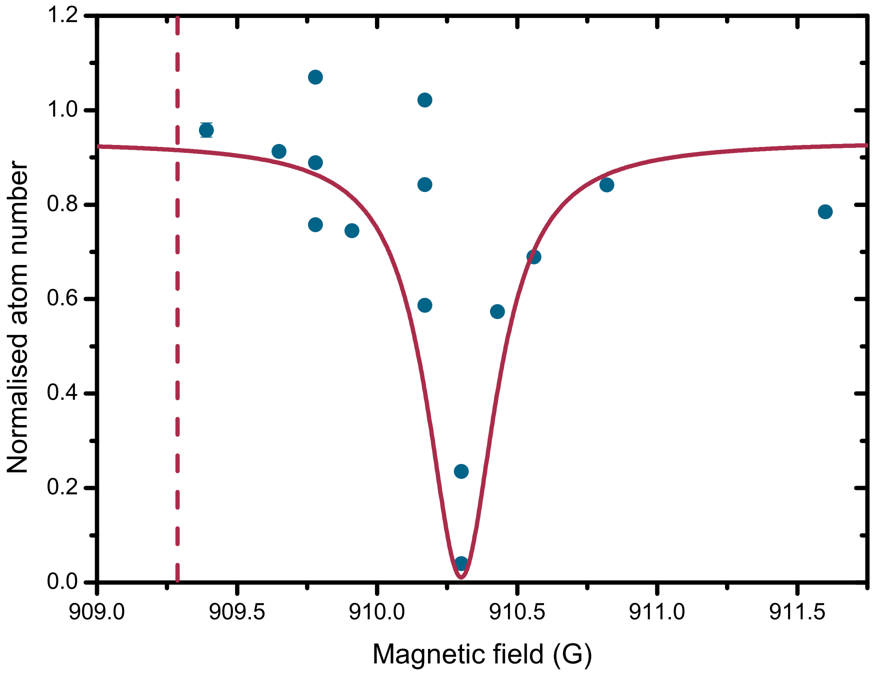

Figure 6.12: Normalised ^{133}Cs atom number remaining after a (0.13 ± 0.01) G magnetic field ramp over 2 s at various fields. The $x-$axis represents the centre of the field sweep. The red dashed line indicates the theoretical location of the predicted interspecies resonance and the red solid line represents the Lorentzian fit to the data. The number remaining off resonance is $(1.3 \pm 0.1) \times 10^4$.

so a similar detection method was applied, with two variations being used for measurements at different temperatures. For the initial measurement the bias field was switched on to (1127.8 ± 0.4) G and the dipole trap beams were logarithmically ramped to 370 mW in 500 ms. The trap depths in this potential are 4.7 μK (6.4 μK) for ^{87}Rb (^{133}Cs) and the frequencies are $\omega_{\rm rad} = 2\pi \times 135.9$ Hz ($\omega_{\rm rad} = 2\pi \times 128.0$ Hz) and $\omega_{\rm ax} = 2\pi \times 27.6$ Hz ($\omega_{\rm ax} = 2\pi \times 25.3$ Hz) for ^{87}Rb (^{133}Cs).

The field was then ramped in 5 ms to the measurement value, and the atoms were imaged after a 500 ms hold. The temperature of the atoms away from the resonance was (0.804 ± 0.005) μK for ^{87}Rb and (0.773 ± 0.008) μK for ^{133}Cs, and the remaining atom numbers were $(8.4 \pm 0.5) \times 10^4$ and $(3.6 \pm 0.6) \times$

10^4 for ^{87}Rb and ^{133}Cs respectively. The second measurement was almost identical, except the evaporation took place at a field of (1137.22 ± 0.04) G and the beams were ramped down to powers of 250 mW. Again the trap depths and frequencies for this beam power have been reported earlier. The atoms were then held at the measurement field for 300 ms. As a consequence of the lower beam power the temperature of the atoms off resonance was lower, (0.416 ± 0.004) μK for ^{87}Rb and (0.390 ± 0.003) μK for ^{133}Cs, and the number ratio was slightly different, with $(7.2 \pm 0.6) \times 10^4$ ^{87}Rb atoms remaining and $(2.19 \pm 0.06) \times 10^4$ ^{133}Cs atoms left in the trap. The results of the two experiments are displayed in figures 6.13 and 6.14.

Figure 6.13 clearly reveals a drop in ^{133}Cs number around the pole of the interspecies Feshbach resonance. A Gaussian fit to the data reveals the pole to be located at (1116 ± 1) G and the zero in scattering length is at a magnetic field of (1126 ± 1) G. This results in a calculated width of (10 ± 1) G. The location of the pole is in excellent agreement with the theoretical prediction of 1116.5 G, whereas the width is in reasonable agreement with the prediction of 8.9 G. Interestingly rethermalisation effects can also be seen in the temperature. In the location of increased scattering length around the resonance pole the ^{133}Cs temperature is reduced by a factor of ≈ 1.3. This is very close to the expected ratio between the ^{133}Cs and ^{87}Rb trap depths of 1.35. Therefore it is believed that due to the increased collision rate close to the resonance the increase in collisions leads to sympathetic cooling of the ^{133}Cs atoms. Another feature in the data is the rather broad region of high number loss around the pole of the resonance. It is believed that due to the finite temperature of the cloud the collision rate is in the unitarity limit here. Following from the arguments in section 6.1 but using the reduced mass of the ^{87}Rb^{133}Cs system to calculate the mean relative velocity and the wavevector, the limit of $ka = 1$ is reached at $a = 1800\ a_0$ for $T = 0.8\ \mu$K and at $a = 2500\ a_0$ for $T = 0.4\ \mu$K, the two experimental temperatures described above. From the theoretical calculations of the scattering length the magnitude of the scattering length is above the limit of $a = 1800\ a_0$ for magnetic fields between 1111.4 G and 1118.9 G. This 7.5 G range is similar to the size of the broadened region of number loss in figure 6.13, hence we believe the mixture to be unitarity limited in this region, and this makes

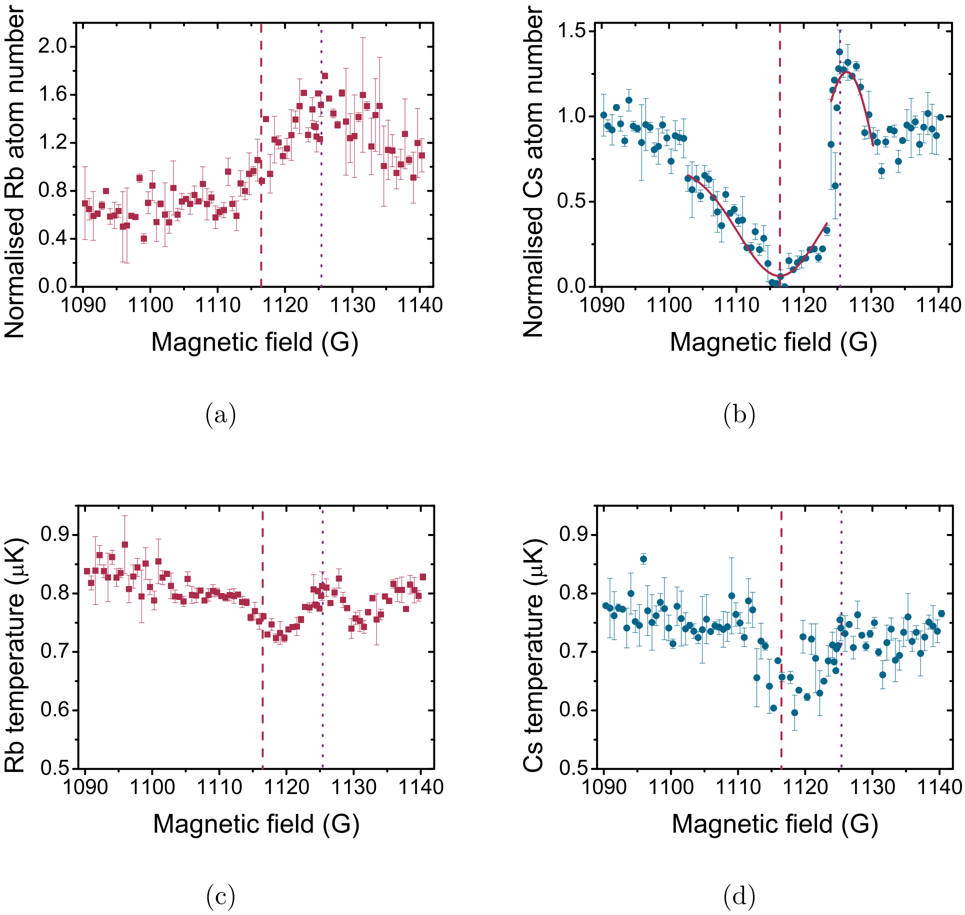

Figure 6.13: Atom number remaining (a,b) and temperature (c,d) after a 500 ms hold at various magnetic fields after dipole trap evaporation at (1127.8 ± 0.4) G for ^{87}Rb (a,c) and ^{133}Cs (b,d). The pole of the resonance can be seen in the ^{133}Cs number data, and the location of the scattering length zero can be seen in the number data for both ^{87}Rb and ^{133}Cs. The temperature data for ^{133}Cs indicates that a region of better rethermalisation exists as the ^{133}Cs temperature is reduced after rethermalisation with ^{87}Rb which has a smaller trap depth than the ^{133}Cs which is sympathetically cooled. The red dashed lines indicate the theoretical location of the interspecies resonance, and the zero in scattering length is marked by the red dotted lines. The red solid lines indicate the Gaussian fits used to measure the locations of the features. The atom numbers are normalised to an off resonant point.

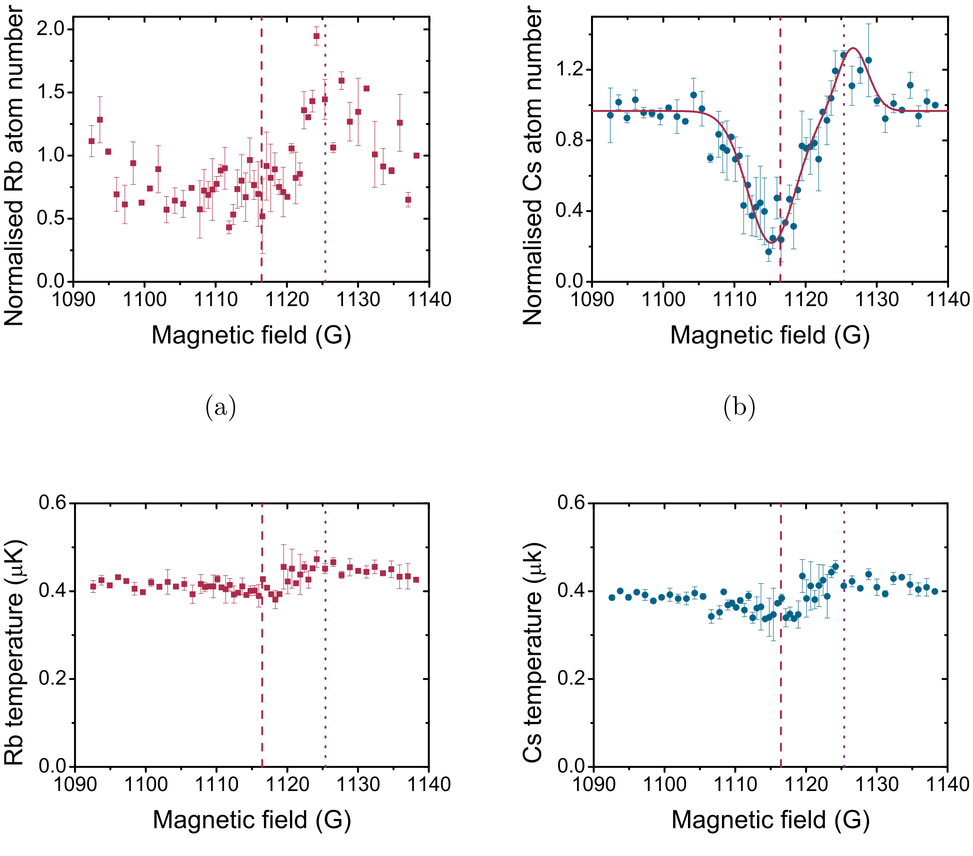

(a) (b)

(c) (d)

Figure 6.14: Atom number remaining (a,b) and temperature (c,d) after a 300 ms hold at various magnetic fields after dipole trap evaporation at (1137.22 ± 0.04) G for ^{87}Rb (a,c) and ^{133}Cs (b,d). Note the lower temperature than in figure 6.13 due to the lower beam powers used. The pole of the resonance can be seen in the ^{133}Cs number data, and the location of the scattering length zero can be seen in the number data for both ^{87}Rb and ^{133}Cs. The temperature data does not clearly indicate any features. The purple dashed lines indicate the theoretical location of the interspecies resonance, and the zero in scattering length is marked by the blue dashed line. The solid red lines indicate the double Gaussian function used to fit the data. All number values are normalised to an off resonant point.

precise determination of the resonance's pole difficult.

For a mixture of ^{87}Rb^{133}Cs at a temperature of 0.4 μK the unitarity limit is reached at scattering lengths of 2500 a_0, which is the case for a magnetic field range of 1113.3 G to 1118.3 G, 5 G wide. We see from figure 6.14 that there is no region in which atom loss that is broadened, hence the limit is not observed in the mixture at this temperature. A double Gaussian fit to the data returns a resonance pole location of (1115.2 ± 0.8) G and a zero scattering length location of (1127 ± 1) G, hence a width of (12 ± 1) G is calculated. The locations of the pole and the scattering length zero are in reasonable agreement with the theoretical predictions, however the calculated width is not. The values are, however, more reliable than the values measured at higher temperature as there is no saturation of atom number loss due to unitarity effects.

The above presents a number of interspecies Feshbach resonances observed in a ^{87}Rb^{133}Cs mixture in our apparatus, some of which have been observed previously, and other high-field resonances which have previously only been predicted. Tables 6.1-6.3 review the different resonances that have been presented in this chapter. A natural extension to the work involves observing resonances in a mixture of ^{85}Rb^{133}Cs, results regarding this follow in the next chapter.

(a) Resonance location

This work		Experimental		Theory
B (G)	ΔB (G)	B_{expt} (G)	ΔB_{expt} (G)	B_{theory} (G)
(1007.6 ± 0.2)	(0.3 ± 0.1)	(1007.40 ± 0.04)	(0.21 ± 0.02)	1008.5

(b) Scattering length zero location

This work	Experimental	Theory	
B (G)	B_{expt} (G)	B_{theory} (G)	ΔB_{theory} (G)
-	(1007.60 ± 0.03)	1008.67	0.17

Table 6.1: Measured resonance location and width (a) of the high-field intraspecies ^{87}Rb Feshbach resonance observed in this and previous work [118, 215, 216]. The location of the zero in scattering length is also presented (b).

(a) Resonance locations

This work		Experimental		Theory
B (G)	ΔB (G)	B_{expt} (G)	ΔB_{expt} (G)	B_{theory} (G)
(543.6 ± 0.4)	-	-	-	544.3
(553.3 ± 0.7)	-	(554.06 ± 0.02)	(0.33 ± 0.03)	554.3
(820.0 ± 0.3)	-	(820.37 ± 0.22)	(1.0 ± 0.2)	820.1

(b) Scattering length zero locations

This work	Experimental	Theory
B (G)	B_{expt} (G)	B_{theory} (G)
(557 ± 1)	(556.26 ± 0.10)	556.19
-	(819.41 ± 0.02)	819.36
(880 ± 1)	(880.9 ± 0.3)	880.66

Table 6.2: Measured resonance locations and widths (a) of the high-field intraspecies ^{133}Cs Feshbach resonances observed in this and previous work [153, 209, 213]. Locations of the zeros in scattering length are also presented (b) for the two large s-wave resonances at fields of approximately 549 G and 787 G, and the $d-$wave resonance at 820 G.

(a) Resonance locations

This work		Experimental		Theory
B (G)	ΔB (G)	B_{expt} (G)	ΔB_{expt} (G)	B_{theory} (G)
(181.55 ± 0.05)	(0.45 ± 0.07)	(181.64 ± 0.08)	(0.27 ± 0.10)	181.650
(197.10 ± 0.03)	(0.1 ± 0.1)	(197.06 ± 0.05)	(0.09 ± 0.01)	197.067
(352.7 ± 0.4)	(3.0 ± 0.5)	(352.65 ± 0.34)	(2.70 ± 0.47)	352.706
(790.6 ± 0.8)	(6.3 ± 0.9)	-	-	791.699
-	-	-	-	799.833
-	-	-	-	808.010
(910.3 ± 0.2)	-	-	-	909.288
-	-	-	-	1033.62
(1115.2 ± 0.8)	(12 ± 1)	-	-	1116.46

(b) Scattering length zero locations

This work	Experimental	Theory	
B (G)	B_{expt} (G)	B_{theory} (G)	$\Delta B_{\mathrm{theory}}$ (G)
-	(181.9 ± 0.1)	181.836	0.186
(197.2 ± 0.1)	(197.15 ± 0.05)	197.121	0.054
(355.7 ± 0.3)	(355.4 ± 0.6)	354.912	2.206
(796.9 ± 0.4)	-	795.919	4.220
-	-	799.907	0.074
-	-	808.016	0.006
-	-	909.294	0.006
-	-	1033.661	0.039
(1127 ± 1)	-	1125.396	8.936

Table 6.3: Measured locations and widths (a) of the interspecies ^{87}Rb^{133}Cs Feshbach resonances observed in this and previous work [72, 121, 209]. Locations of the zeros in scattering length are also presented (b) for the resonances that have been the focus of this work.

Chapter 7

Observation of ^{85}Rb and ^{133}Cs Feshbach resonances

Due to the versatility of the apparatus in addition to the ability to trap ^{87}Rb and ^{133}Cs simultaneously, it is also possible to perform experiments involving a mixture of ^{85}Rb and ^{133}Cs in the same system. In contrast to the ^{87}Rb^{133}Cs case relatively little work has been performed investigating the ^{85}Rb^{133}Cs system, hence there are many interesting experiments possible that will provide valuable insight into the behaviour of a two-species mixture of these atoms. In this chapter the small changes to the experiment that are required to perform ^{85}Rb^{133}Cs experiments are discussed and the results of such experiments are reported.

7.1 Feshbach structure of ^{85}Rb^{133}Cs

During the course of this work the model for the ^{87}Rb^{133}Cs potential and background scattering length has been refined resulting in the current best model of the system [121]. The calculations for this model were based upon observation of Feshbach resonances in a ^{87}Rb^{133}Cs system [72, 121] and upon extrapolation predictions for high-field ^{87}Rb^{133}Cs Feshbach resonances were made, as discussed in chapter 6, but in addition a coupled-channels calculation has also been performed for a ^{85}Rb^{133}Cs system in the absolute internal ground states. This predicts the existence of many s-wave and higher order resonances up to magnetic fields of 1000 G, as shown in figure 7.1. An additional interesting feature of this system is that the background scattering length is small, indicating that collisional loss between the two species would be low, and any rethermalisation poor, unless in the vicinity of a Feshbach resonance. At higher temperatures the contributions from higher partial waves may be significant enough for rethermalisation to occur, however once they become forbidden for energetic reasons the sympathetic cooling will rely on the s-wave scattering length. Hence experiments involving ^{85}Rb and ^{133}Cs may effectively be thought of as single-species experiments, unless the interactions are increased by changing the magnetic field.

The small background scattering length is apparent in figure 7.1, and the scattering length only becomes appreciable in the vicinity of a Feshbach resonance. In addition to the six resonances visible in the figure there are an additional 23 predicted resonances at fields lower than 1000 G, all within range of the apparatus. Five of these predicted resonances are s-wave in origin, these are located at 109.3 G, 187.1 G, 477.5 G, 578.4 G and 642.4 G. With the exception of the resonance at 477.5 G these are all broad resonances. In this system the definition of a resonance width is complicated by the fact the scattering length slowly approaches 0 a_0, hence the width of many resonances would be artificially broad using this definition. In the following the resonance widths or the positions of the zero in scattering length are generally not quoted.

7.2 Implementation of ^{85}Rb locking optics

To perform experiments involving ^{85}Rb the laser table required small changes from the setup that is currently used for ^{87}Rb experiments. The vacuum system and MOT trapping beam alignment remains identical to the case for ^{87}Rb however changes were required in the derivation of laser light. For the MOT cooling light the locking scheme is the direct analogue of the ^{87}Rb case, however for the repump laser there are differences. The splitting of the energy levels in ^{85}Rb is different to that in ^{87}Rb (see figure 3.1) which is problematic due to the central operation frequency of the AOMs that shift the frequency of the repump laser being 80 MHz. When trapping ^{87}Rb the direct laser

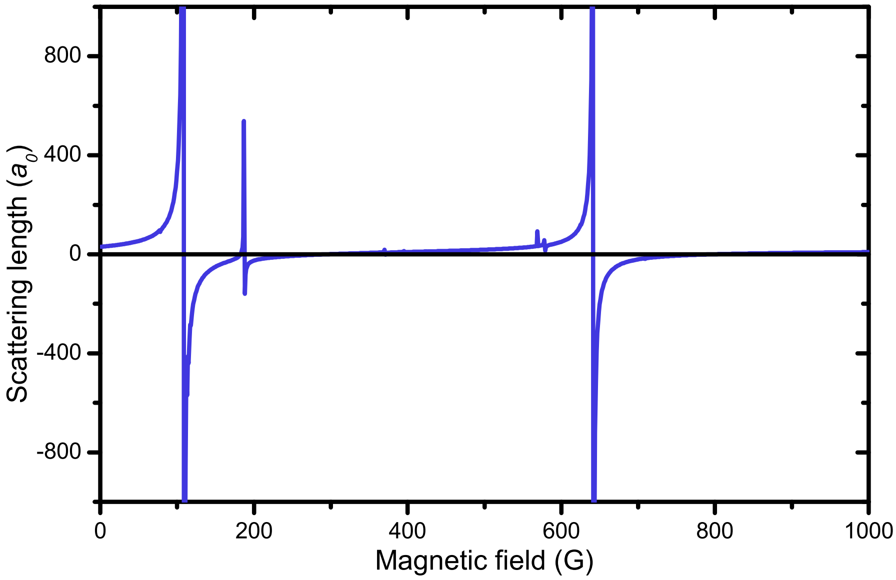

Figure 7.1: Interspecies ^{85}Rb^{133}Cs scattering length as a function of magnetic field for ^{85}Rb and ^{133}Cs atoms in the $|2,+2\rangle$ and $|3,+3\rangle$ states respectively [209]. At present no ^{85}Rb^{133}Cs Feshbach resonances have yet been observed.

output frequency is on the cross-over transition between $F = 1$ to $F' = 1$ and $F' = 2$. This light is then detuned either -78.5 MHz or +78.5 MHz from the repumping and optical pumping transitions respectively. In contrast for ^{85}Rb if the laser is locked to the crossover transition between $F = 2$ to $F' = 2$ and $F' = 3$ the detuning would be ±31.7 MHz from the repumping and optical pumping transitions. A different locking scheme is thus required, or a major overhaul of the Rb locking optics.

To convert the experiment to run ^{85}Rb experiments we have arrived at a scheme whereby the hardware and indeed AOM frequencies can all remain the same as they are in ^{87}Rb experiments. To do this requires the use of a dichroic atomic vapour laser lock (DAVLL) to lock the repump laser as the large Doppler broadened background means this locking technique has a large capture range so the laser can be locked far away from the hyperfine peak that is desired.

7.2.1 Principles of DAVLL

The basic principle of DAVLL involves a linearly polarised beam incident on an atomic vapour as in figure 7.2(a). The beam transmitted through the vapour is split by a PBS cube and the two output branches of the PBS are detected via a differencing photodiode. This detector subtracts one photodiode signal from the other. A $\lambda/4$-plate is used to balance the signal incident on the two photodiodes. If zero B-field is applied to the vapour cell the $m_J = \pm 1$ states are degenerate, hence the absorption profiles of σ^- and σ^+ transitions are identical. Applying a B-field (where the axis of the B-field is the same as the wave-vector of the light) lifts this degeneracy and the medium becomes dichroic. This shifts the absorption profiles for the different circular polarisations in different directions. Rotating the $\lambda/4$-plate prior to the PBS changes the balance of the two signals on the photodiode. The signal output by the differencing photodiode then resembles a dispersion type feature. This signal can be used as a frequency discriminant for laser locking. The location of the zero crossing can be altered by either the $\lambda/4$-plate or by applying an external electronic voltage to the electronic locking circuit, which is the technique applied in this work.

The experimental setup is displayed in figure 7.2(a). The light for the DAVLL locking derives from the branch of light that becomes the optical pumping beam. The polarisation of a beam reflected from a PBS is rotated such that it is transmitted through another PBS. The second PBS is included simply to ensure that the polarisation is pure. The light then impinges on a heated Rb DAVLL cell. The cell consists of a Rb vapour cell of length 5 cm held in place by brass contacts and is surrounded by a solenoid wound from enameled copper [220]. A current of 1.49 A is passed through the solenoid generating a B-field of approximately 30 G in the centre of the cell. The beam is then split by another PBS and is detected by a differencing photodiode. A $\lambda/4$-plate is inserted before the final PBS so that the contribution derived from $\sigma^{\pm}$ light may be varied. This signal is then transmitted to the input of the laser locking circuit.

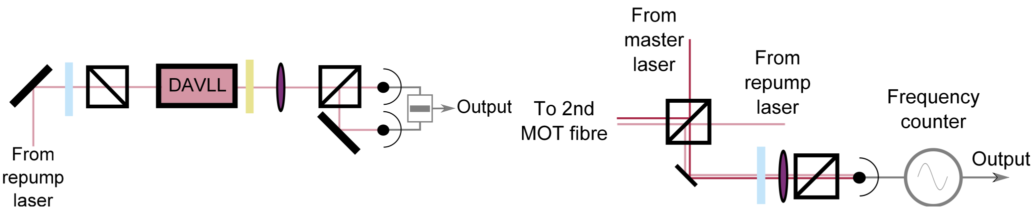

(a) (b)

Figure 7.2: Optical setup for DAVLL on the Rb repump laser (a) and optical setup to measure the beat frequency between the cooling and repump laser (b). In (a) a differencing photodiode calculates the difference in power of the optical signal of both branches of the PBS output. In (b) the light of the incorrect polarisations rejected by the cube are combined on a fast photodiode and the beat signal of the two is measured. Symbols used are defined in figure B.2.

7.2.2 Deriving repumping and optical pumping frequencies

Whilst DAVLL exhibits a large capture range, this can be detrimental as the locking signals are Doppler broadened so it is difficult to determine the laser frequency exactly. To determine the precise frequency of the light output by the laser we measure the beat frequency between light from the cooling laser (when locked to the repump transition) and the repump laser. Light of the incorrect polarisation rejected by the cube used to combine the two frequencies of light prior to fibre coupling for the 2$^{\text{nd}}$ MOT are incident on a $\lambda/2$-plate. This rotates the polarisation such that an appreciable fraction of both beams is transmitted by a PBS cube, and the light is then detected on a fast photodiode (EOT 2030). A frequency counter (Agilent 5313 A) is used to measure the beat frequency of the two beams, which is equal to the difference in frequency of the two beams. This can be understood by superimposing two sine waves (of unit amplitude)

$$\begin{aligned}\sin\left(k_1 x - \omega_1 t\right) + \sin\left(k_2 x - \omega_2 t\right) = 2\cos\left(\frac{k_1 - k_2}{2}x - \frac{\omega_1 - \omega_2}{2}t\right) \times \\ \sin\left(\frac{k_1 + k_2}{2}x - \frac{\omega_1 + \omega_2}{2}t\right).\end{aligned} \tag{7.1}$$

The resultant signal can thus be broken up into two parts. One is the sine component which oscillates faster than the cosine component, hence the cosine part of the right hand side is an envelope function. The perceived beat frequency is the frequency of the envelope function, specifically the difference in frequency of the two signals

$$|f_{\mathrm{B}}| = |f_1 - f_2| \,. \tag{7.2}$$

From equation 7.2 we thus see that the frequency measured by the fast photodiode will be the difference in frequency of the two lasers.

The frequency of the light that is incident on the photodiodes depends on where the laser is locked and any shifting of the frequency that is applied downstream, for example by AOMs. When locking the lasers to the ^{85}Rb transitions we first lock the cooling laser to the ^{85}Rb $F = 2$ to $F' = 1$ repumping transition, the raw laser light is detuned by 251.16 MHz from the transition. The laser is locked to this transition as this is the closed repump transition, and to lock a laser via modulation transfer spectroscopy a closed atomic transition is required. The cooling AOM then steps up the frequency by 240.66 MHz, hence the detuning from the actual transition is then 10.50 MHz. For the repump laser, to obtain MOT light of the correct detuning the laser must be detuned by -80.00 MHz from the $F = 2$ to $F' = 3$ transition. The repump AOM then increases the laser frequency to be resonant, and it is this light that is measured by the fast photodiode. Hence we expect a beat frequency between the two signals of 103.27 MHz. We achieve this by locking the laser and then varying the offset voltage applied to the locking circuitry until we achieve the correct beat frequency, which corresponds to a maximum MOT load.

To set the correct offset so that the optical pumping frequency is correct we again lock the cooling laser to the closed transition and obtain the same frequency of light at the photodiode. For the repump light the signal that is incident at the photodiode is again 80 MHz higher than the frequency of the laser, however since the optical pumping AOM reduces the beam frequency the laser frequency must be increased to take account of this. Thus the expected beat signal between the two beams is 192.37 MHz in this case. Figure 7.3 presents the desired frequencies in a diagrammatic form. The two required offset voltages are set and a digital trigger is applied to switch between the two levels. This is generally set to the repumping voltage, and switched to the level required for optical pumping at the end of the molasses stage. In practice to obtain a maximum magnetic trap load the difference frequency for repumping is slightly different to the value quoted above because only two locking points are set and ideally different detunings should be used during the CMOT, however we do not consider that here.

At present limitations with hardware limit in situ measurement of the beat frequency which would provide a more accurate and stringent measurement of the beam's frequency. The frequency counter is limited to frequencies of 225 MHz hence the beat between the cooling laser when locked to the cooling transition and the repump laser would be out of the detectable range. A modification to the setup has recently been applied whereby a separate laser locked to the ^{85}Rb repump transition has been setup, and the beat signal between this laser and the repump laser is measured such that in situ monitoring is possible.

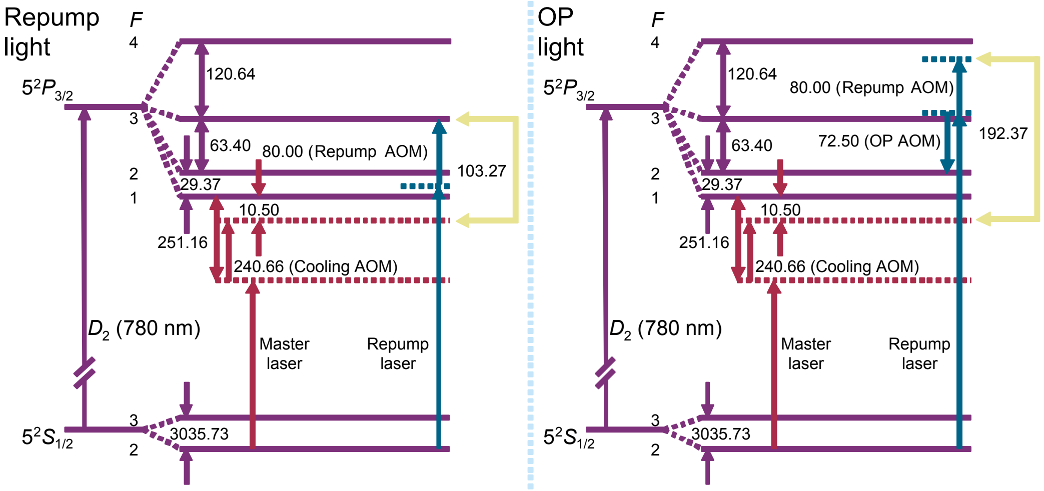

Figure 7.3: Atomic energy level diagram for ^{85}Rb that highlights how the frequencies incident on the fast photodiode that measures the beat frequency are derived. The two cases shown are for the beat frequency expected for repumping (left) and optical pumping (right).

7.3 Magnetic trapping of ^{85}Rb

7.3.1 Loading ^{85}Rb into the magnetic trap

The method of loading ^{85}Rb into the magnetic trap is identical to that for ^{87}Rb because the routine performs well for simultaneous loading of ^{133}Cs hence any change could have effects on the ^{133}Cs loading efficiency. Beam powers for the MOT, CMOT, molasses and optical pumping are all identical to the ^{87}Rb case, as are the field gradients and quantisation fields used. The magnetic trap switch on is also identical to that used in ^{87}Rb experiments. As reported in table 2.2 a magnetic field gradient of 22.37 G cm^{-1} is required to levitate ^{85}Rb in the $|2, -2\rangle$ state. This is approximately 10 G cm^{-1} lower than that required to levitate ^{87}Rb and ^{133}Cs in the magnetically trappable stretched states, however we must perform the same magnetic trap ramping to ensure that ^{133}Cs is not lost by switching on at too small a gradient. As in the ^{87}Rb case the B-field gradient is ramped up to 187 G cm^{-1} and evaporation is performed in this tight trap. At this stage the trap contains $(5.5 \pm 0.9) \times 10^8$ ($(3.5 \pm 0.2) \times 10^7$) ^{85}Rb (^{133}Cs) atoms at a temperature of (220 ± 10) μK ((150 ± 10) μK) and PSD of $(6 \pm 2) \times 10^{-7}$ ($(1.9 \pm 0.5) \times 10^{-7}$).

7.3.2 Evaporation of ^{85}Rb in the magnetic trap

The RF evaporation of ^{85}Rb was optimised via the same method described in section 3.7. The optimum RF evaporation ramps in ^{85}Rb were found to be three linear ramps in the RF frequency. The starting evaporation frequency is 15.0 MHz, and this is ramped to 5.0 MHz in 7.0 s. The RF frequency is continuously reduced to 3.5 MHz in 3.1 s and then to 3.0 MHz in a further 1.1 s. The total time required for RF evaporation is thus 11.2 s. After the RF evaporation sequence the ^{85}Rb (^{133}Cs) PSD has increased to $(1.2 \pm 0.3) \times 10^{-5}$ ($(4.8 \pm 0.6) \times 10^{-6}$). The temperature after evaporation is (51 ± 1) μK ((56 ± 1) μK) and $(1.5 \pm 0.2) \times 10^7$ ($(1.21 \pm 0.06) \times 10^7$) atoms remain trapped in the potential. The PSD versus atom number remaining and the atom number versus temperature during the RF evaporation are displayed in figures 7.4 and 7.5 respectively. Data for single-species cooling of ^{85}Rb are

Ramp	t (s)	f_1 (MHz)	f_2 (MHz)
1	7.0	15.0	5.0
2	3.1	5.0	3.5
3	1.1	3.5	3.0

Table 7.1: Magnetic trap RF evaporation ramps used for evaporation of ^{85}Rb.

Ramp	Species	N ($\times 10^7$)	T (μK)	PSD
Load	^{85}Rb alone	(41 ± 5)	(216 ± 2)	$(5.2 \pm 0.8) \times 10^{-7}$
	^{85}Rb(+Cs)	(55 ± 9)	(220 ± 10)	$(6 \pm 2) \times 10^{-7}$
	^{133}Cs	(3.5 ± 0.2)	(150 ± 10)	$(1.9 \pm 0.5) \times 10^{-7}$
1	^{85}Rb alone	(8.43 ± 0.04)	(105 ± 3)	$(2.7 \pm 0.3) \times 10^{-6}$
	^{85}Rb(+Cs)	(8.0 ± 0.6)	(88 ± 7)	$(6 \pm 2) \times 10^{-6}$
	^{133}Cs	(2.4 ± 0.9)	(106 ± 7)	$(5 \pm 3) \times 10^{-7}$
2	^{85}Rb alone	(2.89 ± 0.07)	(53 ± 1)	$(2.0 \pm 0.2) \times 10^{-5}$
	^{85}Rb(+Cs)	(1.5 ± 0.1)	(52 ± 1)	$(1.1 \pm 0.2) \times 10^{-5}$
	^{133}Cs	(1.4 ± 0.3)	(66 ± 6)	$(3 \pm 1) \times 10^{-6}$
3	^{85}Rb alone	(1.4 ± 0.6)	(40 ± 1)	$(3 \pm 2) \times 10^{-5}$
	^{85}Rb(+Cs)	(1.5 ± 0.2)	(51 ± 1)	$(1.2 \pm 0.3) \times 10^{-5}$
	^{133}Cs	(1.21 ± 0.06)	(56 ± 1)	$(4.8 \pm 0.6) \times 10^{-6}$

Table 7.2: Number, temperature and PSD after each RF evaporation ramp for ^{85}Rb and ^{133}Cs. The ramp labels correspond to those in table 7.1.

also shown. The RF evaporation ramps are summarised in table 7.1.

Figure 7.4 indicates that it is only possible to achieve a PSD of $\sim 10^{-5}$ when cooling ^{85}Rb in the quadrupole trap. This is an order of magnitude lower than the PSD achievable when evaporating ^{87}Rb. The PSD of ^{133}Cs is also roughly an order of magnitude lower than when cooled by ^{87}Rb. The lines of best fit that are used to guide the eye have been used to calculate γ for the evaporation sequence. For ^{85}Rb in the absence of ^{133}Cs $\gamma = (1.3 \pm 0.1)$ and when cooling ^{133}Cs it is (0.6 ± 0.1). Evaporative cooling of ^{85}Rb is less efficient that that of ^{87}Rb due to the larger inelastic collision rates in the ^{85}Rb system [142]. For ^{133}Cs $\gamma = (3.5 \pm 0.4)$, which indicates that the cooling of ^{133}Cs is reasonably efficient as it is above 3, this is due to the effect of sympathetic cooling, however when sympathetically cooled by ^{87}Rb

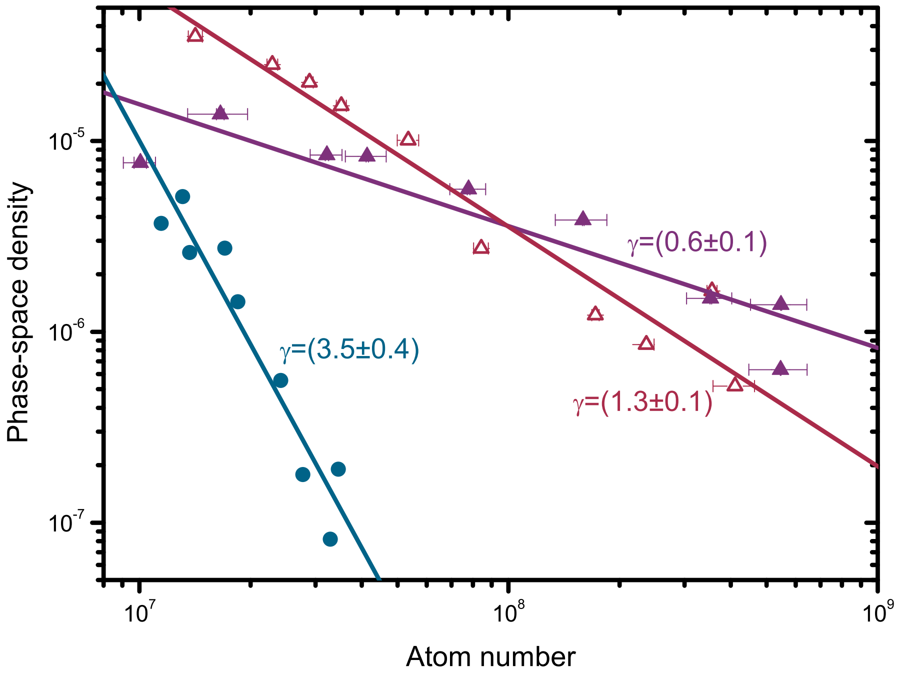

Figure 7.4: PSD as a function of atom number during the quadrupole trap RF evaporation sequence for ^{85}Rb (purple triangles) and ^{133}Cs (blue circles) when ^{85}Rb is cooling ^{133}Cs. Open red triangles correspond to ^{85}Rb number when not in the presence of ^{133}Cs. The lines were used to calculate the values of γ quoted.

the efficiency of ^{133}Cs evaporation was (14 ± 2). The reduction follows from the low efficiency of ^{85}Rb cooling. When not sympathetically cooling ^{133}Cs the ^{85}Rb cooling is not efficient, however the inclusion of ^{133}Cs reduces the ^{85}Rb cooling efficiency further still, which is in contrast to the ^{87}Rb^{133}Cs case where there is no marked effect on the ^{87}Rb cooling by the presence of ^{133}Cs. The reason for this is the comparatively lower ^{85}Rb atom number in the magnetic trap, hence when ^{85}Rb atoms are lost due to collisions with ^{133}Cs the effect on the total atom number in the cloud is comparatively larger.

At this stage the cloud is cold enough to load atoms into the dipole potential (see chapter 4). Even though the presence of ^{133}Cs in the quadrupole trap has a pronounced effect on the ^{85}Rb cloud the atom number and temperature at the end of the RF evaporation sequence is adequate to perform Feshbach

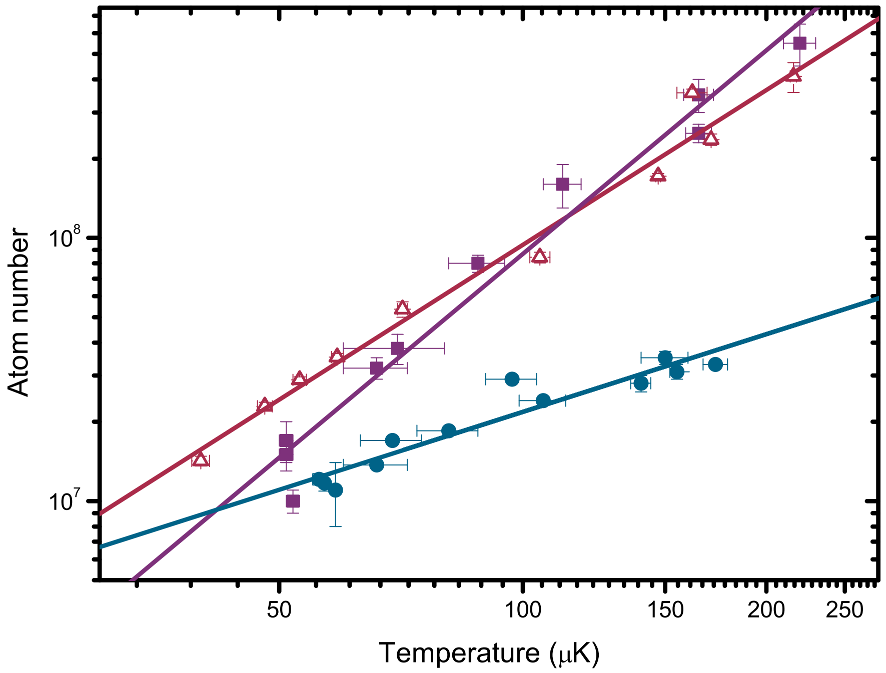

Figure 7.5: Atom number as a function of temperature during the quadrupole trap RF evaporation sequence for ^{85}Rb (purple triangles) and ^{133}Cs (blue circles) when ^{85}Rb is cooling ^{133}Cs. Open red triangles correspond to ^{85}Rb number when not in the presence of ^{133}Cs. The lines have been added to guide the eye.

spectroscopy within the dipole trap.

7.4 Optical trapping of ^{85}Rb

7.4.1 Optical trap loading

It is possible to load ^{85}Rb atoms into the dipole trap with a similar experimental configuration as in the experiments involving ^{87}Rb. Following the same magnetic trap evaporation procedure as described in section 7.3.2 atoms are loaded into the crossed dipole trap by decreasing $\partial B/\partial z$ to 20 G cm^{-1}, which is just below the gradient required to levitate ^{85}Rb atoms in the $|2,-2\rangle$ state. The dipole trapping beams are at a power of 4.05 W during the loading process. The bias field is switched on in two stages, first the field from bias coil 3 is switched on to 36.2 G in 5 ms and secondly the field from bias coils 1 and 2 (which are connected in series) is increased to 124.7 G in 10 ms, the resultant magnetic field at the atoms being 160.9 G. The trap depth and frequencies of this trap are reported in table 7.3. We load $(6.1 \pm 0.2) \times 10^5$ atoms at a temperature of (13.24 ± 0.08) μK after the ramp up to 160.9 G is performed.

Alternatively for experiments in the magnetically untrappable state of $|2, +2\rangle$ the technique of rapid adiabatic passage is also used as in the case for ^{87}Rb and ^{133}Cs. The timings and the magnetic fields used are identical as the bias field required to dress the applied RF field is between that for ^{87}Rb and ^{133}Cs. After the spin flip, at a field of (22.91 ± 0.02) G, $(6.7 \pm 0.4) \times 10^5$ atoms remain at a temperature of (13.80 ± 0.07) μK. The PSD here is $(4.5 \pm 0.3) \times 10^{-5}$. The ^{85}Rb $|2, +2\rangle$ atoms experience a potential with a trap depth of 52.0 μK and the trap frequencies are $\omega_{\text{rad}} = 2\pi \times 453.3$ Hz and $\omega_{\text{ax}} = 2\pi \times 89.8$ Hz.

7.4.2 Optical trap evaporation

Due to the negative background scattering length of ^{85}Rb [221] evaporation to BEC is not possible without exploring the region around a Feshbach resonance. One such broad resonance exists in the $|2, -2\rangle$ state at approximately 155 G where the scattering length is positive between this field and ~ 166 G. Previous experiments report the optimal field for evaporation is in this region [6]. We therefore evaporate atoms in the magnetically trappable $|2, -2\rangle$ state, hence the trap tilting evaporation method is not possible with the experimental configuration in its present state due to the direction of the bias field being set up to levitate the high-field seeking states. A resonance has been predicted at high-field in the $|2, +2\rangle$ state, which, as yet, remains unobserved, but it does present an opportunity to condense in the absolute ground state [222].

We evaporate ^{85}Rb via the plain evaporation method using ramps that are optimised in smaller stages than for experiments with ^{87}Rb. Prior to each stage a 5 ms ramp was included to change from one bias field to another, hence ramp times as well as the bias field were optimised. The first stage of evaporation was a 1 s ramp to beam powers of 1.01 W at 160.9 G followed by ramps to 510 mW at 161.0 G in 1 s and to 370 mW at 164.7 G in 2 s. Two final ramps were performed, both at a bias field of 161.5 G, to 250 mW in 1 s and then to 190 mW in 1 s. The final trap depth is approximately 1 μK with trap frequencies of $\omega_{\text{rad}} = 2\pi \times 111.7$ Hz and $\omega_{\text{ax}} = 2\pi \times 33.8$ Hz. These dipole trap evaporation ramps are summarised in table 7.3. The number of atoms left after each stage of evaporation is reported in table 7.4.

Ramp	P_1 (W)	P_2 (W)	t (s)	B (G)	Trap depth (μK)	f_{rad} (Hz)	f_{ax} (Hz)
Load	-	4.05	-	-	83.1	458.3	124.2
High-field	4.05	4.05	0.02	160.9	83.3	458.3	124.3
1	4.05	1.01	1.00	160.9	23.1	260.6	77.9
2	1.01	0.51	1.00	161.0	10.6	185.2	55.4
3	0.51	0.37	2.00	164.7	7.1	157.7	47.2
4	0.37	0.25	1.00	161.5	4.2	128.1	38.8
5	0.25	0.19	1.00	161.5	2.8	111.7	33.8

Table 7.3: Crossed dipole trap evaporation ramps used for evaporation of ^{85}Rb in the $|2, -2\rangle$ state, performed by simply reducing the beam power. The magnetic field gradient used is 20.0 G cm^{-1}. Trap depths and frequencies quoted are for the power P_2 in each ramp.

Ramp	N	T (μK)	PSD
Load	$(7.0 \pm 0.6) \times 10^5$	(13.83 ± 0.05)	$(4.7 \pm 0.5) \times 10^{-4}$
High-field	$(6.1 \pm 0.2) \times 10^5$	(13.24 ± 0.08)	$(4.5 \pm 0.1) \times 10^{-4}$
1	$(3.0 \pm 0.1) \times 10^5$	(2.92 ± 0.02)	$(2.6 \pm 0.1) \times 10^{-3}$
2	$(1.72 \pm 0.02) \times 10^5$	(1.13 ± 0.01)	$(8.34 \pm 0.07) \times 10^{-3}$
3	$(1.21 \pm 0.02) \times 10^5$	(0.6667 ± 0.0009)	$(1.58 \pm 0.03) \times 10^{-2}$
4	$(6.04 \pm 0.10) \times 10^4$	(0.257 ± 0.003)	$(6.2 \pm 0.2) \times 10^{-2}$
5	$(2.4 \pm 0.1) \times 10^4$	(0.102 ± 0.003)	$(4.0 \pm 0.1) \times 10^{-1}$

Table 7.4: Number, temperature and PSD after each crossed dipole trap evaporation ramp for ^{85}Rb. The ramp numbers correspond to those in table 7.3.

Evaporation proceeds with an efficiency of (2.04 ± 0.04) (see figure 7.6) until the end of the fifth ramp (at a beam power of 190 mW). At this stage the evaporation stagnates and the efficiency decreases rapidly, resulting in degeneracy not being reached, potentially due to the drop in trap frequencies observed at lower beam powers. The evaporation at this stage is in conflict with both background and inelastic collisions (two-body and three-body) and the reduction in atom number does not produce the same increase in PSD as earlier in the evaporation sequence. We note that were evaporation to continue at the same efficiency throughout, a BEC of 1×10^4 atoms would be produced. Previous experiments also observe a reduction in evaporation efficiency within this system [6]. Although degeneracy was not reached, clouds with unity PSD were produced, hence it is believed that with re-wiring of the bias field coils such that the weak-field seeking states are levitated it may be possible to produce a BEC via the trap tilting method. Alternatively, an attempt to produce a condensate near the high-field Feshbach resonance in the high-field seeking state appears favourable, as two-body losses would be suppressed [137]. We also propose that increasing the dipole trap beam size and beam powers would potentially lead to a larger dipole trap load and result in a sufficient number of atoms to reach degeneracy.

BEC of ^{85}Rb has been reached within our group in a similar apparatus to the experiment described here, hence condensation of ^{85}Rb in this system should be possible [8]. We note the aforementioned problems above, most importantly that the beams are potentially too small, increasing collision frequencies and reducing dipole trap loads owing to the small capture volume. The beam waist in the other experiment is 136 μm, with trapping frequencies more than a factor of two lower than those here. The initial load of atoms into the dipole trap is also much larger hence a higher initial PSD is achieved in the dipole trap. If MOT loading of ^{85}Rb is improved, for example by making a move to FM spectroscopy locking of the repump laser, and the corresponding increase in number and PSD that this would bring about in the magnetic trap, a larger load would also be expected. With these proposed changes condensation would be considerably more likely in this apparatus.

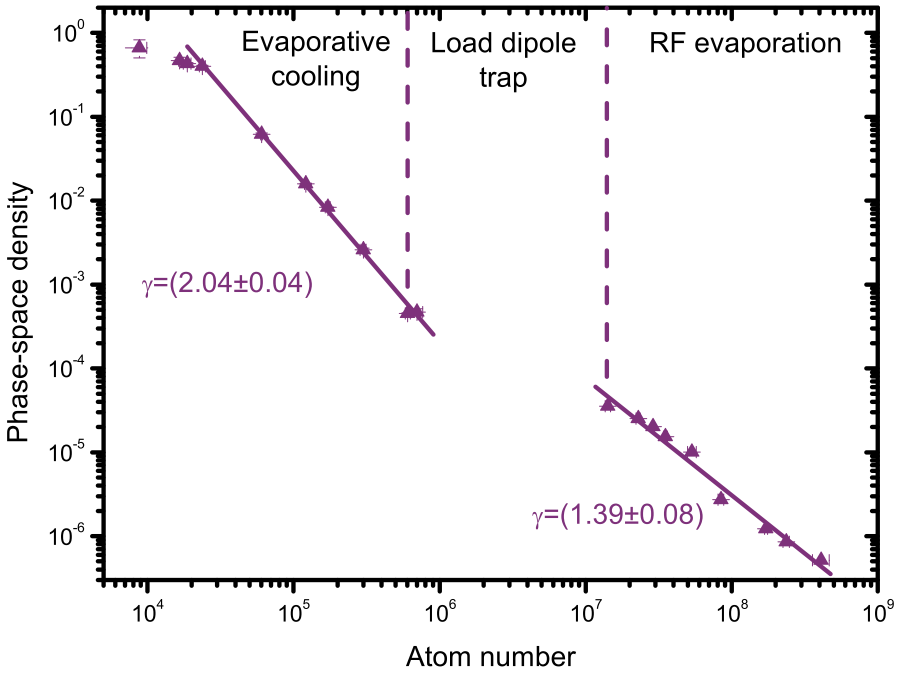

Figure 7.6: ^{85}Rb PSD as a function of atom number throughout the experimental evaporation sequences. The reduction in evaporation efficiency can be observed at high PSD. The line corresponds to a linear fit to the logs of the data points, and the gradient of these fits are the reported values of γ. More efficient evaporation is represented by a steeper line of best fit. Note some points aren't included in these fits, such as the first points after loading the dipole trap, as some of the atoms are still being evaporated at this point, and the final three points where evaporation stagnates. Data in the RF evaporation sequence is identical to that presented in figure 7.4.

7.5 Observation of ^{85}Rb and ^{133}Cs Feshbach resonances

To determine the Feshbach spectrum of ^{85}Rb^{133}Cs the mixture was evaporated at different magnetic fields in the dipole trap via plain evaporation by reducing the beam powers. Given the difference in trap depths between the two species two distinct temperatures were expected to be measured wherever a resonance isn't present as the small scattering length would result in poor rethermalisation. Conversely wherever a resonance is present good rethermalisation should occur, and hence the ^{133}Cs temperature should be reduced to the ^{85}Rb temperature. Similarly to the ^{87}Rb^{133}Cs case a distinct drop in number is expected wherever a Feshbach resonance occurs. As in all experiments involving ^{133}Cs one must also take care to ensure observed features are not simply intraspecies ^{133}Cs resonances, however due to the nature of the ^{85}Rb loss rates, the Rb:Cs ratio is lower than in the ^{87}Rb case, hence many features can be seen clearly in the ^{85}Rb number data, which provides near sufficient evidence of an interspecies feature.

The magnetic trapping of ^{85}Rb and ^{133}Cs has been presented in section 7.3.1, and ^{85}Rb dipole trap loading has been reported in section 7.4. The experimental procedure is not altered for two-species experiments, hence after the spin flip the magnetic field is increased to the final value in 15 ms (applying two different linear ramps in the field using different coils) and then the dipole trapping beams are reduced to a power of 1.01 W in 2 s and the atoms are held in this potential for a further 1 s. The trap depth at low-field in this potential is 12.6 μK (16.5 μK) for ^{85}Rb (^{133}Cs) and the frequencies are $\omega_{\text{rad}} = 2\pi \times 229.2$ Hz ($\omega_{\text{rad}} = 2\pi \times 211.0$ Hz) and $\omega_{\text{ax}} = 2\pi \times 44.1$ Hz ($\omega_{\text{ax}} = 2\pi \times 41.8$ Hz). These trap depths and frequencies are only modified slightly at higher magnetic fields.

The experiment has been performed for magnetic fields between 0 G and 170 G, and then between fields of 605 G and 660 G, which represents the areas most densely populated with predicted resonances. The results of the experiment up to fields of 170 G are presented in figure 7.7, and for the data between 90-150 G the results are presented on a smaller scale in figure 7.8. Results for the higher magnetic field region are presented in figure 7.9.

The ^{85}Rb^{133}Cs evaporation data confirms that the background interspecies scattering length between ^{85}Rb and ^{133}Cs is small, as indicated by the fact the temperatures are out of equilibrium wherever there isn't a Feshbach resonance. A distinct difference in the temperature of the two species is observed where $|a_{^{85}\text{Rb}^{133}\text{Cs}}| \lesssim 60\ a_0$. For scattering lengths of a larger magnitude the rethermalisation is sufficient such that the ^{133}Cs temperature is similar to that of the ^{85}Rb. The temperature is therefore useful in identifying interspecies Feshbach resonances in this system. Four sharp dips exist in the ^{133}Cs temperature at the fields of the resonances at approximately 107 G,

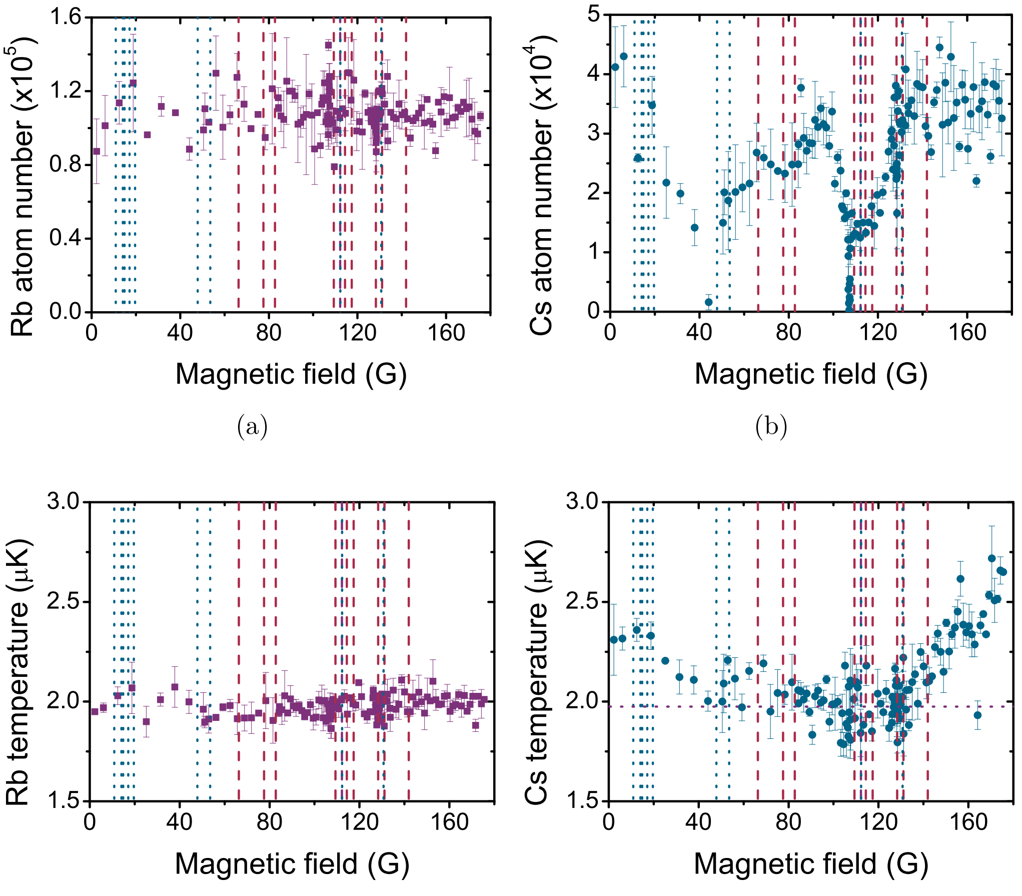

(a)

(b)

(c)

(d)

Figure 7.7: Atom number remaining (a,b) and temperature (c,d) after dipole trap evaporation and a 1 s hold at different magnetic fields, for ^{85}Rb (purple, a,c) and ^{133}Cs (blue, b,c). The vertical dashed lines indicate the locations of predicted interspecies ^{85}Rb^{133}Cs Feshbach resonances (red dashed) and intraspecies ^{133}Cs (blue dotted) Feshbach resonances. Two interspecies resonances are clearly seen in the ^{133}Cs number data, at fields of (107.1 ± 0.2) G and at (112 ± 1) G, with two others which are less clear at fields of (128.1 ± 0.4) G and (143.2 ± 0.6) G. The smaller two resonances are clearer in figures 7.8(c) and 7.8(d). The temperature of the ^{85}Rb cloud is constant throughout the region, however the ^{133}Cs temperature is lower where the interspecies scattering length is higher due to the effects of rethermalisation. The constant ^{85}Rb temperature is marked by the horizontal dotted line in figure 7.7(d).

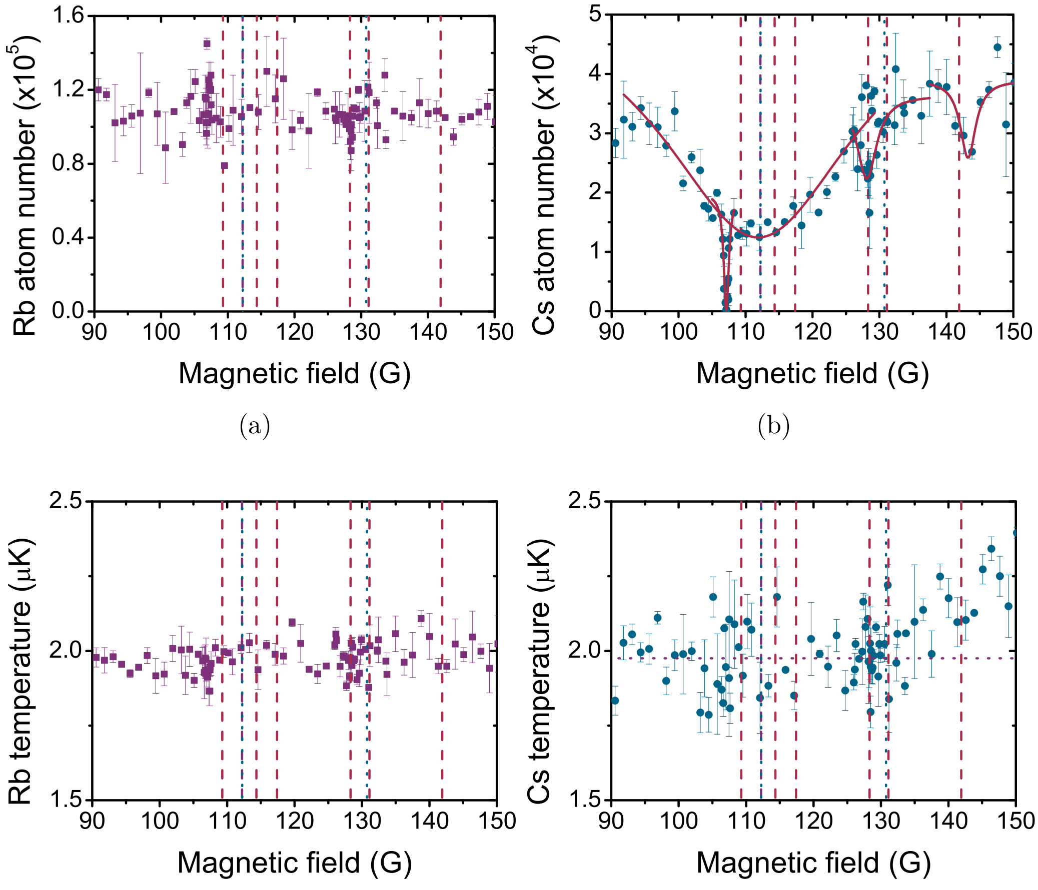

(a) (b)

(c) (d)

Figure 7.8: Atom number remaining (a,b) and temperature (c,d) after dipole trap evaporation and a 1 s hold at different magnetic fields, for ^{85}Rb (purple, a,c) and ^{133}Cs (blue, b,d). The dashed lines indicate the locations of predicted interspecies ^{85}Rb^{133}Cs Feshbach resonances (red dashed) and intraspecies ^{133}Cs (blue dotted) Feshbach resonances. Four interspecies resonances are seen, at (107.1±0.2) G, (112±1) G, (128.1±0.4) G and (143.2±0.6) G. These resonances are most visible in the ^{133}Cs number data. The temperature of the ^{85}Rb cloud is constant throughout the region, however the ^{133}Cs temperature is lower where the interspecies scattering length is higher due to the effects of rethermalisation. The constant ^{85}Rb temperature is marked by the horizontal dotted line in figure 7.8(d). Red solid lines present the Lorentzian fits used to determine the resonance locations.

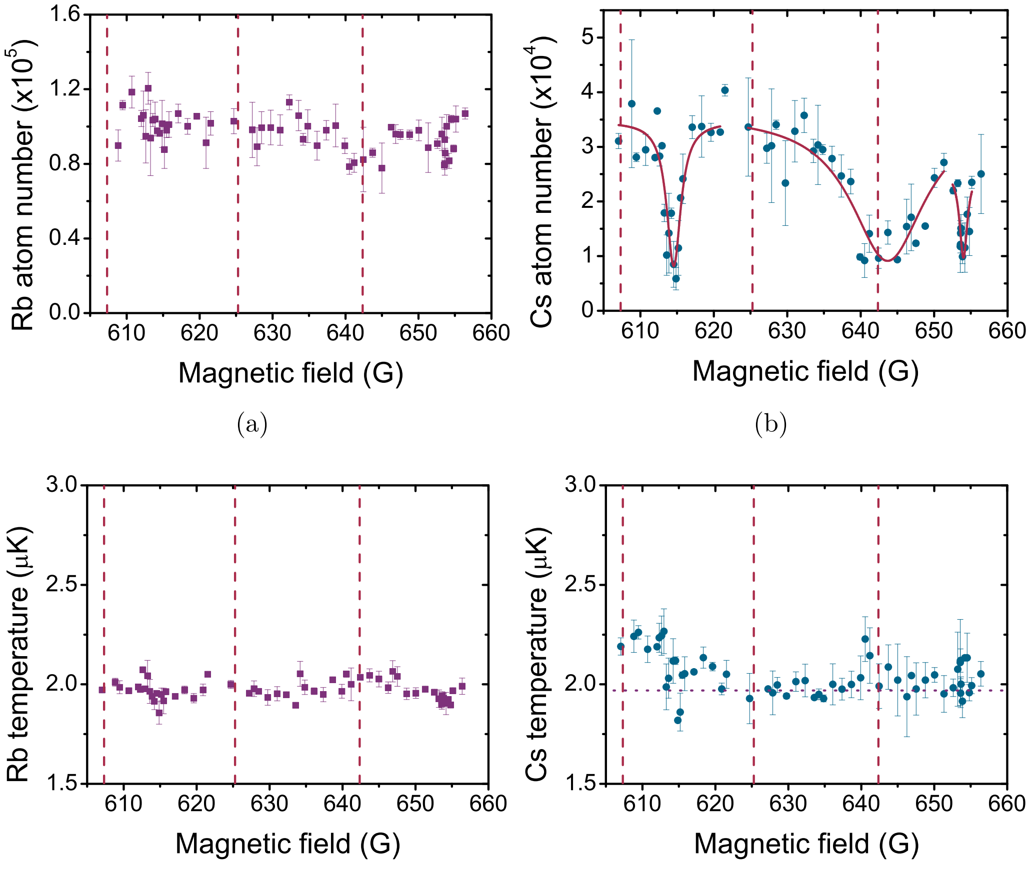

(a) (b)

(c) (d)

Figure 7.9: Atom number remaining (a,b) and temperature (c,d) after dipole trap evaporation and a 1 s hold at different magnetic fields, for ^{85}Rb (purple, a,c) and ^{133}Cs (blue, b,d). The red dashed lines indicate the locations of predicted interspecies ^{85}Rb^{133}Cs Feshbach resonances. Three interspecies resonances are seen in this region, at (614.6±0.4) G, (644±2) G and (654.0±0.3) G. Only one is in agreement with theory. The temperature of the ^{85}Rb atoms remains constant throughout this region, whereas the temperature of the ^{133}Cs varies depending on the interspecies scattering length. The constant ^{85}Rb temperature is marked by the horizontal dotted line in figure 7.9(d). Red solid lines present the Lorentzian fits used to determine the resonance locations.

B (G)	Notes
(107.1 ± 0.2)	No predicted resonance in region
(112 ± 1)	Broad $s-$wave resonance. Disagrees with theory.
(128.1 ± 0.4)	In excellent agreement with theory
(143.2 ± 0.6)	Predicted resonance is very narrow
(614.6 ± 0.4)	No predicted resonance in region
(644 ± 2)	Broad $s-$wave resonance. Agrees with theory.
(654.0 ± 0.3)	No predicted resonance in region

Table 7.5: Measured locations of the interspecies ^{85}Rb^{133}Cs Feshbach resonances observed in this work. Theoretical predictions for locations of resonances taken from [219].

112 G, 128 G and 615 G. We note that it is not possible to see the drop in temperature for the resonances at approximately 143 G, 644 G and 654 G. The ^{85}Rb temperature remains constant throughout the entire field region explored as it acts as a collisional bath for ^{133}Cs and the ^{85}Rb number is much higher than the ^{133}Cs number so the heat load on it is not large enough to significantly heat the ^{85}Rb cloud.

The number loss data reveals the locations of interspecies Feshbach resonances very clearly and the locations are reported in table 7.5. The interspecies Feshbach resonances are detected via a reduction in ^{133}Cs number and repeat measurements with ^{133}Cs alone in the dipole trap confirm that they are indeed interspecies resonances. Intraspecies ^{133}Cs resonances are not observed above the noise in the region as the step size of the points is not small enough and the density of the ^{133}Cs atoms is low in the trap, off resonance it is $(6.2 \pm 0.2) \times 10^{11}$ cm^{-3}. Only with the addition of collisions with ^{85}Rb can atom loss be detected.

The locations of the two broad s-wave resonances were measured to be (112 ± 1) G and (644 ± 2) G. The theoretical predictions for the locations of these resonances is at 109.3 G and 642.4 G. Clearly experimental observation of the lower field resonance is in disagreement with the theory. Given the broad nature of these resonances the number loss occurs over a large magnetic field range, hence the fit to the centre of the resonances is difficult, and produces a large error, however this is not of the same magnitude as the discrepancy. Another possible source of the discrepancy is that there are three predicted interspecies resonances within ±5 G of the $s-$wave resonance. If these resonances are present it is possible that loss from one resonance is disguised due to loss from another, which would have the effect of changing the resonance location and broadening the resonance. Since the other resonances in this region are predicted to be narrow, however, this is unlikely to be the case. Given that the higher field resonance is within twice the error and thus in reasonable agreement with the theory we believe that the theoretical potential utilised to predict the locations of the resonances is valid. There are three further predicted resonances that are s-wave in origin, at 187.1 G, 477.5 G and 578.4 G. Current work is being undertaken to locate these resonances which would provide more evidence in favour or against the theoretical predictions (see section 7.6).

Of the narrower resonances the one at (128.1 ± 0.4) G is in excellent agreement with the predicted 128.3 G. The other four narrow resonances are in disagreement with the theoretical predictions, with their locations being (107.1 ± 0.2) G, (143.2 ± 0.6) G, (614.6 ± 0.4) G and (654.0 ± 0.3) G. For some the nearest predicted resonances are incredibly narrow or > 10 G away so it is unlikely that they are the same resonance. Further study during the course of writing this thesis has shed new light on the Feshbach spectrum of ^{85}Rb^{133}Cs, and is highlighted in the following section.

Broad resonances were also predicted to exist at fields of 77.5 G, 187.1 G and 578.4 G. The two higher field resonances were out of the range that was covered by this initial scan, however they have been observed in the current work. The resonance at 77.5 G was within the range of the initial scan, however the step size between points was not sufficiently fine that this was detected.

7.6 Further study of ^{85}Rb and ^{133}Cs Feshbach resonances

During the course of writing this thesis further measurements have taken place to observe the full range of ^{85}Rb^{133}Cs Feshbach resonances. Improvements to the above work have been implemented as the power of the dipole trapping beam has been reduced and hence the atoms are at lower temperatures. This has the effect that resonances are narrowed, potentially making fitting of the broader resonances more accurate, and reducing the probability that the collision rate is in the unitarity limit. A full study has been performed up to fields of 700 G, providing sufficient data to allow the theoretical predictions to be tested fully and the model refined.

The same experiment as that described in section 7.5 was performed, whereby the beam power was reduced in 2 s and the atoms held in this potential for 1 s, for different magnetic fields. For the new measurement the beam power was ramped to 1.01 W. Here the trap depth is 15 μK (22 μK) and the trap frequencies are $2\pi\times218$ Hz ($2\pi\times211$ Hz) in the radial direction and $2\pi\times61$ Hz ($2\pi\times42$ Hz) in the axial direction for ^{85}Rb (^{133}Cs). Figure 7.10 and table 7.6 present the results of this measurement [223].

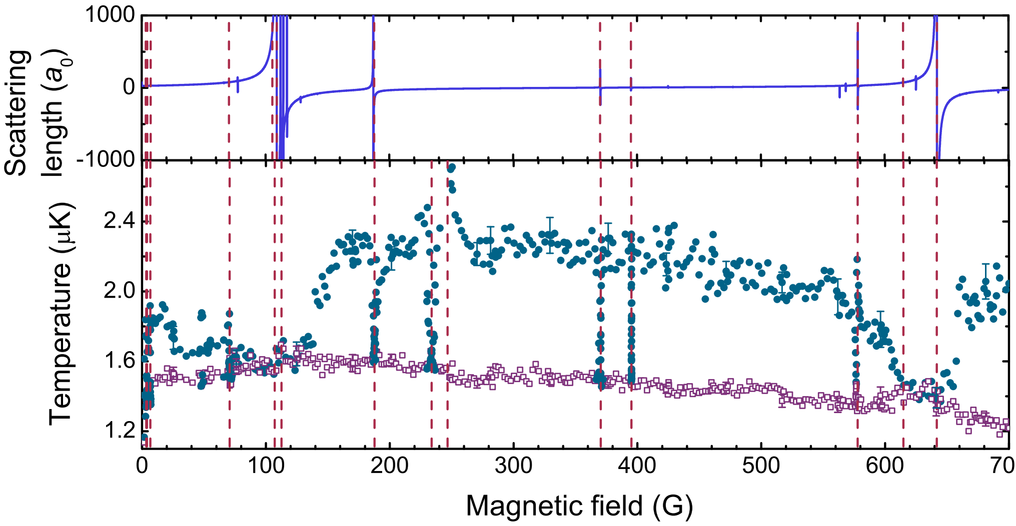

Figure 7.10: Temperature (bottom) of ^{85}Rb atoms (purple) and ^{133}Cs atoms (blue) after evaporation at different magnetic fields between 0-700 G. The red dashed lines indicate the locations of the 14 experimentally observed resonances. The scattering length (top) is also presented for the same field range, as predicted theoretically [209]. Here the red dashed lines indicate the theoretically predicted resonances. Figure adapted from [223].

The recent experimental work has resulted in the observation of fourteen interspecies ^{85}Rb^{133}Cs Feshbach resonances which are clearly evident in figure 7.10 and summarised in table 7.6. Most resonances are in excellent

Experiment		Theory					
		Assignment					
B (G)	ΔB (G)	Inc. Wave	l	f	m_f	B (G)	ΔB (G)
(3.47 ± 0.01)	(0.12 ± 0.02)	s	2	5	3	3.105	0.00005
(3.90 ± 0.02)	(0.33 ± 0.05)	s	2	5	4	4.269	0.000294
(6.76 ± 0.02)	(0.14 ± 0.03)	s	2	5	5	6.804	0.000857
(70.68 ± 0.04)	(0.8 ± 0.1)	p	1	-	-	70.54	-11.62
(107.13 ± 0.01)	(0.6 ± 0.2)	s	0	5	5	109.08	35.0
(112.6 ± 0.4)	(28 ± 5)	s	2	6	6	112.21	-0.1711
(187.66 ± 0.05)	(1.7 ± 0.3)	s	0	6	5	187.070	-4.0580
(233.9 ± 0.2)	(2.1 ± 0.3)	-	-	-	-	-	-
(246.5 ± 0.3)	(14 ± 2)	-	-	-	-	-	-
(370.39 ± 0.01)	(0.08 ± 0.04)	s	2	7	7	370.374	3.909
(395.20 ± 0.01)	(0.08 ± 0.01)	s	2	7	6	395.112	0.4488
(577.8 ± 0.1)	(1.1 ± 0.3)	s	0	6	5	578.365	0.3412
(614.6 ± 0.3)	(1.1 ± 0.4)	p	1	-	-	614.984	-6.773
(641.8 ± 0.3)	(6 ± 2)	s	0	5	5	642.115	576.5

Table 7.6: Location and assignment of recently observed Feshbach resonances in a ^{85}Rb^{133}Cs mixture. The atomic states for ^{85}Rb and ^{133}Cs are $|2, +2\rangle$ and $|3, +3\rangle$ respectively. Additional systematic magnetic field uncertainties of ± 0.1 G and ± 0.5 G are present for the ranges $0 - 400$ and $400 - 800$ G respectively. Table adapted from [223].

agreement with the refined theoretical model, however two have been experimentally observed which have not been theoretically predicted. Single-species scans indicate that these are not single-species effects, although five intraspecies ^{85}Rb Feshbach resonances have additionally been observed between $0 - 900$ G during this work [223]. Experimental and theoretical work is ongoing to understand the origin of the discrepancy.

Chapter 8

Conclusion and outlook

Three main results have been obtained during this work, they are the observation of previously unobserved interspecies $^{87}\text{Rb}^{133}\text{Cs}$ and $^{85}\text{Rb}^{133}\text{Cs}$ Feshbach resonances, and the creation of a ^{133}Cs BEC in a window where previously a condensate of this atomic species had not been made. In the following the measurements presented in the previous chapters are summarised and conclusions are drawn from the results obtained.

8.1 Summary

In this work we have highlighted the various techniques that have been used to create an apparatus capable of optically trapping an ultracold sample of Rb and Cs. Improvements made to the previous system have been discussed in detail and the larger magnetic trap loads achieved have enabled more efficient sympathetic cooling of Cs by collisions with ^{87}Rb within the magnetic trap. After the RF evaporative cooling in the magnetic trap $(5.7 \pm 0.1) \times 10^7$ $((1.13 \pm 0.06) \times 10^7)$ ^{87}Rb (^{133}Cs) atoms remain at temperature of (37.3 ± 0.8) μK ((37.8 ± 0.6) μK) and a PSD of $(7.8 \pm 0.8) \times 10^{-5}$ ($(2.6 \pm 0.3) \times 10^{-5}$), representing a significant improvement over previous results [127].

The optical dipole trap has been realigned stringently and positioned at a lower location where more atoms are trapped in the deeper potential. This change in conjunction with the improvements made to the magnetic trap evaporation allows pure single-species condensates of $(1.10 \pm 0.08) \times 10^6$ ^{87}Rb

atoms and up to 1×10^5 ^{133}Cs atoms to be produced after evaporation in the dipole trap. Many of the ^{133}Cs Feshbach resonances in the 8-57 G magnetic field region have been located, and by modifying the evaporation ramps it is possible to condense ^{133}Cs between 18.1 G and 19.6 G.

Measurements of Feshbach resonances initially focussed on previously measured single-species resonances in order to quantify the stability of the large magnetic fields produced by the system. The measurements also provided a means to improve the method of calibrating magnetic fields by driving transitions between the atomic ground states using microwaves. The performance of the system was then tested by observing previously measured interspecies ^{87}Rb^{133}Cs Feshbach resonances at magnetic fields of approximately 182 G, 197 G and 353 G [72, 121]. The observation of the resonance at 182 G highlighted the marked improvement in the performance of the system, as the width of the resonance has been measured to be (0.45 ± 0.07) G and its location defined to much greater accuracy ((181.55 ± 0.05) G).

The observation of ^{87}Rb^{133}Cs resonances predicted by theoretical modelling of previous results [121] has been performed for three previously unobserved Feshbach resonances at high-fields. This represents the first measurements of these particular resonances and additionally confirms the validity of the model potential used to predict the resonance locations, however small discrepancies between the measured location and the predictions remain.

The same theoretical potential has been used to predict the existence of many interspecies ^{85}Rb^{133}Cs resonances, all of which have not previously been experimentally observed. The inclusion of DAVLL laser locking optics has resulted in the ability to trap mixtures of ^{85}Rb and ^{133}Cs resulting in sympathetic cooling of a sufficient efficiency to optically trap a two-species mixture of these atoms. It has been possible to observe many of these resonances via rethermalisation of the ^{85}Rb and ^{133}Cs. The nature of the method also allows confirmation of the prediction that the background interspecies scattering length is very small, hence little interspecies rethermalisation takes place off resonance. Once again, the observation of these resonances and the agreement with theory [209] confirms the validity of the potential used, and the calculated interspecies scattering length.

8.2 Outlook

The long term goal of the project encompassing this work is to produce samples of ultracold ground state RbCs molecules because their dipole moment is predicted to be large [63] and the dipolar physics that can be investigated is exciting. Other interesting experiments are also possible with small modifications to the current apparatus. The remainder of this section discusses the future direction of the experiment and the steps that must be taken to achieve the goals.

8.2.1 General modifications

There are several modifications that could be made to the apparatus or experimental methods that would make a number of small improvements to the measurements taken in this work. The following is not a comprehensive or exhaustive list, its purpose is simply to highlight features that would improve the experimental results.

The efficiency with which data can be measured can be improved by increasing the reproducibility of measurements. At present it is believed that number stability is limited by a number of parameters. The first is the polaristion of the 2$^{\mathrm{nd}}$ MOT cooling beam. Although polarisation maintaining fibres are used to couple light between the laser table and the experimental bench, there is still some rotation of polarisation apparent when the fibre is placed under stress or if the temperature changes. Improved alignment can combat this effect, however including a $\lambda/4$-waveplate to correct any circular polarisation of the beam will increase the stability [224]. If the polarisation of the MOT beam is changing, the amount of power in each beam will change too due to the nature of using a PBS to split the beam. An imbalance in beam power results not only in smaller MOT numbers, but also a change in MOT position, and hence magnetic trap loading is also affected. Depending on the time scale of polarisation fluctuations the reproducibility of results may also change. A similar improvement would involve servomechanically controlling the intensity of the MOT cooling light power by monitoring the output power of the optical fibre. By stabilising the MOT beam intensity the MOT loads would become more uniform.

The method of locking the repump laser to the ^{85}Rb transitions, and the way its frequency is monitored could also be improved. At present the laser's frequency is only monitored at the time of locking, as the master laser is then locked to the cooling transition and the beat frequency between the beams would be out of the measuring device's range. To allow in situ monitoring of the repump laser's frequency a stand-alone laser has been constructed that is frequency modulation locked [187] to the ^{85}Rb repump $F = 2$ to $F' = 3$ transition. The beat frequency between this laser and the repump light is then monitored to check that the laser frequency isn't drifting, which DAVLL locked lasers are prone to do. Monitoring the laser frequency also simplifies the calculation of the expected beat frequencies presented in figure 7.3.

A more substantial improvement to the laser locking for experiments with ^{85}Rb would be to lock the laser via FM spectroscopy. The result would be a tighter lock as sub-Doppler features are resolvable using FM spectroscopy. This would require an additional laser system that is setup solely for experiments using ^{85}Rb, and then the current laser setup would be used for ^{87}Rb experiments only. The reasons for not simply constructing an FM laser lock for ^{85}Rb experiments with the current system have been explained in chapter 7, hence a new layout for these optics is being designed at the time of writing.

We have seen in chapters 3 and 4 that whilst the magnetic trap evaporative cooling has been significantly improved, the number of atoms loaded into the dipole trap has not increased by the same factor, and similarly the number of atoms within the pure ^{87}Rb and ^{133}Cs BECs has not either. Attempts to condense ^{85}Rb have also not met with success. It is believed that the reason is that the dipole trapping beams are focussed to too small a waist, hence larger beams should be utilised. This would not only increase the trap volume, it should allow more atoms to be trapped in the optical potential, but it would also decrease the collision rate within the trap. The trapping frequencies would be reduced to similar frequencies to those used in other experiments which have brought ^{133}Cs to degeneracy [10, 11]. In the tight trap of this work the harmonic trapping frequencies are very large such that three-body loss is increased. By making a modest change to the size of the beams at the trap centre to ~ 80 μm, 5.8 W of power in each beam would produce a ^{87}Rb trap depth of 52 μK, identical to that of the present trap into which atoms are loaded. There is enough laser power remaining with the current laser to produce two beams of this power. Importantly a trap of such a waist and beam power would have trap frequencies of ~ 355 Hz and ~ 105 Hz in the radial and axial directions respectively, which is approximately 20% smaller than the trap frequencies in the current loading potential. Technically it is a small change to make to the system as the expected beam size at the trap centre can be calculated using equation 2.74 if the final focussing lens' position is changed slightly, assuming that the waist position changes by the same distance. This would create a slightly asymmetric trap, however due to the Rayleigh range being ~ 1 cm and the size of the trap being much smaller the asymmetry amounts to very small changes in the trap depth on either side of the trap.

In order to condense ^{85}Rb it is hypothesised that the above changes may improve the evaporation efficiency by a large enough amount such that the BEC phase transition is reached. However, an experiment of similar construction in our group has recently condensed ^{85}Rb where the initial number of atoms trapped in the dipole trap is approximately a factor of 2 higher [8]. Hence, to increase the initial dipole trap load it may be necessary to change the dipole trap design and alignment. To create a trap with sufficient trap depth may require realignment of the beam into a bow-tie arrangement such that the power is re-used, or the use of another high power fibre laser at a wavelength of 1070 nm with larger total output power (50 W) (IPG Photonics YLR-50-LP). Given the larger possible output power and the wavelength being closer to resonance with ^{85}Rb the trap depths achievable would be much larger. Initial plans are being made now to implement these changes.

On a similar note other less drastic changes could be made to the dipole trap setup that require little or no change to the current dipole trap setup. Other work has found that dual-species evaporation to BEC of ^{87}Rb and ^{133}Cs is more efficient if the two species-are separated within the dipole trap [225]. This could be implemented by inserting a beam of a wavelength that is blue detuned to the ^{133}Cs atomic transition and red detuned from the ^{87}Rb atomic transitions. Since this wavelength would not be greatly detuned an appreciable trap depth could be realised with only the modest output power of a diode laser, however the scattering rate would be reasonably large for the same reason. Currently tests are being performed using a laser diode (EYP-RWE-0870-06010-0750-SOT01-0000) that is capable of output wavelengths between 820 nm and 880 nm. Tuning this laser to a wavelength of approximately 830 nm would produce the desired effect of separating the two atomic species, thus reducing interspecies three-body losses and increasing the lifetime in the dipole trap. The negative effect that this would have is that any sympathetic cooling within the dipole trap would be reduced.

The tunability of the aforementioned diode also makes it interesting for another reason. The diode is capable of output at a wavelength that is situated between the D_1 and D_2 transitions in ^{133}Cs. The AC Stark shift cancellation that results means that there is no effect on ^{133}Cs atoms by light at such a 'magic-wavelength' [226, 227]. Hence the dipole trap could be modified using a beam at this wavelength, potentially opening up new methods with which to sympathetically cool, or conversely to increase the ^{87}Rb trap depth whilst retaining a smaller ^{133}Cs trap depth.

8.2.2 Production of ground-state molecules

The production of ground-state molecules via the STIRAP technique first relies on the association of molecules via a Feshbach resonance. A large, entrance channel dominated resonance is typically chosen, such as the ones presented in figures 6.5 and 6.7 [52]. However, not only is a good molecule production efficiency required, a good overlap of the wavefunction of the Feshbach molecule's state and the intermediate state in the STIRAP process (see below) is required [109]. Hence other work has been performed in which RbCs Feshbach molecules have been associated by ramping over the interspecies resonances at (217.34 ± 0.05) G [109, 121] and (197.06 ± 0.05) G [228]. The resonance at 217 G is of a similar width and magnetic field as the resonance observed in this work at 197 G, hence production of a bias field stable enough should not pose a technical problem. The PSD attainable with current two-species experiments would have to be increased, however, potentially via the methods explained above.

Following the scheme proposed in reference [59] which is graphically demonstrated in figure 8.1, transfer to the molecular ground-state should be possible. Previous work has found that for molecules produced in the initial Feshbach level at 217 G the frequency of light required to drive the transition from state $|1\rangle$ to $|2\rangle$ is 1571.327941 nm. The transition to the ground-state (state $|3\rangle$) has also been identified as 982.772847 nm [109]. The photon of this second frequency removes the (3811.5755 ± 0.0016) cm^{-1} of binding energy from the excited molecule. More efficient transfer has been reported by ramping over the resonance at 197 G to produce the Feshbach molecules [228], requiring a transfer laser frequency of 192.572015 THz. Consequently the transfer to the ground state would require a laser frequency of 306.84017 THz.

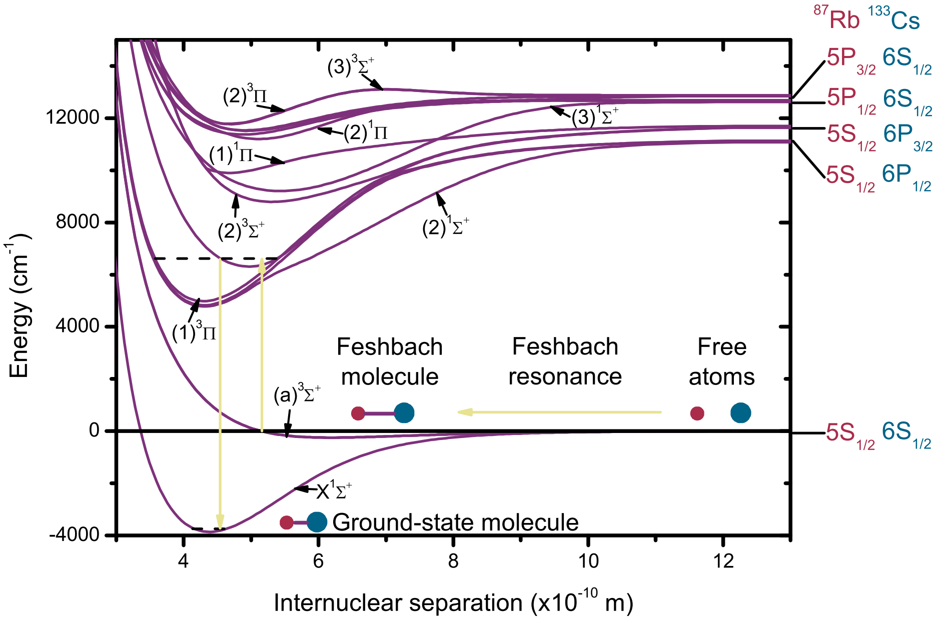

Figure 8.1: Proposed scheme for production of ground-state heteronuclear RbCs molecules via the STIRAP process [59]. Weakly bound RbCs molecules are associated via a magnetic field sweep over a Feshbach resonance, which have high vibrational excitation. Two laser frequencies then couple the initial Feshbach level and the deeply bound ground-state via an intermediate ‘dark-state’ (dashed line). This coherent process transfers the atoms into the rovibrational ground-state with a high efficiency. Molecular potentials have been taken from [229].

A stable laser system is currently being developed for the STIRAP laser transfer. Short term laser stability is to be achieved by locking the lasers to a home-built high finesse cavity, which is in turn to be locked to a laser at a wavelength of 852 nm which would be modulation transfer locked to the ^{133}Cs atomic transition. The laser light for the STIRAP transfer is then to be fibre-coupled to the experimental bench, with frequency and amplitude modulation provided by an AOM for each laser. Development of the laser system and cavity locking is currently well underway.

Given the success of the experiment in observing ^{85}Rb^{133}Cs Feshbach resonances adapting the system to be able to transfer ^{85}Rb^{133}Cs molecules to the ground-state could prove fruitful. From a Feshbach molecule viewpoint the initial PSDs need to be increased via the proposals made already. The STIRAP lasers would also require modifying to produce the correct frequencies, however the transfer may prove to be less technically challenging as the need to separate ^{85}Rb and ^{133}Cs in the dipole trap is not as great as in the case of ^{87}Rb and ^{133}Cs due to the lower background interspecies scattering length.

8.2.3 Additional experiments

Experiments that are not directly linked to the main goal of producing ground-state heteronuclear molecules are possible with the same apparatus due to the way in which it has been designed to be highly versatile. Collapse of a ^{133}Cs BEC has already been observed in this work (figure 5.8), further studies into the collapse would present the opportunity to form ^{133}Cs solitons, in a field region that is very stable. The ability to produce a ^{133}Cs BEC in the field region below 19.6 G is advantageous as it means that the bias field can be ramped smoothly through the zero in scattering length, rather than having to jump the field quickly to avoid three-body loss due to the Feshbach resonance at 19.90 G [210].

At low-field we have found it is possible to condense ^{133}Cs at s-wave scattering lengths between 55-400 a_0, a range that mimicks that at much higher fields between 883.0-900.5 G. The production of a BEC in the high-field region promises to be equally interesting as there are also no resonances there and more precision in control of the scattering length can be achieved as the rate of change of scattering length with magnetic field is lower. The potential to investigate other rich physical phenomena exists here as Efimov effects [230] have been observed in the vicinity of the broad s-wave Feshbach resonance at ~ 792 G [152].

The potential modifications outlined in section 8.2.1 have been discussed with a view to improve evaporation efficiency within the dipole trap. In the current potential it is possible to evaporate ^{85}Rb to PSDs within an order of magnitude of the BEC phase transition, hence any increase in dipole trap loads or evaporation efficiency should result in the ability to condense this atomic species. In parallel with the study of ^{133}Cs condensate collapse and soliton formation, studies of these effects in ^{85}Rb would also be possible.

As a final example of the route that could be taken during future experiments, there is the possibility to revisit the experiments described in this thesis. By evaporating to colder temperatures and measuring Feshbach resonances again it would be possible to measure resonance locations more accurately, for reasons such as there being a smaller field spread over the colder atomic cloud, and any broadening of the Feshbach resonance would be reduced as work would not be being performed in the unitarity limit. Atom numbers would also be more reproducible if interspecies atomic collisions can be reduced for two reasons. Firstly, larger atom numbers would be realised at the end of experiments due to a reduction in three-body losses, however less obviously the effects of an initial number ratio imbalance in the dipole trap would be reduced. Observation of the predicted Feshbach resonances between atoms in the $|1, -1\rangle$ and $|3, -3\rangle$ states in ^{87}Rb and ^{133}Cs respectively would increase confidence in the theoretical model too.

This list is not exhaustive, as many other experimental side roads could be taken, such as the measurement of Rabi-oscillations driven by microwaves amongst others.

8.2.4 Concluding Remarks

The work presented in this thesis outlines the large steps that have been taken by this and other atomic physics experiments that are working towards creating a quantum gas of bosonic ground-state dipolar molecules. At present all of the individual building blocks required to achieve such a feat exist, the final step is all that remains to be taken. At present the Durham mixture experiment is taking strides towards creating such ground-state molecules, however the exact isotopic mixture that work will persist with has not yet been decided. The next few years of experiments offer many exciting possibilities, however the goals are achieved.

Appendix A

Physical constants and Rb and Cs atomic data

Physical values relating to ^{87}Rb, ^{85}Rb and ^{133}Cs are given in table A.1. Values specific to an atomic transition are given for the D_2 transition, ground-state g_F values are given for the upper hyperfine level of the $5S_{1/2}$ state in ^{87}Rb and ^{85}Rb and the $6S_{1/2}$ state in ^{133}Cs and excited state g_F values are given for the upper hyperfine level of the $5P_{3/2}$ state in ^{87}Rb and ^{85}Rb and the $6^2P_{3/2}$ state in ^{133}Cs.

Figures A.1-A.3 present the energy level shift for the different F and m_F states in ^{87}Rb, ^{85}Rb and ^{133}Cs. The splitting of energy levels was used in field calibrations where RF and microwave frequency signals are used to drive transitions between the various ground and hyperfine states. Values are calculated using the Breit-Rabi equation [231]

$$\Delta E = -\frac{hV_{\mathrm{hfs}}}{2(2I+1)} - g_I \mu_{\mathrm{B}} B m_F \pm \frac{1}{2} hV_{\mathrm{hfs}} \left(1 + \frac{4m_F}{2I+1} x + x^2\right)^{1/2}, \tag{A.1}$$

where

$$x = \frac{(g_I + g_J)\,\mu_{\mathrm{B}} B}{hV_{\mathrm{hfs}}}. \tag{A.2}$$

The values used are reported in table A.1.

Property	Symbol	^{87}Rb	^{85}Rb	^{133}Cs	Units
Atomic number	A	87	85	133	u
Mass	m	1.4432×10^{-25}	1.4100×10^{-25}	2.2069×10^{-25}	kg
Nuclear spin	I	3/2	5/2	7/2	-
Ground state hyperfine splitting	V_{hfs}	6.8347	3.0357	9.1926	GHz
Nuclear g-factor	g_I	-9.9514×10^{-4}	-2.9364×10^{-4}	-3.9885×10^{-4}	-
Landé g-factor	g_J	2.0023	2.0025	2.0023	-
Ground state g_F factor	g_F	1/2	1/3	1/4	-
Excited state g_F factor	g_F	2/3	1/2	2/5	-
Natural linewidth	Γ	$2\pi\times6.0666$	$2\pi\times6.0666$	$2\pi\times5.2340$	MHz
Saturation intensity	I_{SAT}	1.6693	1.6693	1.1049	mW cm^{-2}

Table A.1: Atomic properties of ^{87}Rb, ^{85}Rb and ^{133}Cs [193, 232, 233].

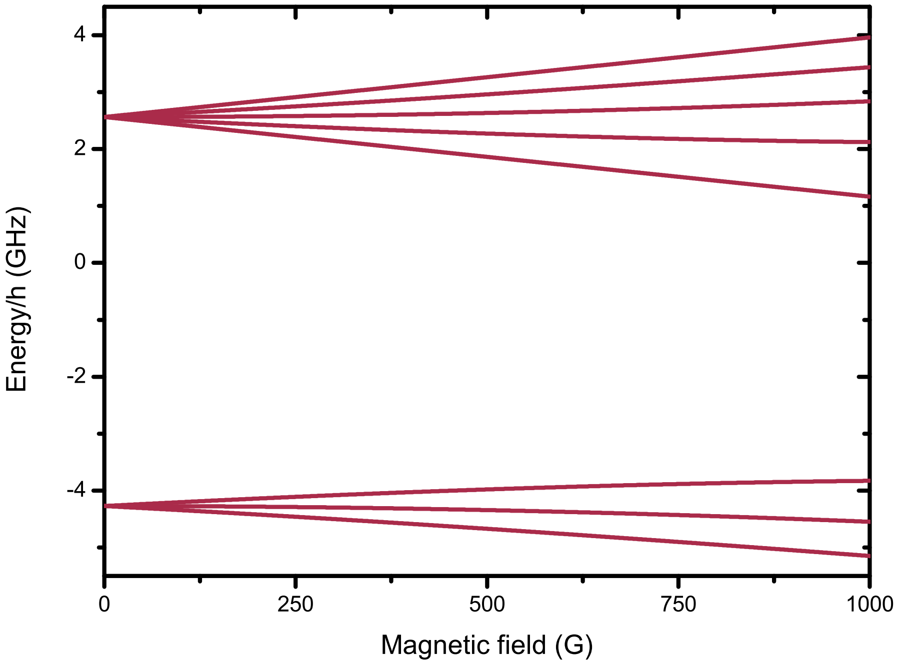

Figure A.1: Breit-Rabi diagram for ^{87}Rb for a field range of 0-1000 G.

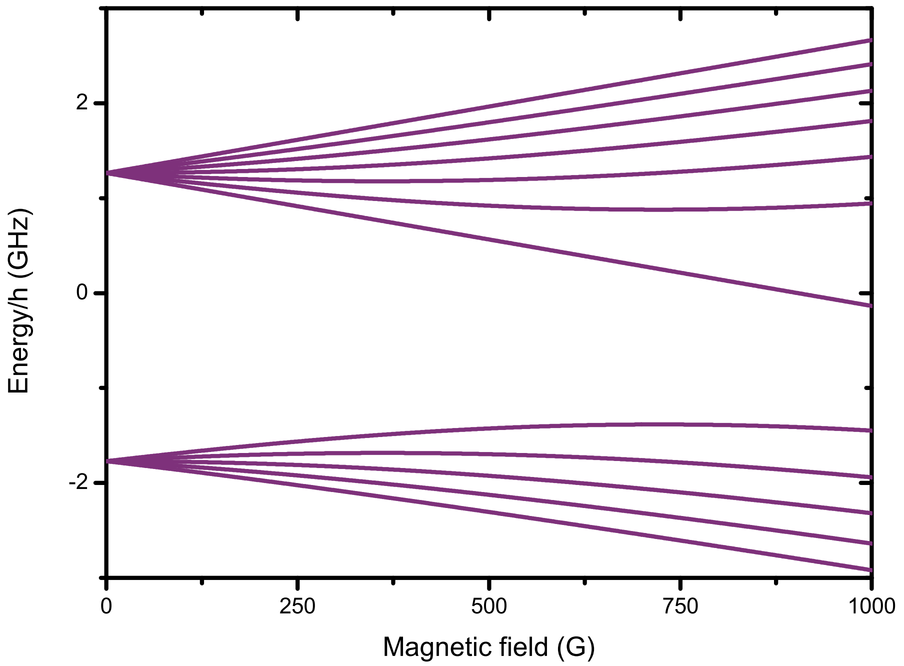

Figure A.2: Breit-Rabi diagram for ^{85}Rb for a field range of 0-1000 G.

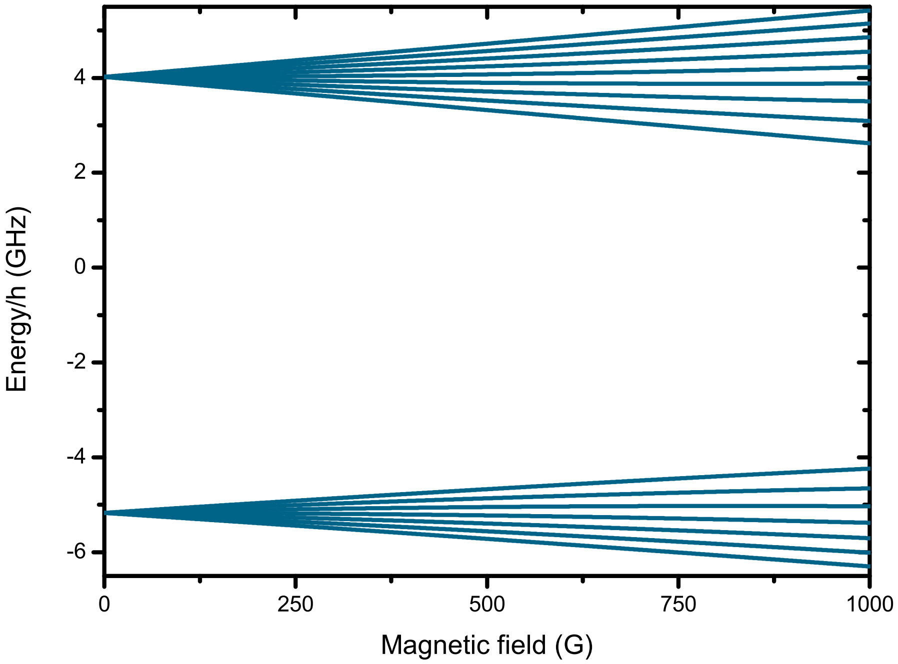

Figure A.3: Breit-Rabi diagram for ^{133}Cs for a field range of 0-1000 G.

Appendix B

Optical setup diagrams

The full optical setup used to derive the different frequencies of light required for the experiment is displayed in figure B.1 and a key to the symols used is given in figure B.2. The optical setup for the optical trap has already been displayed in figure 4.16.

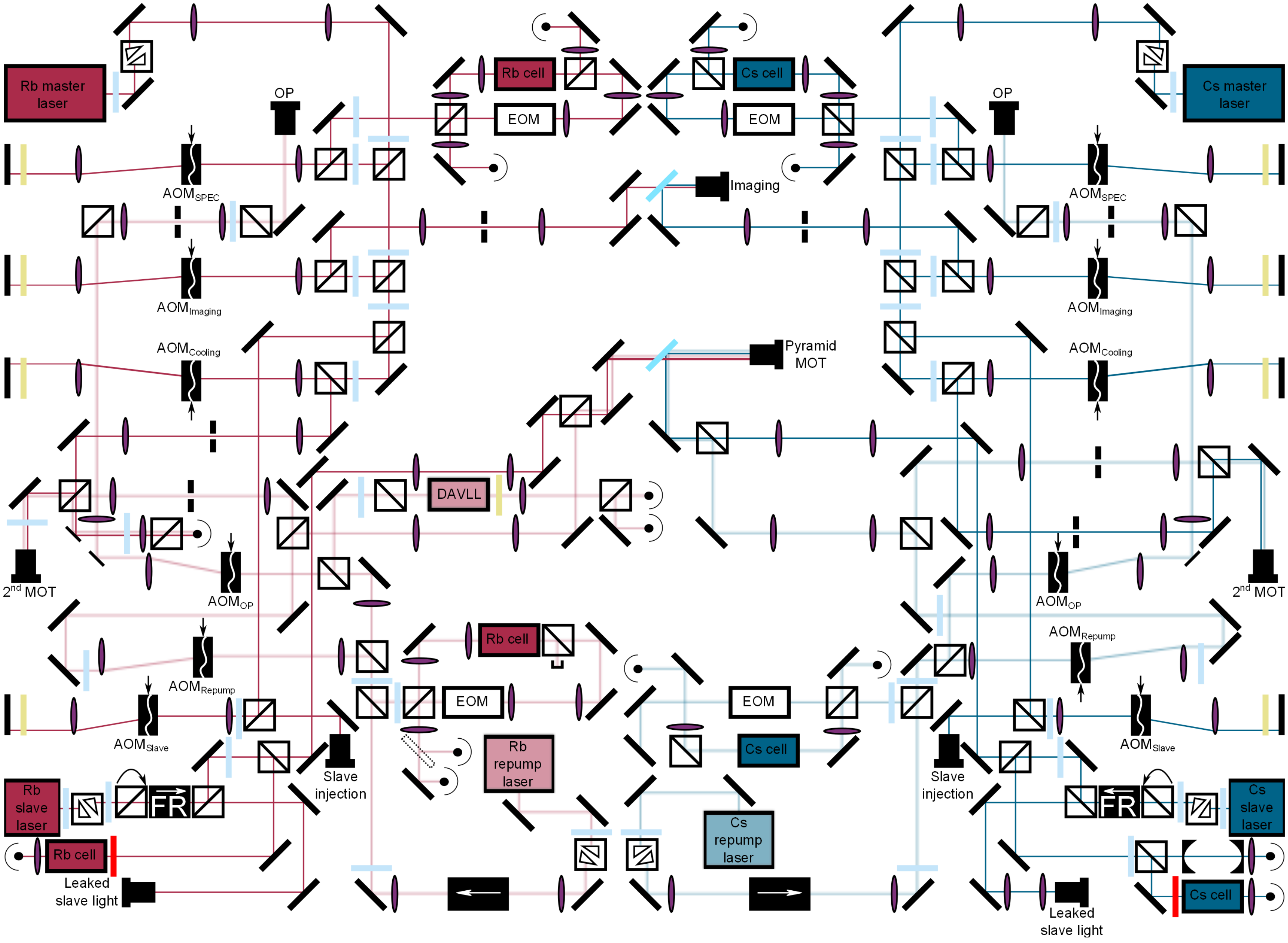

Figure B.1: Optical bench setup. Beam paths are displayed for MOT cooling and imaging (opaque lines) and repumping and optical pumping light (transparent lines) for Rb (red) and Cs (blue). Note that both Rb and Cs master lasers contain an optical isolator before the output. A key to the symbols used is given in figure B.2.

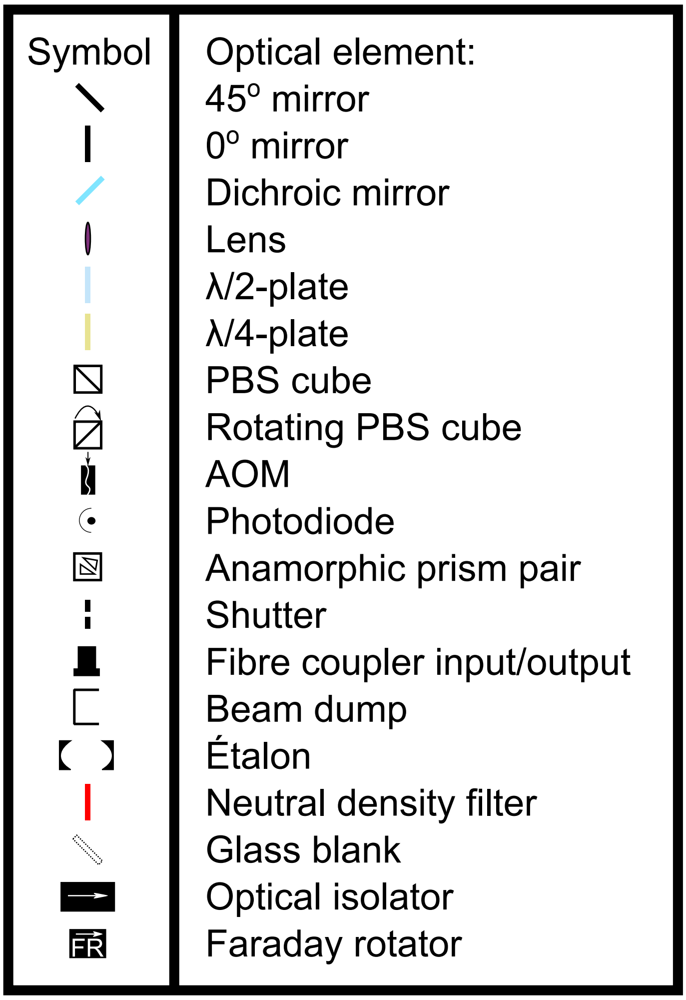

Figure B.2: A key to symobls used in optical setup diagrams throughout this work.

Appendix C

Laser electronics modifications

In this appendix modifications made to the home-built lasers are discussed in detail.

Interplay between various factors determines the specific frequency of light emitted by a laser. The wavelength of the emitted light is generally the frequency with the highest gain, whereupon stimulated emission reduces the emission in other modes, hence the laser emits on a single mode. The gain profile of the medium is set mainly by the temperature, the internal mode gain is set by the laser current and temperature, the diffraction grating gain is set by the angle of the diffraction grating and the external cavity gain is set by the distance between the diode and the diffraction grating (tuned via the piezo). It is essential therefore the tune the various factors affecting the gain such that the laser emission is of the correct wavelength (Figure C.1).

The home-built lasers used in this experiment can generally scan ~ 2 GHz, this is achieved via a sweep of the voltage applied to the piezo. Modulation of the laser current can be used to extend the mode hop free scan range of a laser, a technique often utilised in commercial lasers. The remainder of this section will discuss how this is achieved for the home-built lasers of this experiment.

In this work the frequency scan of the home-built lasers is generated by an Oxford design EW1223 laser diode stabiliser circuit. A sinusoidal signal is output to an amplifier and this signal drives the laser piezo. This is represented schematically in figure C.2. The current used to drive the home-built

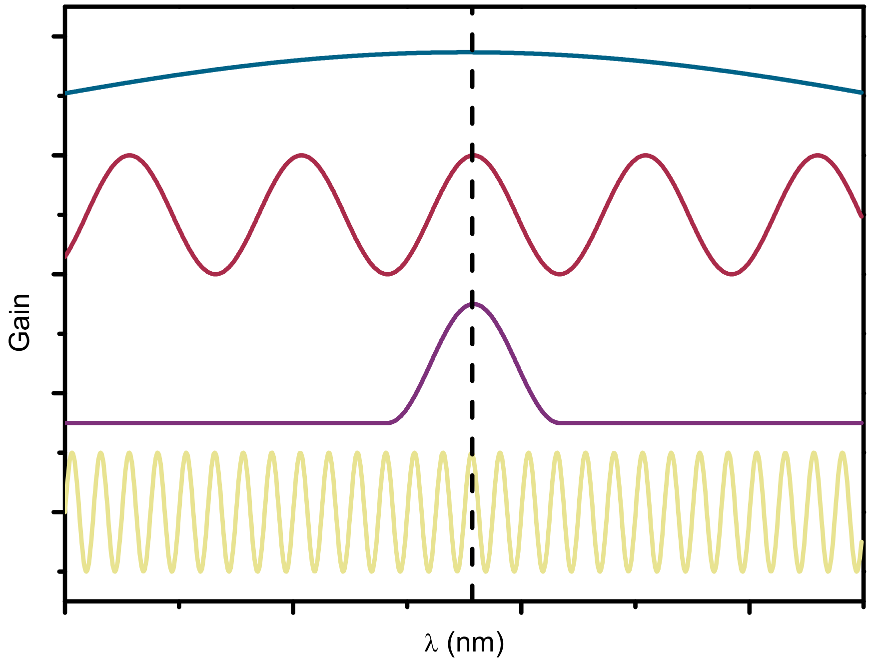

Figure C.1: Graphical representation of the various factors governing optical gain of the laser. Contributions include gain due to the medium (blue), the internal cavity (red), the diffraction grating (purple) and the external cavity (yellow). Lasing occurs at the frequency with the largest net gain. For reasons of clarity the plots have been displaced.

lasers is generated by either the EW1291 (Rb lasers) or the EW1206 (Cs lasers) laser diode supplies. In their intended setup there is no link between the current and piezo drivers. By picking off a small amount of the scan signal from the laser diode stabiliser and manipulating this signal slightly before modulating the current driver with the signal one can increase the scan range of the laser.

The signal picked off from the lock box was input directly to a separate board, which is identified as the ‘current feed forward board’. A circuit diagram of the current feed forward board is provided in figure C.3. The function of this board is simply to amplify the input signal and possibly invert the signal if required. The 100 kΩ resistor on the input was chosen such that the amount of the signal picked off from the scan was sufficient

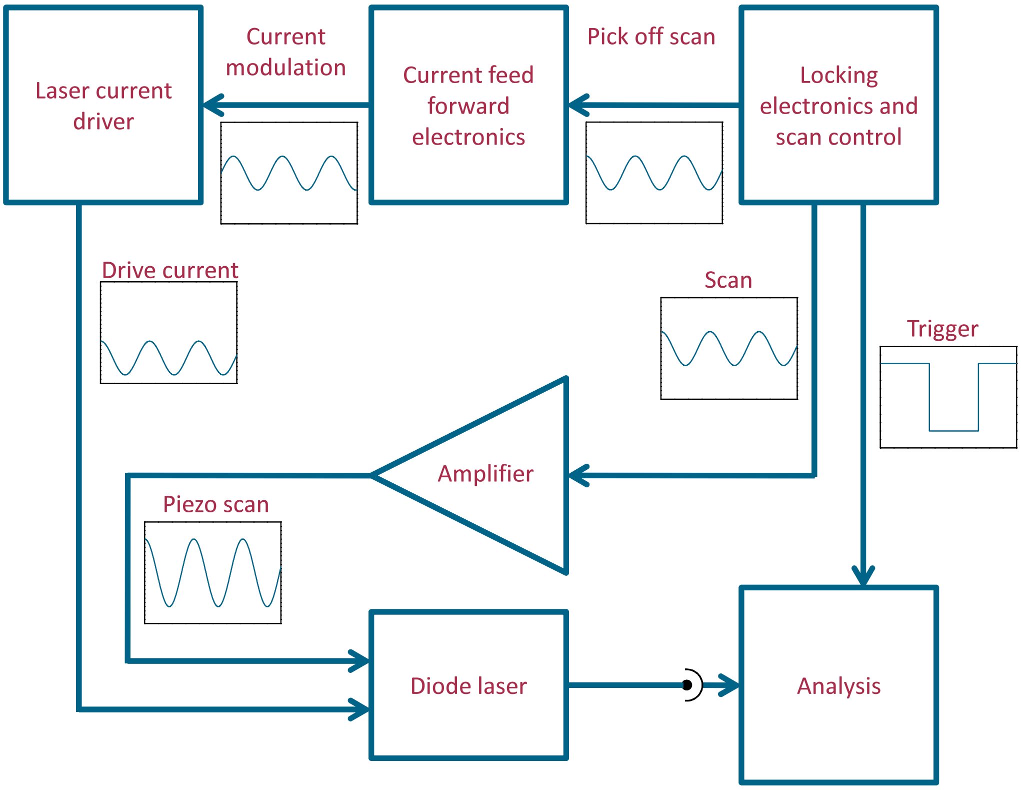

Figure C.2: Electronics setup for laser spectroscopy and locking. The general form of the signals is given by graphical representations of the signals but are not to scale, however any changes in phase or offset are displayed.

to generate an appreciable signal, but not so large that the piezo scan was impaired. The first amplifier of a TL082 op-amp amplified the signal, using a variable resistor as the gain resistor. The value of this resistor was varied to optimise the scan range of the laser, as detailed in the following. The second amplifier in the op-amp was used as an inverting ampifier of unity gain. The jumper switches were connected in order to make inclusion or exclusion of this second amplifier easier. Requirement of this second amplifier depends on how the phase changes throughout the different electronic stages, ultimately in this work the second chip was required. The output of the board was fed into the modulation input of the laser diode supplies.

To achieve the desired level of modulation on the laser current supply output the gain resistors in the modulation branch of this cicuit required modification. To this end R20 in EW1206 was changed to 200 kΩ and in EW1291 R15 and R20 were both changed to 1 MΩ resistors. For the two supplies an input modulation signal of 1 V peak-to-peak resulted in 17 mA modulation on the

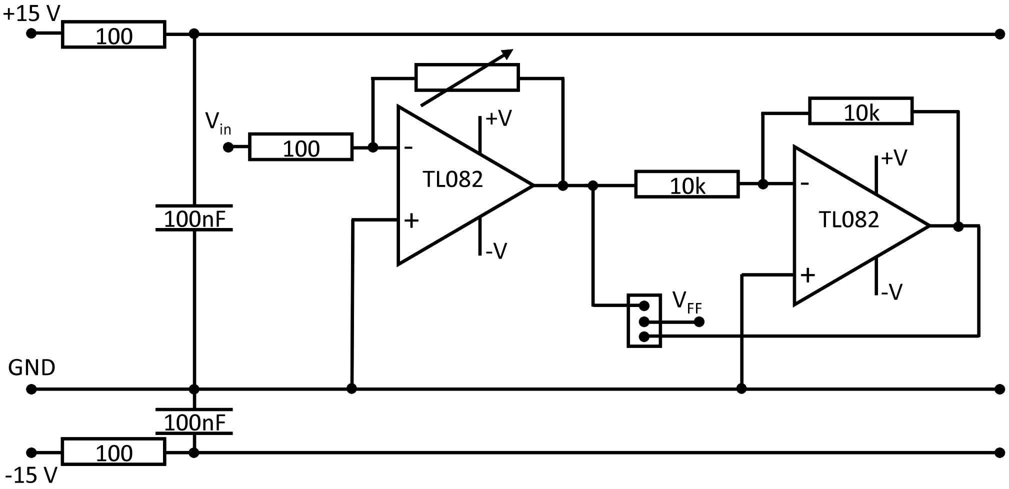

Figure C.3: Circuit diagram for the feed forward board.

output for the EW1206 circuit and for the EW1291 circuit 1 V modulation resulted in 4.33 mA modulation. A switch to allow a change between these values and '0.1×' modulation was included, however was not utilised in this work.

To maximise the amount of modulation available the variable gain resistor on the current feed forward board was varied until the scan range was maximised. Ultimately this was performed by setting up spectroscopy for the laser and analysing the signal on an étalon (of 300 MHz free spectral range). The resistance was varied until the number of étalon peaks was maximised, whilst still maintining a single mode output, detectable on the spectroscopy signal. The maximum scan range obtained was approximately 14.7 GHz, which was achieved with a modulation signal of 20.8 mA. Figure C.4 presents the scan range achieved for different modulation currents, using both the full modulation and '0.1×' modulation. Notice that with '0.1×' modulation it is not possible to maximise the scan range. The DC laser driving current here is 64 mA.

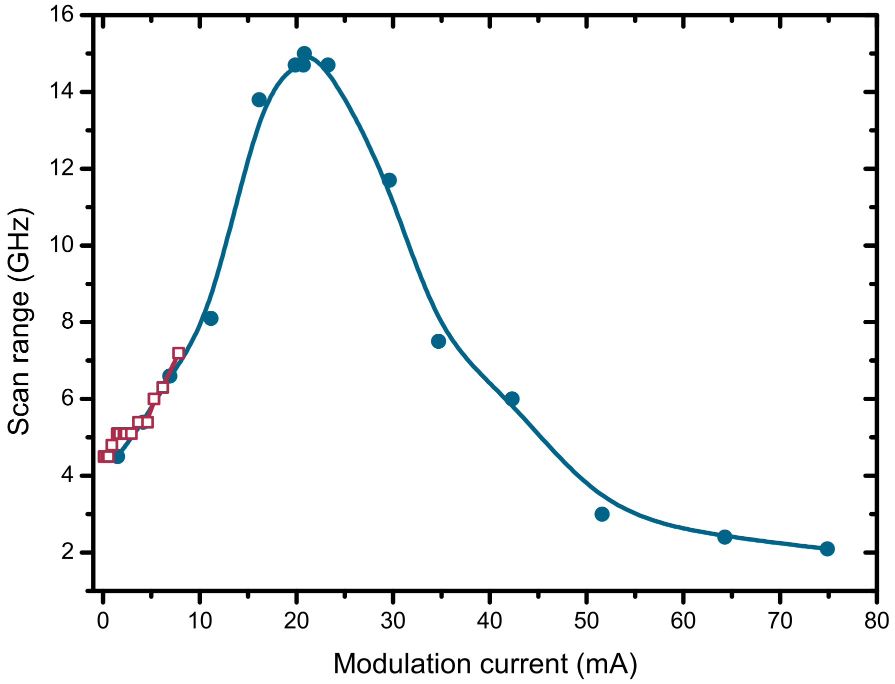

Figure C.4: Scan range (in GHz) of the laser as a function of modulation current. The maximum scan range is achieved for ∼21 mA of modulation current. The blue plot was obtained with the modulation switch set to '1×' and the red plot corresponds to data taken with the modulation set to '0.1×'.

Appendix D

Atom number calculations

This appendix outlines the different calculations required to calculate the number of atoms via the different imaging methods.

D.1 Fluorescence imaging atom number calculations

Using the experimental situation displayed in figure 3.8 it is possible to calculate the atom number trapped in the MOT. In the two-level model the power of fluorescence emitted by N atoms when illuminated by light of intensity I detuned from an atomic resonance by Δ is

$$P_{\mathrm{FLU}} = \frac{\hbar \omega_{\mathrm{L}} \Gamma}{2} \frac{(I/I_{\mathrm{SAT}})}{1 + 4(\frac{2\pi\Delta}{\Gamma})^2 + (I/I_{\mathrm{SAT}})} \tag{D.1}$$

where $\omega_{\mathrm{L}} = 2\pi c/\lambda$ is the laser frequency, Γ is the natural decay rate of the excited state and I_{SAT} is the saturation intensity of the atomic resonance, defined

$$I_{\mathrm{SAT}} = \frac{\pi h c \Gamma}{3\lambda^3}. \tag{D.2}$$

Note this two-level approach can be improved by including empirically determined constants, however this is not discussed here [234].

Assuming the solid angle subtended by the iris outline is Ω the total output power incident on the photodiode is

$$P_{\mathrm{PD}} = \frac{\Omega}{4\pi} P_{\mathrm{FLU}} \tag{D.3}$$

thus, since $\Omega = \pi d^2/4L^2$, where d is the iris diameter and L is the distance of the lens from the atoms as described by figure 3.8, we see

$$P_{\mathrm{PD}} = \frac{d^2}{16L^2} P_{\mathrm{FLU}}. \tag{D.4}$$

The voltage over the 1 MΩ resistor is then

$$V_{\mathrm{PD}} = I_{\mathrm{PD}} R = \Re(\lambda) P_{\mathrm{PD}} R, \tag{D.5}$$

where I_{PD} is the photocurrent produced, R is the resistance and $\Re(\lambda)$ is the responsivity of the photodiode at the wavelength in question. In this work for Rb $\Re(\lambda) = 0.51$ A W^{-1} and for Cs $\Re(\lambda) = 0.55$ A W^{-1}. Finally, the atom number can be calculated using

$$N = \frac{V_{\mathrm{PD}}}{\Re(\lambda) R} \frac{16L^2}{d^2} \frac{\lambda}{hc} \frac{1}{\Gamma}. \tag{D.6}$$

D.2 Absorption imaging atom number calculations

Equation D.1 can be re-written

$$P = \frac{hc}{\lambda} \Gamma_{\mathrm{SCAT}}, \tag{D.7}$$

where Γ_{SCAT} is the scattering rate of probe photons

$$\Gamma_{\mathrm{SCAT}} = \frac{\Gamma}{2} \frac{(I/I_{\mathrm{SAT}})}{1 + 4\left(\frac{2\pi\Delta}{\Gamma}\right)^2 + (I/I_{\mathrm{SAT}})}. \tag{D.8}$$

In the limit of a weak probe beam we may approximate this as

$$\Gamma_{\mathrm{SCAT}} = \frac{\Gamma}{2} I/I_{\mathrm{SAT}} = \frac{3\lambda^3}{2\pi hc} I. \tag{D.9}$$

After transmission through a layer of atoms of thickness δy and atomic density n the intensity of the probe beam is reduced by an amount δI

$$\delta I = n \delta y \Gamma_{\mathrm{SCAT}} \frac{hc}{\lambda} = \frac{3\lambda^2}{2\pi} n I \delta y, \tag{D.10}$$

hence $I = I_0 - \delta I$. Thus for a Gaussian atomic distribution the fractional intensity change is

$$\frac{\delta I}{I_0} = \frac{3\lambda^2}{2\pi} n_{\mathrm{PK}} \exp\left(\frac{-m}{2k_{\mathrm{B}}T}\left(\omega_x^2 x^2 + \omega_y^2 y^2 + \omega_z^2 z^2\right)\right)\delta y, \tag{D.11}$$

where n_{PK} is the peak density of the atoms within the harmonic trap

$$n_{\mathrm{PK}} = N\omega_x\omega_y\omega_z\left(\frac{m}{2\pi k_{\mathrm{B}}T}\right)^{3/2}. \tag{D.12}$$

We thus find that

$$\int_{I_0(x,z)}^{I(x,z)} \frac{\mathrm{dI}}{I} = \frac{3\lambda^2}{2\pi} n_{\mathrm{PK}} \exp\left(\frac{-m}{2k_{\mathrm{B}}T}\left(\omega_x^2 x^2 + \omega_z^2 z^2\right)\right)\int_{-\infty}^{\infty} \exp\left(\frac{-m}{2k_{\mathrm{B}}T}\omega_y^2 y^2\right), \tag{D.13}$$

assuming that the probe beam propagates in the y-direction. This implies

$$\ln\left(\frac{I_0(x,z)}{I(x,z)}\right) = \frac{3\lambda^2 n_{\mathrm{PK}}}{\omega_y}\sqrt{\frac{k_{\mathrm{B}}T}{2\pi m}} \exp\left(\frac{-m}{2k_{\mathrm{B}}T}\left(\omega_x^2 x^2 + \omega_z^2 z^2\right)\right). \tag{D.14}$$

Given the definition of optical depth in section 3.8.2 we can see that the right hand side of equation D.14 is simply the optical depth. Since the atomic distribution is being approximated with a Gaussian function we may assume the centre of the cloud is where the peak optical depth is situated

$$OD_{\mathrm{PK}} = \frac{3\lambda^2 n_{\mathrm{PK}}}{\omega_y}\sqrt{\frac{k_{\mathrm{B}}T}{2\pi m}}, \tag{D.15}$$

where $x = z = 0$ at this location.

Substituting equation D.19 into equation D.15 we see

$$OD_{\mathrm{PK}} = \frac{3\lambda^2 N}{4\pi^2}\frac{m\omega_x\omega_z}{k_{\mathrm{B}}T} = \frac{3\lambda^2 N}{4\pi^2}\frac{1}{\sigma_x\sigma_z}, \tag{D.16}$$

where

$$\sigma_{x,z} = \sqrt{\frac{k_{\mathrm{B}}T}{m\omega_{x,z}^2}}, \tag{D.17}$$

are the widths of the Gaussian fit to the cloud, where the density drops to a factor $1/\sqrt{e}$ of the peak density. Rearranging

$$N = \frac{4\pi^2}{3\lambda^2}\sigma_x\sigma_z OD_{\mathrm{PK}}. \tag{D.18}$$

To calculate the temperature, we first note that the peak density of the cloud can be calculated from the total atom number

$$n_{\mathrm{PK}} = N\omega_x^2\omega_y\left(\frac{m}{2\pi k_{\mathrm{B}}T}\right)^{3/2}. \tag{D.19}$$

Since $\sigma_{x,z}$ are the displacements along the $x-$ and $z-$axes at which n has dropped to $n_{\mathrm{PK}}e^{-1/2}$ we see

$$m\omega_{x,z}^2\sigma_{x,z}^2 = k_{\mathrm{B}}T, \tag{D.20}$$

which can evidently be rearranged to solve for T.

If the atomic cloud is allowed to expand for a set time-of-flight (TOF), the size of the cloud after the expansion, $\sigma_{x,z}(TOF)$, can be determined using kinematics

$$\sigma_{x,z}(TOF) = \sqrt{\sigma_{x,z}^2(0) + \omega_{x,z}^2 TOF^2\sigma_{x,z}^2(0)} = \sigma_{x,z}(0)\sqrt{1+\omega_{x,z}^2 TOF^2}, \tag{D.21}$$

where $i = x, z$ is the spatial direction in which the temperature is being calculated and $\sigma_{x,z}(0)$ is the size of the cloud in the trap. Experimentally, after a time-of-flight expansion it is $\sigma_{x,z}(TOF)$ that is measured, hence equation D.21 can be solved for $\sigma_{x,z}(0)$ and this value can be submitted into equation D.20 in order to calculate the temperature.

Appendix E

Determining the locations of Feshbach resonances

Although the variation in scattering length around a Feshbach resonance can be calculated accurately using coupled-channel calculations there is no definitive model of how this variation translates to an experimental resonance feature observed through variation in atom number and temperature. Nevertheless it is desirable to measure the location of the pole of the resonance and its width for comparison to theory. A number of approaches have been used in the literature and in this thesis depending on the form of the observed resonance. This appendix discusses the various methods used in this work to determine the locations of the resonances and their associated errors.

In this work different experimental signatures of Feshbach resonances and related features have been observed. In general inelastic losses scale with the magnitude of the scattering length (for example three-body loss scales as a^4 [138]) so that the feature expected is that of atom loss at the pole of the resonance and a peak in number where the scattering length is zero, for example, figure 6.7 exhibits this profile. However, the peak in atom number is sometimes not observed in the data, as is the case in figure 6.5. It is also possible that the pole of a narrow resonance may occur in a similar location to a broad resonance which may well modify the atom number in the vicinity of the narrow resonance, for example this occurs in figure 7.8(d). Additionally, due to high experimental densities, such as those achieved in the single species experiments in this work, the atom number can be modified when ramping the magnetic field over a Feshbach resonance in a finite time. Thus the atom number would have decreased before the final hold at the measurement field has taken place leading to asymmetries in the lineshape. This is the case for the measurement of the single species ^{87}Rb Feshbach resonance displayed in figure 6.2. Clearly, as the lineshape of each of these resonances is different, a different model needs to be applied to each set of data in order to determine the resonance centre. Note that in various cases the temperature data is also fit, however the methods described below also apply when this is the case.

For the experiments that are described in this thesis there are various processes that take place in the dipole trap that complicate the analysis of data, such as evaporative and sympathetic cooling, inelastic loss due to two- and three- body mechanisms as well as background gas collisions, and the fact that the there are not only single-species collisions occuring - the interspecies scattering properties further complicate the situation. Since no accepted mathematical model exists for the fitting of the experimental signatures of a Feshbach resonance an ansatz is made for the model that will best fit the data obtained. In this work Lorentzian and Gaussian lineshapes are used to fit the data, in addition to double Lorentzian and Gaussian functions, whereby the atom loss is fitted by a curve of negative amplitude and the peak associated with the scattering length zero is fitted by a curve of positive amplitude. For each set of data obtained in this work the text or figure captions report the function used to fit the data.

Fitting becomes more complicated in the cases where the lineshape is modified, either by other features being in that region or by the density of the atoms being so high that atoms are lost by ramping over the Feshbach resonance. In this case it is necessary to fit a reduced portion of the data. The entire data set is first fit using the chosen function and a note of the value of χ^2 is made. This is likely to be non-unity, especially where there is a large deviation of the data from the model. We then use the same model to fit to a smaller data set, usually removing the data in the outlying regions where the comparison between the model and the data is poor. This process is repeated until the value $\chi^2 \approx 1$. For cases where not all the data is fit, the solid lines displayed on the graphs indicate the regions in which the data was fit, for example this is the case in figure 6.2.

A larger complication arises from the fact that the data are being fit using a model which is not physically expected to describe the data. In other words, although the data look like the function being used to fit it, there is no accepted reason for the data to display the same trends, hence the errors obtained from statistical fits to the data are not accurate and a different method of determining errors is required. Once a fit has been made to the data the location of the centre of the feature is first determined, and the size of the errors bar in the vicinity is calculated. It is accepted that for a value to be in reasonable agreement with another value they must be separated by no more than twice the value of the error bar on the data point. That being the case the location where the number has increased (in the case of a resonance pole) or decreased (in the case of a scattering length zero) by a value that exceeds twice the error bars on the data points is located. The nearest data point for which this corresponds is then recorded, and the difference between this field and the resonance centre is reported as the error. This generally results in the error on the locations being overestimated, however this is deemed less misleading that quoting the errors on values reported via the statistical fits, which drastically tends to underestimate the errors.

Bibliography

[1] M. H. Anderson, J. R. Ensher, M. R. Matthews, C. E. Wieman, and E. A. Cornell, *Observation of Bose-Einstein Condensation in a Dilute Atomic Vapor*, Science **269**, 198 (1995).

[2] K. B. Davis *et al.*, *Bose-Einstein Condensation in a Gas of Sodium Atoms*, Phys. Rev. Lett. **75**, 3969 (1995).

[3] C. C. Bradley, C. A. Sackett, J. J. Tollett, and R. G. Hulet, *Evidence of Bose-Einstein Condensation in an Atomic Gas with Attractive Interactions*, Phys. Rev. Lett. **75**, 1687 (1995).

[4] B. DeMarco and D. S. Jin, *Onset of Fermi Degeneracy in a Trapped Atomic Gas*, Science **285**, 1703 (1999).

[5] G. Modugno *et al.*, *Bose-Einstein Condensation of Potassium Atoms by Sympathetic Cooling*, Science **294**, 1320 (2001).

[6] S. L. Cornish, N. R. Claussen, J. L. Roberts, E. A. Cornell, and C. E. Wieman, *Stable* ^{85}*Rb Bose-Einstein Condensates with Widely Tunable Interactions*, Phys. Rev. Lett. **85**, 1795 (2000).

[7] P. A. Altin *et al.*, ^{85}*Rb tunable-interaction Bose-Einstein condensate machine*, Rev. Sci. Instrum. **81**, 063103 (2010).

[8] A. L. Marchant, S. Händel, S. A. Hopkins, T. P. Wiles, and S. L. Cornish, *Bose-Einstein condensation of* ^{85}*Rb by direct evaporation in an optical dipole trap*, Phys. Rev. A **85**, 053647 (2012).

[9] A. G. Truscott, K. E. Strecker, W. I. McAlexander, G. B. Partridge, and R. G. Hulet, *Observation of Fermi Pressure in a Gas of Trapped Atoms*, Science **291**, 2570 (2001).

[10] T. Weber, J. Herbig, M. Mark, H.-C. Nägerl, and R. Grimm, *Bose-Einstein Condensation of Cesium*, Science **299**, 232 (2003).

[11] C.-L. Hung, X. Zhang, N. Gemelke, and C. Chin, *Accelerating evaporative cooling of atoms into Bose-Einstein condensation in optical traps*, Phys. Rev. A **78**, 011604(R) (2008).

[12] D. J. McCarron, H. Cho, D. L. Jenkin, M. P. Köppinger, and S. L. Cornish, *Dual-species Bose-Einstein condensate of* ^{87}*Rb and* ^{133}*Cs*, Phys. Rev. A **84**, 011603(R) (2011).

[13] S. Kraft, F. Vogt, O. Appel, F. Riehle, and U. Sterr, *Bose-Einstein Condensation of Alkaline-Earth Atoms:* ^{40}*Ca*, Phys. Rev. Lett. **103**, 130401 (2009).

[14] S. Stellmer, M. K. Tey, B. Huang, R. Grimm, and F. Schreck, *Bose-Einstein Condensation of Strontium*, Phys. Rev. Lett. **103**, 200401 (2009).

[15] Y. N. Martinez de Escobar *et al.*, *Bose-Einstein Condensation of* ^{84}*Sr*, Phys. Rev. Lett. **103**, 200402 (2009).

[16] P. G. Mickelson, Y. N. Martinez de Escobar, M. Yan, B. J. DeSalvo, and T. C. Killian, *Bose-Einstein condensation of* ^{88}*Sr through sympathetic cooling with* ^{87}*Sr*, Phys. Rev. A **81**, 051601(R) (2010).

[17] B. J. DeSalvo, M. Yan, P. G. Mickelson, Y. N. Martinez de Escobar, and T. C. Killian, *Degenerate Fermi Gas of* ^{87}*Sr*, Phys. Rev. Lett. **105**, 030402 (2010).

[18] M. K. Tey, S. Stellmer, R. Grimm, and F. Schreck, *Double-degenerate Bose-Fermi mixture of strontium*, Phys. Rev. A **82**, 011608(R) (2010).

[19] S. Stellmer, M. K. Tey, R. Grimm, and F. Schreck, *Bose-Einstein Condensation of* ^{86}*Sr*, Phys. Rev. A **82**, 041602(R) (2010).

[20] A. Griesmaier, J. Werner, S. Hensler, J. Stuhler, and T. Pfau, *Bose-Einstein Condensation of Chromium*, Phys. Rev. Lett. **94**, 160401 (2005).

[21] Y. Takasu *et al.*, *Spin-Singlet Bose-Einstein Condensation of Two-Electron Atoms*, Phys. Rev. Lett. **91**, 040404 (2003).

[22] T. Fukuhara, Y. Takasu, M. Kumakara, and Y. Takahashi, *Degenerate Fermi Gases of Ytterbium*, Phys. Rev. Lett. **98**, 030401 (2007).

[23] T. Fukuhara, S. Sugawa, and Y. Takahashi, *Bose-Einstein condensation of an ytterbium isotope*, Phys. Rev. A **76**, 051604(R) (2007).

[24] T. Fukuhara, S. Sugawa, Y. Takasu, and Y. Takahashi, *All-optical formation of quantum degenerate mixtures*, Phys. Rev. A **79**, 021601(R) (2009).

[25] S. Taie *et al.*, *Realization of a SU(2)×SU(6) System of Fermions in a Cold Atomic Gas*, Phys. Rev. Lett. **105**, 190401 (2010).

[26] S. Sugawa, R. Yamazaki, S. Taie, and Y. Takahashi, *Bose-Einstein condensate in gases of rare atomic species*, Phys. Rev. A **84**, 011610(R) (2011).

[27] D. G. Fried *et al.*, *Bose-Einstein Condensation of Atomic Hydrogen*, Phys. Rev. Lett. **81**, 3811 (1998).

[28] A. Robert *et al.*, *A Bose-Einstein Condensate of Metastable Atoms*, Science **292**, 461 (2001).

[29] F. Pereira Dos Santos *et al.*, *Bose-Einstein Condensation of Metastable Helium*, Phys. Rev. Lett. **86**, 3459 (2001).

[30] H. Deng, G. Weihs, C. Santori, J. Bloch, and Y. Yamamoto, *Condensation of Semiconductor Microcavity Exciton Polaritons*, Science **298**, 199 (2002).

[31] S. O. Demokritov *et al.*, *Bose-Einstein condensation of quasi-equilibrium magnons at room temperature under pumping*, Nature **443**, 430 (2006).

[32] J. Klaers, J. Schmitt, F. Vewinger, and M. Weitz, *Bose-Einstein condensation of photons in an optical microcavity*, Nature **468**, 545 (2010).

[33] S. Chu, *Nobel Lecture: The manipulation of neutral particles*, Rev. Mod. Phys. **70**, 685 (1998).

[34] C. Cohen-Tannoudji, *Nobel Lecture: Manipulating atoms with photons*, Rev. Mod. Phys. **70**, 707 (1998).

[35] W. D. Phillips, *Nobel Lecture: Laser cooling and trapping of neutral atoms*, Rev. Mod. Phys. **70**, 721 (1998).

[36] M.-O. Mewes *et al.*, *Output Coupler for Bose-Einstein Condensed Atoms*, Phys. Rev. Lett. **78**, 582 (1997).

[37] I. Bloch, T. W. Hänsch, and T. Esslinger, *Atom Laser with a cw Output Coupler*, Phys. Rev. Lett. **82**, 3008 (1999).

[38] W. Ketterle, *Nobel lecture: When atoms behave as waves: Bose-Einstein condensation and the atom laser*, Rev. Mod. Phys. **74**, 1131 (2002).

[39] S. L. Rolston and W. D. Phillips, *Nonlinear and quantum atom optics*, Nature **416**, 219 (2002).

[40] M. R. Matthews *et al.*, *Vortices in a Bose-Einstein Condensate*, Phys. Rev. Lett. **83**, 2498 (1999).

[41] F. Dalfovo, S. Giorgini, L. Pitaevski, and S. Stringari, *Theory of Bose-Einstein condensation in trapped gases*, Rev. Mod. Phys. **71**, 463 (1999).

[42] K. W. Madison, F. Chevy, W. Wohlleben, and J. Dalibard, *Vortex Formation in a Stirred Bose-Einstein Condensate*, Phys. Rev. Lett. **84**, 806 (2000).

[43] J. R. Abo-Shaerr, C. Raman, J. M. Vogels, and W. Ketterle, *Observation of Vortex Lattices in Bose-Einstein Condensates*, Science **292**, 476 (2001).

[44] E. A. Donley *et al.*, *Dynamics of collapsing and exploding Bose-Einstein condensates*, Nature **412**, 295 (2001).

[45] J. Denschlag *et al.*, *Generating Solitons by Phase Engineering of a Bose-Einstein Condensate*, Science **287**, 97 (2000).

[46] K. E. Strecker, G. B. Partridge, A. G. Truscott, and H. R. G., *Formation and propagation of matter-wave soliton trains*, Nature **417**, 150 (2002).

[47] K. Khaykovich *et al.*, *Formation of a Matter-Wave Bright Soliton*, Science **296**, 1290 (2002).

[48] S. L. Cornish, S. T. Thompson, and C. E. Wieman, *Formation of Bright Matter-Wave Solitons during the Collapse of Attractive Bose-Einstein Condensates*, Phys. Rev. Lett. **96**, 170401 (2006).

[49] J. Billy *et al.*, *Direct observation of Anderson localization of matter waves in a controlled disorder*, Nature **453**, 891 (2008).

[50] G. Roati *et al.*, *Anderson localisation of a non-interacting Bose-Einstein condensate*, Nature **453**, 895 (2008).

[51] C. Chin, R. Grimm, P. Julienne, and E. Tiesinga, *Feshbach Resonances in Ultracold Gases*, Rev. Mod. Phys. **82**, 1225 (2010).

[52] T. Köhler, K. Góral, and P. S. Julienne, *Production of cold molecules via magnetically tunable Feshbach resonances*, Rev. Mod. Phys. **78**, 1311 (2006).

[53] K. M. Jones, E. Tiesinga, P. D. Lett, and P. S. Julienne, *Ultracold photoassociation spectroscopy: Long-range molecules and atomic scattering*, Rev. Mod. Phys. **78**, 483 (2006).

[54] C. Chin, V. Vuletic, A. J. Kerman, and S. Chu, *High Resolution Feshbach Spectroscopy of Cesium*, Phys. Rev. Lett. **85**, 2717 (2000).

[55] P. J. Leo, C. J. Williams, and P. S. Julienne, *Collision Properties of Ultracold ^{133}Cs Atoms*, Phys. Rev. Lett. **85**, 2721 (2000).

[56] K. Xu *et al.*, *Formation of Quantum-Degenerate Sodium Molecules*, Phys. Rev. Lett. **91**, 210402 (2003).

[57] J. Herbig *et al.*, *Preparation of a Pure Molecular Quantum Gas*, Science **301**, 1510 (2003).

[58] M. Greiner, C. A. Regal, and D. S. Jin, *Emergence of a molecular Bose-Einstein condensate from a Fermi gas*, Nature **426**, 537 (2003).

[59] W. C. Stwalley, *Efficient conversion of ultracold Feshbach-resonance-related polar molecules into ultracold ground state* ($X^1\Sigma^+$ v = 0, J = 0) *molecules*, Eur. Phys. J. D **31**, 221 (2004).

[60] S. Kotochigova, E. Tiesinga, and P. S. Julienne, *Relativistic ab initio treatment of the second-order spin-orbit splitting of the* $a^3\Sigma_u^+$ *potential of rubidium and cesium dimers*, Phys. Rev. A **63**, 012517 (2000).

[61] T. Lahaye *et al.*, *d-Wave Collapse and Explosion of a Dipolar Bose-Einstein Condensate*, Phys. Rev. Lett. **101**, 080401 (2008).

[62] S. Kotochigova, P. S. Julienne, and E. Tiesinga, *Ab initio calculation of the KRb dipole moments*, Phys. Rev. A **68**, 022501 (2003).

[63] S. Kotochigova and E. Tiesinga, *Ab initio relativistic calculation of the RbCs molecule*, J. Chem. Phys. **123**, 174304 (2005).

[64] C. J. Myatt, E. A. Burt, R. W. Ghrist, E. A. Cornell, and C. E. Wieman, *Production of Two Overlapping Bose-Einstein Condensates by Sympathetic Cooling*, Phys. Rev. Lett. **78**, 586 (1997).

[65] J. Stenger *et al.*, *Spin domains in ground-state Bose-Einstein condensates*, Nature **396**, 345 (1998).

[66] I. Bloch, M. Greiner, O. Mandel, T. W. Hänsch, and T. Esslinger, *Sympathetic Cooling of* ^{85}*Rb and* ^{87}*Rb*, Phys. Rev. A **64**, 021402(R) (2001).

[67] S. B. Papp and C. E. Wieman, *Observation of Heteronuclear Feshbach Molecules from a* ^{85}*Rb*-^{87}*Rb Gas*, Phys. Rev. Lett. **97**, 180404 (2006).

[68] G. D. Telles *et al.*, *Trap loss in a two-species Rb-Cs magneto-optical trap*, Phys. Rev. A **63**, 033406 (2001).

[69] M. Anderlini *et al.*, *Sympathetic cooling and collisional properties of a Rb-Cs mixture*, Phys. Rev. A **71**, 061401(R) (2005).

[70] M. Haas *et al.*, *Species-selective microwave cooling of a mixture of rubidium and caesium atoms*, New J. Phys. **9**, 147 (2007).

[71] M. L. Harris, P. Tierney, and S. L. Cornish, *Magnetic trapping of a cold Rb-Cs atomic mixture*, J. Phys. B **41**, 035303 (2008).

[72] K. Pilch *et al.*, *Observation of interspecies Feshbach resonances in an ultracold Rb-Cs mixture*, Phys. Rev. A **79**, 042718 (2009).

[73] G. Roati, F. Riboli, G. Modugno, and M. Inguscio, *Fermi-Bose Quantum Degenerate ^{40}K-^{87}Rb Mixture with Attractive Interaction*, Phys. Rev. Lett. **89**, 150403 (2002).

[74] C. Ospelkaus, S. Ospelkaus, K. Sengstock, and K. Bongs, *Interaction-Driven Dynamics of ^{40}K-^{87}Rb Fermion-Boson Gas Mixtures in the Large-Particle-Number Limit*, Phys. Rev. Lett. **96**, 020401 (2006).

[75] K.-K. Ni *et al.*, *A High Phase-Space-Density Gas Of Polar Molecules*, Science **322**, 231 (2008).

[76] J. Catani, L. De Sarlo, G. Barontini, F. Minardi, and M. Inguscio, *Degenerate Bose-Bose mixture in a three-dimensional optical lattice*, Phys. Rev. A **77**, 011603(R) (2008).

[77] Z. Hadzibabic *et al.*, *Two-Species Mixture of Quantum Degenerate Bose and Fermi Gases*, Phys. Rev. Lett. **88**, 160401 (2002).

[78] C. Silber *et al.*, *Quantum-Degenerate Mixture of Fermionic Lithium and Bosonic Rubidium Gases*, Phys. Rev. Lett. **95**, 170408 (2005).

[79] M. Taglieber, A.-C. Voigt, T. Aoki, T. W. Hänsch, and K. Dieckmann, *Quantum Degenerate Two-Species Fermi-Fermi Mixture Coexisting with a Bose-Einstein Condensate*, Phys. Rev. Lett. **100**, 010401 (2008).

[80] J. Deiglmayr *et al.*, *Formation of Ultracold Polar Molecules in the Rovibrational Ground State*, Phys. Rev. Lett. **101**, 133004 (2008).

[81] F. Münchow, C. Bruni, M. Madalinski, and A. Görlitz, *Two-photon photoassociation spectroscopy of heteronuclear YbRb*, Phys. Chem. Chem. Phys. **13**, 18734 (2011).

[82] S. Ospelkaus, C. Ospelkaus, L. Humbert, K. Sengstock, and K. Bongs, *Tuning of Heteronuclear Interactions in a Degenerate Fermi-Bose Mixture*, Phys. Rev. Lett. **97**, 120403 (2006).

[83] M. Zaccanti *et al.*, *Control of the interaction in a Bose-Fermi mixture*, Phys. Rev. A **74**, 041605(R) (2006).

[84] S. B. Papp, J. M. Pino, and C. E. Wieman, *Tunable Miscibility in a Dual-Species Bose-Einstein Condensate*, Phys. Rev. Lett. **101**, 040402 (2008).

[85] H. Pu and N. P. Bigelow, *Properties of Two-Species Bose Condensates*, Phys. Rev. Lett. **80**, 1130 (1998).

[86] K. Mølmer, *Bose Condensates and Fermi Gases at Zero Temperature*, Phys. Rev. Lett. **80**, 1804 (1998).

[87] F. Riboli and M. Modugno, *Topology of the ground state of two interacting Bose-Einstein condensates*, Phys. Rev. A **65**, 063614 (2002).

[88] D. M. Jezek and P. Capuzzi, *Interaction-driven effects on two-component Bose-Einstein condensates*, Phys. Rev. A **66**, 015602 (2002).

[89] M. Greiner, O. Mandel, T. Esslinger, T. W. Hänsch, and I. Bloch, *Quantum phase transition from a superfluid to a Mott insulator in a gas of ultracold atoms*, Nature **415**, 39 (2002).

[90] E. Altman, W. Hofstetter, E. Demler, and M. D. Lukin, *Phase diagram of two-component bosons on an optical lattice*, New J. Phys. **5**, 113 (2003).

[91] M. Lewenstein, L. Santos, M. A. Baranov, and H. Fehrmann, *Atomic Bose-Fermi Mixtures in an Optical Lattice*, Phys. Rev. Lett. **92**, 050401 (2004).

[92] A. Kuklov, N. Prokof'ev, and B. Svistunov, *Commensurate Two-Component Bosons in an Optical Lattice: Ground State Phase Diagram*, Phys. Rev. Lett. **92**, 050402 (2004).

[93] B. K. Stuhl, B. C. Sawyer, D. Wang, and J. Ye, *Magneto-optical Trap for Polar Molecules*, Phys. Rev. Lett. **101**, 243002 (2008).

[94] E. S. Shuman, J. F. Barry, and D. DeMille, *Laser cooling of a diatomic molecule*, Nature **467**, 820 (2010).

[95] H. L. Bethlem, G. Berden, and G. Meijer, *Decelerating Neutral Dipolar Molecules*, Phys. Rev. Lett. **83**, 1558 (1999).

[96] M. R. Tarbutt *et al.*, *Slowing Heavy, Ground-State Molecules using an Alternating Gradient Decelerator*, Phys. Rev. Lett. **92**, 173002 (2004).

[97] J. D. Weinstein, R. deCarvalho, T. Guillet, B. Friedrich, and J. M. Doyle, *Magnetic trapping of calcium monohydride molecules at millikelvin temperatures*, Nature **395**, 148 (1998).

[98] M. R. Tarbutt *et al.*, *A jet beam source of cold YbF radicals*, J. Phys. B **35**, 5013 (2002).

[99] S. K. Tokunaga *et al.*, *Prospects for sympathetic cooling of molecules in electrostatic, ac and microwave traps*, Eur. Phys. J. D **65**, 141 (2011).

[100] R. Fulton, A. I. Bishop, and P. F. Barker, *Optical Stark Decelerator for Molecules*, Phys. Rev. Lett. **93**, 243004 (2004).

[101] M. Gupta and D. Herschbach, *Slowing and Speeding Molecular Beams by Means of a Rapidly Rotating Source*, J. Phys. Chem. A **105**, 1626 (2001).

[102] W. G. Doherty *et al.*, *Production of cold bromine atoms at zero mean velocity by photodissociation*, Phys. Chem. Chem. Phys. **13**, 8441 (2011).

[103] E. Narevicius *et al.*, *Towards magnetic slowing of atoms and molecules*, New J. Phys. **9**, 96 (2007).

[104] L. D. Carr, D. DeMille, R. V. Krems, and J. Ye, *Cold and ultracold molecules: science, technology and applications*, New J. Phys. **11**, 055049 (2009).

[105] M. Viteau *et al.*, *Optical Pumping and Vibrational Cooling of Molecules*, Science **321**, 232 (2008).

[106] J. M. Sage, S. Sainis, T. Bergeman, and D. DeMille, *Optical Production of Ultracold Polar Molecules*, Phys Rev. Lett. **94**, 203001 (2005).

[107] F. Lang, K. Winkler, C. Strauss, R. Grimm, and J. Hecker Denschlag, *Ultracold Triplet Molecules in the Rovibrational Ground State*, Phys. Rev. Lett. **101**, 133005 (2008).

[108] J. G. Danzl *et al.*, *An ultracold high-density sample of rovibronic ground-state molecules in an optical lattice*, Nat. Phys. **6**, 265 (2010).

[109] M. Debatin *et al.*, *Molecular spectroscopy for ground-state transfer of ultracold RbCs molecules*, Phys. Chem. Chem. Phys. **13**, 18926 (2011).

[110] D. DeMille, *Quantum Computation with Trapped Polar Molecules*, Phys. Rev. Lett. **88**, 067901 (2002).

[111] J. Ye *et al.*, *Precision measurement based on ultracold atoms and cold molecules*, Int. J. Modern Phys. D **16**, 2481 (2007).

[112] T. Zelevinsky, S. Kotochigova, and J. Ye, *Precision Test of Mass-Ratio Variations with Lattice-Confined Ultracold Molecules*, Phys. Rev. Lett. **100**, 043201 (2008).

[113] D. DeMille *et al.*, *Enhanced Sensitivity to Variation of m_e/m_p in Molecular Spectra*, Phys. Rev. Lett. **100**, 043202 (2008).

[114] S. Kotochigova, T. Zelevinsky, and J. Ye, *Prospects for application of ultracold Sr_2 molecules in precision measurements*, Phys. Rev. A **79**, 012504 (2009).

[115] J. J. Hudson, B. E. Sauer, M. R. Tarbutt, and E. A. Hinds, *Measurement of the Electron Electric Dipole Moment Using YbF Molecules*, Phys. Rev. Lett. **89**, 023003 (2002).

[116] M. T. Murphy, V. V. Flambaum, S. Muller, and C. Henkel, *Strong Limit on a Variable Proton-to-Electron Mass Ratio from Molecules in the Distant Universe*, Science **320**, 1611 (2008).

[117] A. M. Thomas, S. Hopkins, S. L. Cornish, and C. J. Foot, *Strong evaporative cooling towards Bose-Einstein condensation of a magnetically trapped caesium gas*, J. Opt. B: Quantum Semiclass. Opt. **5**, S107 (2003).

[118] A. Marte *et al.*, *Feshbach Resonances in Rubidium 87: Precision Measurement and Analysis*, Phys. Rev. Lett. **89**, 283202 (2002).

[119] C. Chin, V. Vuletic, A. J. Kerman, and S. Chu, *High precision Feshbach spectroscopy of ultracold cesium collisions*, Nucl. Phys. A **684**, 641C (2001).

[120] E. Tiesinga, M. Anderlini, and E. Arimondo, *Determination of the scattering length of the a* $^3\Sigma^+$ *potential of* ^{87}*RbCs*, Phys. Rev. A **75**, 022707 (2007).

[121] T. Takekoshi *et al.*, *Towards the production of ultracold ground-state RbCs molecules: Feshbach resonances, weakly bound states, and the coupled-channel model*, Phys. Rev. A **85**, 032506 (2012).

[122] P. S. Żuchowski and J. M. Hutson, *Reactions of ultracold alkali-metal dimers*, Phys. Rev. A **81**, 060703(R) (2010).

[123] A. V. Avdeenkov, M. Kajita, and J. L. Bohn, *Suppression of inelastic collisions of polar* $^1\Sigma$ *state molecules in an electrostatic field*, Phys. Rev. A **73**, 022707 (2006).

[124] J. Deiglmayr, M. Aymar, R. Wester, M. Weidemüller, and O. Dulieu, *Calculations of static dipole polarizabilities of alkali dimers: Prospects for alignment of ultracold molecules*, J. Chem. Phys. **129**, 064309 (2008).

[125] M. L. Harris, *Realisation of a Cold Mixture of Rubidium and Caesium*, PhD thesis, Durham University, UK, 2008.

[126] P. Tierney, *Magnetic Trapping of an Ultracold* ^{87}*Rb*-^{133}*Cs Atomic Mixture*, PhD thesis, Durham University, UK, 2009.

[127] D. J. McCarron, *A Quantum Degenerate Mixture of* ^{87}*Rb and* ^{133}*Cs*, PhD thesis, Durham University, UK, 2011.

[128] J. Weiner, V. S. Bagnato, S. Zilio, and P. S. Julienne, *Experiments and theory in cold and ultracold collisions*, Rev. Mod. Phys. **71**, 1 (1999).

[129] I. Bloch, J. Dalibard, and W. Zwerger, *Many-body physics with ultracold gases*, Rev. Mod. Phys. **80**, 885 (2008).

[130] C. J. Pethick and H. Smith, *Bose-Einstein Condensation in Dilute Gases* (Cambridge University Press, UK, 2002).

[131] J. Dalibard, *Collisional dynamics of ultra-cold atomic gases*, Proceedings of the International School of Physics Enrico Fermi, Varenna, Course CXL , 1 (1998).

[132] C. J. Joachain, *Quantum Collision Theory* (North-Holland, The Netherlands, 1983).

[133] C. Chin, *Cooling, Collisions And Coherence Of Cold Cesium Atoms In A Trap*, PhD thesis, Stanford University, USA, 2001.

[134] A. Derevianko, W. R. Johnson, M. S. Safronova, and J. F. Babb, *High-Precision Calculations of Dispersion Coefficients, Static Dipole Polarizabilities, and Atom-Wall Interaction Constants for Alkali-Metal Atoms*, Phys. Rev. Lett. **82**, 3589 (1999).

[135] M. Marinescu and H. R. Sadeghpour, *Long-range potentials for two-species alkali-metal atoms*, Phys. Rev. A **59**, 390 (1999).

[136] D. Guéry-Odelin, J. Söding, P. Desbiolles, and J. Dalibard, *Is Bose-Einstein condensation of atomic cesium possible?*, Europhys. Lett. **44**, 25 (1998).

[137] D. M. Stamper-Kurn *et al.*, *Optical Confinement of a Bose-Einstein Condensate*, Phys. Rev. Lett. **80**, 2027 (1998).

[138] T. Weber, J. Herbig, M. Mark, H.-C. Nägerl, and R. Grimm, *Three-Body Recombination at Large Scattering Lengths in an Ultracold Atomic Gas*, Phys. Rev. Lett. **91**, 123201 (2003).

[139] E. A. Burt *et al.*, *Coherence, Correlations, and Collisions: What One Learns about Bose-Einstein Condensates from Their Decay*, Phys. Rev. Lett. **79**, 337 (1997).

[140] J. Söding *et al.*, *Three-body decay of a rubidium Bose-Einstein condensate*, App. Phys. B **69**, 257 (1999).

[141] J. Stenger *et al.*, *Strongly Enhanced Inelastic Collisions in a Bose-Einstein Condensate near Feshbach Resonances*, Phys. Rev. Lett. **82**, 2422 (1999).

[142] J. L. Roberts, N. R. Claussen, S. L. Cornish, and C. E. Wieman, *Magnetic Field Dependence of Ultracold Inelastic Collisions near a Feshbach Resonance*, Phys. Rev. Lett. **85**, 728 (2000).

[143] A. H. Thomas, *Ultra-cold Collisions and Evaporative Cooling of Caesium in a Magnetic Trap*, PhD thesis, University of Oxford, UK, 2004.

[144] S. Inouye *et al.*, *Observation of Feshbach resonances in a Bose-Einstein condensate*, Nature **392**, 151 (1998).

[145] A. J. Moerdijk, B. J. Verhaar, and A. Axelsson, *Resonances in ultracold collisions of* ^{6}*Li*, ^{7}*Li, and* ^{23}*Na*, Phys. Rev. A **51**, 4852 (1995).

[146] J. M. Hutson and P. Soldán, *Molecule formation in ultracold atomic gases*, Int. Rev. Phys. Chem. **25**, 497 (2006).

[147] G. Thalhammer *et al.*, *Long-Lived Feshbach Molecules in a Three-Dimensional Optical Lattice*, Phys. Rev. Lett. **96**, 050402 (2006).

[148] J. G. Danzl *et al.*, *Quantum Gas of Deeply Bound Ground State Molecules*, Science **321**, 1062 (2008).

[149] K.-K. Ni, *A Quantum Gas Of Polar Molecules*, PhD thesis, University of Colorado, USA, 2009.

[150] M. Gustavsson *et al.*, *Control of Interaction-Induced Dephasing of Bloch Oscillations*, Phys. Rev. Lett. **100**, 080404 (2008).

[151] P. Julienne, *Rb-Cs scattering length data*, Private Communication (2011).

[152] M. Berninger *et al.*, *Universality of the Three-Body Parameter for Efimov States in Ultracold Cesium*, Phys. Rev. Lett. **107**, 120401 (2011).

[153] F. Ferlaino, *Cs resonance measurements*, Private Communication (2011).

[154] T. Kraemer *et al.*, *Evidence for Efimov quantum states in an ultracold gas of caesium atoms*, Nature **440**, 315 (2006).

[155] S. N. Bose, *Plancks Gesetz und Lichtquantenhypothese*, Z. Phys. **26**, 178 (1924).

[156] A. Einstein, *Quantentheorie des einatomigen idealen Gases. Zweite Abhandlung*, Sitzungber. Preuss. Akad. Wiss. **3**, 3 (1925).

[157] J. F. Annett, *Superconductivity, Superfluids and Condensates* (Oxford University Press, UK, 2004).

[158] B. D. Esry, C. H. Greene, J. J. P. Burke, and J. L. Bohn, *Hartree-Fock Theory for Double Condensates*, Phys. Rev. Lett. **78**, 3594 (1997).

[159] T. Kraemer *et al.*, *Optimized production of a cesium Bose-Einstein Condensate*, Appl. Phys. B **79**, 1013 (2004).

[160] L. Pitaevski and S. Stringari, *Bose-Einstein Condensation* (Clarendon Press, UK, 2003).

[161] Y. Castin and R. Dum, *Bose-Einstein Condensates in Time Dependent Traps*, Phys. Rev. Lett. **77**, 5315 (1996).

[162] D. L. Jenkin *et al.*, *Bose-Einstein condensation of ^{87}Rb in a levitated crossed dipole trap*, Eur. Phys. J. D **65**, 11 (2011).

[163] E. Majorana, *Atomi orientati in campo magnetico variabile*, Nuovo Cimento **9**, 43 (1932).

[164] W. Petrich, M. Anderson, J. R. Ensher, and E. A. Cornell, *Stable, Tightly Confining Magnetic Trap for Evaporative Cooling of Neutral Atoms*, Phys. Rev. Lett. **74**, 3352 (1995).

[165] Y.-J. Lin, A. R. Perry, R. L. Compton, I. B. Spielman, and J. V. Porto, *Rapid production of ^{87}Rb Bose-Einstein condensates in a combined magnetic and optical potential*, Phys. Rev. A **79**, 063631 (2009).

[166] M. D. Barrett, J. A. Sauer, and M. S. Chapman, *All-Optical Formation of an Atomic Bose-Einstein Condensate*, Phys. Rev. Lett. **87**, 010404 (2001).

[167] H. W. Cho, D. J. McCarron, D. L. Jenkin, M. P. Köppinger, and S. L. Cornish, *A high phase-space density mixture of ^{87}Rb and ^{133}Cs: towards ultracold heteronuclear molecules*, Eur. Phys. J. D **65**, 125 (2011).

[168] W. Ketterle and N. J. van Druten, *Evaporative cooling of trapped atoms*, Adv. At., Mol., Opt. Phys. **37**, 181 (1996).

[169] S. Chu, J. E. Bjorkholm, A. Ashkin, and A. Cable, *Experimental Observation of Optically Trapped Atoms*, Phys. Rev. Lett. **57**, 314 (1986).

[170] K. Bergmann, H. Theuer, and B. W. Shore, *Coherent population transfer among quantum states of atoms and molecules*, Rev. Mod. Phys. **70**, 1003 (1998).

[171] N. Hoang, N. Zahzam, S. Guibal, and P. Pillet, *Collisions in a cesium hybrid optical and magnetic trap*, Eur. Phys. J. D **36**, 95 (2005).

[172] D. M. Stamper-Kurn *et al.*, *Reversible Formation of a Bose-Einstein Condensate*, Phys. Rev. Lett. **81**, 2194 (1998).

[173] G. Kleine Büning, J. Will, W. Ertmer, C. Klempt, and J. Arlt, *A slow gravity compensated Atom Laser*, Appl. Phys. B **100**, 117 (2010).

[174] R. Grimm, M. Weidemüller, and Y. B. Ovchinnikov, *Optical Dipole Traps For Neutral Atoms*, Adv. At., Mol., Opt. Phys. **42**, 95 (2000).

[175] M. S. Safronova, B. Arora, and C. W. Clark, *Frequency-dependent polarizabilities of alkali-metal atoms from ultraviolet through infrared spectral regions*, Phys. Rev. A **73**, 022505 (2006).

[176] K. J. Weatherill, *A CO_2 Laser Lattice Experiment for Cold Atoms*, PhD thesis, Durham University, UK, 2007.

[177] G. B. Brooker, *Modern Classical Optics* (Oxford University Press, UK, 2003).

[178] A. E. Siegman, *New developments in laser resonators*, Proc. SPIE **1224**, 2 (1990).

[179] K. I. Lee, J. A. Kim, H. Noh, and W. Jhe, *Single-beam atom trap in a pyramidal and conical hollow mirror*, Opt. Lett. **21**, 1177 (1996).

[180] J. J. Arlt, O. Maragò, S. Webster, S. Hopkins, and C. J. Foot, *A pyramidal magneto-optical trap as a source of slow atoms*, Opt. Commun. **157**, 303 (1998).

[181] A. Camposeo *et al.*, *A cold cesium atomic beam produced out of a pyramidal funnel*, Opt. Commun. **200**, 231 (2001).

[182] M. P. Fewell, B. W. Shore, and K. Bergmann, *Coherent Population Transfer among Three States: Full Algebraic Solutions and the Relevance of Non Adiabatic Processes to Transfer by Delayed Pulses*, Aust. J. Phys. **50**, 281 (1997).

[183] N. Lundblad *et al.*, *Two-species cold atomic beam*, J. Opt. Soc. Am. B **21**, 3 (2004).

[184] R. K. Raj, D. Bloch, J. J. Snyder, G. Camy, and M. Ducloy, *High-Frequency Optically Heterodyned Saturation Spectroscopy Via Resonant Degenerate Four-Wave Mixing*, Phys. Rev. Lett. **44**, 1251 (1980).

[185] J. H. Shirley, *Modulation transfer processes in optical heterodyne saturation spectroscopy*, Opt. Lett. **7**, 537 (1982).

[186] D. J. McCarron, S. A. King, and S. L. Cornish, *Modulation transfer spectroscopy in atomic rubidium*, Meas. Sci. Technol. **19**, 105601 (2008).

[187] G. C. Bjorklund, *Frequency-modulation spectroscopy: a new method for measuring weak absorptions and dispersions*, Opt. Lett. **5**, 15 (1980).

[188] M. Gehrtz, G. C. Bjorklund, and E. A. Whittaker, *Quantum-limited laser frequency-modulation spectroscopy*, J. Opt. Soc. Am. B **2**, 1510 (1985).

[189] B. Chéron, H. Gilles, J. Hamel, O. Moreau, and H. Sorel, *Laser Frequency Stabilisation Using Zeeman Effect*, J. Physique III **4**, 401 (1994).

[190] K. L. Corwin, Z.-T. Lu, C. F. Hand, R. J. Epstein, and C. E. Wieman, *Frequency-stabilized diode laser with the Zeeman shift in an atomic vapor*, Appl. Opt. **37**, 3295 (1998).

[191] W. Petrich, M. H. Anderson, J. R. Ensher, and E. A. Cornell, *Behavior of atoms in a compressed magneto-optical trap*, J. Opt. Soc. Am. B **11**, 1332 (1994).

[192] S. Chu, L. Hollberg, J. E. Bjorkelm, A. Cable, and A. Ashkin, *Three-Dimensional Viscous Confinement and Cooling of Atoms by Resonance Radiation Pressure*, Phys. Rev. Lett. **55**, 48 (1985).

[193] D. A. Steck, *Rubidium 87 D Line Data,* available online `http://steck.us/alkalidata` (revision 2.1.4), 2010.

[194] W. Ketterle, D. S. Durfee, and D. M. Stamper-Kurn, *Making, probing and understanding Bose-Einstein condensates*, Proceedings of the International School of Physics Enrico Fermi, Varenna, Course CXL , 67 (1999).

[195] M. R. Matthews, *Two-Component Bose-Einstein Condensation*, PhD thesis, University Of Colorado, USA, 1994.

[196] E. Hecht, *Optics* (Addison Wesley, USA, 2002).

[197] A. Arnold, *Preparation and Manipulation of an* ^{87}*Rb Bose-Einstein Condensate*, PhD thesis, University of Sussex, UK, 1999.

[198] P. O. Schmidt *et al.*, *Continuous loading of cold atoms into a Ioffe-Pritchard magnetic trap*, J. Opt. B: Quantum Semiclass. Opt. **5**, S170 (2003).

[199] H. Ott, J. Fortagh, G. Schlotterbeck, A. Grossmann, and C. Zimmermann, *Bose-Einstein Condensation in a Surface Microtrap*, Phys. Rev. Lett. **87**, 230401 (2001).

[200] T. A. Savard, K. M. O'Hara, and J. E. Thomas, *Laser-noise-induced heating in far-off resonance optical traps*, Phys. Rev. A **56**, R1095 (1997).

[201] M. J. Gibbons, S. Y. Kim, K. M. Fortier, P. Ahmadi, and M. S. Chapman, *Achieving very long lifetimes in optical lattices with pulsed cooling*, Phys. Rev. A **78**, 043418 (2008).

[202] A. M. Bacon, H. Z. Zhao, L. J. Wang, and J. E. Thomas, *Microwatt shot-noise measurement*, Appl. Opt. **34**, 5326 (1995).

[203] J. Kobayashi, Y. Izumi, M. Kumakura, and Y. Takahashi, *Stable all-optical formation of Bose-Einstein condensate using pointing-stabilized optical trapping beams*, Appl. Phys. B **83**, 21 (2006).

[204] B. Fröhlich *et al.*, *Two-frequency acousto-optic modulator driver to improve the beam pointing stability during intensity ramps*, Rev. Sci. Instrum. **78**, 043101 (2007).

[205] L. D. Landau and E. M. Lifschitz, *Mechanik* (Akademie-Verlag, Berlin, 1964).

[206] C. Adams, H. J. Lee, N. Davidson, M. Kasevich, and S. Chu, *Evaporative Cooling in a Crossed Dipole Trap*, Phys. Rev. Lett. **74**, 3577 (1995).

[207] D. Comparat *et al.*, *Optimized production of large Bose-Einstein condensates*, Phys. Rev. A **73**, 043410 (2006).

[208] J.-F. Clément *et al.*, *All-optical runaway evaporation to Bose-Einstein condensation*, Phys. Rev. A **79**, 061406(R) (2009).

[209] J. Hutson, *Rb-Cs scattering length data*, Private Communication (2010).

[210] C. Chin *et al.*, *Precision Feshbach spectroscopy of ultracold Cs_2*, Phys. Rev. A **70**, 032701 (2004).

[211] J. L. Roberts *et al.*, *Controlled Collapse of a Bose-Einstein Condensate*, Phys. Rev. Lett. **86**, 4211 (2001).

[212] R. V. Krems, W. C. Stwalley, and B. Friedrich, *Cold molecules: Theory, experiments, applications* (CRC Press, USA, 2009).

[213] M. Berninger, *Universal three- and four-body phenomena in an ultracold gas of cesium atoms*, PhD thesis, Universität Innsbruck, Austria, 2011.

[214] C. Buggle, J. Léonard, W. von Klitzing, and J. T. M. Walraven, *Interferometric Determination of the s and d-Wave Scattering Amplitudes in ^{87}Rb*, Phys. Rev. Lett. **93**, 173202 (2004).

[215] T. Volz, S. Dürr, S. Ernst, A. Marte, and G. Rempe, *Characterization of elastic scattering near a Feshbach resonance in ^{87}Rb*, Phys. Rev. A **68**, 010702(R) (2003).

[216] S. Dürr, T. Volz, and G. Rempe, *Dissociation of ultracold molecules with Feshbach resonances*, Phys. Rev. A **70**, 031601(R) (2004).

[217] M. Berninger *et al.*, *Universality of the Three-Body Parameter for Efimov States in Ultracold Cesium*, arXiv:1106.3933v1 (2011).

[218] E. Wille *et al.*, *Exploring an Ultracold Fermi-Fermi Mixture: Interspecies Feshbach Resonances and Scattering Properties of ^6Li and ^{40}K*, Phys. Rev. Lett. **100**, 053201 (2008).

[219] C. R. Le Sueur, *Rb-Cs scattering length data*, Private Communication (2011).

[220] D. J. McCarron, I. G. Hughes, P. Tierney, and S. L. Cornish, *A heated vapor cell unit for dichroic atomic vapor laser lock in atomic rubidium*, Rev. Sci. Instrum. **78**, 093106 (2007).

[221] N. R. Claussen, *Dynamics of Bose-Einstein condensates near a Feshbach resonance in ^{85}Rb*, PhD thesis, University of Colorado, USA, 2003.

[222] P. Julienne, *^{85}Rb scattering length data*, Private Communication (2010).

[223] H.-W. Cho *et al.*, *Feshbach spectroscopy of an ultracold mixture of ^{85}Rb and ^{133}Cs,* In preparation, (2012).

[224] P. Arora, A. Agarwal, and A. Sen Gupta, *Simple alignment technique for polarisation maintaining fibres*, Rev. Sci. Instrum. **82**, 125103 (2011).

[225] A. D. Lercher *et al.*, *Production of a dual-species Bose-Einstein condensate of Rb and Cs atoms*, Eur. Phys. J. D **65**, 3 (2011).

[226] V. V. Flambaum, V. A. Dzuba, and A. Derevianko, *Magic Frequencies for Cesium Primary-Frequency Standard*, Phys. Rev. Lett. **101**, 220801 (2008).

[227] N. Lundblad, M. Schlosser, and J. V. Porto, *Experimental observation of magic-wavelength behavior of ^{87}Rb atoms in an optical lattice*, Phys. Rev. A **81**, 031611(R) (2010).

[228] H.-C. Nägerl, *STIRAP measurements*, Private Communication (2012).

[229] A. R. Allouche *et al.*, *Theoretical electronic structure of RbCs revisited*, J. Phys. B **33**, 2307 (2000).

[230] E. Braaten and H.-W. Hammer, *Efimov physics in cold atoms*, Annals of Physics **322**, 120 (2007).

[231] G. Breit and I. I. Rabi, *Measurement of Nuclear Spin*, Phys. Rev. **38**, 2082 (1931).

[232] D. A. Steck, *Rubidium 85 D Line Data,* available online `http://steck.us/alkalidata` (revision 2.1.4), 2010.

[233] D. A. Steck, *Cesium D Line Data,* available online at `http://steck.us/alkalidata` (revision 2.1.4), 2010.

[234] C. G. Townsend *et al.*, *Phase-space density in the magneto-optical trap*, Phys. Rev. A **52**, 1423 (1995).